UNIVERSIDADE FEDERAL DO PARÁ
INSTITUTO DE GEOSCIÊNCIAS
PROGRAMA DE PÓS-GRADUAÇÃO EM GEOLOGIA E GEOQUÍMICA

TESE DE DOUTORADO Nº 135

PETROLOGIA E EVOLUÇÃO CRUSTAL DA PORÇÃO CENTRAL DO DOMÍNIO CANAÃ DOS CARAJÁS, PROVÍNCIA CARAJÁS

Tese apresentada por:

BHRENNO MARANGOANHA
Orientador: Prof. Dr. Davis Carvalho de Oliveira (UFPA)

BELÉM
2018

Dados Internacionais de Catalogação-na-Publicação (CIP) de acordo com ISBD
Biblioteca do Instituto de Geociências/UFPA-Belém-PA

M311p Marangoanha, Bhrenno.

Petrologia e evolução crustal da porção central do Domínio Canaã dos Carajás, Província Carajás / Bhrenno Marangoanha. – 2018.
xxx, 193 f. : il. ; 30 cm

Orientador: Davis Carvalho de Oliveira
Tese (Doutorado) – Universidade Federal do Pará, Instituto de Geociências, Programa de Pós-Graduação em Geologia e Geoquímica, Belém, 2018.

1. Granulitos - Carajás, Região de (PA). 2. Piroxênio - Carajás, Região de (PA). 3. Geologia estratigráfica - Arqueano. 4. Geocronologia. 5. Isótopos. I. Título.

CDD 22. ed. - 552.4098115

Elaborada por Hélio Braga Martins - CRB-2/698

Universidade Federal do Pará
Instituto de Geociências
Programa de Pós-Graduação em Geologia e Geoquímica

PETROLOGIA E EVOLUÇÃO CRUSTAL DA PORÇÃO CENTRAL DO DOMÍNIO CANAÃ DOS CARAJÁS, PROVÍNCIA CARAJÁS

TESE APRESENTADA POR:

BHRENNO MARANGOANHA

Como requisito parcial à obtenção de Grau de Doutor em Ciências na Área de GEOQUÍMICA E PETROLOGIA

Data de Aprovação: 14/09/2018

Banca Examinadora:

Prof. Dr. Davis Carvalho de Oliveira
Orientador – UFPA

Prof. Dr. Roberto Dall'Agnol
Membro – UFPA/Vale (ITV)

Prof. Dr. Moacir José Buenano Macambira
Membro – UFPA

Prof.ª Dra. Lena Virgínia Soares Monteiro
Membro – USP

Prof. Dr. Carlos Eduardo de Mesquita Barros
Membro – UFPR

À minha família e amigos

AGRADECIMENTOS

A elaboração deste trabalho não teria sido possível sem a colaboração, estímulo e empenho de diversas pessoas e instituições:

Agradeço inicialmente à Universidade Federal do Pará (UFPA), juntamente com o Programa de Pós-Graduação em Geologia e Geoquímica (PPGG), pela infraestrutura e suporte financeiro necessários à realização deste trabalho.

Ao orientador prof. Dr. Davis Carvalho de Oliveira, pela oportunidade, apoio e incentivo durante esses anos.

Ao Conselho Nacional de Desenvolvimento Científico e Tecnológico (CNPq) pela concessão da bolsa de estudo (Processo 163874/2014-0) e taxa de bancada.

Ao Fundo de Amparo à Pesquisa do Estado do Pará (FAPESPA; Processo 133/2008-0), e aos projetos de pesquisa Vale/FAPESPA (ICAAF n. 053/2011) e INCT/GEOCIAM (CNPq/FAPESPA/CAPES/PETROBRAS; Processo 573733/2008-2), pelo apoio financeiro durante a execução desta pesquisa.

Ao Grupo de Pesquisa Petrologia de Granitoides (GPPG) do Instituto de Geociências (IG-UFPA), em especial aos integrantes da sala 3, pelas conversas, companhia e auxílio durante esses anos.

Ao professor Marco Antonio Galarza, do Laboratório de Geologia Isotópica (Pará-Iso) da UFPA, pelo suporte na aquisição dos dados de U-Pb LA-MC-ICP-MS e Sm-Nd, além da ajuda no tratamento dos dados de Lu-Hf referente aos granitoides híbridos de Vila União.

Ao Laboratório de Geocronologia de Alta Resolução da Universidade de São Paulo (GeoLab/USP), em especial ao corpo técnico Dr. Kei Sato e Dr. Artur Takashi Onoe, além da secretária Silvana Macedo, pelo grande auxílio prestado durante as etapas de aquisição de dados U-Pb SHRIMP.

Ao professor Cristiano Lana e à geóloga Ana Alkmim, do Laboratório de Geologia Isotópica da Universidade Federal de Ouro Preto (UFOP), pelo apoio na obtenção das análises de U-Pb LA-SF-ICP-MS e de Lu-Hf em zircão.

Ao professor Cláudio Nery Lamarão e à Gisele T. Marques, pelo suporte na aquisição das imagens BSE e CL de alta resolução dos cristais de zircão, no Laboratório de Microanálises do IG-UFPA.

Aos professores do PPGG, pelo conhecimento transmitido.

Aos funcionários da secretaria do programa de pós-graduação, pelo auxílio nas questões administrativas e pela atenção dispensada.

Aos demais funcionários do IG, pela dedicação e atenção.

Gostaria de expressar toda a minha gratidão e apreço a todos aqueles que, direta ou indiretamente, contribuíram para que esta tarefa se tornasse realidade. A todos quero manifestar os meus sinceros agradecimentos.

“A ciência nunca resolve um problema sem criar pelo menos outros dez.”

George Bernard Shaw

RESUMO

Mapeamento geológico realizado na porção central do Domínio Canaã dos Carajás, parte norte da Província Carajás, aliado a dados geoquímicos, geocronológicos (U-Pb) e isotópicos (Nd e Hf), permitiu a individualização de novas unidades anteriormente agrupadas no Complexo Xingu e na Suíte Plaquê, além da redefinição de limites de outras unidades. Com isso, foram identificados os seguintes eventos responsáveis pela atual configuração deste segmento de crosta: (1) no Mesoarqueano, entre 3,05 e 2,93 Ga, houve a formação de crosta TTG a partir de fusão parcial de platôs oceânicos (basalto enriquecidos) (previamente transformada em granada anfibolito) em ambiente de subducção; (2) ainda no Mesoarqueano, entre 2,89 e 2,84 Ga, já em ambiente colisional, é registrado grande retrabalhamento crustal e consequente formação de granitos anatéticos, os quais foram responsáveis pelo espessamento crustal nessa região. Isto induziu o metamorfismo regional de alta temperatura, de fácies granulito da crosta TTG, formando os ortogranulitos félsicos da área de Ouro Verde; e (3) já no Neoarqueano, entre 2,75 e 2,73 Ga, esse segmento de crosta sofreu processo de delaminação, provocado pelo "descolamento" da base da crosta, que induziu underplating máfico, promovendo a geração de magmas enderbíticos pela fusão parcial da crosta inferior (granulito máfico mesoarqueano). Esse evento também promoveu a fusão do manto superior, que gerou o magma percursor do Diopsídio-Norito Pium. A colocação desse magma máfico no embasamento mesoarqueano, de composição granulítica félsica, induziu sua fusão, gerando líquidos leucogranítico. Ambos os líquidos, de origem mantélica e crustal, sofreram processos de mistura e mingling, que originaram os granitoides híbridos de Vila União. A colocação de seus magmas máfico, além daquele formador dos enderbíticos, foi facilitada por estruturas pré-existentes de orientação E–W, formadas no Mesoarqueano, atribuídas ao desenvolvimento do Cinturão de Cisalhamento Itacaiúnas. A geração e a consolidação dos magmas neoarqueanos ocorreram sob regime tectônico transpressional dominado por cisalhamento puro, atribuindo uma natureza sin-tectônica a essas rochas. Esse regime tectônico foi o responsável pela exumação da crosta granulítica mesoarqueana da área de Ouro Verde por sistemas imbricados. Dados isotópicos de Lu-Hf dos núcleos magmáticos dos cristais de zircão dos ortogranulitos félsicos mesoarqueanos mostram valores Hf-T_{DM2} entre 3,44 e 3,15 Ga, e εHf(t) variando de -1,7 a 3,0, e sugere fonte juvenil para seu protólito. Os enderbitos neoarqueanos apresentam valores de Hf-T_{DM2} entre 3,46 e 3,29 Ga, e εHf(t) entre -4,8 e -1,9, que indica a participação de uma fonte com maior tempo de residência crustal. O comportamento isotópico de Hf dos granitoides neoarqueanos híbridos de Vila União [Hf-

T_{DM2} entre 3,46 e 3,29 Ga, e εHf(t) entre -4,6 e -1,8] é bastante semelhante ao dos enderbitos, sendo esses dados interpretados como representante somente do membro félsico (leucogranito) da mistura. Tal afirmação é corroborada pelos dados isotópicos de Nd, que confirmam a evolução desses granitoides híbridos pela mistura em diferentes proporções de componentes juvenis (membro máfico – magma do Diopsídio-Norito Pium) com componentes reciclados (membro félsico – magma leucogranítico).

Palavras-chave: Granulito. Enderbito. Mesoarqueano. Neoarqueano. Geocronologia. Isótopos. Carajás.

ABSTRACT

Geological mapping allied to microstructural, petrological, geochemical, geochronological (Pb-Pb and U-Pb) and isotopic (Nd and Hf) data performed in the central portion of the Canaã dos Carajás domain, Carajás province (Amazonian craton, Brazil) allowed the individualization of new geological units previously grouped into Xingu complex and Plaquê suite, besides the redefinition of the limits from the other units already mapped as well. Therefore, four main events have been described in this portion of the province as follows: (1) in the Mesoarchean, between 3.0 and 2.93 Ga, TTG crust was generated in an N–S subduction setting by partial melting of LILE-enriched basalts (formerly transformed in garnet amphibolite), similar to oceanic plateau basalts; (2) at 2.89–2.84 Ga, in collisional setting, large volume of anatectic granites was formed and contributed to crustal thickening, which triggered granulite-facies high-temperature metamorphism in the TTG crust, forming the felsic granulite from Ouro Verde area; and (3) in the Neoarchean, between 2.75 and 2.73 Ga, this portion of the crust underwent delamination process (detachment from the weak lower crust), promoting generation of enderbitic melt by partial melting of the lower crust (Mesoarchean mafic granulite). This event also promoted partial melting of the upper crust, which generated the Pium diopside-norite magma. The emplacement of this mafic melt into the Mesoarchean basement (felsic granulite) triggered their melting, and generates a leucogranitic melt, which both melts (mafic and felsic) mixed and mingled, then forming the Vila União hybrid granitoids. The emplacement of the mafic (Pium diopside-norite), felsic magmas (leucogranites), and their mixed products (Vila União hybrid granitoids), as well as the enderbitic magmas, was channeled into pre-existing Mesoarchean shear zones trending E–W in the crust (Itacaiúnas shear zone). The generation and consolidation of the Neoarchean magmas occurred in pure shear-dominated transpressional tectonic regime, giving rise to the syn-tectonic nature on these granitoids. This tectonic regime was responsible to the exhumation of the Mesoarchean granulitic crust in a regional imbricated system. Lu- Lu-Hf isotope data of magmatic cores of the zircons from the Mesoarchean felsic granulites from Ouro Verde area show Hf-T_{DM2} of 3.44–3.15 Ga and εHf(t) values between -1.7 and 3.0, which suggests juvenile source. The Neoarchean enderbite presents Hf-T_{DM2} of 3.46–3.29 Ga and lower εHf(t) values (between -4.8 and -1.9), and points to a longer crustal residence time to the enderbitic rocks. Hf-isotopic behavior for the Vila União granitoids [Hf-T_{DM2} between 3.46 and 3.29 Ga, and εHf(t) between -4.6 and -1.8] is quite similar to the enderbites, which the hybrid granitoids Hf-isotopic data are interpreted as being only the felsic end-member

(leucogranitic magma) from the mixing system. Such statement is supported by the Nd-isotopic data, which confirm the hybrid Neoarchean granitoids evolution from mixing at different proportions of juvenile (mafic end-member – Pium diopside-norite magma) and recycled components (felsic end-member – leucogranitic magma).

Keywords: Granulite. Enderbite. Mesoarchean. Neoarchean. Geochronology. Isotopes. Carajás.

LISTA DE ILUSTRAÇÕES

CAPÍTULO 1

Figura 1 - Mapa de localização e principais acessos da área de estudo. 4

Figura 2 - Mapa de localização do Cráton Amazônico no continente sul-americano, evidenciando as províncias geocronológicas segundo (a) Santos (2003) e (b) Tassinari & Macambira (2004), com destaque para a Província Carajás. 5

Figura 3 - Mapa geológico da Província Carajás (modificado de Gabriel *et al*. 2014), mostrando a mais recente compartimentação tectônica segundo Dall'Agnol *et al*. (2013; linhas tracejadas). 6

CAPÍTULO 2

Figure 1 - Geological map of the Carajás province, showing the limits between the Rio Maria, Sapucaia and Canaã dos Carajás domains, besides Carajás basin (dashed lines; modified from Gabriel *et al*. 2014). 25

Figure 2 - Geological sketch map of the studied area, showing lower hemisphere equal-area (Schmidt-Lambert) stereographic plots of poles to foliation and mineral lineation of the Neoarchean granitoids from Vila União area. Detailed interpretative cross-section A-A' is shown (see map for location). 28

Figure 3 - Mesoscopic-scale features of the granitoids from Vila União area, showing the structural aspects printed on these rocks, characterized by (a) absent, (b) moderate and (c) well-developed mylonitic foliation; (d) mafic enclaves strongly flattened oriented parallel to the foliation. 29

Figure 4 - Q-A-P and Q-(A+P)-M plots for the granitoids from Vila União area (Le Maître *et al*. 2002). Granitic series and their evolutionary trends from Lameyre and Bowden (1982) and Bowden *et al*. (1984): 1 (tholeiitic), 2 (calc-alkaline tonalitic or trondhjemitic), 3 (calc-alkaline granodioritic), 4 (subalkaline monzonitic or shoshonitic) and 5 (alkaline and peralkaline). 30

Figure 5 - Mesoscopic-scale aspects of the (a) leucogranite, (b) biotite-hornblende monzogranite, (c) biotite-hornblende tonalite and (d) quartz diorite varieties of the Neoarchean granitoids from Vila União area, showing the dominant coarse- to medium-grained with heterogranular texture in the first three ones (a, b and c), whereas the less evolved variety (d) tends to exhibit a fine-grained one. 31

Figure 6 - Photomicrographic microstructural features of low-grade domain granitoids from Vila União area. (a) Euhedral to subeuhedral square-shaped feldspar porphyroclasts and subeuhedral amphibole crystals; (b) detail of subeuhedral amphibole associated with small amounts of biotite; (c) quartz showing undulose extinction with subgrains formation by bulging recrystallization (BLG); (d) brittle fracturing in plagioclase porphyroclast; (e) submagmatic microfracture in plagioclase filled with opaque mineral-amphibole-biotite aggregates; and (f) biotite crystal with smooth kink bands. Photomicrographs (a), (c), (d) and (e) under crossed nicols, and (b) and (f) under parallel nicols. Abbreviations: Amp (amphibole), Bt (biotite), Op (opaque minerals), Pl (plagioclase) and Qz (quartz). 33

Figure 7 - Photomicrographic microstructural features of medium-grade domain granitoids from Vila União area. Plagioclase porphyroclasts showing (a) deformation twinning, (b) deformation by kinking and (c) extinction undulose; (d) core-mantle structures in plagioclase porphyroclasts formed by bulging recrystallization (BLG); (e) flame-perthite in K-feldspar porphyroclast; and (f) quartz entirely recrystallized by subgrain rotation recrystallization (SGR). All of photomicrographs under crossed nicols. Abbreviations: Kfs (K-feldspar), Pl (plagioclase) and Qz (quartz).....34

Figure 8 - Photomicrographic microstructural features of high-grade domain granitoids from Vila União area. (a) and (b) showing the general aspect of this domain, which their minerals are practically fully recrystallized; plagioclase showing subgrain rotation recrystallization (SGR) and quartz occurs mostly like ribbon that indicates growth by high-temperature grain boundary migration recrystallization (GBM); (c) and (d) displaying amphibole porphyroclasts with strain shadows of biotite and opaque minerals; (e) large quartz grains with inclusions of titanite, which confirms GBM-recrystallization in quartz; and (f) 'window' microstructure formed by quartz and biotite crystals. Photomicrographs (a), (b), (c), (e) and (f) under crossed nicols, and (d) under parallel nicols. Abbreviations: Amp (amphibole), Bt (biotite), Pl (plagioclase), Qz (quartz) and Tit (titanite).....35

Figure 9 - Harker diagrams (in wt.%) for the granitoids from Vila União area, compared with Vila Jussara (Dall'Agnol *et al.* 2017) and Planalto suites (Feio *et al.* 2012), Estrela granitic complex and Igarapé Gelado granite (Barros *et al.* 2001, 2009), Serra do Rabo granite (Sardinha *et al.* 2006) and Matok pluton (Laurent *et al.* 2014). Abbreviations: QzD (quartz diorite), BtHbTn (biotite-hornblende tonalite), BtHbMzG (biotite-hornblende monzogranite) and LcGr (leucogranite).....38

Figure 10 - Harker diagrams for selected trace elements for granitoids from Vila União area, compared with Vila Jussara (Dall'Agnol *et al.* 2017) and Planalto suites (Feio *et al.* 2012), Estrela granitic complex and Igarapé Gelado granite (Barros *et al.* 2001, 2009), Serra do Rabo granite (Sardinha *et al.* 2006) and Matok pluton (Laurent *et al.* 2014). All trace elements are in ppm, and SiO_2 in wt.%. Abbreviations: QzD (quartz diorite), BtHbTn (biotite-hornblende tonalite), BtHbMzG (biotite-hornblende monzogranite) and LcGr (leucogranite). 39

Figure 11 - (a and c) REE and (b and d) multi-element patterns of the granitoids from Vila União area, with values normalized to C1 chondrite and pyrolite (McDonough & Sun 1995), respectively, compared with average compositions of Vila Jussara (Dall'Agnol *et al.* 2017) and Planalto suites (Feio *et al.* 2012), Estrela granitic complex and Igarapé Gelado granite (Barros *et al.* 2001, 2009), Serra do Rabo granite (Sardinha *et al.* 2006) and Matok pluton (Laurent *et al.* 2014).....40

Figure 12 - Geochemical diagrams for granitoids from Vila União area: (a) P-Q diagram from Debon & Le Fort (1988); (b) Normative feldspar triangle (O'Connor 1965) with fields from Barker (1979); (c) FeO*/(FeO* + MgO) vs. SiO_2 after Frost *et al.* (2001) showing the ferroan character of the studied rocks, with dotted line from Miyashiro (1974); (d) A/CNK [Al_2O_3/($CaO+Na_2O+K_2O$)] vs. A/NK [Al_2O_3/(Na_2O+K_2O)] diagram (Shand 1950); (e) Na_2O+K_2O-CaO (MALI) vs. SiO_2 diagram (Frost *et al.* 2001); and (f) major element discrimination diagram for leucogranites (Sylvester 1989). Abbreviations: QzD (quartz diorite), BtHbTn (biotite-hornblende tonalite), BtHbMzG (biotite-hornblende monzogranite) and LcGr (leucogranite). 41

Figure 13 - (a) Discrimination of tectonic environment diagram (Pearce *et al.* 1984); (b) discrimination diagram proposed by Whalen *et al.* (1987) showing the A-type affinities of the studied rocks; (c) CaO/($FeO^*+MgO+TiO_2$) vs. Al_2O_3 diagram (Dall'Agnol and Oliveira 2007); and d) Nb–Y–Ce diagram. A1 and A2 fields after Eby (1992). Abbreviations: QzD (quartz diorite), BtHbTn (biotite-hornblende tonalite), BtHbMzG (biotite-hornblende monzogranite), LcGr (leucogranite), HFCA (highly fractionated calc-alkaline), WPG (within-plate granites), VAG (volcanic arc granites), syn-COLG (syn-collision granites), ORG (oceanic ridge granites), FG (fractionated granites) and OGT (unfractionated granites). 42

Figure 14 - SHRIMP U-Pb concordia diagram for zircons from the leucomonzogranite BDE 19-B and its representative cathodoluminescence images of zircons. Yellow circles represent the position of the laser spot, scaled to size. Ages are displayed as $^{207}Pb/^{206}Pb$ ages (in Ma) with 1σ error. Error ellipses are 1σ.....45

Figure 15 - LA-MC-ICP-MS U-Pb concordia diagram for zircons from the quartz diorite BVD 12-B and its representative backscattered electron images of zircons. Yellow circles represent the position of the laser spot, scaled to size. Ages are displayed as $^{207}Pb/^{206}Pb$ ages (in Ma) with 1σ error. Error ellipses are 1σ.....46

Figure 16 - Single zircon Pb-evaporation age plot for the sample RDM 9-C from Vila União area. The vertical gray bars correspond the error for each zircon grain and horizontal dashed black line represents the mean age for sample. Each analysis (gray bar) is accompanied by its respective zircon image (photomicrograph). Abbreviation: Zr (zircon).....47

Figure 17 - (a) Al_2O_3 vs. FeO*/(FeO*+MgO) diagram (fields from Dall'Agnol & Oliveira 2007). (b) Al^{IV} vs. Fe/(Fe+Mg) diagram showing the compositional variation of amphibole for the studied granitoids (low, intermediate and high fO_2 fields according to Anderson & Smith 1995). (c) $Al^{IV}+Al^{VI}$ vs. Fe/(Fe+Mg) diagram showing the compositional variation of biotite for the Vila União granitoids. Variation of Fe/(Fe+Mg) in ilmenite and magnetite series, and ΔFMQ values from Anderson *et al.* (2008). Data source: Planalto (Cunha *et al.* 2016) and Vila Jussara suites (Dall'Agnol *et al.* 2017). Figure modified from Oliveira *et al.* (2018).....49

Figure 18 - Representative deformational model showing pure shear-dominated transpression, which explains the vertical maximum stretching and vertical lineation, with sinistral sense, printed on the Neoarchean granitoids from Vila União area. Full arrows indicate horizontal contraction and half arrows indicate synchronous sinistral shearing. Model based on Sanderson & Marchini (1984) and Greene & Schweickert (1995).....51

CAPÍTULO 3

Figure 1 - Geological map of the Carajás province, showing the limits between the Rio Maria, Sapucaia and Canaã dos Carajás domains, besides Carajás basin (dashed lines; modified from Gabriel *et al.* 2014).....66

Figure 2 - Geological sketch map of the studied area, showing lower hemisphere equal-area (Schmidt-Lambert) stereographic plots of poles to foliation and mineral lineation of the Neoarchean granitoids from Vila União area. Detailed interpretative cross-section A-A' is shown (see map for location). 69

Figure 3 - Scheme showing the gradational compositional variation in the granitoids from Vila União area. There is a clear decrease in the mafic mineral content of the figure (a) (diorite) towards (f) (leucomonzogranite), and increase of K-feldspar and quartz in the same sense. The disposition of the sample photos suggests a trend of evolution, given for several degrees of interaction between (a) mafic and (f) felsic end-members. 70

Figure 4 - Mesoscopic-scale features of the granitoids from Vila União area, showing the relationship contact aspects present in these rocks. (a) Mafic enclaves strongly flattened, with sharp contact and ellipsoidal shape, oriented parallel to the foliation, and the occurrence of felsic back-veins into the MME; (b) rounded mafic enclave hosted in the felsic granite; (c) disaggregation of MME rim into the felsic rock, like a typical disequilibrium reaction; (d) plagioclase and K-feldspar phenocrysts from the granite into the MME, result of mechanical transfer of phenocrysts from the felsic host magma into the mafic magma; (e) advanced mechanical transfer of minerals, with a more efficient mineral exchange between the MME (mafic end-member) and the host granitoid (felsic end-member), tending to reach a homogeneous mixture; and (f) some portions of the mixing process still records immiscibility aspects. 72

Figure 5 - Representative photomicrographs of hybridization textures in the granitoids from Vila União area. (a) Plagioclase ocellus rimmed by amphibole, biotite and opaque minerals, showing these mafic minerals nucleating on plagioclase substrate; (b) biotite and amphibole inclusion zone in plagioclase phenocryst, located between the inner portion of plagioclase (Na-rich) to the outer one (Ca-rich); (c) spike zone in plagioclase: note the Ca-rich zone (spike) underlined by sericitization; (d) mafic clots (aggregates), quite common in all varieties of the studied rocks, composed by amphibole, biotite, opaque minerals and orthopyroxene; occurrences of (e) stubby and (f) acicular apatite crystals included in feldspar phenocrysts. All of photomicrographs under crossed nicols. Abbreviations: Amp (amphibole); Ap (apatite); Bt (biotite); Op (opaque minerals); Opx (orthopyroxene); Plc (calcic plagioclase); Pls (sodic plagioclase). 74

Figure 6 - Q-A-P and Q-(A+P)-M plots for the granitoids from Vila União area (Le Maître *et al.* 2002). Granitic series and their evolutionary trends from Lameyre & Bowden (1982) and Bowden *et al.* (1984): 1 (tholeiitic), 2 (calc-alkaline tonalitic or trondhjemitic), 3 (calc-alkaline granodioritic), 4 (subalkaline monzonitic or shoshonitic) and 5 (alkaline and peralkaline). 78

Figure 7 - Photomicrographic microstructural features of low-, medium- and high-grade domains granitoids from Vila União area. Low-grade domain: (a) euhedral to subeuhedral square-shaped feldspar porphyroclasts and subeuhedral amphibole crystals; (b) quartz showing undulose extinction with subgrains formation by bulging recrystallization (BLG); (c) brittle fracturing in plagioclase porphyroclast; (d) submagmatic microfracture in plagioclase filled with opaque mineral-amphibole-biotite aggregates. Medium-grade domain: (e) plagioclase porphyroclast showing deformation by kinking; (f) plagioclase crystals showing core-mantle structures, and quartz entirely recrystallized by subgrain rotation recrystallization (SGR). High-grade domain: (g) general aspect of this domain, which their minerals are practically fully recrystallized, with plagioclase showing SGR and quartz occurring mostly like ribbon, indicating growth by high-temperature grain boundary migration recrystallization (GBM); (h) 'window' microstructure formed by quartz and biotite crystals. All photomicrographs under crossed nicols. Abbreviations: Amp (amphibole), Bt (biotite), Op (opaque minerals), Pl (plagioclase) and Qz (quartz). 80

Figure 8 - Harker diagrams (in wt.%) for the granitoids from Vila União area. Abbreviations: QzD (quartz diorite), BtHbTn (biotite-hornblende tonalite), BtHbMzG (biotite-hornblende monzogranites) and LcGr (leucogranite). 83

Figure 9 - Harker diagrams for selected trace elements for granitoids from Vila União area. All trace elements are in ppm, and SiO_2 in wt.%. Abbreviations: QzD (quartz diorite), BtHbTn (biotite-hornblende tonalite), BtHbMzG (biotite-hornblende monzogranites) and LcGr (leucogranite). 84

Figure 10 - Rare earth elements patterns of the different varieties of the granitoids from Vila União area, with values normalized to C1 chondrite (McDonough and Sun, 1995). 84

Figure 11 - Geochemical diagrams for granitoids from Vila União area: (a) P-Q diagram from Debon & Le Fort (1988); (b) Normative feldspar triangle (O'Connor 1965) with fields from Barker (1979); (c) FeO*/(FeO*+MgO) *vs.* SiO_2 after Frost *et al.* (2001) showing the ferroan character of the studied rocks; (d) A/CNK [Al_2O_3/($CaO+Na_2O+K_2O$)] *vs.* A/NK [Al_2O_3/(Na_2O+K_2O)] diagram (Shand 1950); (e) Na_2O+K_2O–CaO (MALI) *vs.* SiO_2 diagram (Frost *et al.* 2001); and (f) major element discrimination diagram for leucogranites (Sylvester 1989). Abbreviations: QzD (quartz diorite), BtHbTn (biotite-hornblende tonalite), BtHbMzG (biotite-hornblende monzogranites) and LcGr (leucogranite). 85

Figure 12 - (a) Discrimination of tectonic environment diagram (Pearce *et al.* 1984); (b) discrimination diagram proposed by Whalen *et al.* (1987) showing the A-type affinities of the studied rocks; (c) CaO/($FeO^*+MgO+TiO_2$) *vs.* Al_2O_3 diagram (Dall'Agnol & Oliveira 2007); and d) Nb-Y-Ce diagram. A1 and A2 fields after Eby (1992). Abbreviations: QzD (quartz diorite), BtHbTn (biotite-hornblende tonalite), BtHbMzG (biotite-hornblende monzogranites), LcGr (leucogranite), HFCA (highly fractionated calc-alkaline), WPG (within-plate granites), VAG (volcanic arc granites), syn-COLG (syn-collision granites), ORG (oceanic ridge granites), FG (fractionated granites) and OGT (unfractionated granites). 86

Figure 13 - BSE images of representative zircon grains of the granitoids from Vila União area, with their respective *in situ* U-Pb ($^{207}Pb/^{206}Pb$ ages; white values) and Lu-Hf (εHf and T_{DM2}; yellow values) data. The numbers in parentheses correspond to the analyzed spot. The circles and their respective colors (see the legend) indicate the spot location. 90

Figure 14 - U-Pb concordia plots of the granitoids from Vila União area. Plots (a), (b) and (c) show results of SHRIMP U-Pb analyses, and plot (d) shows results of LA-MC-ICP-MS U-Pb analysis. 91

Figure 15 - Plot of time *vs.* εNd values for the granitoids from Vila União area (dataset in Table 6). Abbreviations: QzD (quartz diorite), BtHbTn (biotite-hornblende tonalite), BtHbMzG (biotite-hornblende monzogranites) and LcGr (leucogranite). 92

Figure 16 - Plots of time *vs.* εHf values for the granitoids from Vila União area (dataset in Table 7). 94

Figure 17 - Trace elements models for generation of the (a) mafic and (b) felsic end-members by partial melting of spinel lherzolite and felsic granulite, respectively. Primitive mantle (PM) and chondrite (C1) normalization values are from Sun & McDonough (1989) and McDonough & Sun (1995), respectively. 97

Figure 18 - Major and trace elements *vs.* SiO_2 diagrams. Binary mixing curve (dotted line) between felsic and mafic end-members (BVD 31 and BVD 42-F, respectively), with 10% increments (yellow diamonds). The studied granitoids are plotted along the hyperbola. Abbreviations: QzD (quartz diorite), BtHbTn (biotite-hornblende tonalite), BtHbMzG (biotite-hornblende monzogranites) and LcGr (leucogranite). 99

Figure 19 - REE diagrams with concentration normalized to chondrite (C1) from McDonough & Sun (1995), showing the results of binary mixing models between felsic and mafic end-members (BVD 57 and BVD 42-F, respectively) in different proportion to generate the hybrid granitoids from Vila União area. Abbreviations: QzD (quartz diorite), BtHbTn (biotite-hornblende tonalite), BtHbMzG (biotite-hornblende monzogranites) and LcGr (leucogranite). 100

Figure 20 - Simplified schematic illustration summarizing the petrogenetic/geodynamic model based on mixing/mingling process between both felsic and mafic melts to generate the granitoids of Vila União area that involved (a) extensional followed by (b) transpressional setting. 105

CAPÍTULO 4

Figure 1 - Geological map of the Carajás province, showing the limits between the Rio Maria, Sapucaia and Canaã dos Carajás domains, besides Carajás basin (dashed lines; modified from Gabriel *et al.* 2014). 123

Figure 2 - Summary of ages distribution for the Meso- and Neoarchean geologic units from Canaã dos Carajás domain, Carajás province. (1) Rio Novo, Igarapé Pojuca, Igarapé Bahia, Grão-Pará and Igarapé Salobo groups; (2) Cateté suite and Luanga complex; (3) Igarapé Gelado and Serra do Rabo granites, and Estrela granitic complex. The grey field represents the Mesoarchean anatectic granites crystallization age range (between 2.87–2.83 Ga). The asterisk symbol indicates the geochronological data obtained in this work. All references are in the text..124

Figure 3 - Geological sketch map of the studied area, showing lower hemisphere equal-area (Schmidt-Lambert) stereographic plots of poles to foliation and mineral lineation of both Mesoarchean and Neoarchean orthopyroxene-bearing sodic rocks from the studied area. Detailed interpretative cross-section A–A' is shown (see map for location). 126

Figure 4 - Mesoscopic aspects of the sodic rocks from Ouro Verde area. (a) Felsic granulite with tonalitic to trondhjemitic compositions, brownish greyish colored and greasy looking; (b) and (c) mafic granulite enclave hosted by felsic granulite; (d) tonalitic granitoid showing moderate mylonitic foliation; and (e) and (f) relation between the tonalitic granitoids (leucosome) and mafic rock (paleosome), suggesting migmatization process (metatexite). 127

Figure 5 - Structural aspects of the Meso- and Neoarchean orthopyroxene-bearing sodic rocks from the studied area. (a) rock showing preferred orientation of platy mineral grains and aggregates; (b) planar shape fabric defined by the flattened quartz aggregates (ribbons); (c) flattened mafic enclaves; (d) gneissic banding; (e) folded mafic enclaves (the dashed lines represent the axial traces); (f) N–S-trending foliation crosscut by the E–W one; (g) and (h) moderate mylonitic foliation, associated with subvertical dips; and (i) Neoarchean shear band dislocating Mesoarchean fabrics (the earlier structure: N–S-trending) represented by the felsic granulite and the mafic enclave. 129

Figure 6 - Representative photomicrographs of the felsic granulite. (a) General aspect of this unit, showing a typical porphyroclastic texture (medium- to coarse-grained) represented by plagioclase (Pl_1), with granoblastic matrix (fine-grained), composed mostly by plagioclase (Pl_2 and Pl_3) and quartz (Qz_1 and Qz_2); (b) fine-grained plagioclase (Pl_3) and quartz (Qz_2) neoblasts developing polygonal array in a granoblastic fabric, with strain-free aspects and forming ~120° dihedral angles between them; (c) plagioclase (Pl_1) displaying tapering twins; (d) ribbon-like quartz (Qz_1) with undulose extinction wrapping around plagioclase porphyroclast (Pl_1); (e) lens-like quartz (Qz_1) and biotite flakes (Bt_1) displaying well-developed preferred orientation; (f) detail of orthopyroxene (Opx) rimmed by symplectitic biotite-quartz (Bt_2 + Qz_3), and biotite (Bt_2) occurring along orthopyroxene fractures, both textures suggesting retrometamorphic path; (g) relict biotite (Bt_1) almost completely replaced by orthopyroxene in a prograde metamorphism; (h) orthopyroxene (Opx) + K-feldspar (Kfs_2) formed at the expense of the biotie (Bt_1) breakdown (prograde metamorphism); and (i) K-feldspar (Kfs_1) occurring in the interiors of deformed plagioclase porphyroclasts, forming small islands (‘blebs’). Photomicrographs (a), (b), (c), (d), (e), (h) and (i) under crossed nicols, and (f) and (g) under parallel nicols. 134

Figure 7 - Genetic discriminative diagram for orthopyroxene (Rietmeijer 1983). 135

Figure 8 - Q-A-P and Q-(A+P)-M plots for the enderbites from the studied area (Le Maître *et al.* 2002). 136

Figure 9 - Representative photomicrographs of the enderbite. (a) and (b) core-mantle structures in plagioclase porphyroclasts formed by bulging recrystallization (BLG); (c) general aspect of this unit, defined by the mylonitic foliation, which plagioclase porphyroclasts develop a preferred orientation with strain shadows of quartz and biotite; (d) deformation by kinking in plagioclase porphyroclast; (e) submagmatic microfractures in subhedral plagioclase porphyroclast filled with quartz-feldspar aggregates; (f) subhedral plagioclase porphyroclast mantled by mafic minerals displaying free-strain aspects; (g) incipient to moderate recrystallization to small new grains by BLG in quartz; (h) quartz entirely recrystallized by subgrain rotation recrystallization (SGR); and (i) peritectic reactions in the mafic phases defined by ortho- and clinopyroxene rimmed by amphibole and biotite. Photomicrographs (a), (b), (c), (d), (e), (f), (g) and (h) under crossed nicols, and (i) under parallel nicols. Abbreviations: Amp (amphibole); Bt (biotite), Cpx (clinopyroxene); Op (opaque minerals); Opx (orthopyroxene); Pl (plagioclase) and Qz (quartz). 137

Figure 10 - Harker diagrams (in wt.%) for the felsic granulites and enderbites from the studied area, compared with Mesoarchean Rio Verde TTG and Neoarchean Pedra Branca suite (Feio *et al.* 2013). 140

Figure 11 - Harker diagrams for selected trace elements for the felsic granulite and enderbites from the studied area, compared with Mesoarchean Rio Verde TTG and Neoarchean Pedra Branca suite (Feio *et al.* 2013). 141

Figure 12 - (a and b) REE and (c and d) multi-element patterns of the Meso- and Neoarchean sodic rocks from the studied area, with values normalized to C1 chondrite and pyrolite (McDonough & Sun 1995), respectively, compared with Mesoarchean Rio Verde TTG and Neoarchean Pedra Branca suite (Feio *et al.* 2013). 142

Figure 13 - Geochemical diagrams for the felsic granulites and enderbites from the studied area: (a) P-Q diagram from Debon & Le Fort (1988); (b) Normative feldspar triangle (O'Connor 1965) with fields from Barker (1979); (c) FeO*/(FeO*+MgO) vs. SiO_2 after Frost *et al.* (2001) showing the ferroan character of the studied rocks; (d) A/CNK [Al_2O_3/(CaO+Na_2O+K_2O)] vs. A/NK [Al_2O_3/(Na_2O+K_2O)] diagram (Shand 1943); (e) Na_2O+K_2O-CaO (MALI) vs. SiO_2 diagram (Frost *et al.* 2001); and (f) K-Na-Ca diagram, with trends for calc-alkaline and trondhjemite series as defined by Barker & Arth (1976), and grey field of Archean TTG (Martin 1994); (g) AFM diagram, with fields of tholeiite and calc-alkaline series of Irvine & Baragar 1971); (h) SiO_2 vs. K_2O diagram, with fields of Peccerillo & Taylor (1976); (i) ternary classification diagram proposed by Laurent *et al.* (2014). 143

Figure 14 - CL and BSE images of representative zircon grains of the felsic (a, b and c) and mafic (d) granulites from the studied area, with their respective in situ U-Pb ($^{207}Pb/^{206}Pb$ ages; white values) and Lu-Hf (εHf and T_{DM2}; yellow values) data. The numbers in parentheses correspond to the analyzed spot. The circles (see the legend) mark the position of the laser spot (scaled to size). 148

Figure 15 - U-Pb concordia plots of the felsic (a, b and c) and mafic (d) granulites from the studied area. Plots (a), (b) and (d) show results of SHRIMP U-Pb analyses, and plot (c) shows results of LA-SF-ICP-MS U-Pb analysis. 150

Figure 16 - BSE and CL images of representative zircon grains of the enderbites from the studied area, with their respective in situ U-Pb ($^{207}Pb/^{206}Pb$ ages; white values) and Lu-Hf (εHf and T_{DM2}; yellow values) data. The numbers in parentheses correspond to the analyzed spot. The circles (see the legend) mark the position of the laser spot (scaled to size). 151

Figure 17 - U-Pb concordia plots of the enderbites from the studied area. Plot (a) shows results of LA-SF-ICP-MS U-Pb analysis, and plot (b) shows results of SHRIMP U-Pb analyses. 152

Figure 18 - Single zircon Pb-evaporation age plot for the sample ED 1 from studied area. The vertical gray bars correspond the error for each zircon grain and horizontal dashed black line represents to the mean age for sample. Each analysis (gray bar) is accompanied by its respective zircon image (photomicrograph). Abbreviation: Zr (zircon).....152

Figure 19 - Plots of time vs. εHf for the Meso- and Neoarchean sodic rocks from the studied area (dataset in Tables 10 and 11). 155

Figure 20 - (a) La_N/Yb_N vs. Yb_N, (b) Sr/Y vs. Y and (c) [1/Er]-[(Ba+Sr)/1000]-[Er] (Heilimo *et al.* 2010) diagrams. 157

Figure 21 - Trace elements models for generation of the (a) Mesoarchean felsic granulite protolith (TTG-like) and (b) the Neoarchean enderbite, both by partial melting. Chondrite (C1) normalization values are from Sun McDonough & Sun (1995).160

Figure 22 - Simplified schematic illustration summarizing the proposed petrogenetic/geodynamic model corresponding to the generation of both Meso- and Neoarchean orthopyroxene-bearing sodic rocks from Canaã dos Carajás domain, Carajás province. See text for discussion. 167

Figure 23 - Sketch summarizing the proposed petrogenetic/geodynamic model in the Figure 22. 168

LISTA DE TABELAS

CAPÍTULO 2

Table 1 - Representative modal compositions of the granitoids from Vila União area. 30

Table 2 - Representative chemical compositions of the granitoids from Vila União area. 36

Table 3 - Zircon U-Pb isotopic data obtained by SHRIMP and LA-MC-ICP-MS for the granitoid samples BDE 19-B and BVD 12-B, respectively, from Vila União area. 43

Table 4 - Summary of zircon single-crystal evaporation Pb isotopic data of the granitoid sample RDM 9-C from Vila União area. 44

CAPÍTULO 3

Table 1 - Summary of geochronological and isotopic data of the Neoarchean magmatism from Carajás province. 68

Table 2 - Representative modal compositions of the granitoids from Vila União area. 77

Table 3 - Representative chemical compositions of the granitoids from Vila União area. 82

Table 4 - Zircon U-Pb isotopic data obtained by SHRIMP for granitoids from Vila União area. 87

Table 5 - Zircon U-Pb isotopic data obtained by LA-MC-ICP-MS for the granitoid sample BVD 12-B from Vila União area. 88

Table 6 - Whole-rock Sm-Nd isotopic data for the granitoids from Vila União area. 91

Table 7 - LA-MC-ICP-MS Lu-Hf isotopic data of zircon grains for the granitoids from Vila União area. 93

Table 8 - Modeling major and trace elements compositions and residual mineral assemblages for generation of the mafic end-member by partial melting of spinel lherzolite. ..96

Table 9 - Modeling major and trace elements compositions and residual mineral assemblages for generation of the felsic end-member by partial melting of Mesoarchean felsic granulite. 98

CAPÍTULO 4

Table 1 - Modal compositions of the enderbites from the central portion of Canaã dos Carajás domain, Carajás province. 135

Table 2 - Geochemical compositions of the felsic granulites and enderbites from the central portion of Canaã dos Carajás domain, Carajás province. 139

Table 3 - Zircon U-Pb isotopic data obtained by SHRIMP for the Mesoarchean felsic granulite (BDE 1-A). 145

Table 4 - Zircon U-Pb isotopic data obtained by SHRIMP for the Mesoarchean felsic granulite (BDE 13-A). 145

Table 5 - Zircon U-Pb isotopic data obtained by LA-SF-ICP-MS for the Mesoarchean felsic granulite (BVD 40). 146

Table 6 - Zircon U-Pb isotopic data obtained by SHRIMP for the Mesoarchean mafic granulite (BDE 11-B). 146

Table 7 - Zircon U-Pb isotopic data obtained by LA-SF-ICP-MS for the Neoarchean enderbite (BVD 53). 147

Table 8 - Zircon U-Pb isotopic data obtained by SHRIMP for the Neoarchean enderbite (ED 1). 147

Table 9 - Summary of zircon single-crystal evaporation Pb isotopic data of the Neoarchean enderbite (ED 1). 149

Table 10 - LA-MC-ICP-MS Lu-Hf isotopic data of zircon grains for the Mesoarchean felsic granulite. Ages from U-Pb SHRIMP (Table 4) and U-Pb LA-SF-ICP-MS (Table 5). 153

Table 11 - LA-MC-ICP-MS Lu-Hf isotopic data of zircon grains for the Neoarchean enderbite. Ages from U- U-Pb LA-SF-ICP-MS (Table 7) and Pb SHRIMP (Table 8). 154

Table 12 - Modeling major and trace elements compositions and residual mineral assemblages for generation of the Mesoarchean felsic granulite protolith by partial melting of enriched metabasalt. 159

Table 13 - Modeling major and trace elements compositions and residual mineral assemblages for generation of the Neoarchean enderbite by partial melting of Mesoarchean mafic granulite. 162

SUMÁRIO

DEDICATÓRIA iv

AGRADECIMENTOS v

EPÍGRAFE vii

RESUMO viii

ABSTRACT x

1 INTRODUÇÃO 1

1.1 APRESENTAÇÃO 1

1.2 LOCALIZAÇÃO E ACESSO 3

1.3 CONTEXTO GEOLÓGICO REGIONAL 4

1.3.1 Domínio Rio Maria 5

1.3.2 Domínio Sapucaia 6

1.3.3 Domínio Canaã dos Carajás e Bacia Carajás 7

1.4 APRESENTAÇÃO DO PROBLEMA 10

1.5 OBJETIVOS 12

1.6 MATERIAIS E MÉTODOS 13

1.6.1 Pesquisa bibliográfica 13

1.6.2 Mapeamento geológico e estrutural 14

1.6.3 Análise petrográfica e microestrutural 14

1.6.4 Química Mineral 14

1.6.5 Geoquímica 15

1.6.6 Geocronologia 15

1.6.7 Análise isotópica Lu-Hf 18

1.6.8 Análise isotópica Sm-Nd 19

2 NEOARCHEAN A-TYPE GRANITOIDS FROM CARAJÁS PROVINCE (BRAZIL): NEW INSIGHTS FROM GEOCHEMISTRY, GEOCHRONOLOGY AND MICROSTRUCTURAL ANALYSIS 21

3 A HYBRID ORIGIN FOR THE NEOARCHEAN GRANITOIDS OF THE CARAJÁS PROVINCE, BRAZIL: TEXTURAL, GEOCHEMICAL AND Pb-Nd-Hf ISOTOPIC EVIDENCES.....63

4 ZIRCON U-Pb, Lu-Hf ISOTOPIC AND GEOCHEMICAL CONSTRAINTS ON THE ORIGIN AND TECTONIC SIGNIFICANCE OF THE FELSIC GRANULITES AND Na-GRANITOIDS OF THE NORTHERN ARCHEAN CARAJÁS PROVINCE, BRAZIL.....119

5 CONCLUSÕES E CONSIDERAÇÕES FINAIS.....181

REFERÊNCIAS.....183

1 INTRODUÇÃO

1.1 APRESENTAÇÃO

A Província Carajás representa o principal núcleo arqueano preservado do Cráton Amazônico. Em função de seu enorme potencial metalogenético, esta província tem sido alvo de diversos estudos geológicos ao longo das últimas décadas, resultando na individualização de diversos granitoides, além de algumas associações metamórficas, nas áreas antes atribuídas ao Complexo Xingu, e que possibilitaram, juntamente com estudos geofísicos e estruturais, o desenvolvimento de propostas de compartimentação da província em segmentos crustais tectonicamente distintos (Althoff *et al.* 2000, Costa *et al.* 1995, Dall'Agnol *et al.* 2013, Souza *et al.* 1996). Dentre estes estudos, destacam-se aqueles desenvolvidos nas regiões de Canaã dos Carajás (Cunha *et al.* 2016, Delinardo *et al.* 2014, 2015, Domingos 2009, Feio & Dall'Agnol 2012, Feio *et al.* 2012, 2013, Galarza *et al.* 2017, Moreto *et al.* 2011, Santos *et al.* 2013), Água Azul do Norte (Gabriel *et al.* 2014, Leite-Santos & Oliveira 2014, Marangoanha & Oliveira 2014, Rodrigues *et al.* 2014), Sapucaia (Dall'Agnol *et al.* 2013, Santos *et al.* 2013, Silva *et al.* 2014, Teixeira *et al.* 2013), e Rio Maria (Almeida *et al.* 2011, 2013, Althoff *et al.* 2000, Dall'Agnol *et al.* 2006, Oliveira *et al.* 2009, 2010, 2011, Santos & Oliveira 2016, Silva *et al.* 2017, Souza *et al.* 2001).

Na porção centro-norte da Província Carajás, o Complexo Xingu ainda ocorre de forma expressiva, em especial nas regiões de Água Azul do Norte e a oeste do município Canaã dos Carajás, uma vez que, contrariamente ao que se observa na região de Rio Maria e porção leste de Canaã dos Carajás, as limitações no conhecimento sobre as associações litológicas que ocorrem nestas áreas impedem que seus aspectos evolutivos sejam também esclarecidos. Levando-se em consideração tais aspectos, além do fato de que, historicamente, os trabalhos desenvolvidos nos granitoides indiferenciados do Complexo Xingu mostram que este seria constituído por unidades distintas, passíveis de individualização e afetadas por diferentes eventos deformacionais, a presente tese visa aprimorar a caracterização das associações litológicas arqueanos da porção central do Domínio Canaã dos Carajás.

Busca-se, com isto, alcançar um melhor entendimento dos processos de formação dessas rochas e, consequentemente, dos principais processos que levaram à configuração atual do Domínio Canaã dos Carajás, avançando na compreensão dos aspectos evolutivos da Província Carajás. Para atingir tais objetivos, serão realizados estudos petrográficos, geoquímicos e estruturais, além de geocronologia e geoquímica isotópica, em particular de Sm-Nd e Lu-Hf. A presente tese está vinculada às dissertações de Vinícius Eduardo Silva de

Oliveira e Jully Mylli Lopes Afonso. O primeiro teve como objetivo estabelecer a afinidade petrológica dos corpos graníticos neoarqueanos que ocorrem na região de Vila União, porção a oeste do município de Canaã dos Carajás, o qual já teve sua dissertação concluída, com artigo publicado no periódico *Journal of South American Earth Sciences* no ano de 2018, intitulado "Geology, mineralogy and petrological affinities of the Neoarchean granitoids from the central portion of the Canaã dos Carajás domain, Amazonian craton, Brazil" (volume 85, páginas 135–159). Já o segundo visa caracterizar um pequeno *stock* granítico paleoproterozoico na área de estudo, com base em estudos petrográficos, geoquímicos, geocronológicos (U-Pb SHRIMP em zircão) e isotópicos (Lu-Hf), que se encontra em fase de conclusão. A presente tese, assim como as demais dissertações, faz parte do Grupo de Pesquisa Petrologia de Granitoides (GPPG) e do Programa de Pós-Graduação em Geologia e Geoquímica (PPGG) da Universidade Federal do Pará (UFPA), estando vinculados às metas e objetivos propostos pelo convênio INCT/GEOCIAM (CNPq/FAPESPA/CAPES/PETROBRAS; Processo 573733/2008-2), e contam com o apoio financeiro do Fundo de Amparo à Pesquisa do Estado do Pará (FAPESPA; Processo 133/2008-0) e do convênio Vale/FAPESPA (ICAAF n. 053/2011).

A estrutura organizacional deste documento inclui, inicialmente, o capítulo de caráter introdutório (Capítulo 1), que aborda os pontos relacionados à apresentação e localização da área de estudo; ao contexto geológico regional da Província Carajás, com ênfase aos estudos das associações litológicas do Domínio Canaã dos Carajás até então; à apresentação do problema, aos objetivos a serem alcançados e à metodologia aplicada. Os resultados alcançados neste trabalho serão apresentados e discutidos na forma de três artigos científicos (capítulos 2, 3 e 4), que já foram ou serão submetidos a periódicos internacionais, e abordados de forma integrada no capítulo final (Capítulo 5). Os artigos serão apresentados na seguinte ordem:

CAPÍTULO 2 – Artigo 1: **Neoarchean A-type granitoids from Carajás province (Brazil): New insights from geochemistry, geochronology and microstructural analysis.** Submetido para publicação à revista *PRECAMBRIAM RESEARCH*. Este trabalho reúne dados sobre petrografia, análise microestrutural, geoquímica e geocronologia referentes aos granitoides neoarqueanos de Vila União. Esse estudo permitiu caracterizar petrograficamente tais rochas, definir sua assinatura geoquímica, comparando com rochas análogas da Província Carajás e de outros crátons arqueanos, assim como determinar seu padrão deformacional. Além disso,

também são discutidos alguns parâmetros referentes às condições de cristalização e deformação.

CAPÍTULO 3 – Artigo 2: **A hybrid origin for the Neoarchean granitoids of the Carajás province, Brazil: Textural, geochemical and Pb-Nd-Hf isotopic evidences.** A ser submetido para publicação à revista A (*Qualis* CAPES). Discute os processos petrogenéticos envolvidos para a geração dos granitoides neoarqueanos de Vila União, com base em dados petrográficos, geoquímicos, geocronológicos e isotópicos, além de modelagem geoquímica. Também esclarece o real papel do magmatismo neoarqueano máfico, representado pelo Diopsídio-Norito Pium, na geração desses granitoides, o que possibilitou montar um modelo geodinâmico para a evolução tectono-estrutural neoarqueana nessa porção da crosta.

CAPÍTULO 4 – Artigo 3: **Zircon U-Pb, Lu-Hf isotopic and geochemical constraints on the origin and tectonic significance of the felsic granulites and Na-granitoids of the northern Archean Carajás province, Brazil.** A ser submetido para publicação à revista A (*Qualis* CAPES). Apresenta a caracterização do magmatismo sódico meso- e neoarqueano da porção central do Domínio Canaã dos Carajás, com base em dados petrográficos, (micro)estruturais, geoquímicos, geocronológicos e isotópicos. Também esclarece seus respectivos processos petrogenéticos baseados em modelagem geoquímica de elementos maiores e traço, exibindo, assim, um modelo geodinâmico arqueano mais completo dessa região, elucidando a implicação tectônica referente ao importante papel do ortopiroxênio presente em ambas as rochas.

1.2 LOCALIZAÇÃO E ACESSO

A área de estudo (Figura 1) localiza-se a oeste do município de Canaã dos Carajás, e a norte de Água Azul do Norte, no sudeste do estado do Pará, e está inserida no extremo norte da Folha SB-22-Z-A-V (Rio Parauapebas). O acesso à área de trabalho é feito a partir de Marabá, pela BR 155, até Eldorado dos Carajás. A partir desse município, têm-se duas opções: a primeira é seguindo a mesma rodovia até Xinguara e, em seguida, a PA 279. Após aproximadamente 50 km, entra-se à direita em uma estrada não pavimentada, seguindo 30 km até o limite sul da área. A segunda opção é seguindo a PA 275 até Parauapebas, em seguida a PA 160 até Canaã dos Carajás e, por fim, a estrada de acesso ao projeto S11D (Vale), que fornece acesso aos limites leste e norte da área de trabalho.

1.3 CONTEXTO GEOLÓGICO REGIONAL

A Província Carajás, apontada como o principal núcleo arqueano preservado do Cráton Amazônico (Almeida *et al.* 1981), é considerada uma província geocronológica independente por Santos (2003; Figura 2a), ou parte do contexto geológico da Província Amazônia Central de Tassinari & Macambira (2004; Figura 2b). A mesma é limitada a leste pelo Cinturão Araguaia, de idade neoproterozoica; a norte, pela Província Maroni-Itacaiúnas (segundo a proposta de Tassinari & Macambira 2004); a sul e a oeste é parcialmente coberta pelas sequências sedimentares fanerozoicas da Bacia Parecis e pelas rochas vulcânicas do Grupo Iriri. A referida província é também caracterizada pela sua importância metalogenética no cenário mineral do país, com destaque para as ocorrências de Fe, Au, Cu, Ag e Ni, e pela dominância de rochas arqueanas e ausência de rochas geradas durante o Ciclo Transamazônico.

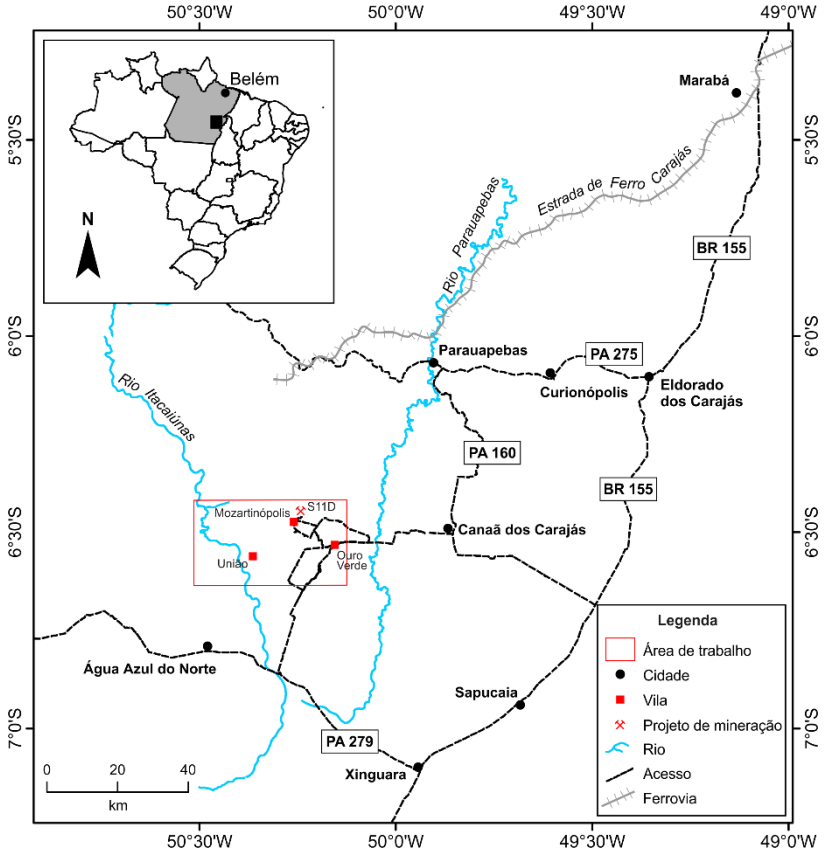

Figura 1 - Mapa de localização e principais acessos da área de estudo.

Em termos gerais, esse núcleo arqueano é formado em grande parte por um embasamento granitoide/granulítico e sequências supracrustais afins de *greenstone belts* (Figura 3). As rochas da porção sul configuram um típico terreno granito-*greenstone* de idade mesoarqueana, com características ígneas bem preservadas, enquanto a porção norte apresenta

um embasamento mesoarqueano marcado por grande retrabalhamento crustal, afetado por eventos de idade neoarqueana, representado por vasta sequência vulcanossedimentar e intrusões granitoides sin-tectônicos. Magmatismo paleoproterozoico de ~1,88 Ga é representado pelos granitos anorogênicos em toda a província (Dall'Agnol *et al.* 2005, Teixeira *et al.* 2017). A seguir, serão apresentadas as principais unidades que formam a Província Carajás, de acordo com a mais recente divisão tectono-estratigráfica apresentada por Dall'Agnol *et al.* (2013).

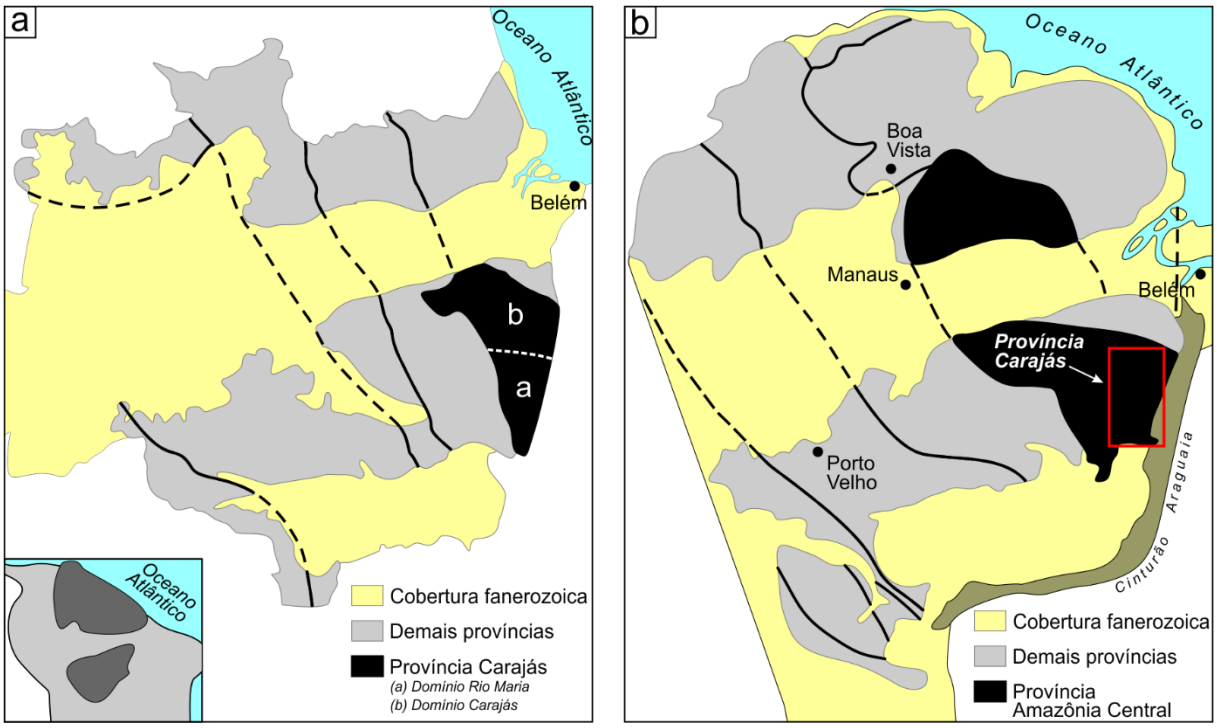

Figura 2 - Mapa de localização do Cráton Amazônico no continente sul-americano, evidenciando as províncias geocronológicas segundo (a) Santos (2003) e (b) Tassinari & Macambira (2004), com destaque para a Província Carajás.

1.3.1 Domínio Rio Maria

O Domínio mesoarqueano de Rio Maria (Dall'Agnol *et al.* 2006) é caracterizado pelas associações *greenstone belts* do Supergrupo Andorinhas, com idade estimada de 3,0 a 2,9 Ga (Avelar 1996, Lafon *et al.* 2000, Macambira & Lancelot 1991, Pimentel & Machado 1994, Rolando & Macambira 2003, Souza *et al.* 2001), e Grupo Tucumã (Araújo & Maia 1991), além de diversos granitoides, similares àqueles caracterizados nos clássicos terrenos arqueanos, que são divididos em: (i) série TTG antiga (2,96–2,93 Ga), representada pelo Tonalito Arco Verde, Trondhjemito Mogno e Tonalito Mariazinha (Almeida *et al.* 2011, Macambira & Lafon 1995, Rolando & Macambira 2003). São batólitos de biotita tonalitos/trondhjemitos foliados (NW–SE a E–W), com exceção do Tonalito Mariazinha, que

exibe orientação NE–SW e variações para N–S; (ii) granitoides de alto-Mg (sanukitoides), como o Granodiorito Rio Maria, de 2,87 Ga, e rochas associadas (Medeiros & Dall'Agnol 1988, Oliveira *et al.* 2009). Relacionadas a esta unidade, ocorrem ainda o Quartzo-Diorito Parazônia (Guimarães 2009) e o Granito Rancho de Deus (Dias 2009); (iii) Suíte Guarantã, de 2,87 a 2,86 Ga (Althoff *et al.* 2000), formada pelos leucogranodioritos-granitos de alto Ba-Sr dos plútons Guarantã, Trairão e Azulona (Almeida *et al.* 2010, Dias 2009). São rochas geoquimicamente similares aos TTG arqueanos (em termos de ETR), e distintos dos granitos de alto-K, e sua origem é interpretada a partir da mistura de magmas de composição trondhjemítica (TTG) e leucogranítica rico em Ba e Sr, derivadas de magmas sanukitoides (Almeida *et al.* 2010); (iv) Leucogranitos potássicos de afinidade cálcio-alcalina, de 2,87 Ga, caraterizados pelo granito Mata Surrão e corpos similares (Lafon *et al.* 1994). Os sedimentos do Grupo Rio Fresco (DOCEGEO 1988), recobrem parte do embasamento arqueano de Rio Maria. Posteriormente, este terreno foi intrudido por granitos tipo-A (1,88 Ga) e diques associados (Dall'Agnol *et al.* 2005, Dall'Agnol & Oliveira 2007).

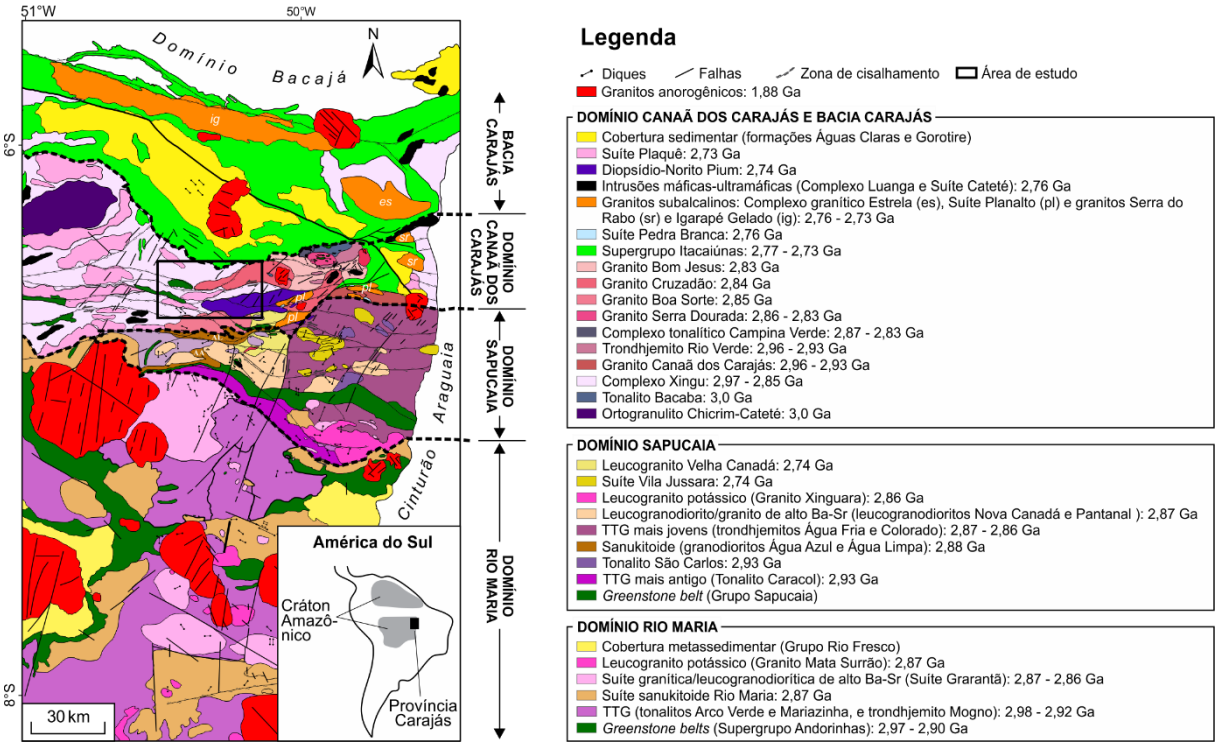

Figura 3 - Mapa geológico da Província Carajás (modificado de Gabriel *et al.* 2014), mostrando a mais recente compartimentação tectônica segundo Dall'Agnol *et al.* (2013; linhas tracejadas).

1.3.2 Domínio Sapucaia

O conhecimento sobre a geologia do Domínio Sapucaia é recente e os estudos realizados na região de Água Azul do Norte levaram ao atual quadro geológico: (i) *greenstone*

belts do Grupo Sapucaia, caracterizadas por rochas metamáficas, metaultramáficas e metassedimentares (Costa *et al.* 1994, DOCEGEO 1988); (ii) Tonalito Caracol, de 2,93 Ga (Almeida *et al.* 2011, Leite *et al.* 2004), que ocorre como uma estreita faixa NW–SE a norte do Domínio Rio Maria; (iii) Tonalito São Carlos, de idade preliminar 2,93 Ga, que é constituído de anfibólio-biotita tonalitos, distintos daqueles da série TTG, e sanukitoides arqueanos (Silva *et al.* 2014); (iv) granodioritos Água Azul e Água Limpa, de afinidade sanukitoide, com idade Pb-Pb de 2,88 Ga (Gabriel *et al.* 2010, Sousa *et al.* 2010); (v) trondhjemitos Água Fria, de 2,86 Ga (Leite 2001, Leite *et al.* 2004) e Colorado, de ~2,87 Ga (Silva *et al.* 2014); (vi) Granito Xinguara, de afinidade cálcio-alcalina e alto-K, que apresenta idade Pb-Pb em zircão de 2,86 Ga (Leite *et al.* 2004), e ocorre intrusivo no Complexo Tonalítico Caracol e Granodiorito Rio Maria e, segundo Leite (2001), tem origem relacionada à fusão parcial de rochas tipo TTG. Esta unidade foi recentemente desvinculada do Domínio Rio Maria (Dall'Agnol *et al.* 2013) em função de seu padrão deformacional muito similar às rochas do Domínio Sapucaia; (vii) leucogranodioritos-granitos de alto Ba-Sr, similares à Suíte Guarantã, foram recentemente descritos no Domínio Sapucaia. Eles estão representados pelos corpos do Leucogranodiorito Nova Canadá (Leite-Santos & Oliveira 2014) e Leucogranodiorito Pantanal (Teixeira *et al.* 2013); (viii) granitos neoarqueanos, representados pelo leucogranito de alto-K Velha Canadá (2,74 Ga; Leite-Santos *et al.* 2016, Santos *et al.* 2010) e granitos subalcalinos agrupados na Suíte Vila Jussara (2,75–2,73 Ga; Dall'Agnol *et al.* 2017).

1.3.3 Domínio Canaã dos Carajás e Bacia Carajás

O Complexo Xingu foi o nome utilizado inicialmente para denominar uma associação litológica heterogênea constituída por gnaisses, migmatitos, granitoides variados, rochas supracrustais tipo *greenstone belt*, e complexos básicos a ultrabásicos (Araújo & Maia 1991, Cordeiro & Saueressig 1980, DOCEGEO 1988, Ianhez *et al.* 1980, Medeiros Filho & Meireles 1985, Silva *et al.* 1974), com idade 2972±16 Ma em granodiorito na região de Tucumã (Avelar *et al.* 1999), e 2859±4 Ma em metagranitoides na região de Curionópolis (Machado *et al.* 1991), idade esta interpretada como de metamorfismo.

O avanço do conhecimento sobre a geologia deste complexo permitiu o reconhecimento de que, na verdade, a unidade carecia de dados para individualização, o que levou ao abandono do termo 'Complexo Xingu' no Domínio Bacajá (Macambira *et al.* 2001, Vasquez *et al.* 2008) e no Domínio Rio Maria (Dall'Agnol *et al.* 2006, Leite 2001, Vasquez *et al.* 2008), ficando restrito apenas aos domínio Sapucaia e Canaã dos Carajás, os quais

trabalhos recém desenvolvidos mostraram que o Complexo Xingu, nesta região, também está passível de individualização em novas unidades (Dall'Agnol *et al.* 2017, Feio *et al.* 2013, Gabriel & Oliveira 2014, Leite-Santos & Oliveira 2016, Moreto *et al.* 2011, 2015, Oliveira *et al.* 2018, Rodrigues *et al.* 2014). Dados geocronológicos recentes indicam idades de 2950 ± 25 Ma e 2857 ± 6,7 Ma atribuídas à cristalização dos protólitos e metamorfismo, respectivamente, de gnaisses do Complexo Xingu na área do Depósito de Cu do Salobo (Melo *et al.* 2014), além daquelas definidas por Delinardo *et al.* (2014, 2015) em ortopiroxênio-diopsídio gnaisses, que atribui essas rochas à unidade Ortogranulito Chicrim-Cateté, que apontam para idades de cristalização do protólito obtidas em zircão (U-Pb SHRIMP e LA-MC-ICP-MS) entre 3,06 e 2,93 Ga, posteriormente metamorfisados entre 2,89 e 2,83 Ga, sob fácies granulito em condições de ultra alta temperatura.

As unidades granitoides são representadas pelo Tonalito Bacaba de 3,0 Ga (Moreto *et al.* 2011), caracterizado por tonalitos de granulação fina, faneríticos, com hornblenda e biotita como principais minerais máficos, hidrotermalmente alterados. O Granito Sequeirinho apresenta coloração cinza claro, textura equigranular e porfirítica, de granulação fina a média, com idade de 3,0 Ga (Moreto *et al.* 2015). O Granito Canaã dos Carajás, de idade 2959±6 Ma (Feio *et al.* 2013) é caracterizado por leucogranitos fortemente deformados, de assinatura cálcio-alcalina e afinidade sódica, que foram afetados por zonas de cisalhamento E–W e NE–SW. O Trondhjemito Rio Verde, datado em 2929±3 Ma e 2868±4 Ma (Feio *et al.* 2012), é composto por rochas foliadas e com bandamento composicional, e são geoquimicamente similares aos típicos TTG arqueanos. O Complexo Tonalítico Campina Verde, datado em 2872±1 Ma e 2850±7 Ma (Feio *et al.* 2013) é representado por duas associações litológicas distintas: biotita tonalitos a granodioritos, com dioritos e monzogranitos subordinados; e biotita-hornblenda tonalitos, com granodioritos e monzogranitos subordinados. Geoquimicamente, estas rochas são distintas dos típicos TTG arqueanos, e definem uma série cálcio-alcalina expandida (Feio *et al.* 2013). O Granito Cruzadão (Feio *et al.* 2013), composto por leucogranitos deformados, segundo o *trend* NW–SE e E–W, têm assinatura geoquímica transicional entre as séries cálcio-alcalina e alcalina, e admite-se 2845±15 Ma como idade mínima de cristalização. O granito Boa Sorte (Rodrigues *et al.* 2014) é representado por biotita monzogranitos de assinatura cálcio-alcalina, fortemente fracionado, e idade de cristalização em torno de 2,85 Ga. O granito Bom Jesus é formado por monzo- e sienogranitos foliados e bandados, com orientação NE–SW e E–W. São rochas cálcio-alcalinas com idade mínima de cristalização em 2833±6 Ma (Feio *et al.* 2013). O Granito Serra Dourada (Feio *et al.* 2013, Moreto *et al.* 2011) é caracterizado por leucomonzogranitos com granulação média a

grossa, deformado, com foliação vertical E–W, e de assinatura cálcio-alcalina, datado em 2,86 Ga (Moreto *et al.* 2011) e 2,83 Ga (Feio *et al.* 2013).

O Supergrupo Itacaiúnas é formado por rochas metavulcanossedimentares que ocupam parte da Bacia Carajás, e representado pelos grupos Igarapé Salobo, Grão-Pará, Igarapé Bahia, Igarapé Pojuca e Buritirama (DOCEGEO 1988). Machado *et al.* (1991) admitem idades em torno de 2,76 Ga para as rochas desata unidade. O magmatismo máfico-ultramáfico neoarqueano é formado por pequenos corpos intrusivos no embasamento mesoarqueano da porção norte da Província Carajás. Seus principais representantes são: (i) Suíte Cateté (Macambira & Vale 1997), composta por gabros, noritos, piroxenitos, serpentinitos e peridotitos, alongados e alinhados preferencialmente segundo as direções E–W e N–S; (ii) Complexo Intrusivo Luanga, representado por rochas ultrabásicas e básicas acamadadas, que ocorrem próximo à Serra Pelada (Jorge João *et al.* 1982, Medeiros Filho & Meireles 1985); (iii) Gabro Santa Inês (DOCEGEO 1988, Meireles *et al.* 1984, Pinheiro 1997), que expõe-se como um corpo constituído por gabros porfiríticos, leucogabros, microgabros e anortositos, de fraca foliação, e alongado segundo NE–SW, no extremo oeste do Domínio Carajás.

A Suíte Pedra Branca (Feio *et al.* 2013) é composta por granitoides sódicos de assinatura toleítica, e ocorrem associados aos granitos da Suíte Planalto, na região de Canaã dos Carajás, que apresentam idade U-Pb 2,76 Ga (TIMS; Sardinha *et al.* 2004) e 2,75 Ga (Feio *et al.* 2013). O Diopsídio-Norito Pium é localizado na porção central do domínio, e é representado por um grande corpo de direção E–W. Segundo Ricci & Carvalho (2006) e Vasquez *et al.* (2008), essa unidade é composta por noritos, gabronoritos, hornblenda gabronoritos e hornblenda gabros, com idade de cristalização de 2746±1 Ma (Santos *et al.* 2013).

O embasamento mesoarqueano e as rochas supracrustais da Bacia Carajás são cortados por granitoides subalcalinos sin-tectônicos do Neoarqueano, representados pelo Complexo Granítico Estrela, de 2,76 Ga (Barros *et al.* 2001, 2009) e pelos granitos Serra do Rabo (2,74 Ga; Barros *et al.* 2009, Sardinha 2002), Igarapé Gelado (2,73 Ga; Barbosa 2004, Barros *et al.* 2009), Sossego e Curral (2,74; Moreto *et al.* 2015). Os granitos da Suíte Planalto (Dall'Agnol *et al.* 2013, Feio *et al.* 2012, Gomes 2003, Hühn *et al.* 1999, Oliveira *et al.* 2010) são formados por sieno- a monzogranitos, com proporções variadas de biotita e hornblenda, apresentam características geoquímicas similares aos de granitos tipo-A, e idades que variam entre 2,74 e 2,71 Ga.

A Suíte Plaquê é caracterizada por uma série de muscovita-biotita leucogranitos peraluminosos, estratoides e alongados segundo o *trend* E–W (Araújo *et al.* 1988, Jorge João

& Araújo 1992), datados em 2,73 Ga (Avelar *et al.* 1999). Acredita-se que sua ocorrência tenha sido superestimada, já que, ao longo dos anos, diversos trabalhos de caracterização destes granitoides apontam para anfibólio-biotita granitos afins daqueles que constituem a Suíte Planalto, o que colocou em xeque o real significado da Suíte Plaquê (Feio *et al.* 2012, Gomes 2003, Oliveira *et al.* 2010).

Sobrepostas ao Supergrupo Itacaiúnas, ocorrem as rochas sedimentares da Formação Águas Claras, que são divididas estratigraficamente, com base nas diferenças litológicas e ambientes de formação (Nogueira *et al.* 1995): (i) membro inferior, formado por pelitos, siltitos e arenitos, possivelmente depositados em plataforma marinha; e (ii) membro superior, caracterizado por arenitos litorâneos (parte inferior), e fluviais (parte superior). Embora sua idade seja bastante controversa, alguns autores ainda consideram essa unidade como arqueana, sendo posicionada no topo do Grupo Grão-Pará (Pinheiro & Holdsworth 2000).

Os granitos anorogênicos da Suíte Serra dos Carajás são similares àqueles afins já descritos na província, particularmente no Domínio Rio Maria, mas apresentam peculiaridades geoquímicas que sugerem fontes e história de cristalização distintos dos demais (Dall'Agnol *et al.* 1994). São representados pelos granitos Central, Carajás, Cigano, Pojuca, Rio Branco e Gogó da Onça (Dall'Agnol *et al.* 2006, Santos *et al.* 2013, Teixeira *et al.* 2017).

1.4 APRESENTAÇÃO DO PROBLEMA

A Província Carajás, principal terreno arqueano do Cráton Amazônico, é formada pelos domínios mesoarqueano de Rio Maria, e meso- a neoarqueanos de Canaã dos Carajás (incluindo a Bacia Carajás) e Sapucaia (Dall'Agnol *et al.* 2013). Trabalhos recentes realizados por pesquisadores do Grupo de Pesquisa Petrologia de Granitoides (GPPG/UFPA) e da Universidade de São Paulo (USP), na região que corresponde à porção leste do Domínio Canaã dos Carajás (Cunha *et al.* 2016, Feio & Dall'Agnol 2012, Feio *et al.* 2012, 2013), mostram que esta região é caracterizada pela dominância de granitos *stricto sensu* (granitos mesoarqueanos Sequeirinho, Canaã dos Carajás, Cruzadão, Boa Sorte, Bom Jesus e Serra Dourada, e neoarqueanos da Suíte Planalto, dos granitos Sossego e Curral, e associações charnoquíticas (Diopsídio-Norito Pium), com restritas ocorrências de TTG e granitos anorogênicos, sendo que as relações de campo entre as associações neoarqueanas ainda são pouco conclusivas (Feio *et al.* 2012, Galarza *et al.* 2017, Moreto *et al.* 2011, 2015, Oliveira *et al.* 2018, Santos *et al.* 2013). Nesse contexto, os diferentes granitoides se mostram imbricados e revelam um padrão muito distinto dos observados no Domínio Sapucaia e ao longo de toda

a extensão do Domínio Rio Maria. Por outro lado, a porção central do Domínio Canaã dos Carajás, mais especificamente nas áreas das vilas União e Ouro Verde, e do projeto S11D da Companhia Vale, não haviam sido até o momento objeto de levantamentos geológicos em escala adequada, o que não permitia confirmar, pela falta de um modelo integrado de evolução crustal e tectônica com áreas adjacentes, a extensão e limites deste domínio ou até mesmo determinar se este é um segmento crustal independente ou um prolongamento do Domínio Rio Maria afetado por eventos neoarqueanos.

Além disso, as rochas pertencentes ao Complexo Xingu continuam sendo as mais expressivas nessa área específica, com ocorrências subordinadas de granitoides tipo Plaquê e cálcico-alcalinos fortemente fracionados, além das rochas máficas do Diopsídio-Norito Pium. Aqueles inseridos no contexto geológico do Complexo Xingu e da Suíte Plaquê permanecem pobremente caracterizados, com carência de dados geocronológicos e ausência de assinaturas isotópicas, o que impossibilita a definição de uma sequência litoestratigráfica para a área. Outro ponto a ser destacado na área de interesse da pesquisa é a ausência de estudos mais aprofundado do magmatismo subalcalino neoarqueano do tipo-A representados, até então, pelos granitos da Suíte Planalto, e que são bastante frequentes em outras regiões da porção norte da Província Carajás (Barros *et al.* 2009, Cunha *et al.* 2016, Feio *et al.* 2012, Galarza *et al.* 2017). Isto pode ser atribuído ao fato destes corpos terem sido inicialmente inseridos no contexto da Suíte Plaquê por Araújo & Maia (1991), sobretudo devido à ausência de trabalhos sistemáticos na área em questão, e estima-se que a ocorrência desse grupo de granitos ainda seja subestimada.

Em decorrência do exposto acima, as informações a serem obtidas acerca do arcabouço tectono-estrutural e da natureza petrológica das diferentes associações magmáticas e metamórficas desta área deverão permitir um avanço considerável para a compreensão dos processos de formação e estabilização da crosta arqueana dessa região. Para tal, inúmeros questionamentos deverão ser esclarecidos em relação à evolução geológica da porção central do Domínio Canaã dos Carajás, dentre os quais podem se destacar:

(1) Os mapas geológicos disponíveis da porção a oeste do município de Canaã dos Carajás foram realizados em escala de 1:250.000 e não permitem uma caracterização detalhada, e tampouco uma individualização adequada das diferentes unidades, em especial daquelas relacionadas ao Complexo Xingu;
(2) As associações magmáticas a serem distinguidas a partir deste complexo podem ser correlacionadas com aquelas já identificadas na porção leste de Canaã dos Carajás? Ou

com aquelas dos domínios Sapucaia e/ou Rio Maria? Ou possuem idades e evolução distintas?

(3) Quais as condições de cristalização (temperatura, pressão, fugacidade de oxigênio, etc.) dos magmas formadores destas associações? Quais suas possíveis fontes e em que período houve a separação das mesmas?

(4) Os corpos graníticos individualizados em trabalhos anteriores, como do tipo Plaquê, correspondem realmente ao grupo de granitos peraluminosos? Ou estão associados ao magmatismo subalcalino do tipo-A formador dos granitoides da Suíte Planalto, se repetindo, dessa forma, ao que vem sendo descrito em outras áreas do Domínio Canaã dos Carajás? Caso sejam confirmados tais questionamentos, em que condições e ambiente estes corpos foram gerados e colocados? Qual a relação deste magmatismo com aquele de caráter toleítico do Diopsídio-Norito Pium? Quais as possíveis fontes de seus magmas?

(5) As rochas aflorantes na área de pesquisa, assim como aquelas das demais regiões dos domínios Canaã dos Carajás e Sapucaia, encontram-se em geral moderadamente a intensamente recristalizadas. Tal aspecto é resultado da atuação de processos no estágio *subsolidus* ligados à colocação de seus magmas ou representam efeitos de metamorfismo regional superimposto? Quais suas implicações para a evolução do Domínio Canaã dos Carajás; e

(6) As rochas que ocorrem na área são equivalentes em termos de assinatura geoquímica com algumas daqueles presentes no Domínio Canaã dos Carajás ou constituem associações magmáticas distintas, similares às descritas nos domínios Rio Maria ou Sapucaia? Tanto o Domínio Canaã dos Carajás, quanto o Domínio Sapucaia, ambos formados por extensa crosta TTG, afetada por eventos neoarqueanos, evoluíram de maneira independente? Qual a real localização do limite entre estes dois terrenos?

1.5 OBJETIVOS

Levando-se em conta o estágio inicial do conhecimento das rochas que afloram na porção oeste do Domínio Canaã dos Carajás, bem como os questionamentos levantados anteriormente sobre seus significados no contexto evolutivo da Província Carajás, o objetivo geral deste trabalho busca contribuir para a definição da natureza e processos de formação dos principais granitoides arqueanos desta porção da província, além de propor um modelo de evolução crustal e tectônica para a área. Pretende-se, dessa forma, contribuir para o avanço do conhecimento sobre a evolução tectônica e magmática do Domínio Canaã dos Carajás e

esclarecer o real significado dessa região no contexto da Província Carajás. Para tanto, deverão ser atingidos os seguintes objetivos específicos:

(1) Elaborar um mapa geológico em escala 1:220.000 das principais unidades estratigráficas individualizadas na região que compreende as áreas das vilas União e Ouro Verde, e do projeto S11D, além da integração com mapas geológicos de áreas adjacentes;
(2) Esclarecer a história deformacional deste segmento do Domínio Canaã dos Carajás, enfatizando os processos de colocação e deformação dos granitoides nele mapeados;
(3) Aprofundar a caracterização geoquímica e mineralógica destes granitoides, reavaliando com isso as suas séries magmáticas e procurar estimar os parâmetros reinantes (condições de fO_2, P, T e xH_2O) durante a cristalização;
(4) Definir e esclarecer as relações de campo entre os granitoides desta porção da província e as rochas do Diopsídio-Norito Pium;
(5) Determinar as assinaturas isotópicas em termos de Sm-Nd e Lu-Hf para que se possa discutir as fontes dos magmas geradores dos granitoides, e propor um modelo de evolução petrológica para os mesmos;
(6) Fazer comparações com base em dados estruturais, petrográficos, geoquímicos, geocronológicos e isotópicos dos granitoides dessa porção do Domínio Canaã dos Carajás, com aqueles que ocorrem na porção leste de Canaã dos Carajás e no Domínio Sapucaia, pretendendo, assim, avaliar as possíveis similaridades e contrastes existentes entre os mesmos; e
(7) Delimitar de forma mais precisa e fundamentada nos resultados obtidos, o limite entre os domínios Canaã dos Carajás e Sapucaia nesta porção da província.

1.6 MATERIAIS E MÉTODOS

1.6.1 Pesquisa bibliográfica

Foi realizado levantamento bibliográfico referente à geologia da Província Carajás, principalmente relacionado à granitogênese neoarqueana da província e às rochas mesoarqueanas do Domínio Canaã dos Carajás, além de temas específicos relacionados à evolução crustal, petrogênese, geologia estrutural, microtexturas e microestruturas, metamorfismo, geoquímica, geocronologia, geoquímica isotópica dos sistemas Sm-Nd e Lu-Hf, e granitoides arqueanos.

1.6.2 Mapeamento geológico e estrutural

Foram realizadas três etapas de campo para o reconhecimento das litologias e de suas feições estruturais, acompanhadas de coleta sistemática de 176 amostras para estudos petrográfico, microestrutural, geoquímico, geocronológico e isotópico. Além desses, estão sendo utilizados bancos de dados do Grupo de Pesquisa Petrologia de Granitoides, da Universidade Federal do Pará (GPPG/UFPA) adquiridos em etapas de campo realizadas entre os anos de 2007 e 2014. Nessas etapas de campo, foram realizados trabalhos de cartografia geológica, com mapeamento na escala 1:220.000 da área, através de perfis transversais à estruturação regional dominante, dando ênfase aos levantamentos de dados estruturais em afloramentos específicos, relações de contato, feições deformacionais atribuídas à atuação de zonas de cisalhamento e outras feições estruturais relevantes. Utilizou-se para isso, imagens de radar SRTM (*Shuttle Radar Topography Mission*), com resolução de 15 metros (banda C), imagens de satélite (Landsat TM e *Google Earth*) e imagens com dados aerogeofísicos (magnetometria e aerogamaespectrometria) levantados pelo Serviço Geológico do Brasil (CPRM) devidamente processados em ambiente SIG. Foram utilizados bússola e, para localização das amostragens, GPS (*Global Position System*) com precisão de aproximadamente 3 metros, com os pontos locados em base georreferenciada.

1.6.3 Análise petrográfica e microestrutural

A partir da análise macroscópica preliminar das amostras coletadas em campo, representativas das diferentes unidades estudadas, foram feitas posterior seleção e confecção de 90 lâminas delgadas ou polidas para o estudo em microscópio petrográfico em luz transmitida, visando: identificação dos minerais (Deer *et al.* 1992, Kerr 1959) e descrição sistemática; estudo das texturas magmáticas, metamórficas, deformacionais e de alteração (Hibbard 1995, Passchier & Trouw 2005, Yardley *et al.* 1990); estimativa da ordem de cristalização dos minerais (Dall'Agnol 1982, Hibbard 1995); obtenção de composições modais (Chayes 1956, Hutchison 1974) com contador automático de pontos Stageledge, da marca Endeeper (entre 1.500 e 2.000 pontos por amostra); e classificação das rochas conforme estabelecido pela IUGS (Le Maître *et al.* 2002).

1.6.4 Química Mineral

Com a finalidade de discriminar o ortopiroxênio das rochas granulíticas, foram realizadas análises de química mineral em três seções polidas representativas do granulito

félsico, no Laboratório de Microanálises da UFPA, através da microssonda eletrônica modelo JEOL JXA-8230, operando sob condições de voltagem de aceleração de 15 kV e corrente do feixe de 20 µA, com distância de trabalho de 11 mm. Os padrões utilizados para calibração foram microclínio (Al, Si e K), albita (Na), forsterita (Mg), andradita (Ca e Fe), vanadinita (V e Cl), topázio (F) e pirofanita (Ti e Mn).

1.6.5 Geoquímica

Após prévia seleção petrográfica, um total de 61 amostras representativas dos diferentes litotipos foram escolhidas para realização de análises litogeoquímica. As amostras selecionadas para as análises foram trituradas, pulverizadas, homogeneizadas e quarteadas na Oficina de Preparação de Amostras (OPA) do Instituto de Geociências (IG) da Universidade Federal do Pará (UFPA). Tais análises foram realizadas nos laboratórios comerciais Acme Analytical Laboratories Ltd. (Canadá) e ALS Geochemistry Laboratories (Brasil), sendo os elementos maiores e menores (SiO_2, TiO_2, Al_2O_3, Fe_2O_3*, MnO, MgO, CaO, Na_2O e P_2O_5) analisados por ICP-AES (*Inductively Coupled Plasma – Atomic Emission Spectrometry*), enquanto que os elementos traço (Ba, Rb, Sr, Zr, Nb, Y, Hf, Ta e Th), incluindo os elementos terras raras (La, Ce, Pr, Nd, Sm, Eu, Gd, Tb, Dy, Ho, Er, Tm, Yb e Lu), foram analisados por ICP-MS (*Inductively Coupled Plasma - Mass Spectrometry*). Os dados obtidos permitiram realizar a caracterização geoquímica, com base nos procedimentos indicados em Ragland (1989) e Rollinson (1993), e diagramas elaborados com auxílio do programa GCDkit (Janoušek *et al.* 2003).

Tais dados geoquímicos obtidos, associados aos dados de química mineral disponíveis na literatura, também foram utilizados em modelagem geoquímica com o objetivo de definir os processos que controlaram a evolução magmática dos granitoides e dos protólitos dos granulitos estudados (fusão parcial, cristalização fracionada, mistura de magmas, assimilação, etc.). Para isso, utilizou-se o programa GENESIS 4.0 desenvolvido por Teixeira (2005) para modelagem de elementos maiores, além de planilhas no programa EXCEL (Microsoft) desenvolvidas pelo autor da tese para modelagem de elementos traço.

1.6.6 Geocronologia

Ao total, foram feitas 12 análises geocronológicas por meio dos métodos U-Pb em zircão (*in situ*) obtidas pelos sistemas SHRIMP IIe (*Sensitive High Resolution Ion Microprobe*), no Laboratório de Geologia de Alta Resolução da Universidade de São Paulo

(GeoLab/USP), LA-SF-ICP-MS (*Laser Ablation Sector Field Ion Coupled Plasma Mass Spectrometry*), no Laboratório de Geologia Isotópica da Universidade Federal de Ouro Preto (UFOP), e LA-MC-ICP-MS (*Laser Ablation Multi-Collector Ion Coupled Plasma Mass Spectrometry*), no Laboratório de Geologia Isotópica (Pará-Iso) da UFPA, além do método de evaporação de Pb em zircão, também conduzido no Pará-Iso (UFPA).

Em torno de 10 a 20 kg de cada amostra representativa foram trituradas, moídas e peneiradas nas frações 125–175 ou 75–125 µm, realizadas na Oficina de Preparação de Amostras (OPA) e no Laboratório de Preparação Mineral (LPM), ambos na UFPA. Os cristais de zircão foram separados por meio de líquido pesado (bromofórmio) e separador magnético isodinâmico do tipo *Frantz*. Entre 60 e 80 cristais de zircão de cada amostra foram selecionados com o auxílio de lupa binocular e, em seguida, montados em um disco de epóxi em conjunto com os padrões analíticos, polidos até a metade de sua espessura a fim de expor o interior dos cristais, e revestida com uma película de carbono. Antes das datações com o método U-Pb, foram examinadas estruturas internas, sobrecrescimentos, fraturas, inclusões e defeitos físicos dos cristais, utilizando imagens de elétrons retroespalhados (BSE – *Backscattered Electron Images*) e catodoluinescência (CL – *Cathodoluminescence*), obtidas pela microssonda eletrônica modelo JEOL JXA-8230, do Laboratório de Microanálises da UFPA, operando sob condições de voltagem de aceleração de 15 kV e corrente do feixe de 20 µA, com distância de trabalho de 11 mm.

As análises realizadas pelo sistema SHRIMP IIe seguem os procedimentos analíticos segundo Stern (1998), Williams (1998) e Sato *et al.* (2008, 2014), e os padrões utilizados são SL 13 para a composição referência do U (238 ppm; Sato *et al.* 2014), e o zircão TEMORA-2 (416,78±0,33 Ma; Black *et al.* 2003) para razões isotópicas padrão. O *spot* apresenta tamanho de 30µm. Os dados foram reduzidos utilizando o *software* SQUID 1.03 (Ludwig 2001) e as idades calculadas usando Isoplot 4.15 (Ludwig 2008). Os erros da razão isotópica são 1σ.

Para o sistema LA-SF-ICP-MS, foi utilizado o equipamento ICP-MS *sector field* da Thermo-Finnigan Element 2 acoplado a um sistema de laser ultravioleta CETAC LSX-213 G2+ (λ = 213 nm) Nd:YAG, através do método definido por Gerdes & Zeh (2006, 2009) e Frei & Gerdes (2009). O diâmetro dos furos realizados pelo laser foi de 20 µm. A profundidade típica das crateras de ablação foi de 15–20 µm. Os dados foram adquiridos no modo *peak jumping* durante 20 segundos de *background* seguidos por 20 segundos de ablação da amostra. O sinal foi ajustado para máxima sensibilidade para Pb e U, mantendo a produção de óxido bem abaixo de 1%. Os dados brutos foram corrigidos para sinal de *background*, Pb comum, fracionamento elementar induzido pelo laser, discriminação instrumental de massa, e

fracionamento elementar de Pb/U, dependente do tempo, usando um programa de planilha *in-house* do Excel (Microsoft). A correção de Pb comum foi baseada no modelo de composição de Pb (Stacey & Kramers 1975). O fracionamento elementar induzido pelo laser e a discriminação instrumental de massa foram corrigidos via normalização pelos zircões de referência GJ-1 (608,5±1,5 Ma; Jackson *et al.* 2004), BB (564±33 Ma; Santos *et al.* 2017) e Plešovice (337±1 Ma; Sláma *et al.* 2008), os quais foram analisados juntamente com as amostras, exatamente sob as mesmas condições. Os dados analíticos foram calculados e plotados usando Isoplot 4.15 (Ludwig 2008). Os erros da razão isotópica são 2σ.

Uma análise foi realizada pelo sistema LA-MC-ICP-MS, utilizando um ICP-MS da Thermo Finnigan Neptune, com diâmetro do *spot* de 50 µm. As razões U-Th-Pb e abundâncias absolutas foram determinadas a partir do padrão GJ-1 (Stacey & Kramers 1975). Os dados analíticos foram refinados com o auxílio do Isoplot 4.15 (Ludwig 2008). Os erros da razão isotópica são 1σ.

Para as análises por evaporação de Pb em zircão, utilizou-se um Espectrômetro de Massa de Termo-Ionização com multicoletores (TIMS), da marca Thermo Finnigan, modelo MAT 262, seguindo a metodologia desenvolvida por Köber (1986, 1987) e procedimentos técnicos segundo Costi *et al.* (2000) e Noce *et al.* (2000). Esse método consiste na evaporação-ionização do Pb contido no cristal de zircão, em etapas sucessivas de aquecimento no TIMS. Essa técnica posiciona frente a frente dois filamentos de Re, sendo um de evaporação em forma de ‘canoa’, onde o cristal de zircão é aprisionado, e outro de ionização, a partir do qual o Pb é analisado (Köber 1987). Três etapas de evaporação são analisadas, com temperaturas de 1450, 1500 e 1550 °C, em intervalos de 3 a 5 minutos de evaporação para cada etapa. O Pb evaporado deposita-se imediatamente no filamento de ionização, o qual é mantido à temperatura ambiente. A necessidade de mais etapas de evaporação é avaliada dependendo da quantidade de Pb que o cristal contém, ou de sua capacidade em fixar-se no filamento de ionização. Em cada etapa de ionização são obtidos 5 blocos de dados (análise em contador de íons), gerando um bloco com 8 razões $^{207}Pb/^{206}Pb$. A partir das médias dessas razões dos blocos, define-se uma idade para cada etapa (temperatura) de ionização. A idade da amostra é calculada a partir dos resultados obtidos nas etapas de mais alta temperatura. As etapas de mais baixa temperatura provavelmente refletem perda de Pb após a cristalização e são descartadas para o cálculo da idade. O cálculo das idades e os erros são obtidos seguindo os procedimentos de Gaudette *et al.* (1998). A correção do Pb comum foi feita de acordo com modelo de Stacey & Kramer (1975). As razões $^{207}Pb/^{206}Pb$ foram corrigidas para um fracionamento de massa de 0,07±0,03% por u.m.a. determinados a partir de análises repetidas

do padrão NBS-982. As análises com razões $^{204}Pb/^{206}Pb$ maior do que 0,0004 foram rejeitadas a fim de evitar erros significantes causados pela imprecisão na correção do Pb comum. O tratamento estatístico final é feito utilizando os *softwares* Zircão, desenvolvido pelo Pará-Iso, e Isoplot, de Ludwig (2008). Os erros da razão isotópica são 2σ.

1.6.7 Análise isotópica Lu-Hf

Das amostras com idades obtidas por U-Pb, 8 foram selecionadas para aquisição de dados pelo método isotópico Lu-Hf (2 dos granulitos félsico, 2 dos enderbitos e 4 dos granitoides híbridos de Vila União), cuja análise pontual foi feita preferencialmente no mesmo site ou no mesmo domínio de idade concordante do zircão. As análises isotópicas de Hf foram realizadas no Laboratório de Geologia Isotópica da Universidade Federal de Ouro Preto (UFOP), utilizando-se um ICP-MS multicoletor da Thermo-Scientific Neptune Plus acoplado a um laser Photon-Machines 193 ArF Excimer. Os dados foram coletados no modo estático durante 60 segundos de ablação com um furo de diâmetro de 50 μm. Introduziu-se nitrogênio (~0,080 l/min) ao gás carregador da amostra (argônio) por meio de um sistema de nebulização Aridus. A intensidade típica do sinal foi cerca de 10 V para o ^{180}Hf. Os isótopos ^{172}Yb, ^{173}Yb e ^{175}Lu foram monitorados simultaneamente durante cada etapa das análises para permitir a correção de interferências isobáricas dos isótopos Lu e Yb na massa 176. Os isótopos ^{176}Yb e ^{176}Lu foram calculados utilizando-se as razões $^{176}Yb/^{173}Yb$ de 0,796218 (Chu *et al.* 2002) e $^{176}Lu/^{175}Lu$ de 0,02658 (valor *in-house* da JWG – Johann Wolfgang Goethe-Universität Frankfurt am Main). A correção para o fracionamento de massa instrumental utilizou uma lei exponencial e um valor $^{179}Hf/^{177}Hf$ de 0,7325 (Patchett & Tatsumoto 1980) para a correção das razões isotópicas de Hf. O viés (bias) de massa dos isótopos de Yb geralmente difere levemente daqueles dos de Hf com um fator típico do βHf/βYb entre 1,04 e 1,06 quando se usam o valor de 1,35274 definido por Chu *et al.* (2002). Esse fator foi determinado para cada sessão analítica por meio da média da razão βHf/βYb de múltiplas análises da solução JMC 475 dopada com variáveis quantidades de Yb, e todas as análises por ablação a laser do zircão (normalmente n > 50) com uma intensidade de sinal ^{173}Yb > 60 mV. O comportamento do viés (bias) de massa do Lu foi assumido seguir aquele do Yb. As razões isotópicas de Yb e Lu foram corrigidas usando o βHf das etapas de integração individual de cada análise (n = 60) dividida pela média do fator da sessão analítica completa. Os resultados foram calibrados com o uso dos zircões padrão Temora (415 Ma; Hf = 0,282680), Mud Tank (730 Ma; Hf = 0,282501) e 91500 (1065 Ma; Hf = 0,282307). Para o cálculo de εHf, foi usado os valores de condrito de Bouvier *et al.* (2008; $^{176}Lu/^{177}Hf$ = 0,0336 e $^{176}Hf/^{177}Hf$ = 0,282785)

e constante de decaimento de 1,865 × 10^{-11} ano^{-1} (Scherer *et al.* 2001). A média do manto empobrecido é definida por Andersen *et al.* (2009) com razões $^{176}Lu/^{177}Hf$ e $^{176}Hf/^{177}Hf$ de 0,0388 e 0,283250, respectivamente, e média da crosta continental de 0,015, definida por Griffin *et al.* (2002).

1.6.8 Análise isotópica Sm-Nd

Análises isotópicas de Sm-Nd foram realizadas em 9 amostras representativas dos granitoides neoarqueanos híbridos de Vila União, utilizando o espectrômetro de massa Finnigan MAT 262 do Laboratório de Geologia Isotópica (Pará-Iso) da UFPA. Os dados de idade modelo obtidos foram utilizados como parâmetro indicativo de fontes de magma, mistura de componentes e evolução crustal. Esse método foi descrito inicialmente por Lugmair (1974) e Lugmair *et al.* (1975), tendo as primeiras aplicações para rochas ígneas determinadas por DePaolo & Wasserburg (1976) e Hamilton *et al.* (1977). Os procedimentos analíticos adotados por este laboratório para a determinação de idade modelo em rocha total estão descritos em Avelar (2002) e Moura (1992).

A preparação prévia das amostras consiste, primeiramente, na trituração, feita pelos trituradores de mandíbula primário e secundário, realizada na OPA/UFPA, seguida de pulverização, feita com o gral de ágata, no Laboratório de Sedimentologia (UFPA), e quarteamento de ~500g/amostra. A técnica analítica de abertura e separação do sistema isotópico de Sm-Nd é iniciada utilizando uma solução traçadora mista de $^{150}Nd/^{149}Sm$ em 100 mg de material, conforme a metodologia descrita por Oliveira *et al.* (2008) e, em seguida, digeridos HF:HNO_3 em frasco de Teflon dentro de recipiente PARR a 150ºC por uma semana. Após a evaporação, a solução é novamente atacada com os mesmos ácidos e colocada para secar e, em seguida, diluída com HCl (6N). Após a evaporação, o resíduo é solubilizado em HCl (2N). Após a última evaporação, os lantanídios foram separados dos outros elementos por troca cromatográfica usando a resina *BioRad Dowex 50WX-8*, HCl (2N) e HNO_3 (3N). A extração de Sm e Nd dos demais lantanídeos foi executada por troca cromatográfica aniônica usando resina *Dowex AG1-X4* com a mistura de HNO_3 (7N) e metanol. As frações concentradas de Sm e Nd coletadas são então evaporadas. Em seguida, 1 ml de HNO_3^{**} (2%) é adicionado em cada fração separada de Sm e Nd, sendo as amostras levadas ao espectrômetro ICP-MS para leitura de suas razões isotópicas em média de dez (Nd) a seis (Sm) blocos cada amostra. As razões isotópicas são normalizadas para $^{146}Nd/^{144}Nd = 0,7219$ (o fracionamento de massa foi corrigido no modo exponencial) e a constante de desintegração usada é de 6,54 × 10^{-12} ano^{-1}. Os padrões de Nd “La Jolla” e a solução de calibração Neptune

forneceram valores de $^{143}Nd/^{144}Nd$ de 0,511834 (±5) e 0,511732 (±9) (2σ, média de 50 leituras), respectivamente. Os valores de T_{DM} foram calculados usando o modelo de DePaolo (1981) por meio da macro Isoplot 4.15 (Ludwig 2008) que funciona no programa EXCEL (Microsoft).

2 NEOARCHEAN A-TYPE GRANITOIDS FROM CARAJÁS PROVINCE (BRAZIL): NEW INSIGHTS FROM GEOCHEMISTRY, GEOCHRONOLOGY AND MICROSTRUCTURAL ANALYSIS

Autores:
Bhrenno Marangoanha
Davis Carvalho de Oliveira
Vinícius Eduardo Silva de Oliveira
Marco Antonio Galarza
Cláudio Nery Lamarão

Artigo submetido à revista PRECAMBRIAN RESEARCH

Dear Mr. Marangoanha,

Thank you for submitting your manuscript for consideration for publication in Precambrian Research. Your submission was received in good order.

To track the status of your manuscript, please log into EVISE® at: http://www.evise.com/evise/faces/pages/navigation/NavController.jspx?JRNL_ACR=PRECAM and locate your submission under the header 'My Submissions with Journal' on your 'My Author Tasks' view.

Thank you for submitting your work to this journal.

Kind regards,

Precambrian Research

Neoarchean A-type granitoids from Carajás province (Brazil): New insights from geochemistry, geochronology and microstructural analysis

Bhrenno Marangoanha [a,b], Davis Carvalho de Oliveira [a,b], Vinícius Eduardo Silva de Oliveira [a,b], Marco Antonio Galarza [b,c],Cláudio Nery Lamarão [a,b,d]

[a] Grupo de Pesquisa Petrologia de Granitoides (GPPG), Instituto de Geociências (IG), Universidade Federal do Pará (UFPA), Rua Augusto Corrêa, 01, CEP 66075-110, Belém, Pará, Brazil

[b] Programa de Pós-graduação em Geologia e Geoquímica (PPGG), IG-UFPA, Belém, Pará, Brazil

[c] Laboratório de Geologia Isotópica (Pará-Iso), IG-UFPA, Belém, Pará, Brazil

[d] Laboratório de Microanálises, IG-UFPA, Belém, Pará, Brazil

ABSTRACT

The Neoarchean granitogenesis in Carajás province, southeastern portion of the Amazonian craton (Brazil), is marked by a huge volume magmatic rocks, and occur strictly in Sapucaia and Canaã dos Carajás domains (including Carajás basin). New data from the central portion of Canaã dos Carajás domain, Vila União area, show that these granitoids could reach a wide composition range, from syenogranites, through monzogranites and granodiorites, to tonalites and (quartz) diorites. Geochemical data reveal a metaluminous to slightly peraluminous character as well as affinity with the oxidized and reduced ferroan A-type granites from Neoarchean Vila Jussara suite. High crystallization conditions were recorded in these granitoids, with temperature between 926–831°C and pressure of 814–532 MPa, which represent crystallization at ~23–13 km deep. Detailed microstructural analysis corroborates the syn-tectonic emplacement conditions, as indicated by microtextural evidences of continuous magmatic to sub-magmatic deformational processes. Moreover, these microtextures point to dominant deformational temperatures about 500–400°C, but could eventually reach 250–700°C. U-Pb and Pb-evaporation dating of zircon grains defined homogeneous ages ranging between 2.74–2.73 Ga, interpreted as crystallization ages, and corroborates to those recorded about Neoarchean magmatism in Carajás province. The integrated data suggest a two-stage model responsible to generate these granitoids: (1) at 2.74 Ga, this portion of the crust was submitted by an N–S extensional tectonic regime, responsible for generation of the magma; (2) around 10 Ma later, the magma rising and emplacement were accompanied by the inversion of Carajás basin, described by N–S pure shear-dominated

transpressional regime, with E–W sinistral sense. These evidences show that cooling and deformation of these rocks took place coevally, and confirm the syn-tectonic character of the Neoarchean granitoids from Vila União area.

Keywords: Neoarchean granitoids; Syn-tectonic; Deformation; Geochronology; Carajás province.

1. Introduction

Until three decades ago, the knowledge about the Neoarchean granitoids from Carajás province was very limited, which were composed strictly by the Plaquê suite and initially classified as S-type granites (Araújo et al., 1988; Araújo and Maia, 1991). Only in the last twenty years – with emphasis on last 10 years – these granitoids have considerably been studied, which enabled to individualize some granitic plutons, later grouped into suites based on shared similarities in field, petrographic and compositional data. These rocks would be cogenetic in the sense that they share similar petrogenesis and were derived from source materials of essentially same composition. The recent studies have showed that they were wrongly grouped into S-type granites, due to these granitoids do not display any signature related to sedimentary source. Their origin has been associated to partial melting of mafic to intermediate lower crustal rocks, and classified as 'deformed' A-type, alkaline, metaluminous to weakly peraluminous granitoids (Sardinha et al., 2006; Barros et al., 2009; Feio et al., 2012; Dall'Agnol et al., 2017). Analogous granitoids are recorded by the 2.69 Ga-old Matok magmatic suite in Limpopo belt, South Africa. However, its genesis is explained by both (1) interaction (mixing) between highly evolved magmas and granitic melts derived from reworking of local crust, and (2) differentiation of a mafic parent (Laurent et al., 2014).

Despite recent significant advances in knowledge concerning Neoarchean granites from Carajás province – especially the ones located in the Carajás basin and in the central portion of Canaã dos Carajás domain – there is still a lack of data related to their origin and the structural framework printed on these rocks as well. The wide both compositional and deformational ranges identified in the Neoarchean A-type granitoids from Vila União area point to the need of detailed study concerning their petrographic, microstructural, geochemical and geochronological aspects, in order to provide new constraints and elucidate the processes related to their genesis and the tectonic regime that acted during the emplacement (deformation conditions) of the plutons, as well as become clearer their role in the evolution of Carajás province.

2. Geological setting

The Carajás province represents the main well-preserved Archean nucleus of the Amazonian craton, northern Brazil (Almeida et al., 1981; Figure 1). According to the most recent geologic framework, established by Dall'Agnol et al. (2013), the Carajás province comprises three domains: Rio Maria, Sapucaia and Canaã dos Carajás (Figure 1), and these authors consider the last one as the basement of the Carajás basin. The Rio Maria domain, located in the southern part of the province, represents a typical granite-greenstone terrane. It is formed by greenstone belts (2.97–2.90 Ga; Souza et al., 2001), TTG suites (2.98–2.92 Ga; DOCEGEO, 1998; Althoff et al., 2000; Souza et al., 2001; Leite et al., 2004; Dall'Agnol et al., 2006; Almeida et al., 2011), sanukitoid suite (2.87 Ga; Oliveira et al., 2009) and leucogranites (2.87–2.86 Ga; Althoff et al., 2000; Souza et al., 2001; Leite et al., 2004; Almeida et al., 2010). The Sapucaia domain shows strong lithologic similarity to the Rio Maria domain, however, their rocks were intensely affected by Neoarchean events, represented by deformed A-types granitoids (Dall'Agnol et al., 2017).

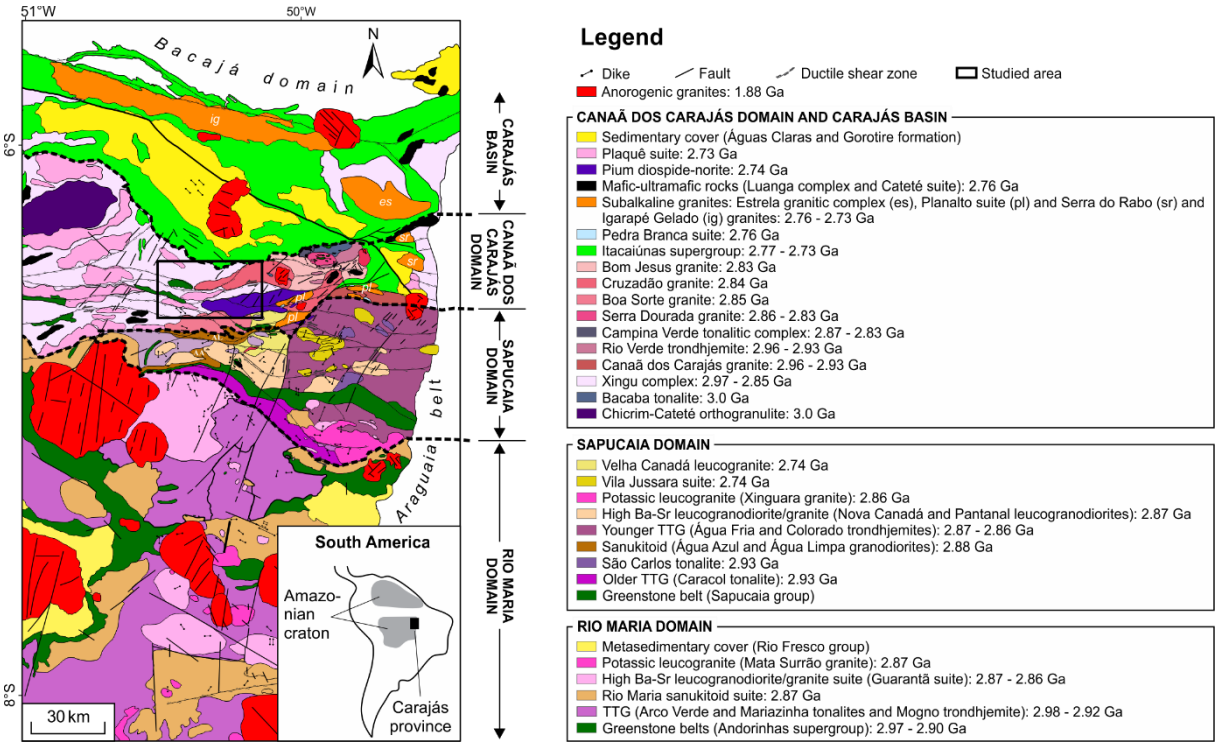

Figure 1. Geological map of the Carajás province, showing the limits between the Rio Maria, Sapucaia and Canaã dos Carajás domains, besides Carajás basin (dashed lines; modified from Gabriel et al., 2014).

The Canaã dos Carajás domain is interpreted as the basement of Carajás basin and shows a more reworked crust compared with Rio Maria and Sapucaia ones (Dall'Agnol et al., 2013. The Mesoarchean units are Chicrim-Cateté orthogranulite, with crystallization and metamorphism age of 3.0 and 2.85, respectively (Pidgeon et al., 2000; Vasquez et al., 2008),

Bacaba tonalite (3.0 Ga; Moreto et al., 2011), Xingu complex – an heterogeneous lithologic association formed mainly by gneiss, migmatites and granitoids –, with crystallization age varying from 3.06 to 2.85 Ga (Machado et al., 1991; Avelar et al., 1999; Melo et al., 2014; Delinardo et al., 2014, 2015), Canaã dos Carajás granite and Rio Verde trondhjemite, both formed between 2.96 and 2.93 Ga (Feio et al., 2013), and Campina Verde tonalitic complex, Rio Verde trondhjemite, and Bom Jesus, Serra Dourada, Cruzadão and Boa Sorte granites, all with crystallization age ranging from 2.87 to 2.83 Ga (Feio et al., 2013; Rodrigues et al., 2014). This domain was intensely affected by Neoarchean events, more specifically between 2.77 and 2.70 Ga, as recorded by granitic and mafic-ultramafic magmatism, as well as greenstone belts and sedimentary rocks (Nogueira et al., 1995; Vasquez et al., 2008; Dall'Agnol et al., 2013). Around 1.88 Ga, the entire Carajás province was affected by the emplacement of anorogenic granites and associated dikes (Dall'Agnol et al., 2005; Teixeira et al., 2017).

3. Neoarchean magmatism from Carajás province

The Neoarchean events in Carajás province is registered in both Canaã dos Carajás – including Carajás basin – and Sapucaia domains, which Rio Maria domain does not record any event during this time span related to its evolution (Vasquez et al., 2008; Dall'Agnol et al., 2013). They are represented by greenstone belts, sedimentary rocks and mafic-ultramafic and granitic magmatism, as well as sodic granitoids and diorites (Nogueira et al., 1995; Vasquez et al., 2008; Feio et al., 2012; Dall'Agnol et al., 2013).

Concerning granitoids, the Neoarchean granitic magmatism is formed by Estrela granitic complex, Planalto, Vila Jussara and Plaquê suites, as well as Serra do Rabo, Igarapé Gelado, Sossego, Curral and Velho Salobo granites. They show crystallization age between 2.77 and 2.70 Ga – except Velho Salobo granite, which records age of 2.57 Ga (Machado et al., 1991) – and are composed essentially of monzogranites, and subordinate tonalites, granodiorites and syenogranites. Geochemically, these rocks are classified as alkaline granites, although some show calc-alkaline signature as well (Vasquez et al., 2008; Dall'Agnol et al., 2017). Recently, Dall'Agnol et al. (2017) made a detailed study on the main aspects of Neoarchean granites from Carajás province, which classified these ones based on the oxygen fugacity aspect, and grouped these rocks as reduced ferroan, oxidized ferroan and magnesian. There is a controversy concerning the deformational structures of the Neoarchean granites. Barros et al. (2001, 2009), Feio et al. (2012, 2013) and Dall'Agnol et al. (2017) state that these granites were deformed between 2.75 and 2.73 Ga, concomitant with the closing of

Carajás basin, therefore being classified as syn-tectonic granites, whereas Tavares (2015) interprets these granites as pre-tectonic, which were formed in extensional setting, and later deformed/metamorphosed, between 2.68 and 2.63 Ga.

On the other hand, the mafic-ultramafic magmatism generated during the Neoarchean Era is represented by Luanga complex, Cateté intrusive suite, Santa Inês gabbro and basalts of Grão-Pará group (Parauapebas formation; Martins et al., 2017). They were formed at 2.76 Ga (Machado et al., 1991) and are constituted essentially by tholeiitic rocks generated in island arc (Suita, 1988) or continental rift (Ferreira Filho et al., 2007). Besides these, there is also the Pium diopside-norite, an elongated igneous intrusion following E–W regional trend, formed essentially by norites, gabbronorites and quartz gabbros, with crystallization age of 2.74 Ga (Santos et al., 2013).

4. Geology of the Vila União area

The Neoarchean granitoids from Vila União area are exposed over an area of ~350 km2 within the Canaã dos Carajás domain. The main granitic crust is located in the central-western portion of the studied area, which can reach up to 32 km long (Figure 2). It is composed of (at least) two coalescent plutons, amalgamated and elongated parallel to the major E–W-trending compressional/shear structure of Neoarchean age. Other minor exposure forms an E–W-trending elongated massif in the southeastern portion, which can reach up to 8 km long. These bodies occur oriented concordantly to the dominant E–W regional trend and crosscut 3.06–2.83 Ga Mesoarchean rocks (Feio et al., 2013; Delinardo et al., 2014, 2015), represented by orthogranulites, TTG and K-leucogranites, and are coeval with Pium diopside-norite, charnockites and greenstone belts related to Itacaiúnas supergroup (Vasquez et al., 2008; Santos et al., 2013; Marangoanha and Oliveira, unpublished; Figure 2). A small circular pluton of isotropic granite emplaced at 1.89 Ga crosscuts all the units aforementioned (Afonso et al., 2017, unpublished).

Based on fieldwork observations, it was possible establish two different structural domains in the studied area: (1) an E–W to NW–SE steeply inclined foliation towards mostly the N, associated with shallow-to-moderately plunging mineral stretching lineation, present in the Mesoarchean basement rocks; and (2) an E–W steeply inclined well-developed foliation towards both the N and S, and steep-to-subvertically plunging mineral stretching lineation, printed on Neoarchean granitoids (Figure 2). We will focus only on the latter, which represents exclusively the Neoarchean granitoids from Vila União area. On map scale, foliation trajectory and shear zones form a main E–W trend, accompanied by subordinate

NW–SE and NE–SW trends, forming a sigmoidal and anastomosing array (Figure 2). These shear zones show sinistral kinematics and occur as widespread and few kilometers long structures (~30 km), which mark the contact between the amalgamated plutons and the Mesoarchean wall rocks.

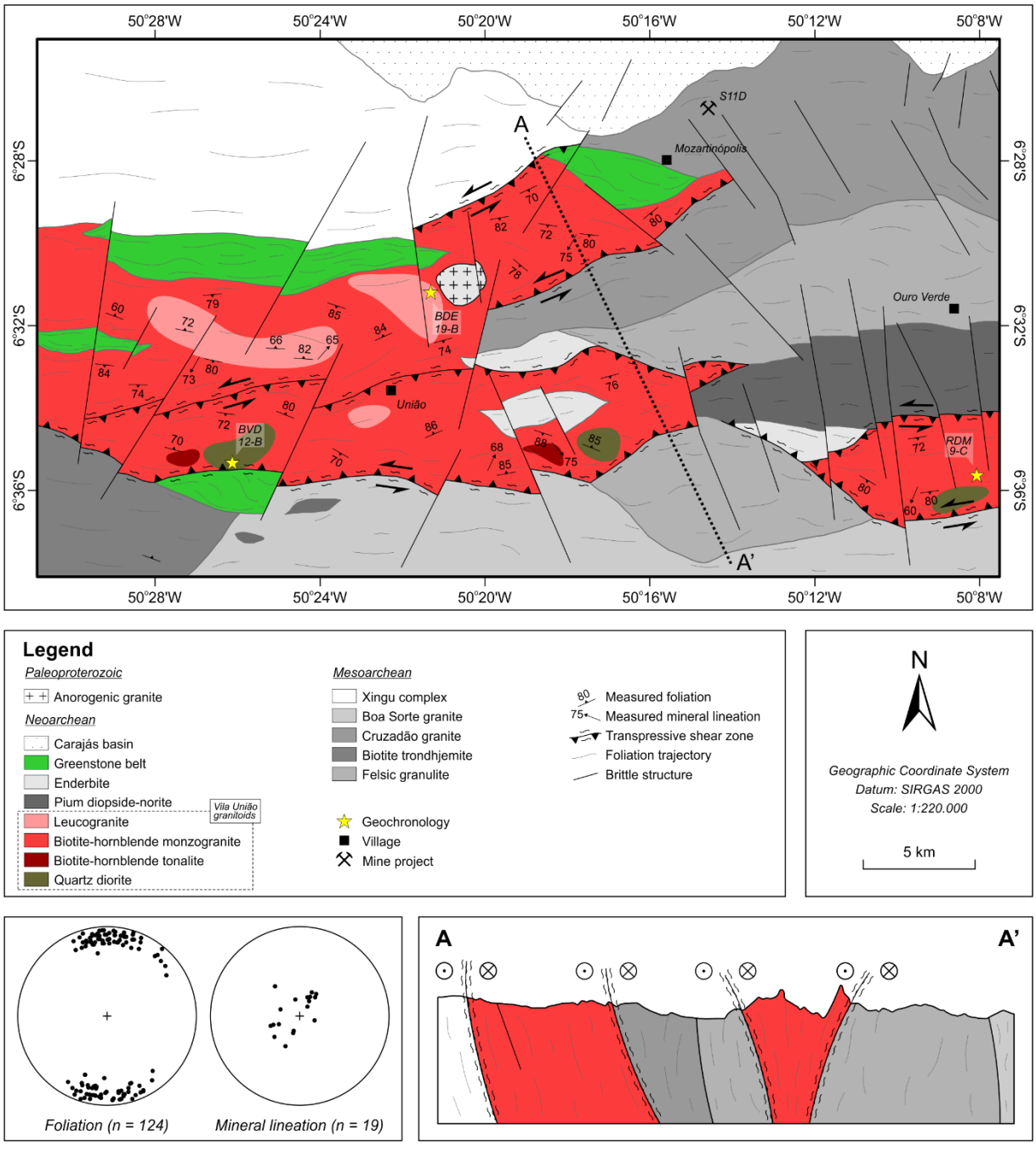

Figure 2. Geological sketch map of the studied area, showing lower hemisphere equal-area (Schmidt-Lambert) stereographic plots of poles to foliation and mineral lineation of the Neoarchean granitoids from Vila União area. Detailed interpretative cross-section A-A' is shown (see map for location).

On the outcrop scale, the structures present in the studied rocks are defined by absent to well-developed mylonitic foliation (Figures 3a, b and c) accompanied by mineral stretching lineation, although mafic enclaves strongly flattened oriented parallel to the foliation are

common (Figure 3d). This foliation trends E–W with steep to subvertical dips (mostly 70–85°) towards both N and S, and the mineral stretching lineation plunges are steep to subvertical as well (60–85°), towards both N and S (cf. Figure 2).

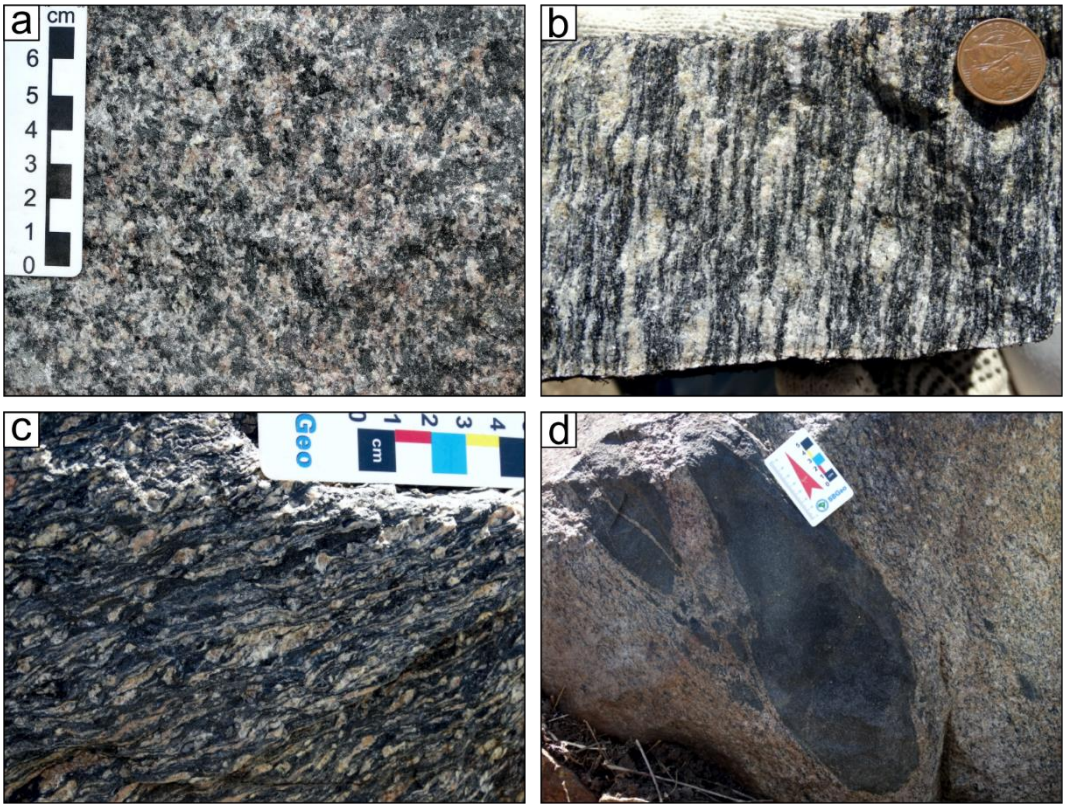

Figure 3. Mesoscopic-scale features of the granitoids from Vila União area, showing the structural aspects printed on these rocks, characterized by (a) absent, (b) moderate and (c) well-developed mylonitic foliation; (d) mafic enclaves strongly flattened oriented parallel to the foliation.

5. Petrography

5.1. Modal classification

Modal composition was performed counting an average of 2,000 points on rock-thin sections of 43 representative samples of granitoids from Vila União area by using Stageledge (Endeeper) point counter. The modal compositions are given in Table 1. These rocks are composed of K-feldspar, quartz and plagioclase as essential minerals; amphibole, biotite and opaque minerals are the main mafic phases, although clino- and orthopyroxene are also present (both rarely in the most felsic varieties, but can reach about 10% in less evolved rocks); titanite, epidote, allanite, apatite, scapolite and zircon as primary accessory minerals; and muscovite and chlorite constitute the secondary minerals.

According to Q-A-P diagram (Le Maître et al., 2002; Figure 4), these rocks show a wide compositional range, and were divided into four varieties: (i) leucogranite (LcGr), (ii) biotite-hornblende monzogranite (BtHbMzG), (iii) biotite-hornblende tonalite (BtHbTn) and

(iv) quartz diorite (QzD). Concerning mafic mineral contents (cf. Table 1 and Figure 4), these rocks are mostly hololeucocratic and leucocratic (M' = 2–32.77%), with rare mesococratic occurrences (M' = 41–42.40%). The varieties LcGr, BtHbMzG and BtHbTn are dominantly coarse- to medium-grained with heterogranular texture (Figure 5a, b and c, respectively), whereas the less evolved variety (QzD) tends to exhibit a fine-grained one (Figure 5d). Additional detailed petrographic and mineralogical descriptions of the granitoids from Vila União area are given in Oliveira et al. (2018).

Table 1. Representative modal compositions of the granitoids from Vila União area.

Sample	BVD 42-F	BVD 42-I	BVD 12-B	BVD 12-A	BVD 48	TDM 7	TDM 11	BVD 42-H	BVD 34-A	RDM 9-C	BVD 47-A	BVD 19	BVD 44	BVD 42-B	BVD 26	BVD 18-B	BDE 19-B	BVD 17	BVD 28
Variety	Quartz diorite			Biotite-hornblende tonalite				Biotite-hornblende monzogranite								Leucogranite			
Minerals (vol.%)																			
Quartz	2.55	4.70	6.67	17.30	20.90	23.85	24.51	18.80	22.42	22.70	26.00	26.65	27.71	31.48	37.30	22.05	23.45	26.80	26.90
Plagioclase	55.05	54.30	66.39	52.50	53.30	42.90	42.20	44.35	45.34	30.35	26.95	26.30	35.78	29.07	27.20	17.20	30.35	21.00	14.85
Alkali feldspar	-	-	-	0.35	5.45	3.45	0.90	10.40	14.24	33.25	31.95	23.30	13.61	28.30	21.95	58.75	42.70	42.55	49.30
Hornblende	20.40	24.95	15.20	20.75	12.80	21.75	20.94	20.50	9.67	7.40	11.60	8.40	9.95	6.60	7.10	-	-	4.70	0.85
Biotite	0.95	0.70	5.79	4.35	4.90	6.55	9.35	1.95	6.17	0.30	-	10.65	9.00	2.90	5.20	0.60	0.70	-	3.50
Clinopyroxene	10.40	6.00	0.99	-	-	-	-	0.10	-	0.65	-	-	-	-	-	-	-	-	-
Orthopyroxene	8.25	6.75	1.11	-	-	-	-	-	-	0.95	-	-	-	-	-	-	-	-	-
Opaque minerals	1.80	2.10	3.27	2.70	0.60	0.15	0.30	3.80	0.21	4.20	0.50	1.50	2.60	0.95	-	0.65	0.45	0.50	0.30
Titanite	-	-	-	0.35	0.70	0.70	0.90	-	1.54	0.10	-	1.40	-	-	0.90	-	0.30	1.75	0.80
Epidote	0.40	0.15	-	0.15	0.10	-	0.48	-	0.10	-	0.95	1.00	0.10	0.15	0.35	-	0.20	0.05	0.10
Scapolite	-	-	0.23	1.55	1.25	-	0.42	-	0.31	-	-	0.60	1.15	0.55	-	-	-	-	-
Apatite	0.20	0.25	-	-	-	-	-	0.05	-	-	0.05	0.20	-	-	-	-	-	-	-
Zircon	-	0.10	-	-	-	-	-	0.05	-	0.10	-	-	-	-	-	-	-	-	-
Chlorite	-	-	0.35	-	-	0.65	-	-	-	-	2.00	-	0.10	-	-	0.75	1.85	2.65	3.40
Bt/Hb	0.05	0.03	0.38	0.21	0.38	0.30	0.45	0.10	0.64	0.04	-	1.27	0.90	0.44	0.73	-	-	-	4.12
A+P	55.05	54.30	66.39	52.85	58.75	46.35	43.10	54.75	59.58	63.60	58.90	49.60	49.39	57.37	49.15	75.95	73.05	63.55	64.15
Colour index (M')	42.40	41.00	26.94	29.85	20.35	29.80	32.39	26.45	18.00	13.70	15.10	23.75	22.90	11.15	13.55	2.00	3.50	9.65	8.95

Abbreviations: A+P (alkali feldspar + plagioclase sum); - (not determined).

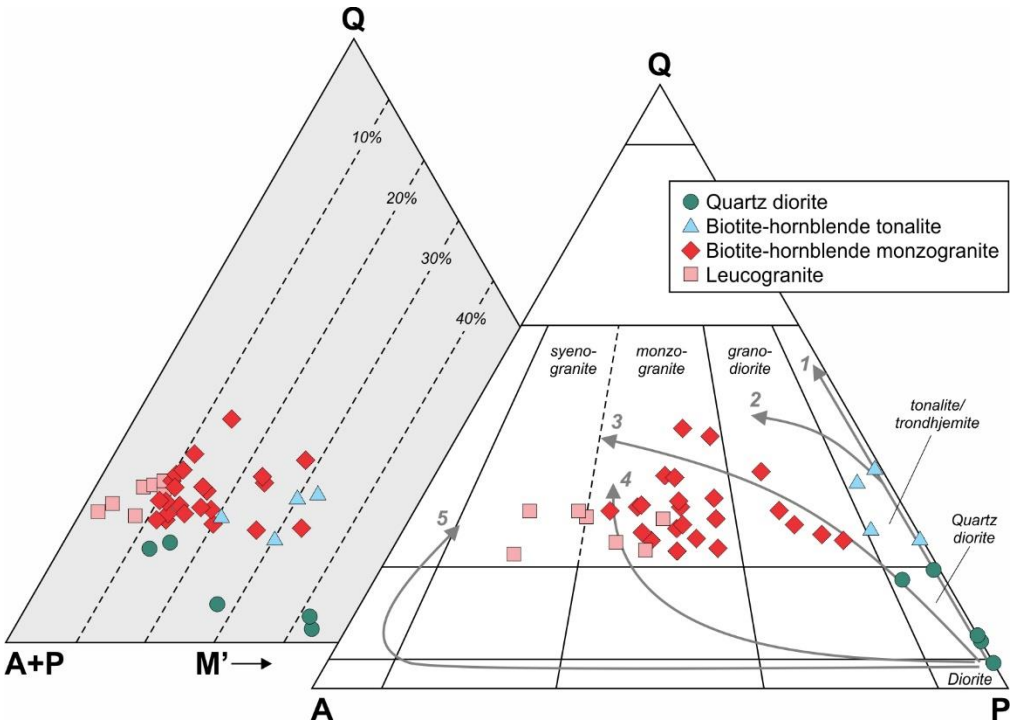

Figure 4. Q-A-P and Q-(A+P)-M plots for the granitoids from Vila União area (Le Maître et al., 2002). Granitic series and their evolutionary trends from Lameyre and Bowden (1982) and Bowden et al. (1984): 1 (tholeiitic), 2 (calc-alkaline tonalitic or trondhjemitic), 3 (calc-alkaline granodioritic), 4 (subalkaline monzonitic or shoshonitic) and 5 (alkaline and peralkaline).

5.2. Textural aspects and deformational effects

The studied area is entirely situated on the Itacaiúnas shear zone, a portion of Carajás province that was affected by intense shearing in the Neoarchean Era (Araújo and Maia, 1991). Therefore, a detailed analysis based on microstructures and microtextures of the granitoids from Vila União area was performed in order to establish a deformational pattern that these rocks were submitted. Thus, according to mylonites classification established by Passchier and Trouw (2005) and Trouw et al. (2010), which consider temperature and strain as the main features to form mylonites, these rocks were divided into three different domains: low, medium and high-grade mylonitic domains.

It is worth to mention that, as the studied area is crosscut by many shear zones then, as a result, these zones exert a huge influence on these domains. Furthermore, it is important to make it clear that all domains exhibit some common features like the alignment of the minerals, mainly feldspar porphyroclasts, quartz, biotite and amphibole, which defines an E–W planar fabric.

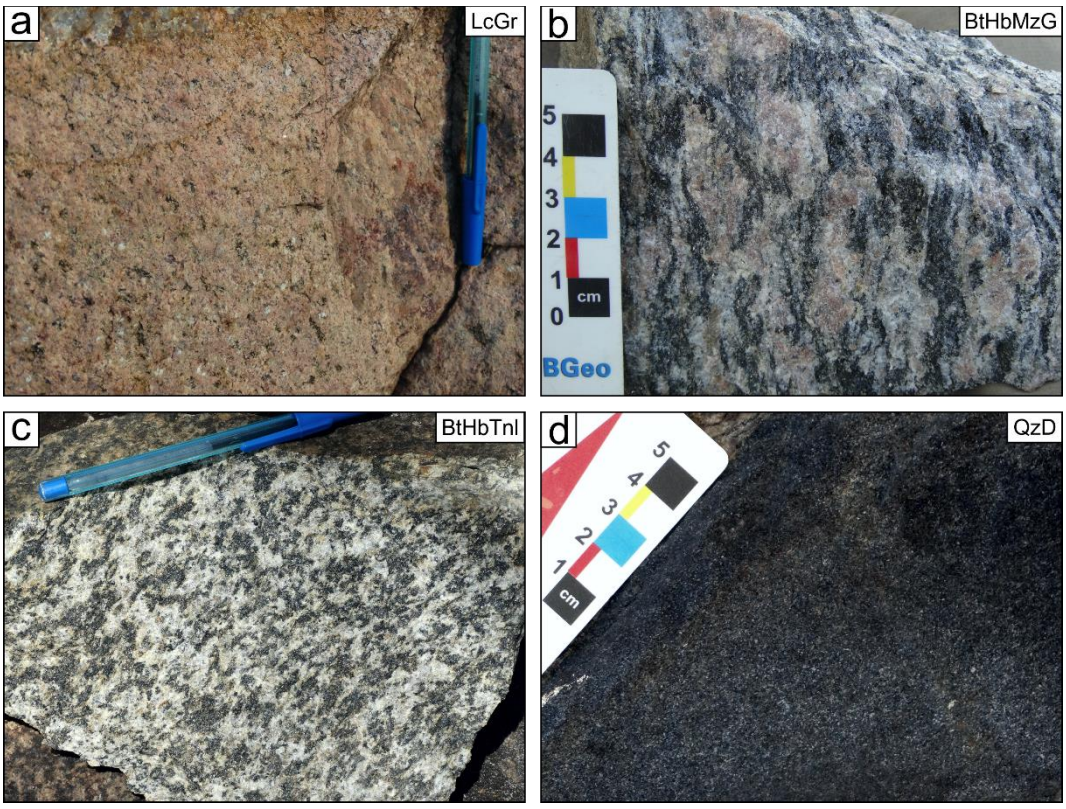

Figure 5. Mesoscopic-scale aspects of the (a) leucogranite, (b) biotite-hornblende monzogranite, (c) biotite-hornblende tonalite and (d) quartz diorite varieties of the Neoarchean granitoids from Vila União area, showing the dominant coarse- to medium-grained with heterogranular texture in the first three ones (a, b and c), whereas the less evolved variety (d) tends to exhibit a fine-grained one.

5.2.1. Low-grade mylonitic domain

This domain comprises rocks with igneous texture almost entirely preserved, characterized mainly by euhedral to subeuhedral square-shaped feldspar porphyroclasts (Figure 6a) and amphibole (Figures 6a and b). Recovery process is quite common and is described chiefly by quartz, which shows undulose extinction with subgrains formation (Figure 6c). As well, bulging recrystallization (BLG-recrystallization) occurs in deformed quartz (Figure 6c). Plagioclase crystals frequently show brittle fracturing (Figure 6d), which sometimes may present submagmatic microfractures filled with opaque mineral-amphibole-biotite aggregates (Figure 6e), or even quartz-feldspar aggregates, suggesting that this deformational process occurred during the crystallization stage (Bouchez et al., 1992). Feldspars with undulose extinction and kink band in this domain are rather rare. Biotite occasionally develops smooth kink bands (Figure 6f), and corroborates with the low-temperature deformation processes in these rocks.

5.2.2. Medium-grade mylonitic domain

The medium-grade mylonites are the most abundant in the studied area. Deformation twinning (Figure 7a) and by kinking (Figure 7b), besides undulose extinction (Figure 7c) in plagioclase porphyroclasts are typical in this domain. At increasing temperature, the recrystallization process becomes more prominent, as demonstrated by BLG-recrystallization in feldspars, which describes core-mantle structures (Figure 7d), besides flame-perthite in K-feldspar (Figure 7e). Moreover, quartz is entirely recrystallized, mainly by subgrain rotation recrystallization (SGR-recrystallization; Figure 7f), albeit BLG-recrystallization is also present.

5.2.3. High-grade mylonitic domain

It is the least common group of rocks in the studied area, and the minerals are practically fully recrystallized. Most plagioclase shows SGR-recrystallization, which the boundary between core and mantle is weakly pronounced (Figures 8a and b), whereas BLG-recrystallization still can be found. Amphibole porphyroclasts with strain shadows of biotite and opaque minerals are quite common (Figures 8c and d). Quartz occurs as ribbon, which indicates growth by high-temperature grain boundary migration recrystallization (GBM-recrystallization; Figures 8a, b and c). Other evidences of quartz affected by GBM-recrystallization in this domain are large grains with inclusions of other minerals (Figure 8e) and the ‘window’ microstructure, which a grain boundary between two grains of a mineral (in

this case, quartz) bulges between two grains of another mineral (in this case, biotite; Passchier and Trouw, 2005; Figure 8f).

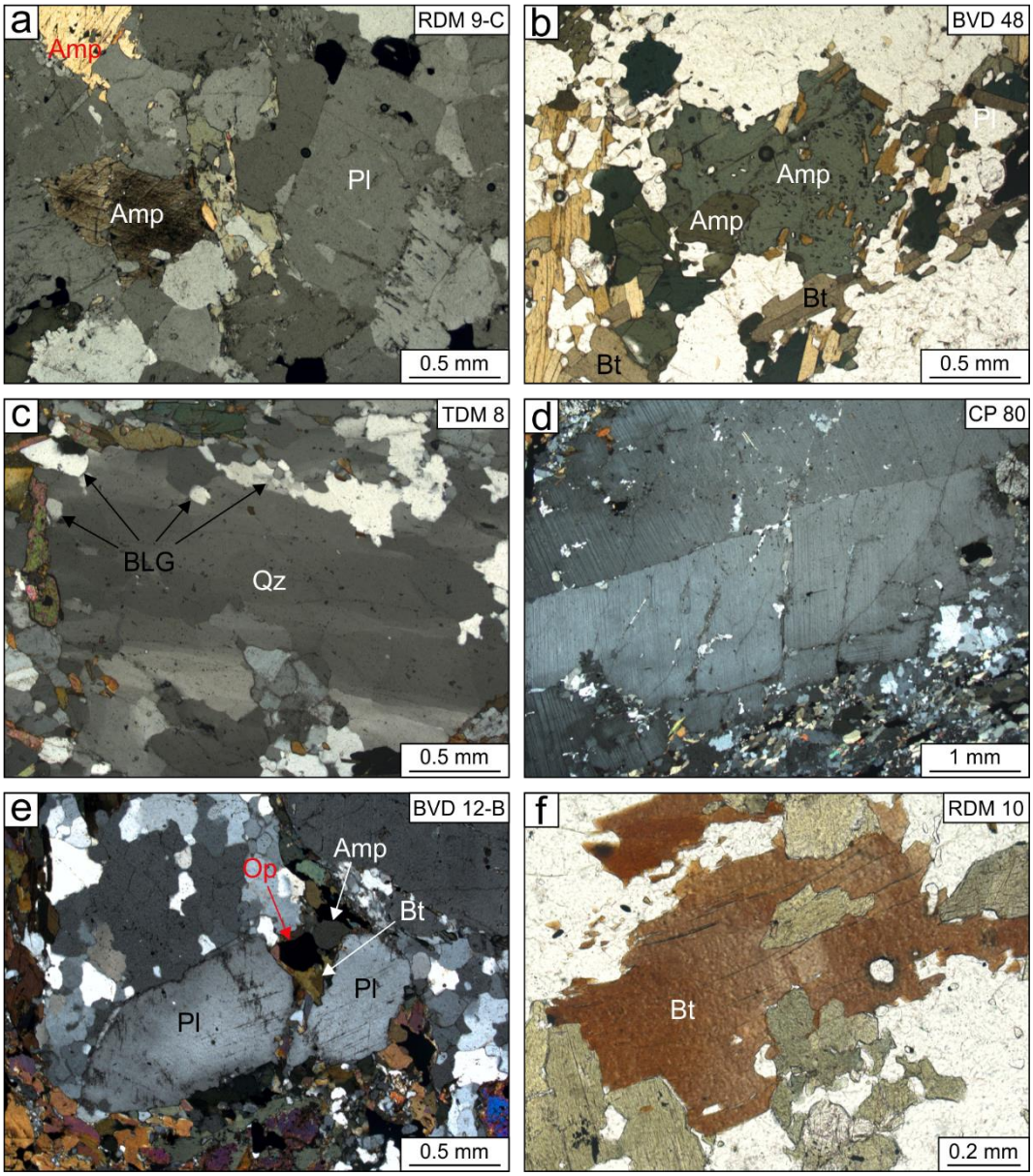

Figure 6. Photomicrographic microstructural features of low-grade domain granitoids from Vila União area. (a) Euhedral to subeuhedral square-shaped feldspar porphyroclasts and subeuhedral amphibole crystals; (b) detail of subeuhedral amphibole associated with small amounts of biotite; (c) quartz showing undulose extinction with subgrains formation by bulging recrystallization (BLG); (d) brittle fracturing in plagioclase porphyroclast; (e) submagmatic microfracture in plagioclase filled with opaque mineral-amphibole-biotite aggregates; and (f) biotite crystal with smooth kink bands. Photomicrographs (a), (c), (d) and (e) under crossed nicols, and (b) and (f) under parallel nicols. Abbreviations: Amp (amphibole), Bt (biotite), Op (opaque minerals), Pl (plagioclase) and Qz (quartz).

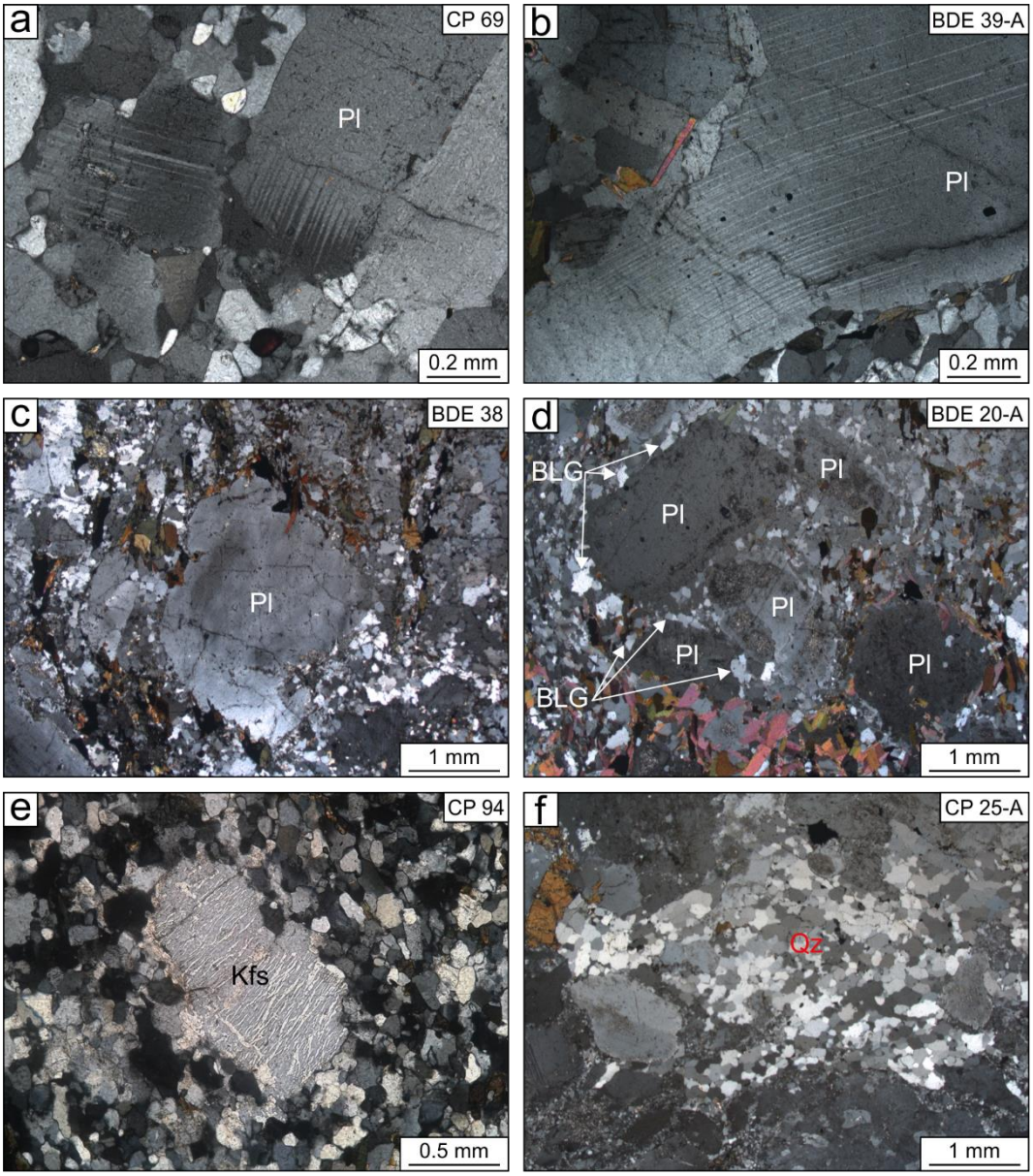

Figure 7. Photomicrographic microstructural features of medium-grade domain granitoids from Vila União area. Plagioclase porphyroclasts showing (a) deformation twinning, (b) deformation by kinking and (c) extinction undulose; (d) core-mantle structures in plagioclase porphyroclasts formed by bulging recrystallization (BLG); (e) flame-perthite in K-feldspar porphyroclast; and (f) quartz entirely recrystallized by subgrain rotation recrystallization (SGR). All of photomicrographs under crossed nicols. Abbreviations: Kfs (K-feldspar), Pl (plagioclase) and Qz (quartz).

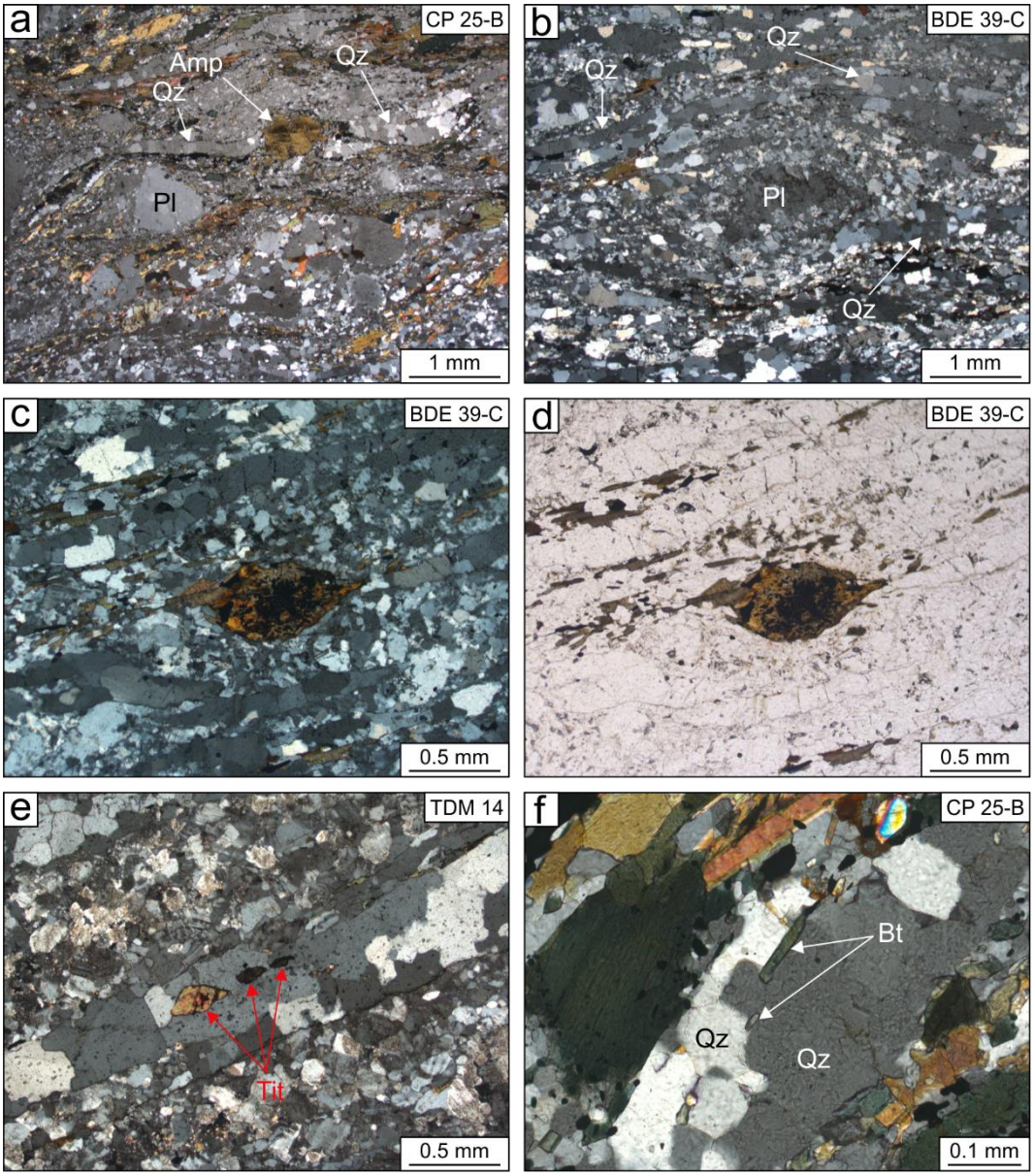

Figure 8. Photomicrographic microstructural features of high-grade domain granitoids from Vila União area. (a) and (b) showing the general aspect of this domain, which their minerals are practically fully recrystallized; plagioclase showing subgrain rotation recrystallization (SGR) and quartz occurs mostly like ribbon that indicates growth by high-temperature grain boundary migration recrystallization (GBM); (c) and (d) displaying amphibole porphyroclasts with strain shadows of biotite and opaque minerals; (e) large quartz grains with inclusions of titanite, which confirms GBM-recrystallization in quartz; and (f) 'window' microstructure formed by quartz and biotite crystals. Photomicrographs (a), (b), (c), (e) and (f) under crossed nicols, and (d) under parallel nicols. Abbreviations: Amp (amphibole), Bt (biotite), Pl (plagioclase), Qz (quartz) and Tit (titanite).

6. Geochemistry

6.1. Introduction

Whole-rock analyses of 41 samples of the different facies distinguished in the granitoids from Vila União area are reported in Table 2. Descriptions of sample preparation and analytical procedures are given in Appendix A.

Table 2. Representative chemical compositions of the granitoids from Vila União area.

Sample	BVD 42-F	BVD 42-I	BVD 42-D	BVD 47-C	BDE 38	BVD 47-E	BVD 12-A	BVD 42-C	BVD 42-E	BVD 48	BVD 42-H	BVD 47-A	BVD 34-A	BVD 47-H	BVD 29	BVD 20	BVD 15	BVD 26	BVD 57	BVD 18-A	BDE 19-B	BVD 31
Variety	Quartz diorite					Biotite-hornblende tonalite					Biotite-hornblende monzogranite								Leucogranite			
Major elements (wt.%)																						
SiO_2	55.30	55.60	55.90	57.20	59.40	60.50	61.70	62.60	64.90	67.40	63.90	65.00	66.30	66.40	67.60	69.90	70.10	71.90	72.90	74.30	74.76	75.60
TiO_2	1.18	1.36	1.30	1.85	1.42	1.29	1.51	0.74	0.99	0.89	1.08	0.90	0.83	0.78	0.75	0.59	0.54	0.51	0.57	0.49	0.36	0.30
Al_2O_3	15.25	13.85	14.50	13.50	14.24	12.90	13.75	13.20	13.85	14.15	13.00	13.90	14.25	12.50	12.90	12.35	13.10	12.70	12.25	12.65	12.34	11.55
Fe_2O_3*	11.50	11.15	10.75	12.60	9.56	9.40	9.04	8.18	7.70	6.81	8.00	6.45	6.86	8.39	5.44	4.97	3.78	4.82	4.91	3.49	2.18	3.28
MnO	0.17	0.18	0.14	0.12	0.12	0.11	0.12	0.10	0.11	0.08	0.09	0.07	0.08	0.06	0.08	0.06	0.03	0.06	0.07	0.03	0.02	0.04
MgO	5.00	3.55	4.34	2.46	2.72	2.29	1.87	3.40	1.90	0.83	1.26	0.81	0.92	1.69	1.39	0.58	0.91	0.42	0.46	0.70	0.34	0.20
CaO	7.33	6.53	7.06	6.46	5.65	5.47	4.85	4.38	4.35	3.70	3.60	3.34	3.86	2.61	2.70	2.04	2.02	1.84	1.96	1.31	1.08	1.14
Na_2O	4.33	4.03	4.16	3.62	3.51	3.58	3.59	3.40	3.84	4.04	3.47	3.46	4.11	3.13	3.28	3.44	3.29	3.41	3.50	3.13	2.86	2.84
K_2O	1.12	1.63	1.87	2.12	1.95	2.01	2.31	2.87	2.91	2.86	3.20	3.57	2.58	3.53	3.48	3.78	4.03	4.05	4.07	4.48	5.12	4.36
P_2O_5	0.37	0.44	0.42	0.62	0.45	0.37	0.43	0.21	0.33	0.22	0.31	0.19	0.18	0.21	0.20	0.10	0.11	0.09	0.10	0.08	0.05	0.04
LOI	0.32	0.26	0.70	1.19	0.60	0.76	0.51	0.69	0.55	0.49	0.45	0.80	0.43	0.86	0.76	0.63	1.18	0.72	0.74	0.85	0.60	1.10
Total	101.87	98.58	101.14	101.74	99.62	98.68	99.68	99.77	101.43	101.47	98.36	98.49	100.40	100.16	98.58	98.44	99.09	100.52	101.53	101.51	99.71	100.45
Trace elements (ppm)																						
Ba	592	870	740	1040	1197	1255	1595	1295	1495	1960	2260	2630	1965	2000	1230	1940	1350	1690	2180	1300	1343	1585
Sr	353.0	320.0	329.0	294.0	465.2	309.0	405.0	260.0	314.0	314.0	302.0	321.0	322.0	202.0	264.0	180.0	198.5	138.5	163.0	168.0	164.6	96.8
Rb	21.9	35.1	28.0	48.0	44.9	39.9	59.3	76.4	61.2	65.6	64.7	73.7	69.3	114.0	125.0	111.0	144.5	108.5	109.0	165.5	165.3	118.5
Zr	147.0	231.0	187.0	334.0	274.0	333.0	529.0	309.0	351.0	699.0	578.0	593.0	813.0	522.0	366.0	522.0	281.0	529.0	608.0	357.0	286.6	424.0
Y	20.7	25.8	22.5	49.1	32.3	29.4	56.0	52.8	24.0	46.2	29.0	35.6	62.1	46.0	31.3	46.1	24.9	47.2	60.9	33.8	32.1	50.9
Hf	3.7	5.4	4.8	7.5	6.6	7.9	12.7	8.2	8.0	15.1	12.9	12.9	18.7	12.7	9.8	13.3	8.0	12.6	14.4	10.2	8.4	11.7
Nb	7.5	13.0	7.1	19.7	11.8	14.6	17.1	21.0	9.9	18.9	10.0	16.7	25.8	15.8	14.0	20.1	13.2	19.5	21.3	13.2	12.0	21.1
Ta	0.9	1.0	0.6	1.4	0.7	1.5	1.3	1.7	1.0	1.5	1.2	2.0	1.7	1.4	2.0	2.1	1.9	1.6	1.9	1.8	1.3	2.0
Th	4.9	4.5	3.6	17.1	5.3	9.2	8.0	11.9	5.0	16.1	5.0	7.3	15.2	9.9	16.0	16.9	20.7	22.8	23.7	14.2	15.2	22.2
La	31.7	52.1	32.8	84.8	60.2	51.4	84.2	71.3	46.1	76.5	51.7	52.2	88.0	58.8	67.1	70.2	37.0	72.3	106.5	39.0	54.6	96.0
Ce	59.4	95.9	68.7	176.0	126.9	103.5	173.0	147.0	89.7	148.0	98.3	115.5	192.0	134.5	151.5	152.0	82.4	163.5	199.5	94.7	113.0	185.0
Pr	6.88	10.45	8.58	21.20	15.46	11.40	20.90	17.35	10.40	17.00	11.85	13.60	21.50	14.90	16.05	16.50	9.63	17.75	23.30	11.45	13.46	21.40
Nd	25.6	37.4	32.8	77.0	59.8	42.0	84.7	67.4	40.7	62.3	45.9	55.2	78.7	60.1	57.9	61.7	37.0	67.2	82.6	44.9	48.4	75.8
Sm	4.83	6.45	6.23	14.25	10.50	7.64	14.60	13.00	7.11	11.15	8.42	10.20	14.05	11.60	10.20	11.40	6.47	11.70	15.00	8.11	8.40	12.60
Eu	1.34	1.77	1.42	3.96	2.31	2.25	3.18	2.45	2.03	3.44	2.97	3.63	3.38	2.75	1.50	2.41	1.04	2.16	3.33	1.26	1.20	2.01
Gd	4.09	5.39	4.89	12.80	8.63	7.01	13.10	11.55	5.40	10.40	7.13	9.06	12.60	10.25	7.12	10.10	5.70	11.15	14.15	7.73	6.72	10.85
Tb	0.63	0.84	0.73	1.67	1.20	1.11	1.60	1.77	0.78	1.43	1.02	1.15	1.69	1.56	1.00	1.42	0.82	1.62	1.90	1.19	1.02	1.60
Dy	3.81	4.60	4.08	9.39	6.48	6.21	9.07	9.48	4.36	8.02	5.61	6.88	10.40	8.46	5.19	8.63	4.42	9.04	10.60	6.38	5.78	8.69
Ho	0.76	0.94	0.87	1.84	1.19	1.16	1.79	1.95	0.84	1.65	1.09	1.23	2.08	1.67	1.00	1.62	0.88	1.74	2.16	1.04	1.13	1.99
Er	2.25	2.62	2.50	5.02	3.32	3.11	5.07	5.85	2.50	4.67	3.01	3.50	6.42	4.94	3.57	4.86	2.80	5.27	6.12	4.11	3.27	5.57
Tm	0.35	0.40	0.33	0.72	0.47	0.47	0.76	0.81	0.35	0.68	0.40	0.59	1.02	0.68	0.44	0.77	0.41	0.82	0.84	0.53	0.49	0.83
Yb	2.15	2.55	2.19	4.20	3.06	3.01	4.60	4.86	1.99	4.28	2.55	3.39	5.75	4.45	3.16	4.74	2.46	4.81	5.46	3.48	3.29	5.07
Lu	0.31	0.44	0.32	0.63	0.45	0.44	0.78	0.81	0.33	0.71	0.42	0.60	0.92	0.67	0.46	0.68	0.40	0.70	0.82	0.40	0.48	0.77

Fe_2O_3* = total iron recalculated as Fe_2O_3; LOI = loss on ignition.

6.2. Major and trace elements

In general, these rocks show a wide chemical compositional range; SiO_2 contents vary from 69.03 to 74.76 wt.% in the LcGr, from 63.90 to 73.19 wt.% in the BtHbMzG, from 60.50 to 67.40 wt.% in the BtHbTn and from 55.30 to 59.40 wt.% in the QzD. In Harker diagrams (Figure 9), TiO_2, Al_2O_3, Fe_2O_3*, CaO, MgO and P_2O_5 display a negative correlation with SiO_2, while K_2O shows a positive one and Na_2O exhibits a scattered pattern. Concerning trace elements (Figure 10), the Rb contents display a positive correlation with SiO_2, while Sr shows a negative one. Rb values are higher in the LcGr (78.5–165.5 ppm) and decrease progressively in the BtHbMzG, BtHbTn and QzD (53.9–161.5 ppm, 39.9–86.5 ppm and 21.9–48 ppm, respectively), whereas Sr presents lower contents in the LcGr (163–191.8 ppm) and increase towards the BtHbMzG, BtHbTn and QzD (107.8–322 ppm, 253–405 ppm and 294–465.2 ppm, respectively). Ba and Zr exhibit a peculiar behavior, defined by inflection points closer to 64 and 66 wt.% SiO_2, respectively. To both elements, their respective contents increase with increasing SiO_2 but sharply decrease in their respective inflection points.

The chondrite-normalized REE patterns (Figure 11a) show no difference between the varieties of granitoids from Vila União area, except by the negative Eu anomaly, which becomes slightly more negative in the more evolved varieties. All the varieties are similar, as shown by moderate to high REE contents (La = 31.7–106.5 ppm; Gd = 4.09–14.15 ppm; Yb = 1.83–5.75 ppm) and moderately fractionated patterns (La_N/Yb_N = 7.61–21.12). In the mantle-normalized multi-element diagram (McDonough and Sun, 1995; Figure 11b), the studied rocks display overall Large Ion Lithophile Elements (LILE)-enriched patterns (Rb, Ba, Th and K), with most values between 30 and 400 times higher than the primitive mantle values, which the most evolved varieties (LcGr and BtHbMzG) present the highest values compared to the least evolved ones (BtHbTn and QzD). The same behavior is observed for Nb-Ta, Sr, P and Ti, which show larger negative anomalies in the most evolved varieties, and become smoother in the least evolved ones.

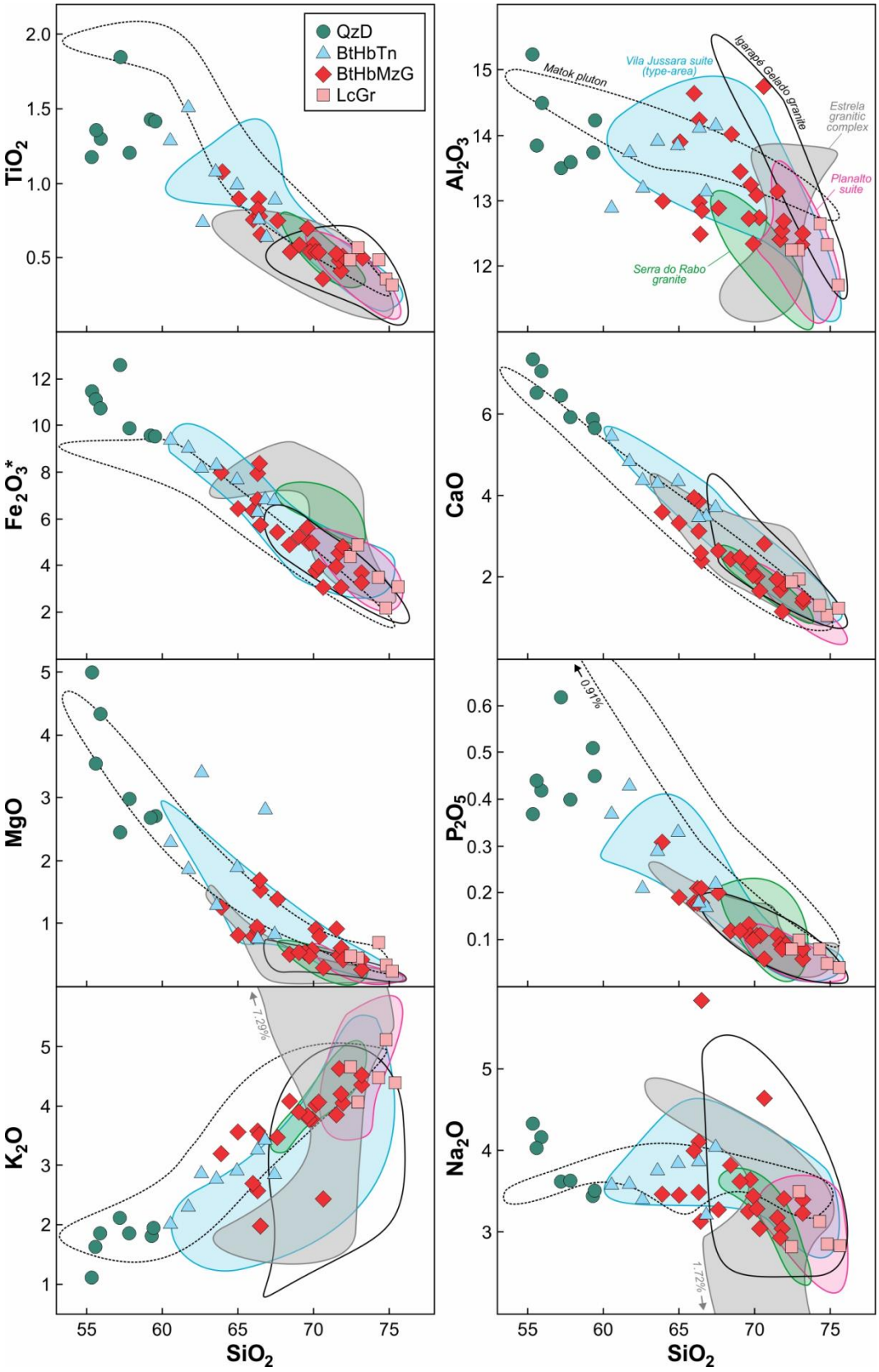

Figure 9. Harker diagrams (in wt.%) for the granitoids from Vila União area, compared with Vila Jussara (Dall'Agnol et al., 2017) and Planalto suites (Feio et al., 2012), Estrela granitic complex and Igarapé Gelado granite (Barros et al., 2001, 2009), Serra do Rabo granite (Sardinha et al., 2006) and Matok pluton (Laurent et al., 2014). Abbreviations: QzD (quartz diorite), BtHbTn (biotite-hornblende tonalite), BtHbMzG (biotite-hornblende monzogranite) and LcGr (leucogranite).

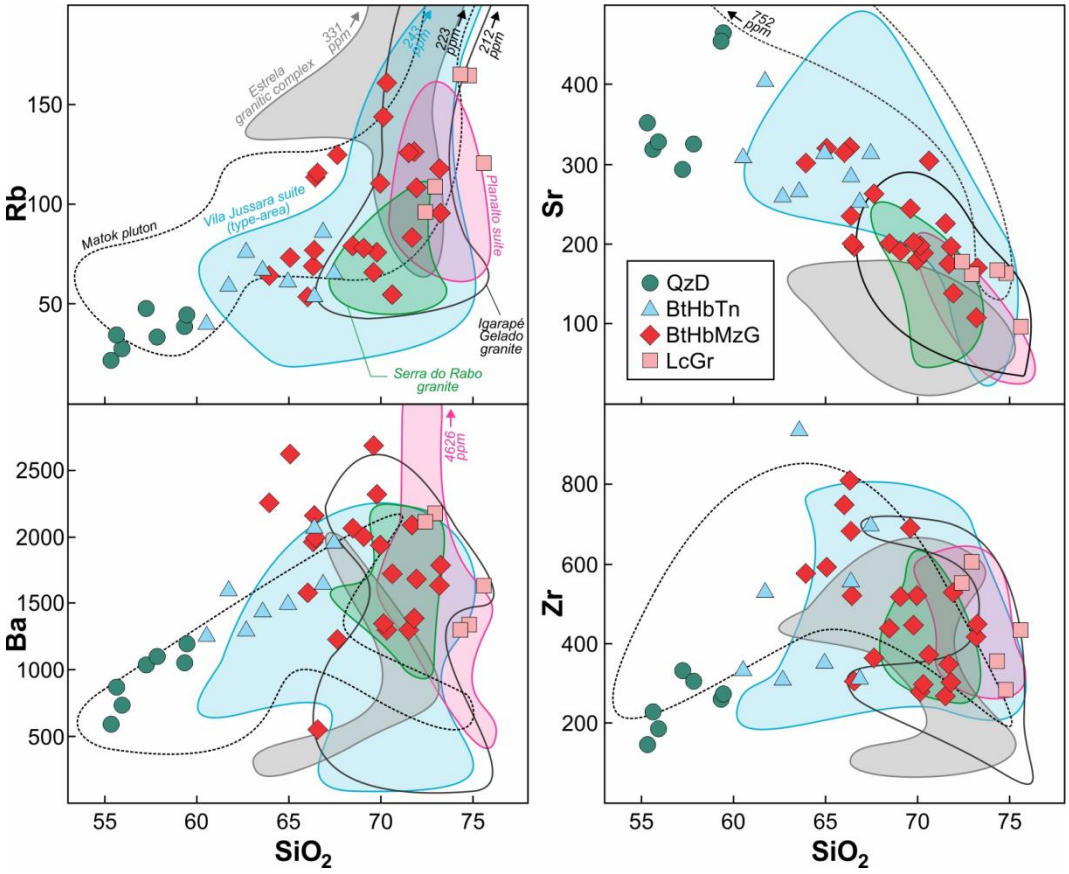

Figure 10. Harker diagrams for selected trace elements for granitoids from Vila União area, compared with Vila Jussara (Dall'Agnol et al., 2017) and Planalto suites (Feio et al., 2012), Estrela granitic complex and Igarapé Gelado granite (Barros et al., 2001, 2009), Serra do Rabo granite (Sardinha et al., 2006) and Matok pluton (Laurent et al., 2014). All trace elements are in ppm, and SiO_2 in wt.%. Abbreviations: QzD (quartz diorite), BtHbTn (biotite-hornblende tonalite), BtHbMzG (biotite-hornblende monzogranite) and LcGr (leucogranite).

6.3. Classification and granitoids typology

As stated by the P-Q diagram (Debon and Le Fort, 1988; Figure 12a), the granitoids from Vila União area are classified predominantly as monzogranites and granodiorites, with subordinate syenogranites, tonalites and (quartz) diorites. In the normative An-Ab-Or diagram (O'Connor, 1965, with fields from Barker, 1979; Figure 12b), the samples plot in the granites, granodiorites and tonalites fields. In the SiO_2 *vs.* Fe-index diagram, the LcGr and BtHbMzG varieties are predominantly akin to ferroan granitoids, while the dioritic and tonalitic rocks (strongly enriched in mafic mineral) cross into the magnesian field (Figure 12c). The same diagram shows that, in the fields delimited by Miyashiro (1974), the enrichment in Fe is responsible by tholeiitic nature of the studied rocks, which are metaluminous to slightly peraluminous according to Shand's (1950) parameters (Figure 12d). When plotted in the MALI diagram (Frost et al., 2001), these rocks lie mostly within the calc-alkaline field (Figure 12e), although they show a strong alkaline tendency when plotted in the diagram of Sylvester (1989; Figure 12f).

According to Y *vs.* Nb tectonic discriminant diagram (Pearce et al., 1984), the studied rocks show intraplate affinity, although a significant number of samples fall in volcanic arc and syn-collisional granites field. In granite classification diagrams proposed by Whalen et al. (1987; Figure 13b) and Dall'Agnol and Oliveira (2007; Figure 13c), these rocks present A-type granite affinities. They are classified as A2-subtype granites (Eby, 1992), which comprises magmas derived from (underplated) lower continental crust (Figure 13d).

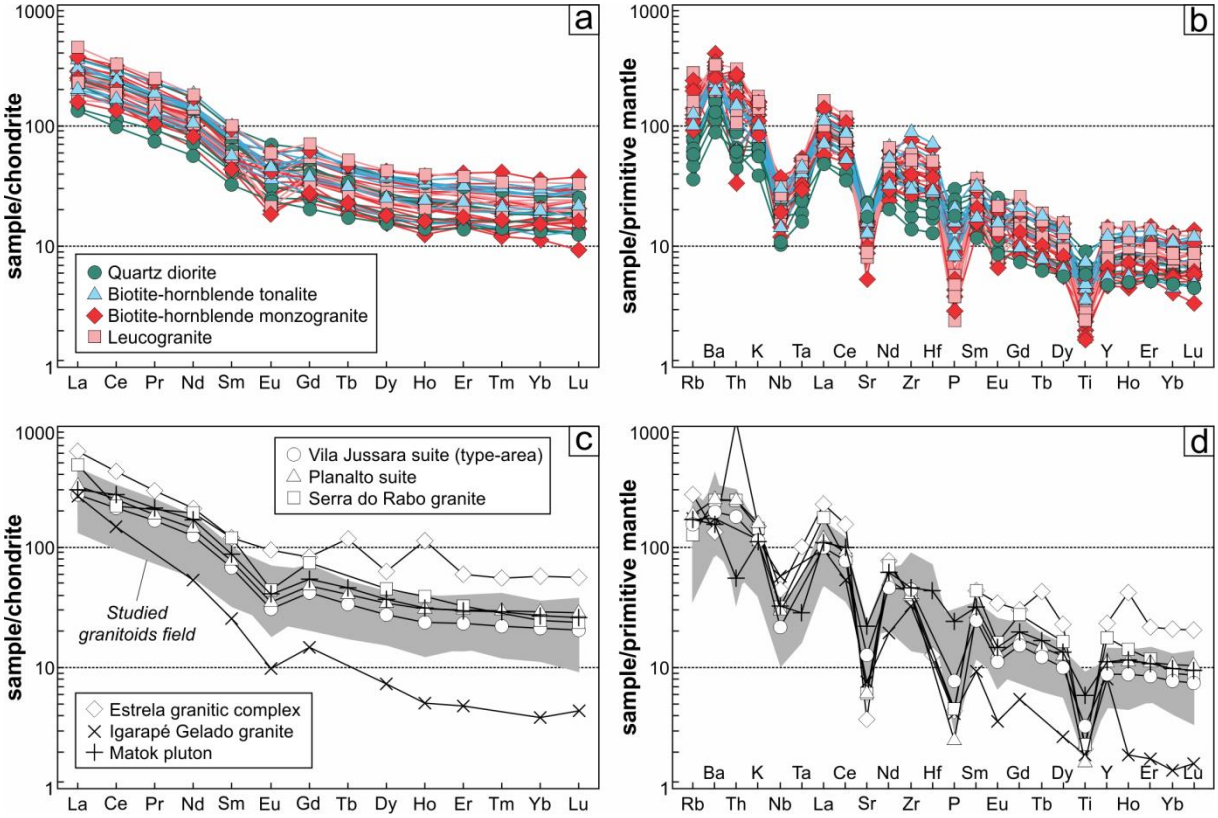

Figure 11. (a and c) REE and (b and d) multi-element patterns of the granitoids from Vila União area, with values normalized to C1 chondrite and pyrolite (McDonough & Sun, 1995), respectively, compared with average compositions of Vila Jussara (Dall'Agnol et al., 2017) and Planalto suites (Feio et al., 2012), Estrela granitic complex and Igarapé Gelado granite (Barros et al., 2001, 2009), Serra do Rabo granite (Sardinha et al., 2006) and Matok pluton (Laurent et al., 2014).

7. Geochronology

7.1. Introduction

New geochronological data for the granitoids from Vila União area are presented here. These rocks were analyzed by the single zircon Pb-Pb evaporation, U-Pb SHRIMP and U-Pb LA-MC-ICP-MS methods. The location of the dated samples is shown in Figure 2 and their analytical data are summarized in tables 3 and 4. The analytical techniques and data processing are described in Appendix B.

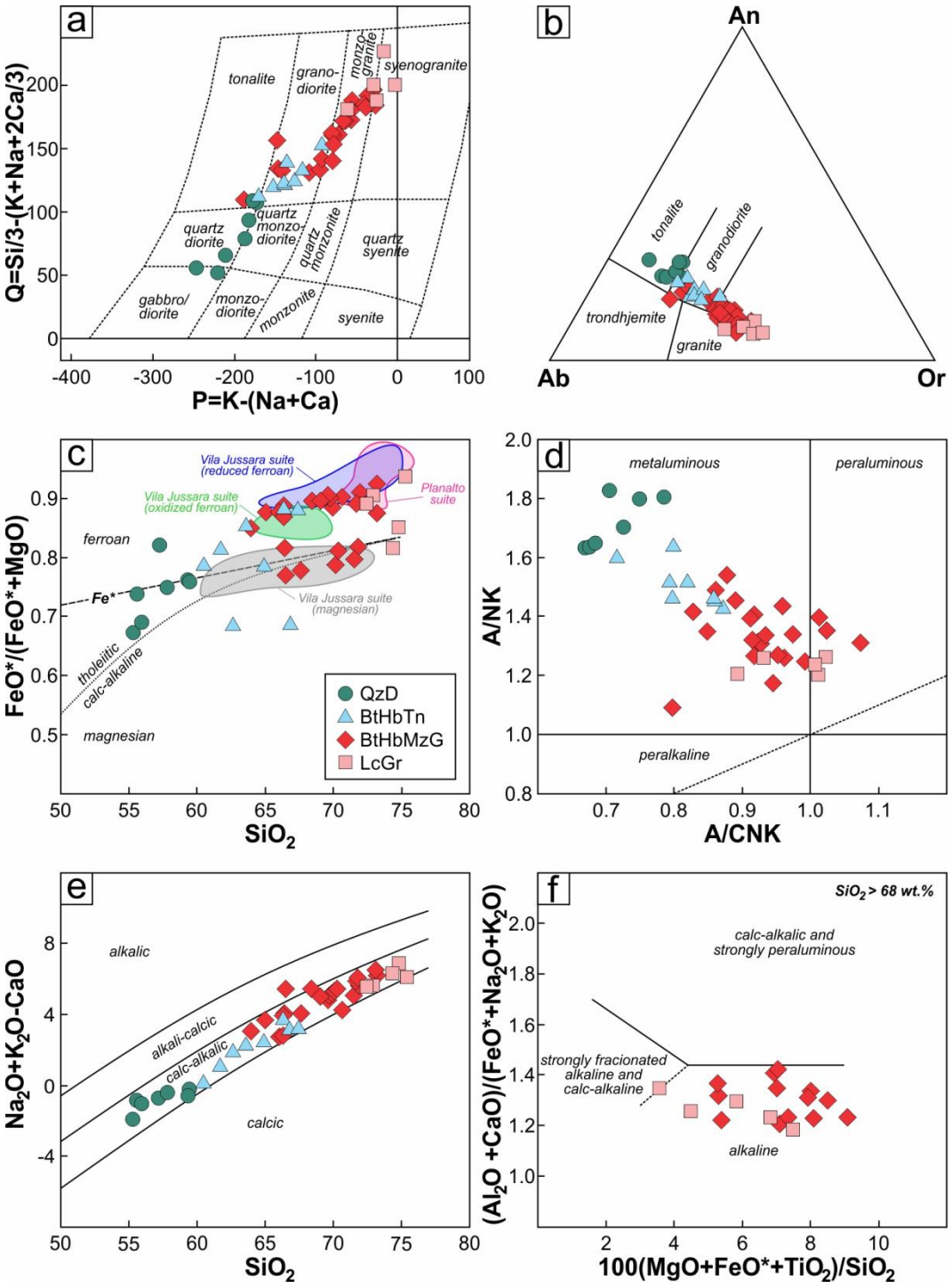

Figure 12. Geochemical diagrams for granitoids from Vila União area: (a) P-Q diagram from Debon & Le Fort (1988); (b) Normative feldspar triangle (O'Connor, 1965) with fields from Barker (1979); (c) FeO*/(FeO* + MgO) *vs.* SiO_2 after Frost et al. (2001) showing the ferroan character of the studied rocks, with dotted line from Miyashiro (1974); (d) A/CNK [$Al_2O_3/(CaO+Na_2O+K_2O)$] *vs.* A/NK [$Al_2O_3/(Na_2O+K_2O)$] diagram (Shand, 1950); (e) Na_2O+K_2O-CaO (MALI) *vs.* SiO_2 diagram (Frost et al., 2001); and (f) major element discrimination diagram for leucogranites (Sylvester, 1989). Abbreviations: QzD (quartz diorite), BtHbTn (biotite-hornblende tonalite), BtHbMzG (biotite-hornblende monzogranite) and LcGr (leucogranite).

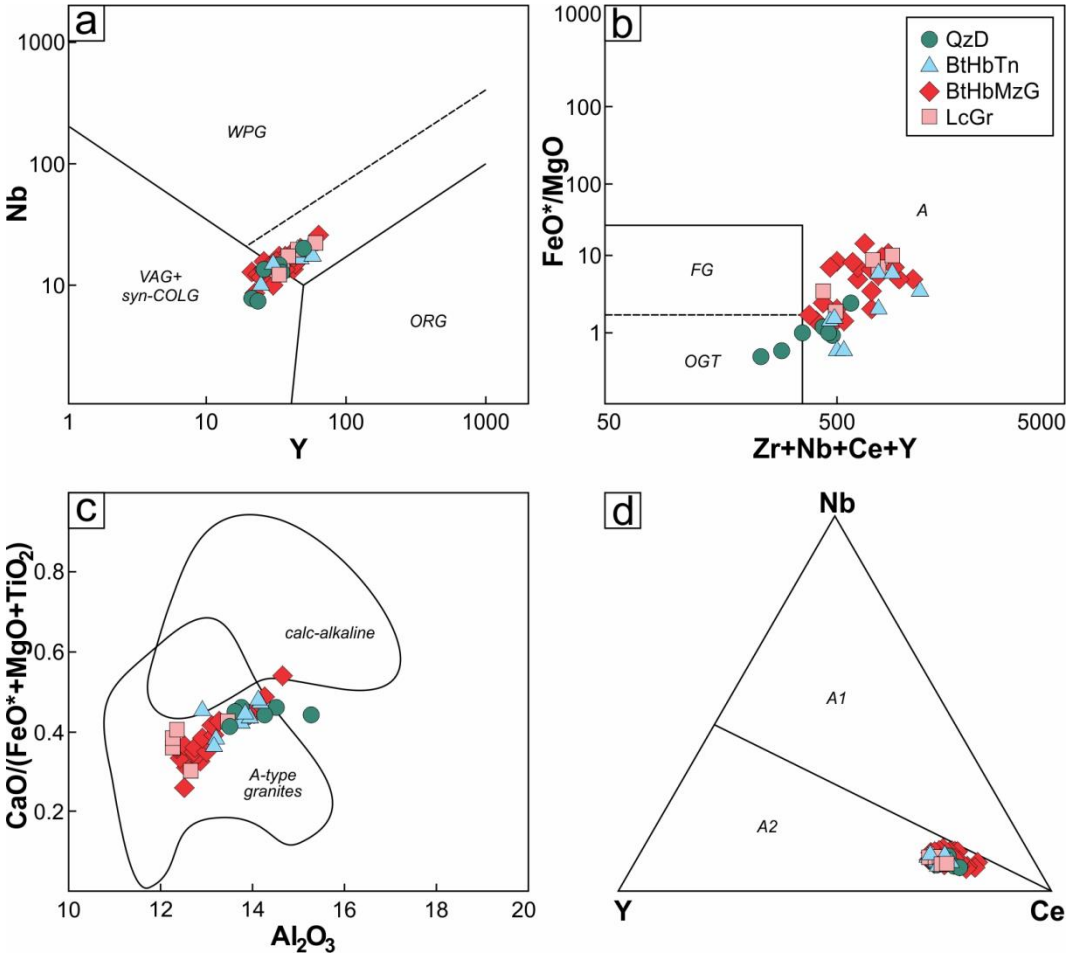

Figure 13. (a) Discrimination of tectonic environment diagram (Pearce et al., 1984); (b) discrimination diagram proposed by Whalen et al. (1987) showing the A-type affinities of the studied rocks; (c) $CaO/(FeO^*+MgO+TiO_2)$ *vs.* Al_2O_3 diagram (Dall'Agnol and Oliveira, 2007); and d) Nb–Y–Ce diagram. A1 and A2 fields after Eby (1992). Abbreviations: QzD (quartz diorite), BtHbTn (biotite-hornblende tonalite), BtHbMzG (biotite-hornblende monzogranite), LcGr (leucogranite), HFCA (highly fractionated calc-alkaline), WPG (within-plate granites), VAG (volcanic arc granites), syn-COLG (syn-collision granites), ORG (oceanic ridge granites), FG (fractionated granites) and OGT (unfractionated granites).

7.2. Results

Three representative samples of different varieties from these granitoids were selected for geochronological analyses: a leucomonzogranite (BVD 19-B) were analyzed by the U-Pb SHRIMP method, a quartz diorite (BVD 12-B) by the U-Pb LA-MC-ICP-MS method and a biotite-hornblende monzogranite (RDM 9-C) by the single zircon Pb-Pb evaporation method. In general, the zircon grains from these granitoids are colorless and transparent to dark brown or pink, euhedral to subhedral, long to shortly elongated with length varying from 150 to 300 μm, and an aspect ratio (length/width) that ranges from 2 to 3. Cathodoluminescence images of zircon grains reveal weak to high luminescence and a regular oscillatory zoning is common but not systematic. Most grains contain small inclusions of opaque minerals and apatite. Moreover, they do not present inherited cores.

Table 3. Zircon U-Pb isotopic data obtained by SHRIMP and LA-MC-ICP-MS for the granitoid samples BDE 19-B and BVD 12-B, respectively, from Vila União area.

Spot	U	Th	Th/U	$^{206}Pb_c$	Isotopic ratios					Age		Discordance
	(ppm)	(ppm)		(%)	$^{207}Pb/^{235}U$	1σ (%)	$^{206}Pb/^{238}U$	1σ (%)	ρ	$^{207}Pb/^{206}Pb$	1σ (%)	(%)
BDE 19-B (Leucomonzogranite) - SHRIMP												
1.1	40	32	0.82	1.75	13.7470	1.4	0.5217	1.1	0.825	2751.7	12.6	2
2.1	61	71	1.20	5.54	13.6522	1.6	0.5260	1.0	0.606	2726.8	21.2	0
3.1	100	49	0.50	1.51	14.0034	1.0	0.5355	0.8	0.850	2739.3	8.4	-1
4.1	61	37	0.62	0.89	14.0997	1.2	0.5405	1.0	0.867	2735.2	9.9	-2
5.1	37	30	0.85	0.03	13.9701	1.4	0.5339	1.1	0.828	2740.4	12.6	-1
6.1	37	29	0.81	0.69	13.9122	1.4	0.5296	1.2	0.838	2746.6	12.3	0
7.1	45	38	0.86	0.02	13.7134	1.2	0.5208	1.0	0.846	2750.5	10.7	2
8.1	40	30	0.79	0.46	14.3742	1.5	0.5499	1.1	0.763	2738.5	15.7	-3
9.1	41	31	0.78	1.93	13.8725	1.4	0.5335	1.1	0.809	2729.9	13.4	-1
10.1	61	23	0.38	2.43	13.3443	1.2	0.5195	1.0	0.804	2709.8	11.9	0
11.1	52	42	0.83	0.35	14.1733	1.2	0.5410	1.0	0.856	2742.4	10.1	-2
12.1	557	347	0.64	-0.02	14.0176	0.6	0.5351	0.6	0.960	2742.0	3.0	-1
13.1	183	148	0.84	0.14	14.1240	0.8	0.5405	0.7	0.916	2738.0	5.2	-2
BVD 12-B (Quartz diorite) - LA-MC-ICP-MS												
1.1	4	3	0.80	0.35	15.3948	3.2	0.5976	2.0	0.619	2714.4	69.1	-6
2.1	12	12	1.02	0.21	14.2087	1.6	0.5532	1.3	0.802	2709.6	26.4	-3
3.1	54	57	1.06	0.12	12.6276	0.5	0.4770	0.4	0.731	2759.3	9.7	5
4.1	23	16	0.73	0.40	15.5870	2.5	0.6150	2.3	0.927	2687.7	25.4	-8
5.1	13	15	1.15	0.35	13.7508	1.4	0.5289	0.9	0.629	2729.6	30.6	0
6.1	11	10	0.93	0.37	14.5832	1.1	0.5629	0.5	0.456	2723.8	25.8	-3
7.1	5	4	0.76	0.16	15.7820	7.3	0.5752	4.3	0.588	2818.1	167.2	-2
8.1	50	25	0.52	0.12	13.5118	1.3	0.5256	0.8	0.599	2711.2	28.0	0
9.1	8	8	1.06	1.39	13.1417	2.7	0.5029	1.0	0.384	2738.0	67.4	2
10.1	18	16	0.91	0.47	14.4454	1.5	0.5452	1.3	0.866	2760.7	20.3	-1
11.1	13	13	1.02	0.39	15.7883	2.8	0.5805	1.2	0.438	2803.8	71.2	-3
12.1	26	20	0.78	0.23	14.7969	0.9	0.5669	0.6	0.619	2736.3	19.3	-3
13.1	12	8	0.66	0.48	16.9746	3.5	0.6132	2.3	0.665	2832.6	73.2	-5
14.1	15	16	1.11	0.40	14.6943	1.1	0.5663	0.8	0.706	2726.3	21.2	-3
15.1	17	14	0.83	0.37	15.3991	0.8	0.5835	0.4	0.500	2754.4	18.3	-4
16.1	16	15	0.91	0.28	14.8885	0.7	0.5681	0.5	0.732	2742.9	13.0	-3
17.1	30	51	1.71	0.52	13.9524	1.0	0.5326	0.9	0.931	2742.1	9.6	0
18.1	43	11	0.26	0.53	14.1648	3.0	0.5333	2.3	0.787	2764.9	50.8	0
19.1	120	18	0.16	0.43	8.7728	3.4	0.3864	3.3	0.971	2504.3	20.2	9
19.2	101	11	0.11	0.23	11.0678	1.4	0.4663	1.3	0.981	2578.6	6.9	2
20.1	12	10	0.87	0.38	13.2829	1.4	0.5027	0.8	0.570	2756.3	31.8	3
21.1	16	15	0.95	0.41	14.2941	0.8	0.5470	0.5	0.618	2738.0	17.3	-2
22.1	84	60	0.72	0.52	11.1455	1.3	0.4394	0.8	0.583	2689.1	29.3	7
23.1	14	13	0.89	0.31	14.9863	0.9	0.5889	0.5	0.523	2694.3	20.8	-6
24.1	61	29	0.49	0.32	14.0728	1.7	0.5539	1.6	0.979	2691.7	9.1	-3
25.1	65	9	0.14	0.12	15.3446	0.9	0.6136	0.9	0.928	2665.4	9.2	-9
26.1	19	13	0.66	0.34	13.8139	1.0	0.5273	0.6	0.616	2742.3	21.1	0
27.1	9	8	0.85	0.39	14.0254	2.1	0.5493	1.1	0.505	2700.0	49.0	-3
28.1	39	33	0.86	0.33	13.4486	0.6	0.5139	0.5	0.812	2740.3	9.7	1
29.1	13	14	1.05	0.30	14.4146	1.1	0.5617	0.7	0.625	2708.1	22.9	-3
30.1	12	11	0.91	1.32	13.7347	1.2	0.5219	0.7	0.526	2749.5	29.0	1
31.1	11	13	1.24	1.75	13.3305	1.4	0.5100	1.1	0.776	2738.3	23.8	2
32.1	24	24	1.00	0.28	13.4178	0.8	0.5080	0.6	0.658	2755.8	17.4	2
33.1	22	15	0.71	0.24	13.6670	1.2	0.5248	1.0	0.861	2732.3	16.7	0
34.1	22	26	1.21	0.21	13.5694	1.0	0.5202	0.7	0.672	2735.1	20.6	1
35.1	19	16	0.86	0.58	11.6072	2.6	0.4494	1.1	0.412	2718.7	65.3	7
36.1	32	31	0.99	0.57	13.2420	1.0	0.5100	0.6	0.536	2727.4	24.0	1
37.1	11	12	1.11	0.32	13.8377	1.8	0.5233	1.0	0.593	2757.6	39.3	1
38.1	13	15	1.09	0.34	13.1717	1.2	0.5168	0.7	0.572	2696.9	25.9	0
39.1	31	33	1.08	0.17	13.4024	0.5	0.5159	0.4	0.676	2728.2	10.8	1

Pb_c: common Pb corrected using measured ^{204}Pb.

Table 4. Summary of zircon single-crystal evaporation Pb isotopic data of the granitoid sample RDM 9-C from Vila União area.

Zircon	Evaporation temperature (°C)	Number of ratios	$^{204}Pb/^{206}Pb$	2σ	$(^{208}Pb/^{206}Pb)_c$	2σ	$(^{207}Pb/^{206}Pb)_c$	2σ	Age (Ma)	2σ
5	1500	34/34	0.000028	0.000005	0.15700	0.00052	0.19075	0.00034	2749.0	2.9
6	1500	26/26	0.000040	0.000007	0.16688	0.00030	0.19078	0.00021	2749.3	1.8
6	1550	38/38	0.000060	0.000007	0.18450	0.00206	0.19033	0.00026	2745.4	2.3
7	1500	28/28	0.000049	0.000006	0.17310	0.00037	0.19032	0.00034	2745.3	2.9
11	1450	06/06	0.000078	0.000014	0.19013	0.00159	0.19077	0.00037	2749.2	3.2
13	1500	34/34	0.000138	0.000007	0.16897	0.00072	0.19071	0.00077	2748.6	6.6
14	1500	34/34	0.000040	0.000002	0.17223	0.00027	0.19036	0.00030	2745.6	2.6
14	1550	26/26	0.000057	0.000003	0.17722	0.00043	0.19045	0.00034	2746.4	3.0
15	1500	38/38	0.000157	0.000021	0.15850	0.00048	0.19000	0.00045	2742.6	3.9
15	1550	30/30	0.000140	0.000011	0.17259	0.00120	0.19022	0.00048	2744.4	4.1
16	1500	32/32	0.000085	0.000037	0.14640	0.00103	0.19065	0.00068	2748.1	5.9
16	1550	16/38	0.000054	0.000024	0.19047	0.00129	0.19032	0.00058	2745.3	5.0
Mean age (Ma)									*2746.9*	*1.2*

The SHRIMP analytical results for sample BDE 19-B (Figure 14) display eleven spot analyses in different zircon grains, which gave an average $^{207}Pb/^{206}Pb$ age of 2744.1 ± 5.5 Ma (MSWD = 0.15), whereas the four most concordant spots yielded a concordia age of 2744 ± 5.6 Ma (MSWD = 1.6). A total of thirteen spot analyses were acquired in sample BVD 12-B, carried out by the U-Pb LA-MC-ICP-MS method, which yielded an upper intercept age of 2738.8 ± 7.9 Ma (MSWD = 0.64), and five concordant analyses defined a concordia age of 2734.5 ± 9 Ma (MSWD = 1.8; Figure 15). Sixteen zircon grains, from the sample RDM 9-C, have been analyzed by the Pb-evaporation method, which eight grains yielded an age of 2746.9 ± 1.2 Ma (MSWD = 1.8; Figure 16). All the ages presented above display a homogeneous pattern, about 2.74–2.73 Ga, and are interpreted as crystallization ages.

8. Discussions

8.1. Petrological affinities

The studied rocks are designed as ‘deformed A-type granitoids’ and display a single Neoarchean age of ~2.74 Ga. Although they could show some similarities with the ‘classical A-type granites’ of Carajás province, the granitoids from Vila União area exhibit significant differences with them, especially due to the latter are undeformed granites and have Paleoproterozoic age. In order to establish some geochemical similarities, it will be presented comparisons between the Neoarchean granitoids from Vila União area and other similar granitoids from Carajás province, represented by Vila Jussara (Dall’Agnol et al., 2017) and Planalto suites (Feio et al., 2012), Estrela granitic complex (Barros et al., 2009) and Serra do Rabo (Sardinha, et al., 2006) and Igarapé Gelado granites (Barros et al., 2009), besides the Neoarchean Matok pluton from the collisional Limpopo belt, South Africa (Laurent et al., 2014).

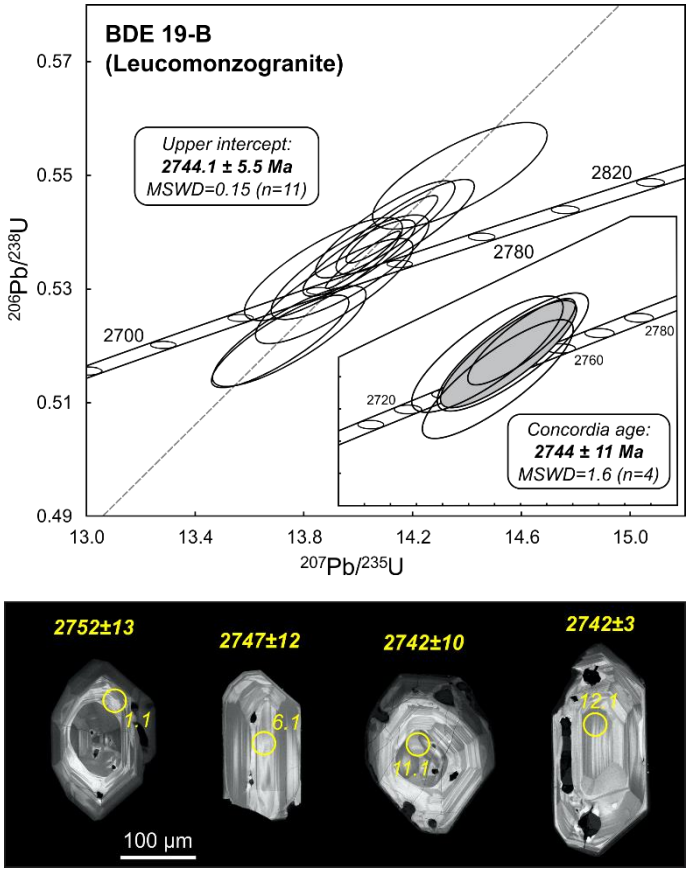

Figure 14. SHRIMP U-Pb concordia diagram for zircons from the leucomonzogranite BDE 19-B and its representative cathodoluminescence images of zircons. Yellow circles represent the position of the laser spot, scaled to size. Ages are displayed as $^{207}Pb/^{206}Pb$ ages (in Ma) with 1σ error. Error ellipses are 1σ.

Overall, granitoids from Vila União area share remarkable similarities with Vila Jussara and Planalto suites, Serra do Rabo granite and Matok pluton, although some minor contrasts are noticed. When compared with the Vila Jussara suite, the studied rocks present a little wider range in SiO_2, mainly related to low-silica members. Regarding to Planalto suite, these rocks display a narrow range of SiO_2, which are comparable to the most evolved varieties of the Vila União area. Besides, the rocks from Vila União area are slightly richer in Sr than those of Planalto suite. Serra do Rabo granite shows a narrower range of SiO_2 compared to the studied rocks (similar to Planalto suite). Moreover, the studied rocks have higher Al_2O_3, MgO, Na_2O, Rb, Sr and Ba, and lower Fe_2O_3* contents than Serra do Rabo granite. Unlike the granites aforementioned, the Matok pluton exhibits a slightly larger range in SiO_2 than the granitoids from Vila União area, which are characterized by more low-silica members. Additionally, the granitoids from Vila União area are slightly richer in CaO, Fe_2O_3* and Ba, and poorer in TiO_2, P_2O_5, Rb and Sr, when compared to Matok pluton.

On the other hand, the Estrela granitic complex and the Igarapé Gelado granite show significant geochemical differences with the studied rocks. The granitoids from Vila União

area have wider range of SiO_2, higher MgO, Na_2O, Zr, Sr, Ba, and lower Fe_2O_3*, K_2O and Rb values than Estrela granitic complex. Besides, the Estrela granitic complex shows scattered distribution of Al_2O_3 and Na_2O contents and a high positive Th anomaly, whereas the studied rocks display a more prominent negative Eu anomaly and more fractionated REE patterns in relation to the former. When compared to the Igarapé Gelado granite, the studied rocks are richer in MgO, K_2O, Zr and Sr, poorer in Al_2O_3, show a less fractionated REE patterns and more pronounced negative Nb anomaly.

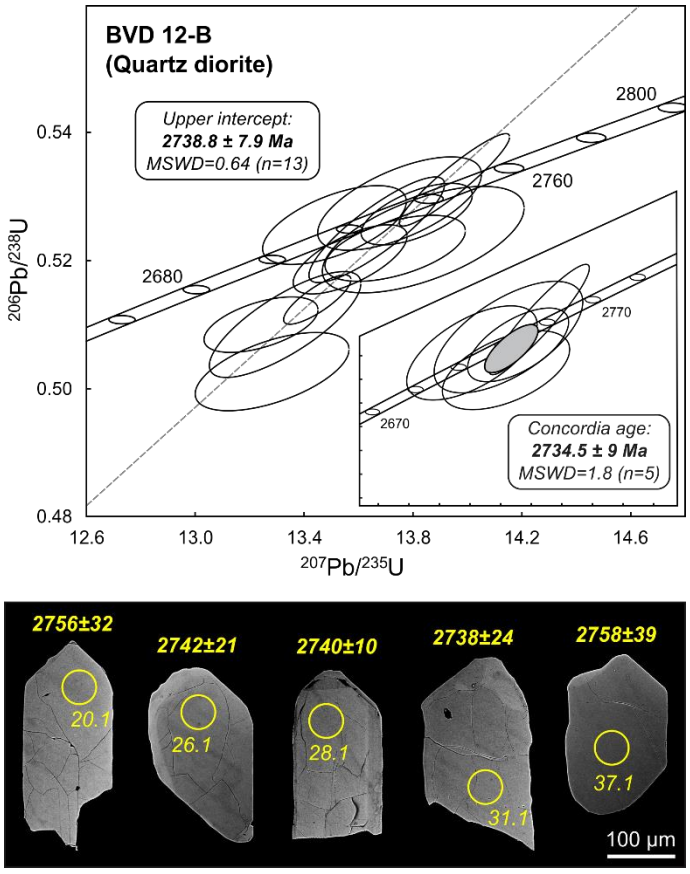

Figure 15. LA-MC-ICP-MS U-Pb concordia diagram for zircons from the quartz diorite BVD 12-B and its representative backscattered electron images of zircons. Yellow circles represent the position of the laser spot, scaled to size. Ages are displayed as $^{207}Pb/^{206}Pb$ ages (in Ma) with 1σ error. Error ellipses are 1σ.

The A-type granites also show significant contrasts as indicated by the variation of the FeO*/(FeO*+MgO) ratios. As discussed below, such feature has important implications concerning the oxygen fugacity conditions under which these rocks were crystallized. In the Al_2O_3 *vs.* FeO*/(FeO*+MgO) diagram (fields from Dall'Agnol and Oliveira, 2007; Figure 17a) these ratios are generally high and uniform (>0.87) in the Planalto suite and define an entirely coincident field to those attributed to reduced A-type granites. On the other hand, the granitoids from Vila União area exhibit lower values and an accentuate variation of this ratio

compared to Planalto suite. They share a similar behavior with the Vila Jussara granites, which varies from slightly reduced to oxidized A-type granites.

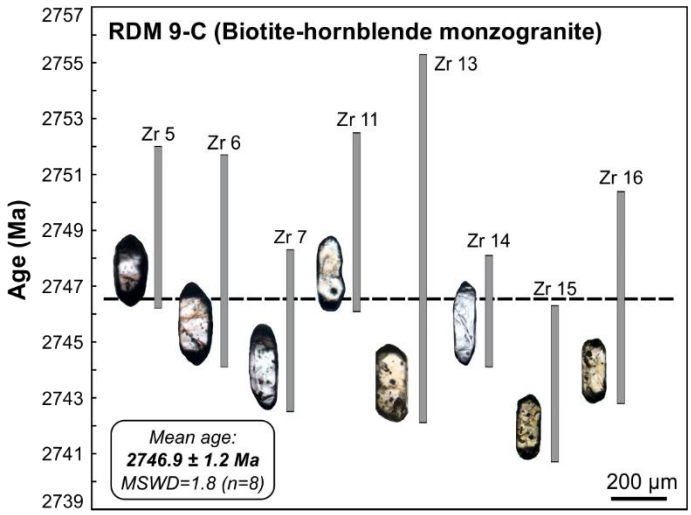

Figure 16. Single zircon Pb-evaporation age plot for the sample RDM 9-C from Vila União area. The vertical gray bars correspond the error for each zircon grain and horizontal dashed black line represents the mean age for sample. Each analysis (gray bar) is accompanied by its respective zircon image (photomicrograph). Abbreviation: Zr (zircon).

8.2. Crystallization parameters

Oliveira et al. (2018) estimated some crystallization parameters in the same rocks from the present work, based on temperature, pressure and oxygen fugacity (fO_2). These authors estimated temperature about 926–831°C to granitoids from Vila União area, obtained by the geothermometer of Ridolfi et al. (2010). These values are quite similar to those obtained to analogous granitoids of Vila Jussara suite from type-area (914–833°C; Dall'Agnol et al., 2017) and Planalto suite (910–850°C; Cunha et al., 2016). The pressure estimated by these authors to the granitoids from Vila União area, by using the Al-in-hornblende geobarometer of Anderson and Smith (1995), is about 814–532 MPa, which represent an initial crystallization at deep crustal depths, at ~23 km, and final emplacement at shallower levels in the crust, between 19 and 13 km deep.

Regarding the fO_2, it is assumed that these rocks evolved in a wide range, which is consistent with the presence of both ilmenite and magnetite. Composition of amphibole and biotite further stresses the previous ambiguity, whose Fe/(Fe+Mg) ratios vary, respectively, from 0.49 to 0.92 and 0.47 to 0.81. The amphiboles (hastingsite) with lower Fe/(Fe+Mg) ratios belong to samples containing magnetite as the sole oxide phase (0.49–0.81), while those which the early ilmenite is the dominant Fe-Ti oxide mineral, these ferromagnesian minerals show relatively high Fe# values (0.76–0.92), pointing to moderate to low fO_2, as opposed to the high oxidizing crystallization conditions (high fO_2) of the magnetite-series granites

(Figure 17b). A similar pattern is observed in the primary biotite from these granitoids, which also has variable Fe/(Fe+Mg) ratios and shows transitional affinities with ilmenite- and magnetite-series granites (Figure 17c). It is also worth noting that samples with low magnetic susceptibility values correspond to granites crystallized under low fO_2 and akin to ilmenite-series granites. In contrast, those samples with higher magnetic susceptibility values show evidence of crystallization under relatively oxidizing conditions. A similar pattern is shown by the amphibole and biotite Fe/(Fe+Mg) ratios from Vila Jussara granitoids, which vary greatly of 0.48 to 0.95 and 0.52 to 0.88, respectively. On the other hand, in the Planalto suite, amphibole and biotite have high Fe/(Fe+Mg) ratios (>0.80) and plot essentially in the low fO_2 and magnetite-free ilmenite-series granite fields, respectively (Figures 17b and c).

The granitoids from Vila União area demonstrate both oxidized ferroan and reduced ferroan characters, which make them akin to the Vila Jussara suite. As mentioned above and reported by Oliveira et al. (2018), these granitoids were formed under more oxidizing conditions (NNO±0.5), similar to those of the HITMQ buffer (Wones, 1989) defined by the titanite-magnetite-quartz assemblage. The reduced-ferroan granites are similar to those of the Planalto suite and evolved at low fO_2 (FMQ±0.5). In spite of some mineralogical and geochemical contrasts, besides be formed under distinct oxygen fugacity conditions, Cunha et al. (2016) and Dall'Agnol et al. (2017) show that the Neoarchean granites from Carajás province have counterparts in other cratons, as the Neoarchean Matok pluton from Limpopo belt, South Africa (Laurent et al., 2014).

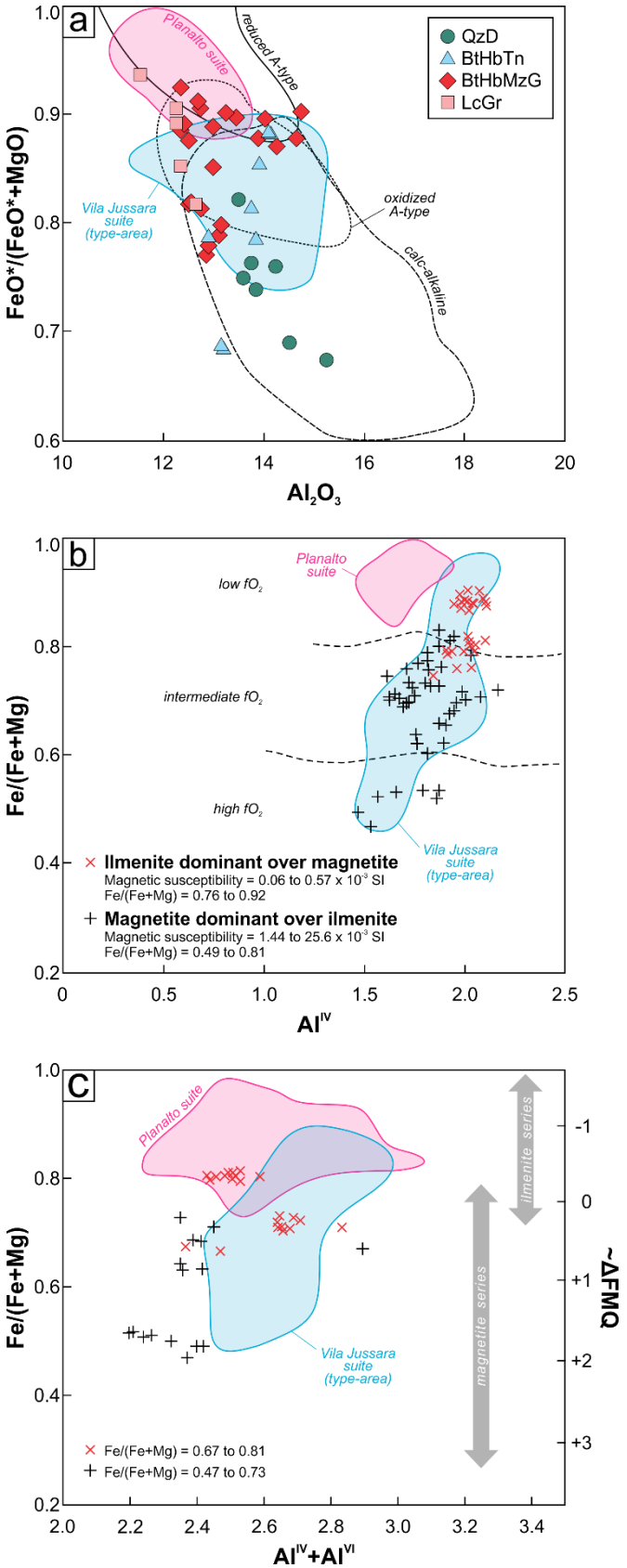

Figure 17. (a) Al_2O_3 *vs.* FeO*/(FeO*+MgO) diagram (fields from Dall'Agnol and Oliveira, 2007). (b) Al^{IV} *vs.* Fe/(Fe+Mg) diagram showing the compositional variation of amphibole for the studied granitoids (low, intermediate and high fO_2 fields according to Anderson and Smith, 1995). (c) $Al^{IV}+Al^{VI}$ *vs.* Fe/(Fe+Mg) diagram showing the compositional variation of biotite for the Vila União granitoids. Variation of Fe/(Fe+Mg) in ilmenite and magnetite series, and ΔFMQ values from Anderson et al. (2008). Data source: Planalto (Cunha et al., 2016) and Vila Jussara suites (Dall'Agnol et al., 2017). Figure modified from Oliveira et al. (2018).

8.3. Conditions of deformation and tectonic significance

When analyzing the microstructures and microtextures on these granitoids, it is possible stablish some deformation parameters that these rocks were submitted. The rocks from low-grade mylonitic domain are characterized by igneous texture almost entirely preserved, with euhedral to subeuhedral crystals. Quartz is usually deformed by recovery process (undulose extinction), besides BLG-recrystallization takes over as well. Most feldspars shows submagmatic microfractures and biotite rarely displays kink bands. All these features suggest deformation temperature ranging between 250 and 400°C to these rocks (Passchier and Trouw, 2005). The medium-grade domain shows feldspars with deformation twinning and by kinking, undulose extinction and, at increasing temperature, BLG-recrystallization, besides quartz is entirely recrystallized by BLG and SGR-recrystallization. According to Passchier and Trouw (2005), these features are typical of mylonites formed between 400 and 500°C. The rocks from high-grade domain are composed of minerals practically fully recrystallized, with feldspars showing SGR-recrystallization, and amphibole porphyroclasts with strain shadows of biotite and opaque minerals. Quartz occurs like ribbon, affected by GBM-recrystallization. The characteristics described in this mylonitic grade suggest deformation temperature between 500 and 700°C (Vernon, 2004; Passchier and Trouw, 2005).

Concerning emplacement conditions to the rocks from Vila União area, it is assumed that they represent syn-tectonic granitoids, as demonstrated in the section 5.2, and postulated by many authors on Neoarchean granitoids from Carajás province such as Barros et al. (2001, 2009), Cunha et al. (2016) and Oliveira et al. (2018). Besides this information, it is important to discuss the structural aspects mentioned in the section 4. The homogeneous structural pattern printed on the granitoids from Vila União area, characterized by an E–W steeply inclined well-developed mylonitic foliation towards both the N and S, and steep-to-subvertically plunging mineral stretching lineation (cf. Figure 2), matches with the conceptual deformational model described by Sanderson and Marchini (1984) and Greene and Schweickert (1995; Figure 18). This model shows that a horizontal contraction (shortening; full arrows in the Figure 18) combined with a vertical extension (parallel to the vorticity axis), in a ductile shear zone, results in a development of vertical lineation visible on vertical surface (foliation), defined as pure shear-dominated transpression – a tectonic regime characterized by combined ductile shear (less expressive) and compressional movements (dominant). Therefore, it is reasonable to assume the pure shear-dominated transpression model, with sinistral sense, to the Vila União granitoids, which explains all the structural

framework printed on them, besides matches with the regional tectonic history from this portion of Carajás province.

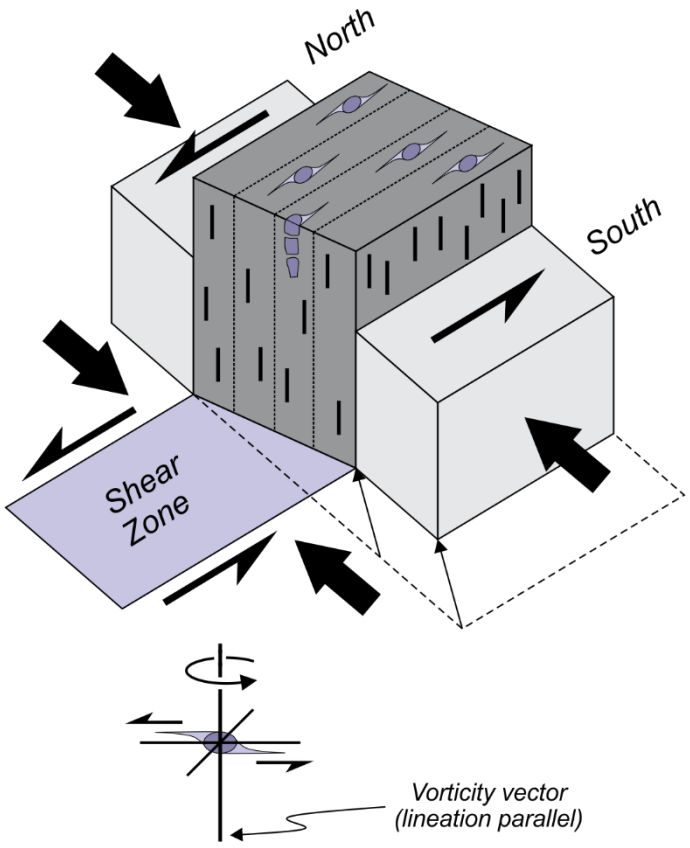

Figure 18. Representative deformational model showing pure shear-dominated transpression, which explains the vertical maximum stretching and vertical lineation, with sinistral sense, printed on the Neoarchean granitoids from Vila União area. Full arrows indicate horizontal contraction and half arrows indicate synchronous sinistral shearing. Model based on Sanderson and Marchini (1984) and Greene and Schweickert (1995).

9. Conclusions

(1) The 2.74–2.73 Ga granitoids from Vila União area crosscut 3.06–2.83 Ga Mesoarchean rocks and correspond to coalescent plutons, amalgamated and elongated parallel to the major E–W-trending compressional/shear structure. Monzogranite is the dominant variety, with subordinate occurrences of syenogranites, granodiorites, tonalites, and (quartz) diorites. They are subalkaline, metaluminous to slightly peraluminous, and are akin to A-type granites (Vila Jussara and Planalto suites, and Serra do Rabo granite). Moreover, Vila União granitoids present strong geochemical similarities to Neoarchean Matok pluton (Limpopo belt, South Africa), especially related to CaO, MgO, K_2O and Rb contents, and high HFSE and REE, as well as the wide SiO_2 content, which reflects the wide compositional range (monzogranites, granodiorites and diorites from Matok pluton). Likewise, similarly to the genesis of Matok pluton, an origin from variable degrees of

interactions between crust- and mantle-derived magmas could be suggested for the Vila União granitoids.

(2) Based on mineralogy, geochemistry and crystallization parameters, it is concluded that the Vila União granitoids demonstrate both oxidized ferroan and reduced ferroan characters, which make them akin to Vila Jussara suite. Despite several similarities with Planalto suite, the studied rocks differ significantly with respect to their variable whole rock FeO*/(FeO*+MgO) and Fe/(Fe+Mg) ratios in amphibole and biotite, implying that they were formed under more oxidizing conditions (NNO±0.5), while reduced ferroan granites are similar to those of Planalto suite and evolved at low fO_2 (FMQ±0.5).

(3) Combined field, petrographic, geochemical and geochronological features indicate that, at 2.74 Ga, this portion of the crust was submitted initially by an N–S extensional tectonic regime and was responsible by generation of the magma. Around 10 Ma later, the magma rising and emplacement were accompanied by the inversion of Carajás basin, described by an N–S pure shear-dominated transpressional regime, with E–W sinistral sense of tectonic movement. These evidences show that cooling and deformation of these rocks took place coevally, and confirm the syn-tectonic character to the Neoarchean granitoids from Vila União area.

(4) High crystallization temperatures were recorded in these granitoids, between 926–831°C, and suggest initial crystallization at deep crustal depths, at ~23 km, followed by final emplacement at shallower levels in the crust, between 19 and 13 km deep, as defined by the interval of 814–532 MPa.

(5) Microstructural and microtextural analyses revealed dominant deformation temperatures ranging from 400 to 500°C, which is defined by medium-grade domain granitoids, but can reach minimum and maximum values of 250 and 700°C, respectively.

Acknowledgements

BM thanks Conselho Nacional de Desenvolvimento Científico e Tecnológico (CNPq) for a doctor thesis scholarship (Proc. 163874/2014-0). The authors thank J.R.M. Mesquita, E.O. Gabriel, M.N.S. dos Santos and P.J.L. dos Santos for their support in geological mapping. G.T. Marques and A.P.P. Corrêa are thanked for their support with the acquisition of the cathodoluminescence and backscattered electron images conducted at Laboratório de Microanálises of Federal University of Pará (UFPA). Funding for this project has come from CNPq (D.C. Oliveira – Proc. 311388/2016-7 and 485806/2013-4), Fundo de Amparo à Pesquisa do Estado do Pará (FAPESPA; Proc. 133/2008-0), Vale/FAPESPA (ICAAF n.

053/2011) and INCT program (CNPq/FAPESPA/CAPES/PETROBRAS; Proc. 573733/2008-2). This paper is a contribution to the Brazilian Institute of Amazonian Geosciences (INCT/GEOCIAM).

Appendix A: Analytical methods for whole-rock analysis

0.5–5 kg fresh samples were reduced in chips in two stages of crushing: firstly by using a primary jaw crusher, producing chips with 0.5–20 mm in size, and then by using a secondary one, with 0.1–0.3 mm in size. After, this material was powdered in an agate swing mill until reaches a particle size <10 µm. All these procedures were performed at the Federal University of Pará (Brazil). Thirty-one analyses were obtained both at ACME Analytical and ALS Geochemistry laboratories. These analyses were performed by ICP-AES for major elements and ICP-MS for trace elements (including the rare-earth elements). Geochemical diagrams were generated by using GCDkit software (Janoušek et al., 2003). Detailed information about analytical procedures can be found at www.acmelab.com and www.alsglobal.com.

Appendix B: Geochronology methods for SHRIMP and LA-MC-ICP-MS U-Pb and Pb-evaporation analysis in zircon

Individual zircon grains from the representative granitoids from Vila União area were separated at the Laboratório de Geologia Isotópica, Federal University of Pará (Pará-Iso/UFPA). 10–20 kg rock for each sample were crushed, grinded and sieving into fractions between 125–175 µm, and then processed using heavy-liquid (bromoform) and isodynamic magnetic separator, followed by hand picking under a binocular microscope.

To performed both the SHRIMP (Sensitive High Resolution Ion Microprobe) and LA-MC-ICP-MS (Laser Ablation-Multi Collector Ion Coupled Plasma Mass Spectrometer) U-Pb dating methods, ca. 60–80 representative zircon grains were mounted in an epoxy resin and then polished to about half their thickness. Cathodoluminescence (CL) and backscattered electron (BSE) images were obtained using a JEOL JXA-8230 scanning electron microprobe (SEM) working at 15 kV, 20 µA and 11 mm working distance, equipped at Laboratório de Microanálises, Federal University of Pará (Brazil), in order to investigate the internal structures, overgrowths, fractures, inclusions and physical defects of the zircon grains to choose spots for U-Pb dating analyses. One U-Pb zircon analysis was carried out using a SHRIMP IIe system installed at Laboratório de Geocronologia de Alta Resolução, University of São Paulo, Brazil (GeoLab/USP), whose instrumental performance and analytical procedures are documented by Sato et al. (2014). The standards used were SL 13 for U

composition reference (238 ppm; Sato et al., 2014), and TEMORA-2 zircon (416.78 ± 0.33 Ma) as isotope ratios standard. The spot size of the primary ion beam was 30μm. Isoplot 4.15 software of Ludwig (2008) was used to calculate the $^{207}Pb/^{206}Pb$ ages and build concordia plots.

One U-Pb analysis was conducted by *in situ* LA-MC-ICP-MS at Laboratório de Geologia Isotópica, Federal University of Pará (Pará-Iso/UFPA), with a Nd:YAG 213 nm (LSX-213 G2 model) Laser Ablation Microprobe coupled to a Thermo Finnigan Neptune MC-ICP-MS. Helium was used as the carrier gas to enhance the transport efficiency of ablated material. Individual analytical spots were typically of 50 μm in diameter. U-Th-Pb ratios and absolute abundances were determined relative to the GJ-1 zircon standard (Stacey and Kramers, 1975). The analytical data were calculated and plotted using the Isoplot 4.15 software (Ludwig, 2008).

One single zircon Pb-evaporation analysis was performed on a Finnigan MAT 262 TIMS (Thermal Ionization Mass Spectrometry) at Pará-Iso/UFPA, following the method stablished by Kober (1986, 1987), and according to the detailed technical procedure described by Costi et al. (2000) and Noce et al. (2000). Whole zircon grains were analyzed using a rhenium filament configuration. Three evaporation steps were performed, at 1450, 1500 and 1550°C, during 5 minutes each one. After each step the Pb isotopic composition was measured using the ion counting collector, and then each step provides an age from the average of the $^{207}Pb/^{206}Pb$ ratios. The age of the sample is calculated from the results of the highest temperature step of all crystals. Steps with lower ages probably reflect Pb loss after crystallization and were not used to sample age calculation. Weighted mean and errors on the ages were calculated following Gaudette et al. (1998). Common Pb correction was performed using the model of Stacey and Kramer (1975). Analyses with $^{204}Pb/^{206}Pb$ ratios higher than 0.0004 were rejected in order to avoid significant errors caused by inaccurate common Pb correction. Uncertainties are given at the 2σ level.

References

Afonso, J.M.L., Oliveira, D.C., Silva, F.F., 2017. Novas ocorrências de granitos tipo A na Província Carajás, in: Lima, A.M.M., Gorayeb, P.S.S. (Eds.), Contribuições à Geologia da Amazônia, vol. 10. Sociedade Brasileira de Geologia – Núcleo Norte. Belém, pp. 209–224 (in Portuguese).

Almeida, F.F.M., Hasui, Y., Brito-Neves, B.B., Fuck, R.A., 1981. Brazilian structural provinces: an introduction. Earth-Science Reviews 17, 1–29.

Almeida, J.A.C., Dall'Agnol, R., Dias, S.B., Althoff, F.J., 2010. Origin of the Archean Leucogranodiorite-granite suites: evidence from the Rio Maria terrane and implications for granite magmatism in the Archean. Lithos 120, 235–257.

Almeida, J.A.C., Dall'Agnol, R., Oliveira, M.A., Macambira, M.J.B., Pimentel, M.M., Rämö, O.T., Guimarães, F.V., Leite, A.A.S., 2011. Zircon geochronology and geochemistry of the TTG suites of the Rio Maria granite-greenstone terrane: implications for the growth of the Archean crust of Carajás Province, Brazil. Precambrian Research 187, 201–221.

Althoff, F.J., Barbey, P., Boullier, A.M., 2000. 2.8–3.0 Ga plutonism and deformation in the SE Amazonian craton: the Archean granitoids of Marajoara (Carajás Mineral Province, Brazil). Precambrian Research 104, 187–206.

Anderson, J.L., Barth, A.P., Mazdab, J.L.W.F., 2008. Thermometers and thermobarometers in granitic systems. Reviews in Mineralogy and Geochemistry 69, 121–142.

Anderson, J.L., Smith, D.R., 1995. The Effects of temperature and fO_2 on the Al-in-hornblende barometer. American Mineralogist 80, 549–559.

Araújo, O.J.B, Maia, R.G.N, João, X.S.J., Costa, J.B.S., 1988. A megaestruturação arqueana da Folha da Serra dos Carajás, in: Congresso Latino Americano de Geologia, vol. 7. Anais do 35º Simpósio Brasileiro de Geologia. SBG, Belém, pp. 324–338 (in Portuguese).

Araújo, O.J.B., Maia, R.G.N., 1991. Projeto especial mapas de recursos minerais, de solos e de vegetação para a área do Programa Grande Carajás; Subprojeto Recursos Minerais; Folha SB.22-Z-A: Serra dos Carajás – Estado do Pará. DNPM/CPRM, Brasília, 164 pp. (in Portuguese).

Avelar, V.G., Lafon, J.M., Correia Jr., F.C., Macambira, E.M.B., 1999. O Magmatismo arqueano da região de Tucumã – Província Mineral de Carajás: novos resultados geocronológicos. Revista Brasileira de Geociências 29, 454–460 (in Portuguese).

Barker, F., 1979. Trondhjemite: a definition, environment and hypotheses of origin, in: Barker, F. (Ed.), Trondhjemites, Dacites and Related Rocks. Elsevier, Amsterdam, pp. 1–12.

Barros, C.E.M., Barbey, P., Boullier, A.M., 2001. Role of magma pressure, tectonic stress and crystallization progress in the emplacement of the syntectonic A-type Estrela Granite Complex (Carajás Mineral Province, Brazil). Tectonophysics 343, 93–109.

Barros, C.E.M., Sardinha, A.S., Barbosa, J.P.O., Macambira, M.J.B., 2009. Structure, petrology, geochemistry and zircon U-Pb and Pb-Pb geochronology of the synkinematic

Archean (2.7 Ga) A-type granites from the Carajás Metallogenic Province, northern Brazil. Canadian Mineralogist 47, 1423–1440.

Bouchez, J.L., Delas, C., Gleizes, G., Nédélec, A., Cuney, M., 1992. Submagmatic microfractures in granites. Geology 20, 35–38.

Bowden, P., Batchelor, R.A., Chapell, B.W., Didier, J., Lameyre, J., 1984. Petrological, geochemical and source criteria for the classification of granitic rocks: a discussion. Physics of the Earth and Planetary Interiors 35, 1–11.

Costi, H.T., Dall'Agnol, R., Moura, C.A.V., 2000. Geology and Pb–Pb geochronology of Paleoproterozoic volcanic and granitic rocks of Pitinga province, Amazonian craton, northern Brazil. International Geology Review 42, 832–849.

Cunha, I.R.V., Dall'Agnol, R., Feio, G.R.L., 2016. Mineral chemistry and magnetic petrology of the Archean Planalto Suite, Carajás Province – Amazonian Craton: Implications for the evolution of ferroan Archean granites. Journal of South American Earth Sciences 67, 100–121.

Dall'Agnol, R., Cunha, I.R.V, Guimarães, F.V, Oliveira, D.C., Teixeira, M.F.B., Feio, G.R.L., Lamarão, C.N., 2017. Mineralogy, geochemistry, and petrology of Neoarchean ferroan to magnesian granites of Carajás Province, Amazonian Craton: The origin of hydrated granites associated with charnockites. Lithos 277, 3–32.

Dall'Agnol, R., Oliveira, D.C., 2007. Oxidized, magnetite-series, rapakivi-type granites of Carajás, Brazil: implications for classification and petrogenesis of A-type granites. Lithos 93, 215–233.

Dall'Agnol, R., Oliveira, D.C., Guimarães, F.V., Gabriel, E.O., Feio, G.R.L., Lamarão, C.N., Althoff, F.J., Santos, P.A., Teixeira, M.F.B., Silva, A.C., Rodrigues, D.S., Santos, M.J.P., Silva, C.R.P., Santos, R.D., Santos, P.J.L., 2013. Geologia do Subdomínio de Transição do Domínio Carajás – Implicações para a evolução arqueana da Província Carajás - Pará. Anais do 13º Simpósio de Geologia da Amazônia. SBG, Belém, CD-rom (in Portuguese).

Dall'Agnol, R., Oliveira, M.A., Almeida, J.A.C., Althoff, F.J., Leite, A.A.S., Oliveira, D.C., Barros, C.E.M., 2006. Archean and Paleoproterozoic granitoids of the Carajás metallogenetic province, eastern Amazonian craton, in: Dall'Agnol, R., Rosa-Costa, L.T., Klein, E.L. (Eds.), Symposium on Magmatism: Crustal Evolution, and Metallogenesis of the Amazonian Craton. Abstracts Volume and Field Trips Guide. Belém, PRONEX-UFPA/SBG-NO, pp. 99–150.

Dall'Agnol, R., Teixeira, N.P., Rämö, O.T., Moura, C.A.V., Macambira, M.J. B., Oliveira, D.C., 2005. Petrogenesis of the Paleoproterozoic, rapakivi, A-type grantites of the Archean Carajás Metallogenic Province, Brazil. Lithos 80, 101–129.

Debon, F., Le Fort, P., 1988. A cationic classification of common plutonic rocks and their magmatic associations: principles, method, applications. Bulletin of Mineralogy 111, 493–510.

Delinardo, M.A.S., Monteiro, L.V.S., Moreto, C.P.N., Sousa, S.D., Melo, G.H.C., 2014. Complexo Xingu: Uma secção da crosta inferior exumada durante a evolução do Domínio Carajás, PA. Anais do 47º Congresso Brasileiro de Geologia. SBG, Salvador, CD-rom (in Portuguese).

Delinardo, M.A.S., Monteiro, L.V.S., Santos, T.J.S., Moreto, C.P.N., Sousa, S.D., 2015. Partial melting and magma generation in the Mesoarchean (ca. 3.0 Ga) TTG gneisses of the Xingu Complex, Carajás Province, Amazon Craton. 8th Hutton Symposium on granites and related rocks. Florianópolis, CD-rom.

DOCEGEO (Rio Doce Geologia e Mineração – Distrito Amazônia), 1988. Revisão litoestratigráfica da Província Mineral de Carajás, Pará. 35º Congresso Brasileiro de Geologia. SBG, Belém, pp. 11–54 (in Portuguese).

Eby, G.N., 1992. Chemical subdivision of the A-type granitoids: petrogenesis and tectonic implications. Geology 20, 641–644.

Feio, G.R.L., Dall'Agnol, R., Dantas, E.L., Macambira, M.J.B., Gomes, A.C.B., Sardinha, A.S., Oliveira, D.C, Santos, R.D., Santos, P.A., 2012. Geochemistry, geochronology and origin of the Neoarchean Planalto Granite suite, Carajás, Amazonian craton: A-type or hydrated charnockitic granites? Lithos 151, 57–73.

Feio, G.R.L., Dall'Agnol, R., Dantas, E.L., Macambira, M.J.B., Santos, J.O.S., Althoff, F.J., Soares, J.E.B., 2013. Archean granitoid magmatism in the Canaã dos Carajás area: implications for crustal evolution of the Carajás province, Amazonian craton, Brazil. Precambrian Research 227, 157–185.

Ferreira Filho, C.F., Cancado, F., Corrêa, C., Macambira, E.M.B., Junqueira-Brod, T.C., Siepierski, L., 2007. Mineralizações estratiformes de PGE-Ni associadas a complexos acamadados em Carajás: os exemplos de Luanga e Serra da Onça. Contribuições à Geologia da Amazônia 5, 1–14 (in Portuguese).

Frost, B.R., Barnes, C., Collins, W., Arculus, R., Ellis, D., Frost, C., 2001. A chemical classification for granitic rocks. Journal of Petrology 42, 2033–2048.

Gabriel, E.O., Oliveira, D.C., 2014. Geologia, petrografia e geoquímica dos granitoides arqueanos de alto magnésio da região de Água Azul do Norte, porção sul do Domínio Carajás, Pará. Boletim do Museu Paraense Emílio Goeldi, Ciências Naturais, 9(3), 533–564 (in Portuguese).

Gaudette, H.E., Lafon, J.M., Macambira, M.J.B., Moura, C.A.V., Scheller, T., 1998. Comparison of single filament Pb evaporation/ionization zircon ages with conventional U-Pb results: examples from the Precambrian of Brazil. Journal South American Earth Science 11, 351–363.

Greene, D.C., Schweickert, R.A., 1995. The Gem Lake shear zone: Cretaceous dextral transpression in the Northern Ritter Range pendant, eastern Sierra Nevada, California. Tectonics 14(4), 945–961.

Hühn, S.R.B., Macambira, M.J.B, Dall'Agnol, R., 1999. Geologia e Geocronologia Pb–Pb do Granito Alcalino Arqueano Planalto, Região da Serra do Rabo – Carajás – PA, in: Resumos Expandidos do 6º Simpósio de Geologia da Amazônia. SBG, Manaus, 463–466 (in Portuguese).

Janoušek, V., Farrow, C.M., Erban, V., 2003. GCDkit: New PC software for interpretation of whole-rock geochemical data from igneous rocks. Godschmidt Conference Abstract, A186.

Kober, B., 1986. Whole-grain evaporation for $^{207}Pb/^{206}Pb$-age-investigations on single zircons using a double-filament thermal ion source. Contributions to Mineralogy and Petrology 93, 482–490.

Kober, B., 1987. Single-zircon evaporation combined with Pb+-emitter bedding for $^{207}Pb/^{206}Pb$-age investigations using thermal ion mass spectroscopy, and implications to zirconology. Contributions to Mineralogy and Petrology 96, 63–71.

Lameyre, J., Bowden, P., 1982. Plutonic rock type series: discrimination of various granitoid series and related rocks. Journal of Volcanology and Geothermal Research 14, 169–186.

Laurent, O., Rapopo, M., Stevens, G., Moyen, J.F., Martin, H., Doucelance, R., Bosq, C., 2014. Contrasting petrogenesis of Mg-K and Fe-K granitoids and implications for post-collisional magmatism: case study from the Late-Archean Matok pluton (Pietersburg block, South Africa). Lithos 196–197, 131–149.

Le Maître, R.W., Streckeisen, A., Zanettin, B., Le Bas, M.J., Bonin, B., Bateman, P., Bellieni, G., Dudek, A., Efremova, J., Keller, J., Lameyre, J., Sabine, P.A., Schmidt, R., Sørensen, H., Woolley, A.R., 2002. Igneous rocks. A classification and glossary of terms.

Recommendations of the International Union of Geological Sciences Subcommission on the Systematics of Igneous Rocks. Cambridge University Press, Cambridge, 252 pp.

Leite, A.A.S., Dall'Agnol, R., Macambira, M.J.B., Althoff, F.J., 2004. Geologia e geocronologia dos granitóides arqueanos da região de Xinguara (PA) e suas implicações na evolução do terreno granito–greenstone de Rio Maria. Revista Brasileira de Geociências 34, 447–458 (in Portuguese).

Ludwig, K.R., 2008. User's Manual for Isoplot 3.6: a Geochronological Toolkit for Microsoft Excel. Berkeley Geochronology Center Special Publication, Berkeley.

Machado, N., Lindenmayer, Z.G., Krogh, T.E., Lindenmayer, D., 1991. U–Pb geochronology of Archean magmatism and basement reactivation in the Carajás area, Amazon shield, Brazil. Precambrian Research 49, 329–354.

Martins, P.L.G, Toledo, C.L.B, Silva, A.M., Chemale Jr, F., Santos, J.O.S., Assis, L.M., 2017. Neoarchean magmatism in the southeastern Amazonian Craton, Brazil: Petrography, geochemistry and tectonic significance of basalts from the Carajás Basin. Precambrian Research 302, 340–357.

McDonough, W.F., Sun, S.S., 1995. The composition of the Earth. Chemical Geology 120(3–4), 223–253.

Melo, G.H.C., Monteiro, L.V.S., Xavier, R.P., Santiago, E.B.S., 2014. Geocronologia U–Pb e uma nova perspectiva sobre a evolução do depósito IOCG de classe mundial Salobo, Província Carajás, Brasil. Anais do 47º Congresso Brasileiro de Geologia. SBG, Salvador, CD-rom (in Portuguese).

Moreto, C.P.N., Monteiro, L.V.S., Xavier, R.P., Amaral, W.S., Santos, T.J.S., Juliani, C., Souza Filho, C.R., 2011. Mesoarchean (3.0 and 2.86 Ga) host rocks of the iron oxide–Cu–Au Bacaba deposit, Carajás Mineral Province: U–Pb geochronology and metallogenetic implications. Mineralium Deposita 46, 789–811.

Myashiro, A., 1974. Volcanic rock series in island arcs and active continental margins. American Journal of Science 274, 321–355.

Noce, C.M., Macambira, M.J.B., Soares, A.C.P., 2000. Chronology of Neoproterozoic-Cambrian granite magmatism in the Araçuai belt, eastern Brazil, based on single zircon evaporation dating. Revista Brasileira de Geociências 30, 25–29.

Nogueira, A.C.R., Truckenbrodt, W., Pinheiro, R.V.L., 1995. Formação Águas Claras, Pré-Cambriano da Serra dos Carajás: redescrição e redefinição litoestratigráfica. Boletim do Museu Paraense Emílio Goeldi 7, 177–277 (in Portuguese).

O'Connor, J.T., 1965. A classification for quartz-rich igneous rocks based on feldspar rations. US Geological Survey Professional Papers 525, 79–84.

Oliveira, M.A., Dall'Agnol, R., Althoff, F.J., Leite, A.A.S., 2009. Mesoarchean sanukitoid rocks of the Rio Maria Granite-Greenstone Terrane, Amazonian Craton, Brazil. Journal of South American Earth Sciences 27, 146–160.

Oliveira, V.E.S., Oliveira, D.C., Marangoanha, B., Lamarão, C.N, 2018. Geology, mineralogy and petrological affinities of the Neoarchean granitoids from the central portion of the Canaã dos Carajás domain, Amazonian craton, Brazil. Journal of South American Earth Sciences 85, 135–159.

Passchier, C.W., Trouw, R.A.J., 2005. Microtectonics, second ed. Springer-Verlag, Berlin–Heidelberg–New York.

Pearce, J.A., Harris, N.B.W., Tindle, A.G., 1984. Trace element discrimination diagrams for the tectonic interpretation of granitic rocks. Journal of Petrology 25, 956–983.

Pidgeon, R., Macambira, M.J.B., Lafon, J.M., 2000. Th–U–Pb isotopic systems and internal structures of complex zircons from an enderbite from the Pium Complex, Carajás Province, Brazil: evidence for the ages of granulite facies metamorphism and the source of the enderbite. Chemical Geology 166, 159–171.

Ridolfi, F., Renzulli, A., Puerini, M., 2010. Stability and chemical equilibrium of amphibole in calc-alkaline magmas: an overview, new thermobarometric formulations and application to subduction-related volcanoes. Contributions to Mineralogy and Petrology 160, 45–66.

Rodrigues, D.S., Oliveira, D.C., Macambira, M.J.B., 2014. Geologia, geoquímica e geocronologia do Granito Mesoarqueano Boa Sorte, município de Água Azul do Norte, Pará – Província Carajás. Boletim do Museu Paraense Emílio Goeldi. Série Ciências da Terra 9(3), 597–633 (in Portuguese).

Sanderson, D., Marchini, R.D., 1984. Transpression. Journal of Structural Geology 6, 449–458.

Santos, R.D., Galarza, M.A., Oliveira, D.C., 2013. Geologia, geoquímica e geocronologia do Diopsídio-Norito Pium, Província Carajás. Boletim do Museu Paraense Emílio Goeldi, Série Ciências da Terra 8, 355–382 (in Portuguese).

Sardinha, A.S., Barros, C.E.M., Krymsky, R., 2006. Geology, geochemistry, and U–Pb geochronology of the Archean (2.74 Ga) Serra do Rabo granite stocks, Carajás Metallogenetic Province, northern Brazil. Journal South American Earth Science 20, 327–339.

Sato, K., Tassinari, C.C.G., Basei, M.A.S., Siga Júnior, O., Onoe, A.T., Souza, M.D., 2014. Sensitive High Resolution Ion Microprobe (SHRIMP IIe/MC) of the Institute of Geosciences of the University of São Paulo, Brazil: analytical method and first results. Geologia USP, Série Científica 14(3), 3–18.

Shand, S.J., 1950. Eruptive rocks their genesis, composition, classification and their relation to ore deposit, fourth ed. Murby, London, 488 pp.

Souza, Z.S., Potrel, H., Lafon, J.M., Althoff, F.J., Pimentel, M.M., Dall'Agnol, R., Oliveira, C.G., 2001. Nd, Pb and Sr isotopes of the Identidade Belt, an Archaean greenstone belt of the Rio Maria region (Carajás Province, Brazil): implications for the Archaean geodynamic evolution of the Amazonian Craton. Precambrian Research 109, 293–315.

Stacey, J.S., Kramers, J.D., 1975. Approximation of terrestrial lead isotope evolution by a two-stage model. Earth and Planetary Science Letters 26, 207–221.

Suita, M.T.F., 1988. Geologia da área Luanga com ênfase na petrologia do complexo máfico-ultramáfico de Luanga e depósitos de cromita associados. Dissertação de Mestrado – Universidade de Brasília, Brasília. 337 pp. (in Portuguese).

Sylvester, P.J., 1989. Post-collisional alkaline granites. Journal of Geology 97, 261–280.

Tavares, F.M., 2015. Evolução geotectônica do nordeste da Província Carajás. Tese de Doutorado – Universidade Federal do Rio de Janeiro, Rio de Janeiro, 115 pp. (in Portuguese).

Teixeira, M.F.B, Dall'Agnol, R., Santos, J.O.S., Sousa, L.A.M., Lafon, J.M., 2017. Geochemistry, geochronology and Nd isotopes of the Gogó da Onça granite: A new Paleoproterozoic A-type granite of Carajás province, Brazil. Journal of South American Earth Sciences 80, 47–65.

Trouw, R.A.J., Passchier, C.W., Wiersma, D.J., 2010. Atlas of Mylonites- and related microstructures. Springer-Verlag, Berlin–Heidelberg.

Vasquez, L.V., Rosa-Costa, L.R., Silva, C.G., Ricci, P.F., Barbosa, J.O., Klein, E.L., Lopes, E.S., Macambira, E.B., Chaves, C.L., Carvalho, J.M., Oliveira, J.G., Anjos, G.C., Silva, H.R., 2008. Escala 1:1.000.000, in: Vasquez, M.L., Rosa-Costa, L.T. (Eds.), Geologia e Recursos Minerais do Estado do Pará: Sistema de Informações Geográficas e SIG: texto explicativo dos mapas Geológico e Tectônico e de Recursos Minerais do Estado do Pará. CPRM, Belém, 328 pp. (in Portuguese).

Vernon, R.H., 2004. A practical guide to rock microstructures. Cambridge University Press, pp. 594

Whalen, J.W., Currie, K.L., Chappel, B.W., 1987. A-type granites: geochemical characteristics, discrimination and petrogenesis. Contribution to Mineralogy and Petrology 95, 407–419.

Wones, D.R., 1989. Significance of the assemblage titanite + magnetite + quartz in granitic rocks. American Mineralogist 74, 744–749.

3 A HYBRID ORIGIN FOR THE NEOARCHEAN GRANITOIDS OF THE CARAJÁS PROVINCE, BRAZIL: TEXTURAL, GEOCHEMICAL AND Pb-Nd-Hf ISOTOPIC EVIDENCES

Autores:
Bhrenno Marangoanha
Davis Carvalho de Oliveira
Vinícius Eduardo Silva de Oliveira
Marco Antonio Galarza
Gisele Tavares Marques

Artigo a ser submetido para publicação à revista A (*Qualis* CAPES)

A hybrid origin for the Neoarchean granitoids of the Carajás province, Brazil: Textural, geochemical and Pb-Nd-Hf isotopic evidences

Bhrenno Marangoanha [a,b], Davis Carvalho de Oliveira [a,b], Vinícius Eduardo Silva de Oliveira [a,b], Marco Antonio Galarza [b,c], Gisele Tavares Marques [a,d]

[a] Grupo de Pesquisa Petrologia de Granitoides (GPPG), Instituto de Geociências (IG), Universidade Federal do Pará (UFPA), Rua Augusto Corrêa, 01, CEP 66075-110, Belém, Pará, Brazil

[b] Programa de Pós-graduação em Geologia e Geoquímica (PPGG), IG-UFPA, Belém, Pará, Brazil

[c] Laboratório de Geologia Isotópica (Pará-Iso), IG-UFPA, Belém, Pará, Brazil

[d] Laboratório de Microanálises, IG-UFPA, Belém, Pará, Brazil

ABSTRACT

The Neoarchean granitoids from Vila União area are located in the central portion of Canaã dos Carajás domain, Carajás province (Amazonian craton, Brazil) and represent hybrid granitoids which suggest that magma mixing events have been playing an important role in their origin. According to whole evidences, such field observations, petrography, geochemical modelling, zircon SHRIMP and LA-MC-ICP-MS U-Pb ages, and Nd-Hf isotopic data we propose a geodynamic model based on two stages. Firstly, at ~2.75 Ga, in an N-S extensional tectonic regime, underplating generates mantle-derived mafic melts that are injected into the lower/middle crust (composed by Mesoarchean enderbites), which causes partial melting and produces leucogranitic melts. The interaction between these two contrasting felsic and mafic magmas occurs both by mixing and mingling. Around 20 Ma later, the hybrid magma rising and emplacement were accompanied by the inversion of Carajás basin, described by a pure shear-dominated transpressional regime, with sinistral sense, which the hybrid melt was channeled into pre-existing shear zones trending E-W (Itacaiúnas shear zone), in the upper crust. This new tectonic regime (transpressional) played coevally with the hybrid magma cooling, giving rise to the Neoarchean deformed A-type granitoids from Vila União area, besides the Pium diopside-norite, that represents the mafic end-member generated by the underplating.

Keyword: Hybridization; Neoarchean granitoids; Geochemical modeling; U-Pb dating; Nd-Hf isotopes.

1. Introduction

The Neoarchean granitoids and related rocks in Carajás province have been well studied in the last 20 years and are characterized by a well-defined ~2.74 Ga magmatism (Barros and Barbey, 1998; Sardinha et al., 2006; Barros et al., 2009; Feio et al., 2013; Moreto et al., 2015; Cunha et al., 2016; Dall'Agnol et al., 2017; Figure 1 and Table 1). However, these authors have focused their study separately – either on the granites (*stricto sensu*) or on the gabbros/diorites – as well most of them have concentrated their efforts only on geochemical classification, typology and geochronology, and set aside other important data, as structural (and microstructural), geochemical modelling and isotopic ones. Thus, the real relationship between both Neoarchean felsic and mafic granitoids still remains obscure, especially with regard to their petrogenesis. Partial melting of a single source has been considered as the only process able to generate the granites so far (Barros et al., 2009; Feio et al., 2013; Dall'Agnol et al., 2017).

In the central portion of the Canaã dos Carajás domain (Figure 2), we have documented outstanding field evidences that suggest mixing/mingling processes involved in the genesis of these granitoids, which could support the proposal of a more consistent petrogenetic model to drive the Neoarchean evolution in this domain. Although it is the first time that is mentioned mixing process to generate Neoarchean granitoids in Carajás province, it is widely accepted that generation of large volumes of silicic magmas is commonly accompanied by mafic magma underplating, which provides heat and, potentially, materials for the generation of the felsic magmas (Annen and Sparks, 2002; Annen et al., 2006; Dan et al., 2015).

This paper address on the link between contrasting felsic and mafic magmas to generate large volume of hybrid granitoids with a wide compositional spectrum that outcrop in the central portion of Canaã dos Carajás domain, as well to explain the role of this process in a suitable geodynamic model. Accordingly, this paper aims to define the relationships between plutonism and tectonism for the origin, ascent, emplacement of the Vila União granitoids, as result of a detailed study integrating petrography, geochemistry, whole-rock Sm-Nd isotopes and combined U-Pb and Lu-Hf isotopic analyses in zircon. In order to support our field-based interpretations and those provided by isotopic data, modelling of melt and residue compositions allows us to determinate the specific sources and quantify the processes involved in the origin of these granitoids, as well as helps understanding the role of these rocks for the Neoarchean crustal evolution of the Carajás province.

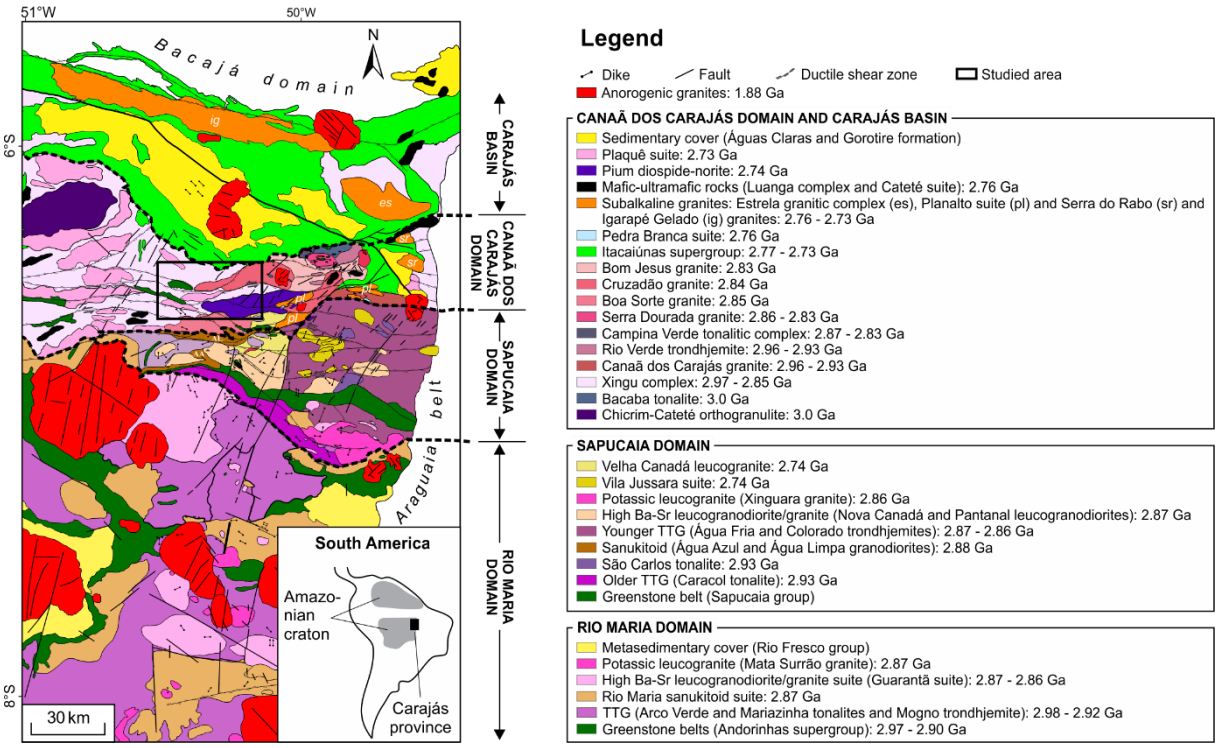

Figure 1. Geological map of the Carajás province, showing the limits between the Rio Maria, Sapucaia and Canaã dos Carajás domains, besides Carajás basin (dashed lines; modified from Gabriel et al., 2014).

2. Geological setting

The Carajás province (CP) is located in the southeastern portion of the Central Amazonian geochronological province and represent the oldest Archean nuclei in the Amazonian craton, Brazil (Tassinari and Macambira, 2004; Figure 1). Dall'Agnol et al. (2013) subdivided the CP in three domains: Rio Maria, Sapucaia and Canaã dos Carajás – which the last one is considered as the basement of the Carajás basin (Figure 1). The Rio Maria domain is located in the southern part of the province and comprises rocks ranging between 2.98 – 2.86 Ga, represented by greenstone belts, TTG and sanukitoid suites, and leucogranites (DOCEGEO, 1988; Althoff et al., 2000; Souza et al., 2001; Leite et al., 2004; Dall'Agnol et al., 2006; Oliveira et al., 2009; Guimarães et al., 2010; Almeida et al., 2010, 2011). The Sapucaia domain displays practically the same lithology compared with Rio Maria domain, except by the fact that the first one was intensely affected by Neoarchean granitic events, represented by deformed A-types granitoids (Dall'Agnol et al., 2013, 2017).

Differently from the aforementioned domains, the Canaã dos Carajás domain represents a more reworked crust, being composed majorly by granites *stricto sensu* (Feio et al., 2013). The Mesoarchean units are composed by Chicrim-Cateté orthogranulite, with crystallization and metamorphism age of 3.0 and 2.85, respectively (Pidgeon et al., 2000; Vasquez et al., 2008), Bacaba tonalite (3.0 Ga; Moreto et al., 2011), Xingu complex – an

heterogeneous lithologic association formed mainly by gneiss, migmatites and granitoids – with crystallization age ranging from 2.97 to 2.85 Ga (Machado et al., 1991; Avelar et al., 1999; Melo et al., 2014; Delinardo et al., 2014, 2015), Canaã dos Carajás granite and Rio Verde trondhjemite, both formed between 2.96 and 2.93 Ga (Feio et al., 2013), and Campina Verde tonalitic complex, Rio Verde trondhjemite, and Bom Jesus, Serra Dourada, Cruzadão and Boa Sorte granites, all with crystallization age ranging from 2.87 to 2.83 Ga (Feio et al., 2013; Rodrigues et al., 2014). This domain was intensely affected by Neoarchean events, more specifically between 2.77 and 2.70 Ga, as recorded by granitic and mafic-ultramafic magmatism, as well as greenstone belts and sedimentary rocks (Nogueira et al., 1995; Vasquez et al., 2008; Dall'Agnol et al., 2013). Around 1.88 Ga, the entire Carajás province was affected by the emplacement of anorogenic granites and associated dikes (Dall'Agnol et al., 2005; Teixeira et al., 2017).

3. Field and textural aspects

The Neoarchean granitoids from Vila União area are exposed in the central portion of the Canaã dos Carajás domain, which can reach up to 32 km long (Figure 2). They are characterized by occurrence of a wide variety of rocks, which vary from syenogranites to diorites (Oliveira et al., 2018). These rocks form at least two coalescent plutons, amalgamated and elongated parallel to the major E–W-trending compressional/shear structure. Other minor exposure forms an E–W-trending elongated massif in the southeastern portion, which can reach up to 8 km long. These plutons are emplaced along the anastomosing high strain shear zones, concordantly to the dominant E–W regional trend, and display an E–W steeply inclined well-developed foliation (mostly 70–85°) towards both the N and S, and steep-to-subvertically plunging mineral stretching lineation (60–85°; Figure 2). These granitoids crosscut 3.06–2.85 Ga Mesoarchean rocks (Feio et al., 2013; Delinardo et al., 2014, 2015), represented by orthogranulites, TTG and K-leucogranites, and are coeval with Pium diopside-norite and enderbitic rocks. A small circular pluton of isotropic granite emplaced at 1.89 Ga crosscuts all the aforementioned units (Afonso et al., 2017).

Table 1. Summary of geochronological and isotopic data of the Neoarchean magmatism from Carajás province.

Canaã dos Carajás domain						
Unit	Lithology	Zircon age (Ma)	Method	T_{DM} (Ga)	εNd(t)	Reference
Estrela granitic complex	Granite	2763±7	Pb-evaporation	(3.19 to 2.97)	(-2.06 to -0.38)	Barros et al. (2009)
Serra do Rabo granite	Hornblende syenogranite	2743±1.6	U-Pb TIMS			Sardinha et al. (2006)
Igarapé Gelado granite	Granite	2731±26	Pb-evaporation			Barros et al. (2009)
Velho Salobo granite	Granite	2573±2	U-Pb TIMS			Machado et al. (1991)
Sossego granophyric granite	Granite	2740±26	U-Pb ICP-MS			Moreto et al. (2015)
Curral granite	Granite	2739±4.2	U-Pb SHRIMP			Moreto et al. (2015)
Plaquê suite	Granite	2727±29	Pb-evaporation			Avelar (1996)
	Granite	2736±24	Pb-evaporation			Avelar et al. (1999)
Planalto suite	Granite	2747±2	Pb-evaporation			Huhn et al. (1999)
	Biotite-hornblende syenogranite	2733±2	Pb-evaporation			Feio et al. (2012)
	Hornblende-biotite syenogranite	2731±1	Pb-evaporation			Feio et al. (2012)
	Biotite syenogranite	2736±4	Pb-evaporation			Feio et al. (2012)
	Hornblende syenogranite	2729±17	U-Pb ICP-MS	2.98	-0.86	Feio et al. (2012)
	Hornblende-biotite syenogranite	2710±10	U-Pb ICP-MS	2.99	-0.85	Feio et al. (2012)
	Biotite syenogranite	2706±5	U-Pb ICP-MS	3.08	-2.25	Feio et al. (2012)
	Biotite-hornblende syenogranite	2738±3	U-Pb SHRIMP			Feio et al. (2013)
	Hornblende-biotite syenogranite	2730±5	U-Pb SHRIMP			Feio et al. (2013)
	Biotite-hornblende tonalite	2741.2±0.8	Pb-evaporation	2.91	0.30	Galarza et al. (2017)
	Biotite-hornblende syenogranite	2737±3.5	Pb-evaporation	2.96	-1.18	Galarza et al. (2017)
	Biotite-hornblende granodiorite	2732.6±1.3	Pb-evaporation	3.11	-2.22	Galarza et al. (2017)
	Biotite-hornblende granodiorite	2738.9±1.3	Pb-evaporation	3.07	-1.73	Galarza et al. (2017)
	Biotite-hornblende granodiorite	2739.5±1.5	Pb-evaporation	2.98	-0.83	Galarza et al. (2017)
	Biotite-hornblende monzogranite	2731.9±0.8	Pb-evaporation	2.94	-0.38	Galarza et al. (2017)
	Biotite-hornblende monzogranite	2735.6±2.3	Pb-evaporation	2.91	0.08	Galarza et al. (2017)
	Biotite-hornblende monzogranite	2741.9±0.5	Pb-evaporation	2.96	-0.88	Galarza et al. (2017)
	Biotite-hornblende monzogranite	2739.7±0.7	Pb-evaporation	2.95	-0.29	Galarza et al. (2017)
Pedra Branca suite	Trondhjemite	2749±6	Pb-evaporation			Sardinha et al. (2006)
	Trondhjemite	2765±39	U-Pb TIMS			Sardinha et al. (2006)
	Trondhjemite	2750±5	U-Pb ICP-MS	3.14	-2.16	Feio et al. (2013)
	Trondhjemite	2701±6	U-Pb ICP-MS	2.95	-1.21	Feio et al. (2013)
Parauapebas formation	Basalt	2749.6±6.5	U-Pb SHRIMP	(3.36 to 3.02)	(-4.11 to -1.53)	Martins et al. (2017)
	Basalt	2745±5	U-Pb SHRIMP	(3.35 to 3.22)*	(-2.75 to -0.79)**	Martins et al. (2017)
Cristalino diorite	Diorite	2738±6	Pb-evaporation			Huhn et al. (1999)
Luanga complex	Anorthositic gabbro	2763±6	U-Pb TIMS			Machado et al. (1991)
Cateté intrusive suite	Gabbro	2766±6	U-Pb SHRIMP			Lafon et al. (2000)
(Undetermined)	Gabbronorite	2739±5.9	U-Pb SHRIMP			Moreto et al. (2015)
Pium diopside-norite	Diopside norite	2745.2±1.2	Pb-evaporation	3.06	-1.8	Santos et al. (2013)
	Hornblende gabbronorite	2744.5±0.8	Pb-evaporation	3.09	-1.8	Santos et al. (2013)
	Quartz gabbro	2744.2±1.2	Pb-evaporation			Santos et al. (2013)
	Quartz gabbro	2735±5	U-Pb ICP-MS	3.05	-1.59	Feio et al. (2013)
Sapucaia domain						
Unit	Lithology	Zircon age (Ma)	Method	T_{DM} (Ga)	εNd(t)	Reference
Velha Canadá leucogranite	Biotite granodiorite	2733±1.5	Pb-evaporation			Santos et al. (2010)
	Biotite granodiorite	2747±2	Pb-evaporation			Sousa et al. (2010)
Vila Jussara suite	Hornblende-biotite granodiorite	2725±5	Pb-evaporation			Dall'Agnol et al. (2017)
	Hornblende-biotite granodiorite	2743±1	Pb-evaporation			Dall'Agnol et al. (2017)
	Biotite-hornblende tonalite	2769±10	U-Pb SHRIMP			Dall'Agnol et al. (2017)
	Biotite-hornblende tonalite	2743±3	Pb-evaporation			Dall'Agnol et al. (2017)
	Biotite-hornblende monzogranite	2735±4	Pb-evaporation			Dall'Agnol et al. (2017)
	Biotite-hornblende monzogranite	2743±9	Pb-evaporation			Dall'Agnol et al. (2017)
	Hornblende-biotite monzogranite	2749±3	Pb-evaporation			Oliveira et al. (2010)
	Hornblende-biotite monzogranite	2748±2	Pb-evaporation			Oliveira et al. (2010)
	Biotite-hornblende monzogranite	2754±2	U-Pb SHRIMP			Oliveira et al. (2010)

Legend: *Hf T_{DM2}; **εHf(t).

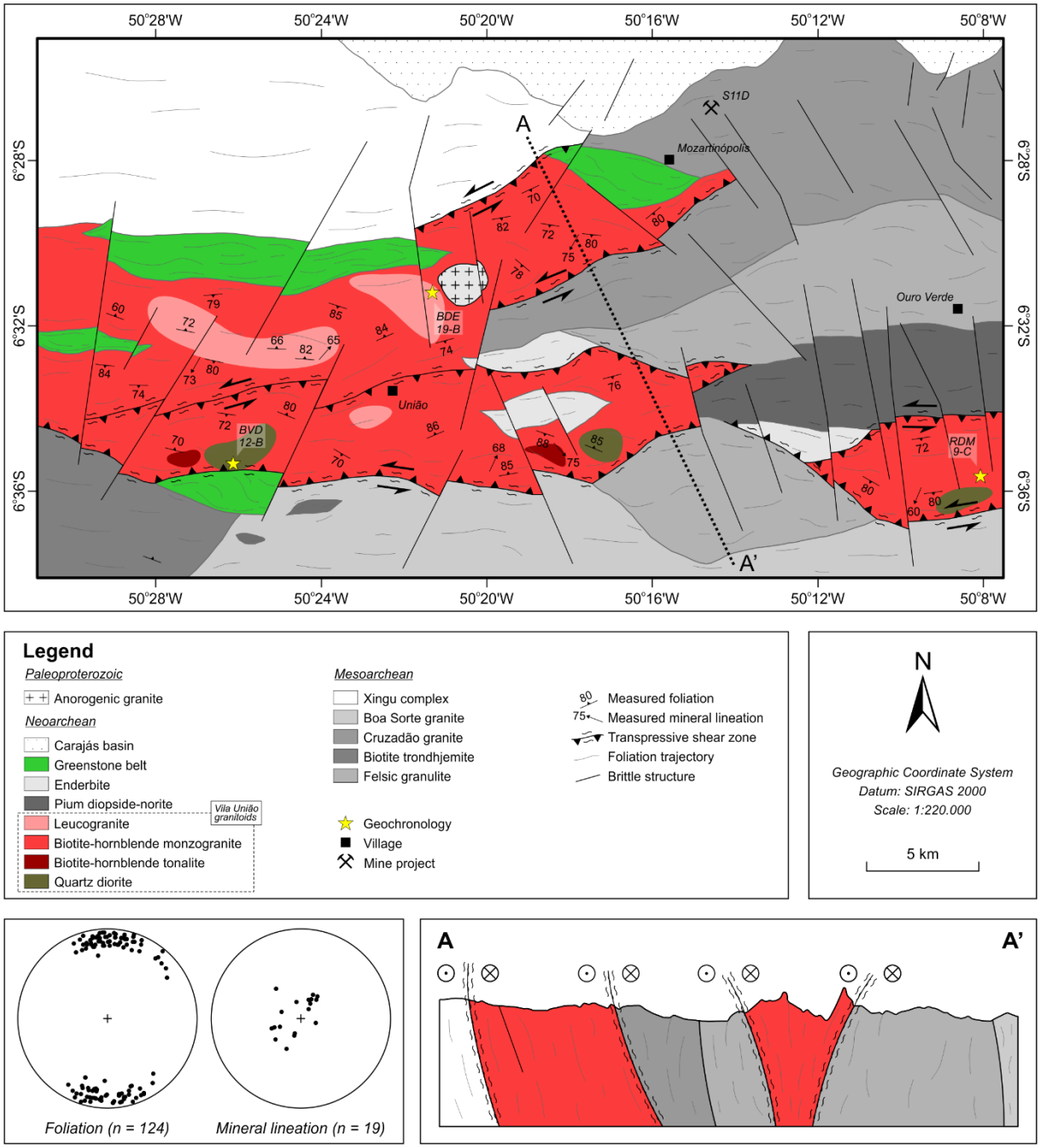

Figure 2. Geological sketch map of the studied area, showing lower hemisphere equal-area (Schmidt-Lambert) stereographic plots of poles to foliation and mineral lineation of the Neoarchean granitoids from Vila União area. Detailed interpretative cross-section A-A' is shown (see map for location).

The granitoids from Vila União area present some important evidences that support their origin involving hybridization processes between mafic and felsic magmas (mixing and mingling). The listed evidences are both at outcrop/map and at thin-section/crystal scales. The first evidence – and the more remarkable one – is the gradational variation in the composition of the rocks, which suggests various degrees of interaction between mafic and felsic end-members (Figure 3). In some key outcrops, it is found a huge and wide range of rocks that clearly grade from syenogranites to diorites, and show many intermediate compositions

between them. It is worth highlighting that, on the map scale, these outcrops above mentioned, which display these ranges of interaction, are recorded majorly quite near to the contact with Pium diopside-norite.

Figure 3. Scheme showing the gradational compositional variation in the granitoids from Vila União area. There is a clear decrease in the mafic mineral content of the figure (a) (diorite) towards (f) (leucomonzogranite), and increase of K-feldspar and quartz in the same sense. The disposition of the sample photos suggests a trend of evolution, given for several degrees of interaction between (a) mafic and (f) felsic end-members.

The second evidence is related to the large occurrence of mafic microgranular enclaves (MME) that could represent the mafic end-member in the hybridization process. The MME occur hosted in the most felsic rocks from Vila União area and seem to be part of the mingling process. These enclaves generally show ellipsoidal and elongated (Figure 4a) or rounded (Figure 4b) shapes, and their size commonly reaches up to 30 centimeters across. The

occurrence of felsic back-veins into the MME is frequent as well (cf. Figure 4a), and suggest that rapid crystallization and solidification resulted in cracks forming in the enclaves when the high-temperature mafic melt entered the relatively low-temperature granitic magma (as described by Zhang et al., 2016). When in contact with the felsic host, the MME seems to have its rims disaggregated, or even "dissolved", into the felsic rock, like a typical disequilibrium reaction (Figure 4c). Plagioclase and K-feldspar phenocrysts in the MME are common (Figure 4d), and are interpreted as a result of the mechanical transfer of phenocrysts from a more felsic magma into mafic magma during magma-mixing process. Furthermore, as more advanced the mechanical transfer of minerals, more efficient is the mineral exchange between the MME (mafic end-member) and the host granitoid (felsic end-member), which both end-members tend to reach a homogeneous mixture (Figure 4e), although some portions still record immiscibility aspects (Figure 4f).

Regarding the petrographic perspective, it is enumerated some textural evidences in order to support and ratify the hybridization process in these rocks, which include: (i) plagioclase and K-feldspar ocelli, (ii) biotite and amphibole inclusion zones in feldspar, (iii) plagioclase crystals with spike zoning, (iv) mafic clots, and (v) stubby and acicular apatite inclusions in feldspar phenocrysts.

Feldspar ocelli, especially plagioclase (Figure 5a), occur rimmed by a medium to fine-grained matrix composed of amphibole and biotite, suggesting mineral disequilibrium leading by hybridization and quenching processes (Vernon, 1990; Hibbard, 1991). The ocelli are formed by partial dissolution of feldspar crystals from the felsic magma injected into mafic magma and, subsequently, dissolution extracts latent heat from adjacent liquid, leading to surface undercooling, which becomes substrate for the nucleation of amphibole and biotite from the mafic magma (Vernon, 1990; Hibbard, 1991; Palivcová et al., 1995; Burda et al., 2011). According to Hibbard (1991), it is common in MME worldwide and is interpreted to indicate magma mingling processes.

Biotite and amphibole inclusion zones in feldspar (Figure 5b) occur when plagioclase or K-feldspar crystals from the more felsic magma is brought into contact with the biotite and amphibole crystals from the more mafic magma, which the later form a kind of "shield" on the feldspar (Dorais et al., 1990; Doraire et al., 2005). Subsequently, overgrowth of feldspar on the mafic shield "locks in" the mafic minerals and forms the zones of inclusion (Baxter and Feely, 2002). Vernon (2010) describes these zoning discontinuities and mantled crystals to spasmodic re-heating episodes during the magma mixing process.

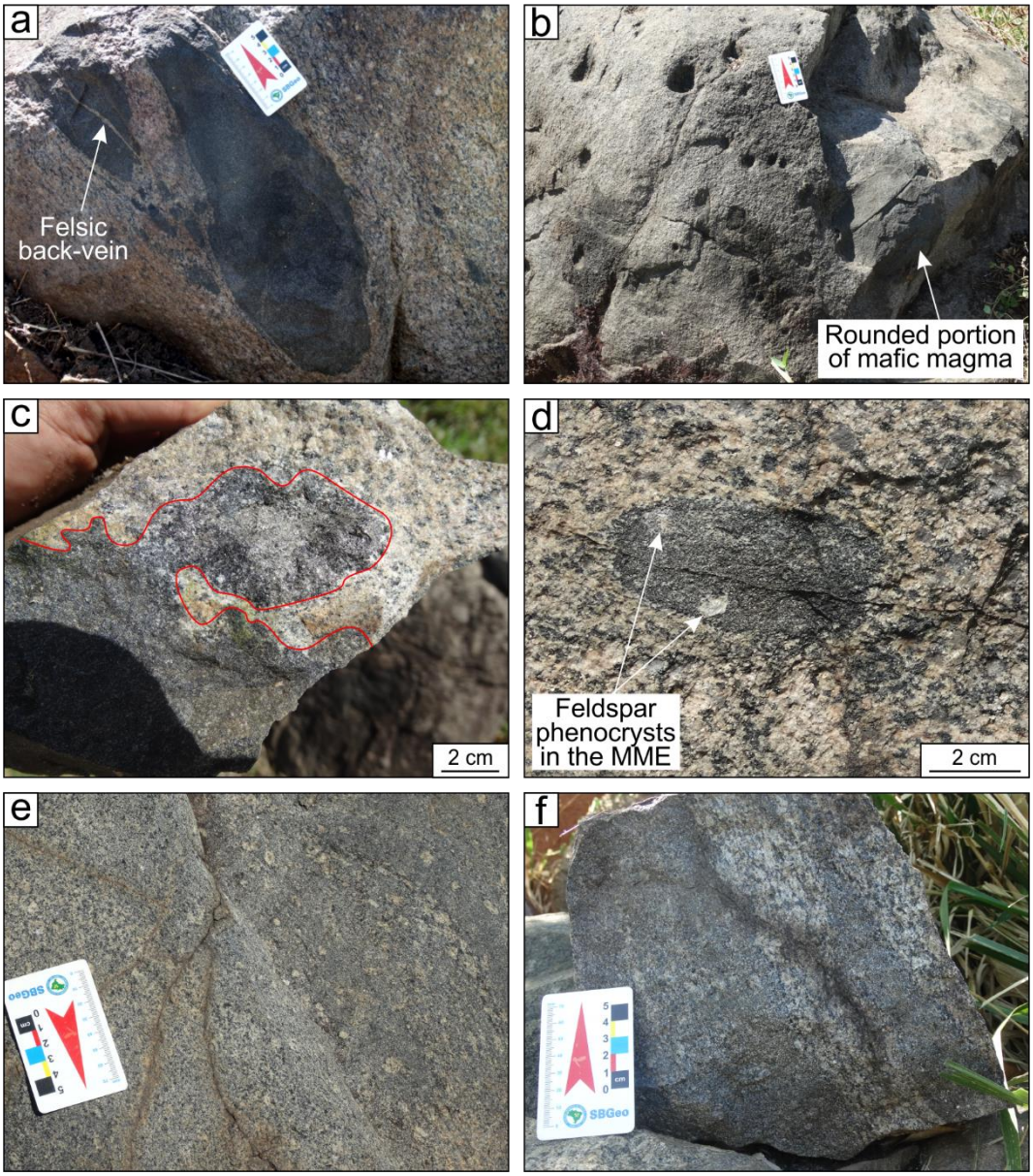

Figure 4. Mesoscopic-scale features of the granitoids from Vila União area, showing the relationship contact aspects present in these rocks. (a) Mafic enclaves strongly flattened, with sharp contact and ellipsoidal shape, oriented parallel to the foliation, and the occurrence of felsic back-veins into the MME; (b) rounded mafic enclave hosted in the felsic granite; (c) disaggregation of MME rim into the felsic rock, like a typical disequilibrium reaction; (d) plagioclase and K-feldspar phenocrysts from the granite into the MME, result of mechanical transfer of phenocrysts from the felsic host magma into the mafic magma; (e) advanced mechanical transfer of minerals, with a more efficient mineral exchange between the MME (mafic end-member) and the host granitoid (felsic end-member), tending to reach a homogeneous mixture; and (f) some portions of the mixing process still records immiscibility aspects.

Plagioclase with Ca-rich spike zonation (Figure 5c) is common in the granitoids from Vila União area, which shows a sharp compositional discontinuity. Wiebe (1968), Hibbard (1991) and Baxter and Feely (2002) attribute its origin to magma mixing process by the introduction of a more sodic plagioclase – from a felsic melt – into a mafic magma, resulting in a more calcic zonation. Baxter and Feely (2002) state that the return to normal composition

(more sodic zonation) may be achieved either through equilibration of the hybrid system, with zoning continuing out to a more sodic rim, or through a second mixing event, which brings the crystal back into a more felsic magma.

The most abundant micro-textural aspect related to hybridization process in the granitoids from Vila União area is the presence of mafic clots (Figure 5d), which are ubiquitous in all varieties of these rocks, from the most to the least evolved ones. In these rocks, the mafic clots have a granular texture, are 0.1–0.6 mm in size and are composed mainly by amphibole + biotite + opaque minerals + titanite ± orthopyroxene ± clinopyroxene. Barbarin and Didier (1992) and Baxter and Feely (2002) interpret mafic clots in granites as converted mineral aggregates from coeval mafic magma globules. The abundance of mafic clots in the granitoids from Vila União area suggests that these clots originated within the mafic magma, which has formed the MME, and had a huge interaction with more felsic magma.

According to Baxter and Feely (2002), the coexistence of two different apatite morphologies – stubby and acicular ones – may be explained by magma mixing/mingling process. In the studied rocks, it is observed both, all as inclusions in feldspar phenocrysts. The stubby apatite (Figure 5e) represents the earlier crystallization episode from the felsic magma, whereas the acicular apatite in MME (Figure 5f) suggests a thermal contrast caused by quenching process (undercooling) when a hot mafic magma was injected into a cooler felsic magma (Wyllie et al., 1962).

4. Analytical methods

4.1. Whole-rock geochemistry

Sample preparation was performed at the Oficina de Preparação de Amostras, Federal University of Pará (OPA/UFPA), Brazil. Approximately 0.5–5 kg fresh samples were comminuted in chips by using both primary and secondary jaw crushers. Subsequently, this material was powdered in an agate swing mill until reaches a particle size <10 μm. Quartered powder rocks were conducted for whole-rock chemical analysis – fourteen analyses were obtained at ACME Laboratories (Canada) and twenty-eight ones at ALS Geochemistry Laboratories (Brazil), totalizing 42 samples. These analyses were performed by ICP-AES for major elements and ICP-MS for trace elements (including the rare earth elements). Geochemical diagrams were generated by using GCDkit software (Janoušek et al., 2003). Detailed information about analytical procedures can be found at www.acmelab.com and www.alsglobal.com.

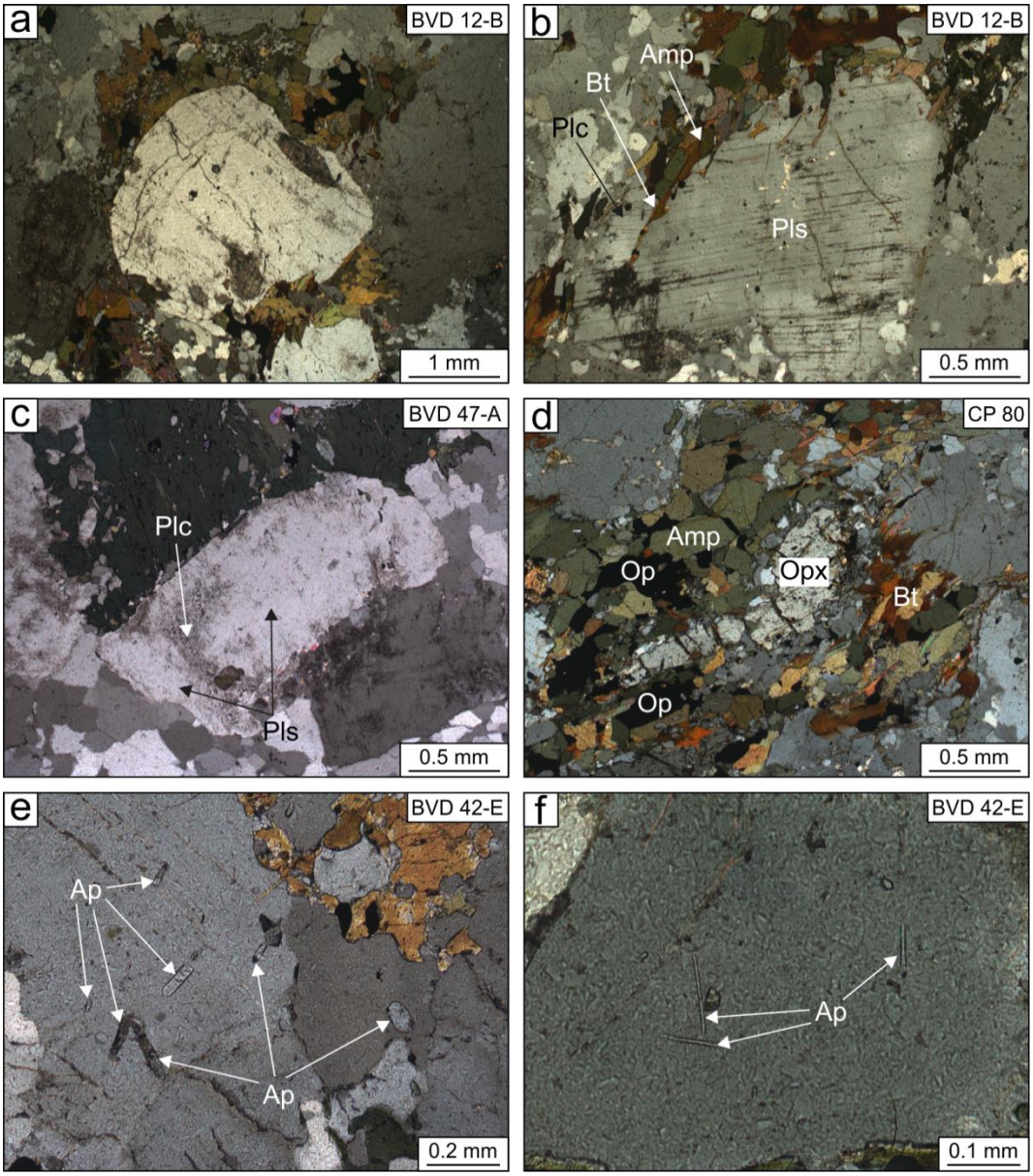

Figure 5. Representative photomicrographs of hybridization textures in the granitoids from Vila União area. (a) Plagioclase ocellus rimmed by amphibole, biotite and opaque minerals, showing these mafic minerals nucleating on plagioclase substrate; (b) biotite and amphibole inclusion zone in plagioclase phenocryst, located between the inner portion of plagioclase (Na-rich) to the outer one (Ca-rich); (c) spike zone in plagioclase: note the Ca-rich zone (spike) underlined by sericitization; (d) mafic clots (aggregates), quite common in all varieties of the studied rocks, composed by amphibole, biotite, opaque minerals and orthopyroxene; occurrences of (e) stubby and (f) acicular apatite crystals included in feldspar phenocrysts. All of photomicrographs under crossed nicols. Abbreviations: Amp (amphibole); Ap (apatite); Bt (biotite); Op (opaque minerals); Opx (orthopyroxene); Plc (calcic plagioclase); Pls (sodic plagioclase).

4.2. Whole-rock Sm-Nd isotope

For the Sm-Nd isotopic analyses, it was used the batches of nine representative sample powders that had been previously prepared for the whole-rock major and trace elements analyses. The analyses were conducted using a Thermo Finnigan Neptune MC-ICP-MS with

Faraday collectors, at the Laboratório de Geologia Isotópica, Federal University of Pará (Pará-Iso/UFPA).

For each sample, ~100mg of rock powder was weighed out in a Teflon high-pressure vessel, mixed with a $^{150}Nd/^{149}Sm$ tracer solution and HF + HNO_3 acids, and reacted at 150°C for one week, following the procedures described by Oliveira et al. (2008). After 7 days of digestion, the solution is evaporated to dryness and then redissolved in HF + HNO_3 acids. This solution is then dried and taken up in 6N HCl, being followed by sequential drying down and addition of 2N HCL. After evaporation, rare earth elements (REE) were isolated by chromatographic exchange using *BioRad Dowex 50WX-8* cationic resin, 2N HCl and 3N HNO_3. Sm and Nd were separated from the other REE and collected by passing the solution through a further set of ion exchange columns loaded with *Dowex AGI-X4*, 7N HNO_3 and methanol. After evaporation, each separated Sm and Nd fraction was diluted with 1 ml HNO_3^{**} (2%), and then analyzed in the MC-ICP-MS. During the course of this study, mass fractionation correction for $^{143}Nd/^{144}Nd$ was carried out relative to a $^{146}Nd/^{144}Nd$ of 0.7219 using the exponential law. The La Jolla standard gave an average $^{143}Nd/^{144}Nd$ value of 0.511834 (±5).

4.3. Zircon U-Pb dating

Around 10–20 kg of each representative sample of the granitoids from Vila União area were crushed, grinded and sieving into fractions between 125–175 μm at Pará-Iso/UFPA. Zircon grains were separated using the conventional heavy-liquid (bromoform) and magnetic techniques. Representative zircon grains were handpicked under a binocular microscope (ca. 60–80 grains/sample), mounted in epoxy resin discs and then polish to about half their thickness to expose crystals interiors. Prior to U–Pb dating, internal structures, overgrowths, fractures, inclusions and physical defects of the zircon grains was examined using backscattered electron (BSE) images obtained using a JEOL JXA-8230 scanning electron microprobe (SEM) working at 15 kV, 20 μA and 11 mm working distance, equipped at Laboratório de Microanálises, Federal University of Pará (Brazil).

Three U-Pb zircon analyses were carried out using a SHRIMP IIe (Sensitive High Resolution Ion Microprobe) system installed at the Laboratório de Geologia de Alta Resolução, University of São Paulo, Brazil (GeoLab/USP), whose instrumental performance and analytical procedures are documented by Stern (1998), Williams (1998) and Sato et al. (2008, 2014). The standards used were SL 13 for U composition reference (238 ppm; Sato et al., 2014), and TEMORA-2 zircon (416.78±0.33 Ma; Black et al., 2003) as isotope ratios

standard. The spot size of the primary ion beam was 30µm. Isoplot 4.15 software of Ludwig (2008) was used to calculate the $^{207}Pb/^{206}Pb$ ages and build Concordia plots.

One U-Pb analysis was conducted by *in situ* LA-MC-ICP-MS (Laser Ablation Multi-Collector Ion Coupled Plasma Mass Spectrometer) at Pará-Iso/UFPA, with a Nd:YAG 213 nm (LSX-213 G2 model) Laser Ablation Microprobe coupled to a Thermo Finnigan Neptune MC-ICP-MS. Helium was used as the carrier gas to enhance the transport efficiency of ablated material. Individual analytical spots were typically of 50 µm in diameter. U-Th-Pb ratios and absolute abundances were determined relative to the GJ-1 zircon standard (Stacey and Kramers, 1975). The analytical data were calculated and plotted using the Isoplot 4.15 software (Ludwig, 2008).

4.4. Zircon Lu-Hf isotope

Lu-Hf isotopic analyses were carried out at the Laboratório de Geoquímica Isotópica of Federal University of Ouro Preto (UFOP), Brazil, using a multi-collector ICP-MS Thermo-Scientific Neptune Plus system coupled to a Photon-Machines 193 ArF Excimer laser ablation system, following the methods suggesting by Gerdes and Zeh (2006, 2009). Hf isotopic data reported in this study were obtained from the zircon grains with U-Pb data. Laser spots for Lu-Hf analyses were drilled on or immediately beside the previous U-Pb spots, but always within the same zircon domain characterized by cathodoluminescence and BSE imaging.

Data were collected in static mode during 60 seconds of ablation with a spot size of 50 µm. Nitrogen (~0.080 l/min) was introduced into the Ar sample carrier gas. Typical signal intensity was ca. 10 V for ^{180}Hf. The isotopes ^{172}Yb, ^{173}Yb and ^{175}Lu were simultaneously monitored during each analysis step to allow for correction of isobaric interferences of Lu and Yb isotopes on mass 176. The ^{176}Yb and ^{176}Lu were calculated using a $^{176}Yb/^{173}Yb$ of 0.796218 (Chu et al., 2002) and $^{176}Lu/^{175}Lu$ of 0.02658 (JWG in-house value). The correction for instrumental mass bias utilized an exponential law and a $^{179}Hf/^{177}Hf$ value of 0.7325 (Patchett and Tatsumoto, 1980) for correction of Hf isotopic ratios. The mass bias of Yb isotopes generally differs slightly from that of the Hf isotopes with a typical offset of the βHf/βYb of ca. 1.04 to 1.06 when using the $^{172}Yb/^{173}Yb$ value of 1.35274 from Chu et al. (2002). This offset was determined for each analytical session by averaging the βHf/βYb of multiple analyses of the JMC 475 solution doped with variable Yb amounts and all laser ablation analyses (typically n >50) of zircon with a ^{173}Yb signal intensity of >60 mV. The mass bias behavior of Lu was assumed to follow that of Yb. The Yb and Lu isotopic ratios were corrected using the βHf of the individual integration steps (n = 60) of each analysis

divided by the average offset factor of the complete analytical session. The results were calibrated with the standard zircon Temora (415 Ma; Hf = 0.282680), Mud Tank (730 Ma; Hf = 0.282501) and 91500 (1065 Ma; Hf = 0.282307). For the calculation of εHf, we have used the chondritic values of Bouvier et al. (2008; $^{176}Lu/^{177}Hf$ = 0.0336, and $^{176}Hf/^{177}Hf$ = 0.282785) and decay constant (1.865×10^{-11} yr^{-1}) of Scherer et al. (2001). The average Depleted Mantle (DM) is that defined by Andersen et al. (2009), with $^{176}Lu/^{177}Hf$ and $^{176}Hf/^{177}Hf$ values of 0.0388 and 0.283250, respectively, and the average Continental Crust value of 0.015, defined by Griffin et al. (2002).

5. Petrography and microstructures

5.1. Modal composition and petrographic classification

The petrography of the granitoids from Vila União area was discussed by Oliveira et al. (2018) and Marangoanha et al. (unpublished results). The modal mineralogy are composed of K-feldspar, quartz and plagioclase as essential minerals; amphibole, biotite and opaque minerals are the main mafic phases, although clino- and orthopyroxene are also present (both rarely in the most felsic varieties, but can reach about 10% in less evolved rocks); titanite, epidote, allanite, apatite, scapolite and zircon as primary accessory minerals; and muscovite and chlorite constitute the secondary minerals. Modal data of representative samples are given in Table 2.

Table 2. Representative modal compositions of the granitoids from Vila União area.

Sample	BVD 42-F	BVD 42-I	BVD 12-B	BVD 12-A	BVD 48	TDM 7	TDM 11	BVD 42-H	BVD 34-A	RDM 9-C	BVD 47-A	BVD 19	BVD 44	BVD 42-B	BVD 26	BVD 18-B	BDE 19-B	BVD 17	BVD 28
Variety	Quartz diorite			Biotite-hornblende tonalite				Biotite-hornblende monzogranite								Leucogranite			
Minerals (vol.%)																			
Quartz	2.55	4.70	6.67	17.30	20.90	23.85	24.51	18.80	22.42	22.70	26.00	26.65	27.71	31.48	37.30	22.05	23.45	26.80	26.90
Plagioclase	55.05	54.30	66.39	52.50	53.30	42.90	42.20	44.35	45.34	30.35	26.95	26.30	35.78	29.07	27.20	17.20	30.35	21.00	14.85
Alkali feldspar	-	-	-	0.35	5.45	3.45	0.90	10.40	14.24	33.25	31.95	23.30	13.61	28.30	21.95	58.75	42.70	42.55	49.30
Hornblende	20.40	24.95	15.20	20.75	12.80	21.75	20.94	20.50	9.67	7.40	11.60	8.40	9.95	6.60	7.10	-	-	4.70	0.85
Biotite	0.95	0.70	5.79	4.35	4.90	6.55	9.35	1.95	6.17	0.30	-	10.65	9.00	2.90	5.20	0.60	0.70	-	3.50
Clinopyroxene	10.40	6.00	0.99	-	-	-	-	0.10	-	0.65	-	-	-	-	-	-	-	-	-
Orthopyroxene	8.25	6.75	1.11	-	-	-	-	-	-	0.95	-	-	-	-	-	-	-	-	-
Opaque minerals	1.80	2.10	3.27	2.70	0.60	0.15	0.30	3.80	0.21	4.20	0.50	1.50	2.60	0.95	-	0.65	0.45	0.50	0.30
Titanite	-	-	-	0.35	0.70	0.70	0.90	-	1.54	0.10	-	1.40	-	-	0.90	-	0.30	1.75	0.80
Epidote	0.40	0.15	-	0.15	0.10	-	0.48	-	0.10	-	0.95	1.00	0.10	0.15	0.35	-	0.20	0.05	0.10
Scapolite	-	-	0.23	1.55	1.25	-	0.42	-	0.31	-	-	0.60	1.15	0.55	-	-	-	-	-
Apatite	0.20	0.25	-	-	-	-	-	0.05	-	-	0.05	0.20	-	-	-	-	-	-	-
Zircon	-	0.10	-	-	-	-	-	0.05	-	0.10	-	-	-	-	-	-	-	-	-
Chlorite	-	-	0.35	-	-	0.65	-	-	-	-	2.00	-	0.10	-	-	0.75	1.85	2.65	3.40
Bt/Hb	0.05	0.03	0.38	0.21	0.38	0.30	0.45	0.10	0.64	0.04	-	1.27	0.90	0.44	0.73	-	-	-	4.12
A+P	55.05	54.30	66.39	52.85	58.75	46.35	43.10	54.75	59.58	63.60	58.90	49.60	49.39	57.37	49.15	75.95	73.05	63.55	64.15
Colour index (M)	42.40	41.00	26.94	29.85	20.35	29.80	32.39	26.45	18.00	13.70	15.10	23.75	22.90	11.15	13.55	2.00	3.50	9.65	8.95

Abbreviations: Bt/Hb (biotite/hornblende ratio); A+P (alkali-feldspar + plagioclase sum).

The Q-A-P diagram (Le Maître et al., 2002; Figure 6) show that the granitoids from Vila União area present a wide compositional range, which were divided into four varieties: (i) leucogranites (LcGr), composed of monzogranite and syenogranite; (ii) biotite-hornblende monzogranite (BtHbMzG), formed mostly by monzogranite, with scarce granodiorite; (iii)

biotite-hornblende tonalite (BtHbTn); and (iv) quartz diorite (QzD), that includes also a dioritic sample. Concerning mafic mineral contents (cf. Table 2 and Figure 6), these rocks are mostly hololeucocratic and leucocratic (M' = 2–32.77%), with rare mesococratic occurrences (M' = 41–42.4%). The varieties LcGr, BtHbMzG and BtHbTn are dominantly coarse- to medium-grained with heterogranular texture, while the less evolved variety (QzD) tends to exhibit a fine-grained one.

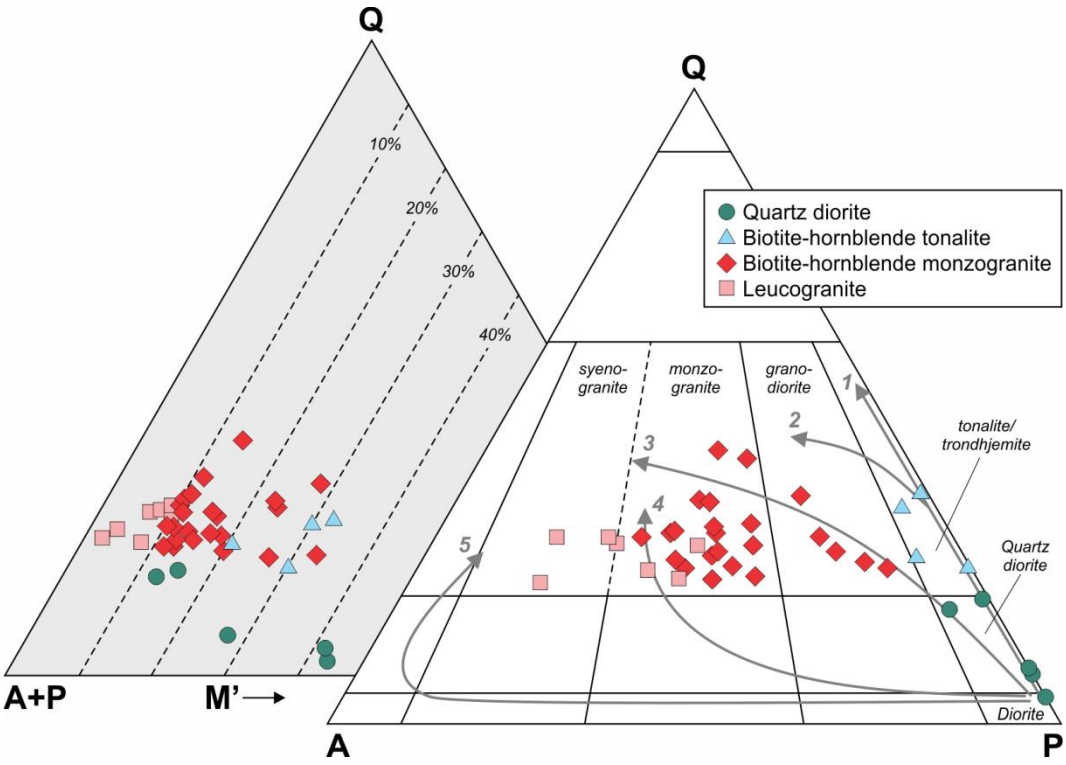

Figure 6. Q-A-P and Q-(A+P)-M plots for the granitoids from Vila União area (Le Maître et al., 2002). Granitic series and their evolutionary trends from Lameyre and Bowden (1982) and Bowden et al. (1984): 1 (tholeiitic), 2 (calc-alkaline tonalitic or trondhjemitic), 3 (calc-alkaline granodioritic), 4 (subalkaline monzonitic or shoshonitic) and 5 (alkaline and peralkaline).

5.2. Deformational effects

In order to establish a deformational pattern that these rocks were submitted, a brief microstructural/microtextural analysis was made based on the mylonites classification of Passchier and Trouw (2005) and Trouw et al. (2010), which consider temperature and strain as the main features to form mylonites. Therefore, these granitoids were divided into three different mylonitic domains: low, medium and high-grade mylonitic domains.

It is worth to mention that, as the studied area is crosscut by many shear zones then, as a result, these zones exert a huge influence on these domains. Furthermore, it is important to make it clear that all domains exhibit some common features like the alignment of the

minerals, mainly feldspar porphyroclasts, quartz, biotite and amphibole, which defines an E–W planar fabric.

The low-grade mylonitic domain comprises rocks with igneous texture almost entirely preserved, characterized mainly by euhedral to subeuhedral square-shaped feldspar porphyroclasts and amphibole (Figure 7a). Recovery process is quite common and is described chiefly by quartz, which shows undulose extinction with subgrains formation (Figure 7b). As well, bulging recrystallization (BLG-recrystallization) occurs in deformed quartz (Figure 7b). Plagioclase crystals frequently show brittle fracturing (Figure 7c), which sometimes may present submagmatic microfractures filled with opaque mineral-amphibole-biotite aggregates (Figure 7d), or even quartz-feldspar aggregates, suggesting that this deformational process occurred still during the crystallization stage (Bouchez et al., 1992). Feldspars with undulose extinction and kink band in this domain are rather rare. Biotite eventually develops smooth kink bands.

The medium-grade mylonites are the most abundant in the studied area. Deformations by kinking (Figure 7e) and by twinning, besides extinction undulose in plagioclase porphyroclasts, are typical in this domain. At increasing temperature, the recrystallization process becomes more prominent, as demonstrated by BLG-recrystallization in feldspars, which describes core-mantle structures (Figure 7f), besides flame-perthite in K-feldspar. Moreover, quartz is entirely recrystallized, mainly by subgrain rotation recrystallization (SGR-recrystallization; Figure 7f), albeit BLG-recrystallization is also present.

The high-grade mylonitic domain is the least common group of rocks in the studied area, and their minerals are practically fully recrystallized. Most plagioclase shows SGR-recrystallization, which the boundary between the core and the mantle is weakly pronounced (Figure 7g), whereas BLG-recrystallization still can be found. Amphibole porphyroclasts with strain shadows of biotite and opaque minerals are quite common (Figure 7g). Quartz occurs basically like ribbon, which indicates growth by high-temperature grain boundary migration recrystallization (GBM-recrystallization; Figure 7g). Other evidences of quartz affected by GBM-recrystallization in this domain are large grains with inclusions of other minerals and the ‘window’ microstructure, which a grain boundary between two grains of a mineral (in this case, quartz) bulges between two grains of another mineral (in this case, biotite; Passchier and Trouw, 2005; Figure 7h).

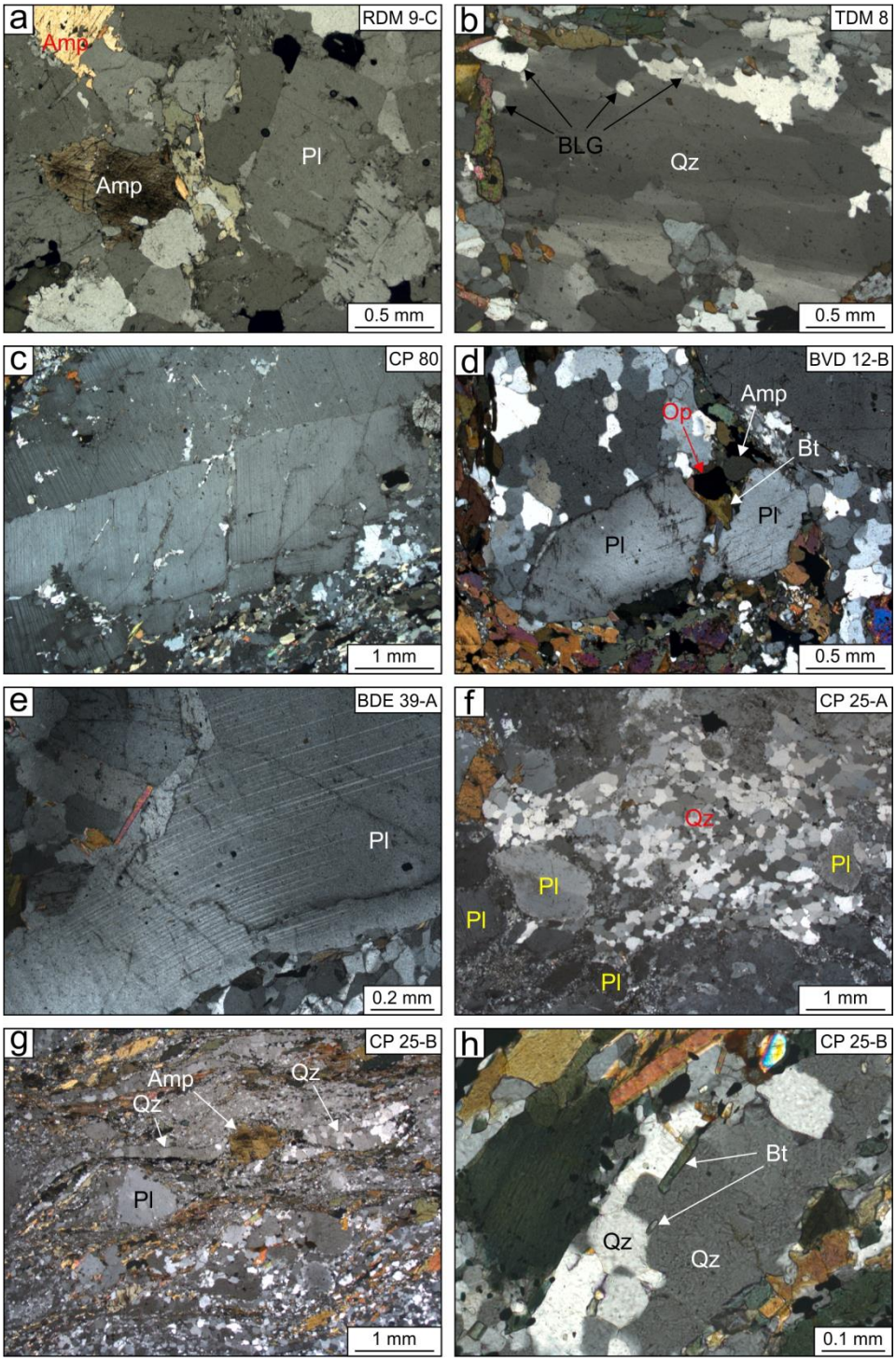

Figure 7. Photomicrographic microstructural features of low-, medium- and high-grade domains granitoids from Vila União area. Low-grade domain: (a) euhedral to subeuhedral square-shaped feldspar porphyroclasts and subeuhedral amphibole crystals; (b) quartz showing undulose extinction with subgrains formation by bulging recrystallization (BLG); (c) brittle fracturing in plagioclase porphyroclast; (d) submagmatic microfracture in plagioclase filled with opaque mineral-amphibole-biotite aggregates. Medium-grade domain: (e) plagioclase porphyroclast showing deformation by kinking; (f) plagioclase crystals showing core-mantle structures, and quartz entirely recrystallized by subgrain rotation recrystallization (SGR). High-grade domain: (g) general aspect of this domain, which their minerals are practically fully recrystallized, with plagioclase showing SGR and quartz occurring mostly like ribbon, indicating growth by high-temperature grain boundary migration recrystallization (GBM); (h) 'window' microstructure formed by quartz and biotite crystals. All photomicrographs under crossed nicols. Abbreviations: Amp (amphibole), Bt (biotite), Op (opaque minerals), Pl (plagioclase) and Qz (quartz).

6. Geochemistry

6.1. Major and trace elements

Whole-rock analyses of different varieties of the granitoids from Vila União area are reported in Table 3. In general, these rocks show a wide chemical compositional range (SiO_2 values between 55.30 and 75.60 wt.%). In Harker diagrams (Figure 8), TiO_2, Al_2O_3, Fe_2O_3*, CaO, MgO and P_2O_5 display a negative correlation with SiO_2, while K_2O show a positive one. Na_2O exhibits a scattered pattern in this diagram. They present low to moderate Rb contents (21.9–165.5 ppm) and display a positive correlation with SiO_2 (Figure 9a), unlike Sr which shows a negative correlation and moderate contents, between 96.8 and 465.2 ppm (Figure 9b). Ba and Zr exhibit high contents (553–2693 ppm and 147–936.8 ppm, respectively) and show a peculiar behavior in these diagrams, defined by inflection points closer to 64 and 67 wt.%, respectively (figures 9c and d, respectively). To both elements, their respective contents increase with increasing SiO_2 but abruptly decrease in their respective inflection points.

The chondrite-normalized rare earth elements (REE) diagrams (figures 10a-d) show practically no difference between the varieties from Vila União area, except by the negative Eu anomaly, which becomes slightly stronger as more evolved the variety. Apart from this peculiarity, all the facies are closely similar, as shown by moderate to high REE contents (La = 31.7–106.5 ppm; Gd = 4.09–14.15 ppm; Yb = 1.83–5.75 ppm) and moderately fractionated patterns (La_N/Yb_N = 7.61–21.12).

6.2. Classification and granitoid typology

The P-Q diagram (Debon and Le Fort, 1988; Figure 11a) displays that the granitoids from Vila União area are classified predominantly as monzogranites and granodiorites, with subordinate syenogranites, tonalites and quartz diorites. In the normative An-Ab-Or diagram (O'Connor, 1965, with fields from Barker, 1979; Figure 11b), the samples plot mostly on granites and granodiorites fields, while scarce samples plot on tonalites and trondhjemites fields. These rocks show a clear ferroan character, as displayed in the SiO_2 *vs.* FeO*/(FeO*+MgO) diagram (Frost et al., 2001; Figure 11c), and are metaluminous to slightly peraluminous, according to Shand's (1950) parameters (Figure 11d). When plotted in the MALI diagram (Frost et al., 2001; Figure 11e), these rocks lie mostly within the calc-alkaline field, although they show a strong alkaline tendency when plotted in the diagram of Sylvester (1989; Figure 11f).

Table 3. Representative chemical compositions of the granitoids from Vila União area.

Sample	BVD 42-F	BVD 42-I	BVD 42-D	BVD 47-C	BDE 38	BVD 47-E	BVD 12-A	BVD 42-C	BVD 42-E	BVD 48	BVD 42-H	BVD 47-A	BVD 34-A	BVD 47-H	BVD 29	BVD 20	BVD 15	BVD 26	BVD 57	BVD 18-A	BDE 19-B	BVD 31
Variety	Quartz diorite					Biotite-hornblende tonalite					Biotite-hornblende monzogranite								Leucogranite			
Major elements (wt.%)																						
SiO_2	55.30	55.60	55.90	57.20	59.40	60.50	61.70	62.60	64.90	67.40	63.90	65.00	66.30	66.40	67.60	69.90	70.10	71.90	72.90	74.30	74.76	75.60
TiO_2	1.18	1.36	1.30	1.85	1.42	1.29	1.51	0.74	0.99	0.89	1.08	0.90	0.83	0.78	0.75	0.59	0.54	0.51	0.57	0.49	0.36	0.30
Al_2O_3	15.25	13.85	14.50	13.50	14.24	12.90	13.75	13.20	13.85	14.15	13.00	13.90	14.25	12.50	12.90	12.35	13.10	12.70	12.25	12.65	12.34	11.55
Fe_2O_3*	11.50	11.15	10.75	12.60	9.56	9.40	9.04	8.18	7.70	6.81	8.00	6.45	6.86	8.39	5.44	4.97	3.78	4.82	4.91	3.49	2.18	3.28
MnO	0.17	0.18	0.14	0.12	0.12	0.11	0.12	0.10	0.11	0.08	0.09	0.07	0.08	0.06	0.08	0.06	0.03	0.06	0.07	0.03	0.02	0.04
MgO	5.00	3.55	4.34	2.46	2.72	2.29	1.87	3.40	1.90	0.83	1.26	0.81	0.92	1.69	1.39	0.58	0.91	0.42	0.46	0.70	0.34	0.20
CaO	7.33	6.53	7.06	6.46	5.65	5.47	4.85	4.38	4.35	3.70	3.60	3.34	3.86	2.61	2.70	2.04	2.02	1.84	1.96	1.31	1.08	1.14
Na_2O	4.33	4.03	4.16	3.62	3.51	3.58	3.59	3.40	3.84	4.04	3.47	3.46	4.11	3.13	3.28	3.44	3.29	3.41	3.50	3.13	2.86	2.84
K_2O	1.12	1.63	1.87	2.12	1.95	2.01	2.31	2.87	2.91	2.86	3.20	3.57	2.58	3.53	3.48	3.78	4.03	4.05	4.07	4.48	5.12	4.36
P_2O_5	0.37	0.44	0.42	0.62	0.45	0.37	0.43	0.21	0.33	0.22	0.31	0.19	0.18	0.21	0.20	0.10	0.11	0.09	0.10	0.08	0.05	0.04
LOI	0.32	0.26	0.70	1.19	0.60	0.76	0.51	0.69	0.55	0.49	0.45	0.80	0.43	0.86	0.76	0.63	1.18	0.72	0.74	0.85	0.60	1.10
Total	101.87	98.58	101.14	101.74	99.62	98.68	99.68	99.77	101.43	101.47	98.36	98.49	100.40	100.16	98.58	98.44	99.09	100.52	101.53	101.51	99.71	100.45
Trace elements (ppm)																						
Ba	592	870	740	1040	1197	1255	1595	1295	1495	1960	2260	2630	1965	2000	1230	1940	1350	1690	2180	1300	1343	1585
Sr	353.0	320.0	329.0	294.0	465.2	309.0	405.0	260.0	314.0	314.0	302.0	321.0	322.0	202.0	264.0	180.0	198.5	138.5	163.0	168.0	164.6	96.8
Rb	21.9	35.1	28.0	48.0	44.9	39.9	59.3	76.4	61.2	65.6	64.7	73.7	69.3	114.0	125.0	111.0	144.5	108.5	109.0	165.5	165.3	118.5
Zr	147.0	231.0	187.0	334.0	274.0	333.0	529.0	309.0	351.0	699.0	578.0	593.0	813.0	522.0	366.0	522.0	281.0	529.0	608.0	357.0	286.6	424.0
Y	20.7	25.8	22.5	49.1	32.3	29.4	56.0	52.8	24.0	46.2	29.0	35.6	62.1	46.0	31.3	46.1	24.9	47.2	60.9	33.8	32.1	50.9
Hf	3.7	5.4	4.8	7.5	6.6	7.9	12.7	8.2	8.0	15.1	12.9	12.9	18.7	12.7	9.8	13.3	8.0	12.6	14.4	10.2	8.4	11.7
Nb	7.5	13.0	7.1	19.7	11.8	14.6	17.1	21.0	9.9	18.9	10.0	16.7	25.8	15.8	14.0	20.1	13.2	19.5	21.3	13.2	12.0	21.1
Ta	0.9	1.0	0.6	1.4	0.7	1.5	1.3	1.7	1.0	1.5	1.2	2.0	1.7	1.4	2.0	2.1	1.9	1.6	1.9	1.8	1.3	2.0
Th	4.9	4.5	3.6	17.1	5.3	9.2	8.0	11.9	5.0	16.1	5.0	7.3	15.2	9.9	16.0	16.9	20.7	22.8	23.7	14.2	15.2	22.2
La	31.7	52.1	32.8	84.8	60.2	51.4	84.2	71.3	46.1	76.5	51.7	52.2	88.0	58.8	67.1	70.2	37.0	72.3	106.5	39.0	54.6	96.0
Ce	59.4	95.9	68.7	176.0	126.9	103.5	173.0	147.0	89.7	148.0	98.3	115.5	192.0	134.5	151.5	152.0	82.4	163.5	199.5	94.7	113.0	185.0
Pr	6.88	10.45	8.58	21.20	15.46	11.40	20.90	17.35	10.40	17.00	11.85	13.60	21.50	14.90	16.05	16.50	9.63	17.75	23.30	11.45	13.46	21.40
Nd	25.6	37.4	32.8	77.0	59.8	42.0	84.7	67.4	40.7	62.3	45.9	55.2	78.7	60.1	57.9	61.7	37.0	67.2	82.6	44.9	48.4	75.8
Sm	4.83	6.45	6.23	14.25	10.50	7.64	14.60	13.00	7.11	11.15	8.42	10.20	14.05	11.60	10.20	11.40	6.47	11.70	15.00	8.11	8.40	12.60
Eu	1.34	1.77	1.42	3.96	2.31	2.25	3.18	2.45	2.03	3.44	2.97	3.63	3.38	2.75	1.50	2.41	1.04	2.16	3.33	1.26	1.20	2.01
Gd	4.09	5.39	4.89	12.80	8.63	7.01	13.10	11.55	5.40	10.40	7.13	9.06	12.60	10.25	7.12	10.10	5.70	11.15	14.15	7.73	6.72	10.85
Tb	0.63	0.84	0.73	1.67	1.20	1.11	1.60	1.77	0.78	1.43	1.02	1.15	1.69	1.56	1.00	1.42	0.82	1.62	1.90	1.19	1.02	1.60
Dy	3.81	4.60	4.08	9.39	6.48	6.21	9.07	9.48	4.36	8.02	5.61	6.88	10.40	8.46	5.19	8.63	4.42	9.04	10.60	6.38	5.78	8.69
Ho	0.76	0.94	0.87	1.84	1.19	1.16	1.79	1.95	0.84	1.65	1.09	1.23	2.08	1.67	1.00	1.62	0.88	1.74	2.16	1.04	1.13	1.99
Er	2.25	2.62	2.50	5.02	3.32	3.11	5.07	5.85	2.50	4.67	3.01	3.50	6.42	4.94	3.57	4.86	2.80	5.27	6.12	4.11	3.27	5.57
Tm	0.35	0.40	0.33	0.72	0.47	0.47	0.76	0.81	0.35	0.68	0.40	0.59	1.02	0.68	0.44	0.77	0.41	0.82	0.84	0.53	0.49	0.83
Yb	2.15	2.55	2.19	4.20	3.06	3.01	4.60	4.86	1.99	4.28	2.55	3.39	5.75	4.45	3.16	4.74	2.46	4.81	5.46	3.48	3.29	5.07
Lu	0.31	0.44	0.32	0.63	0.45	0.44	0.78	0.81	0.33	0.71	0.42	0.60	0.92	0.67	0.46	0.68	0.40	0.70	0.82	0.40	0.48	0.77

Fe_2O_3* = total iron recalculated as Fe_2O_3; LOI = loss on ignition.

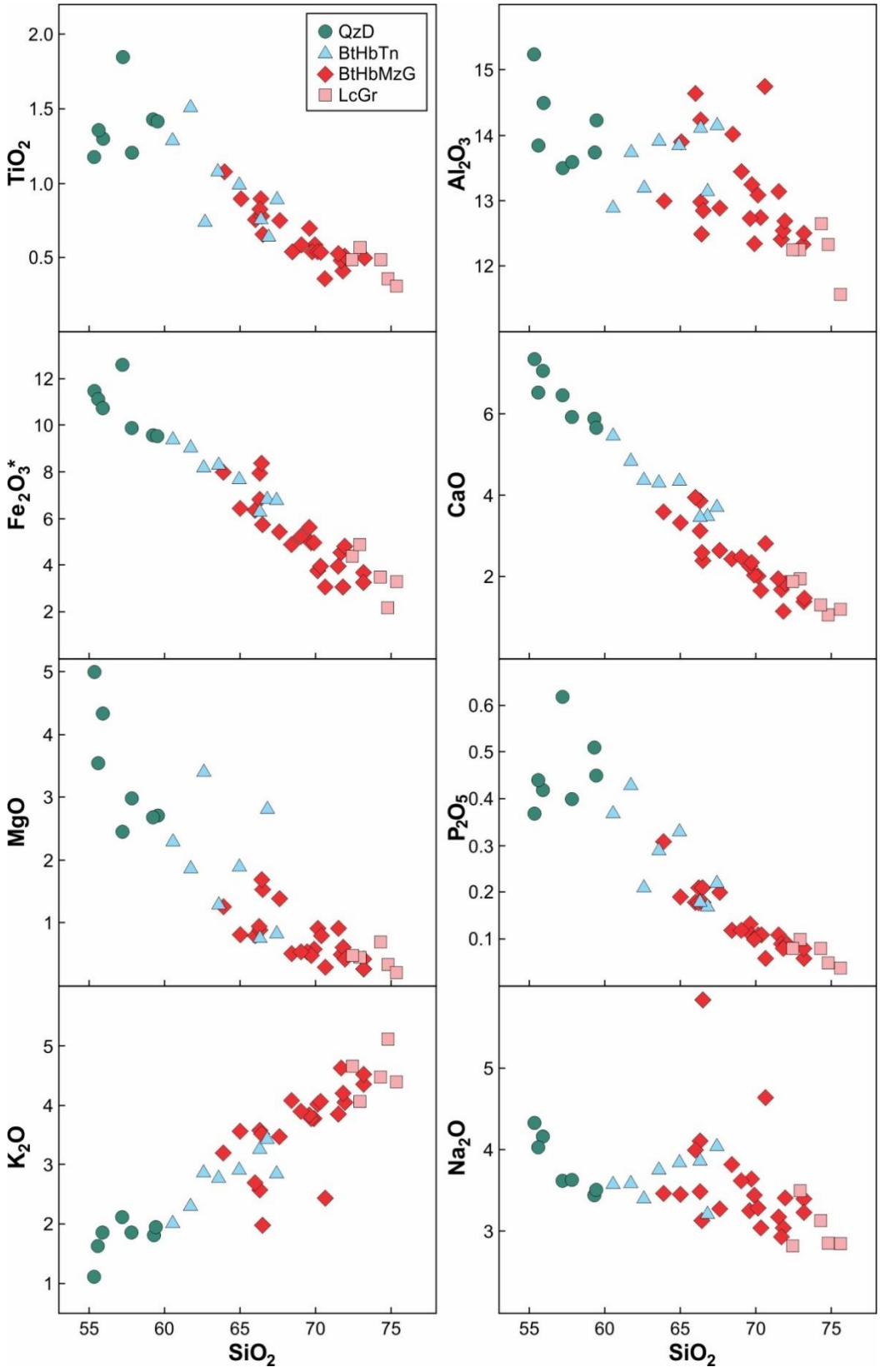

Figure 8. Harker diagrams (in wt.%) for the granitoids from Vila União area. Abbreviations: QzD (quartz diorite), BtHbTn (biotite-hornblende tonalite), BtHbMzG (biotite-hornblende monzogranites) and LcGr (leucogranite).

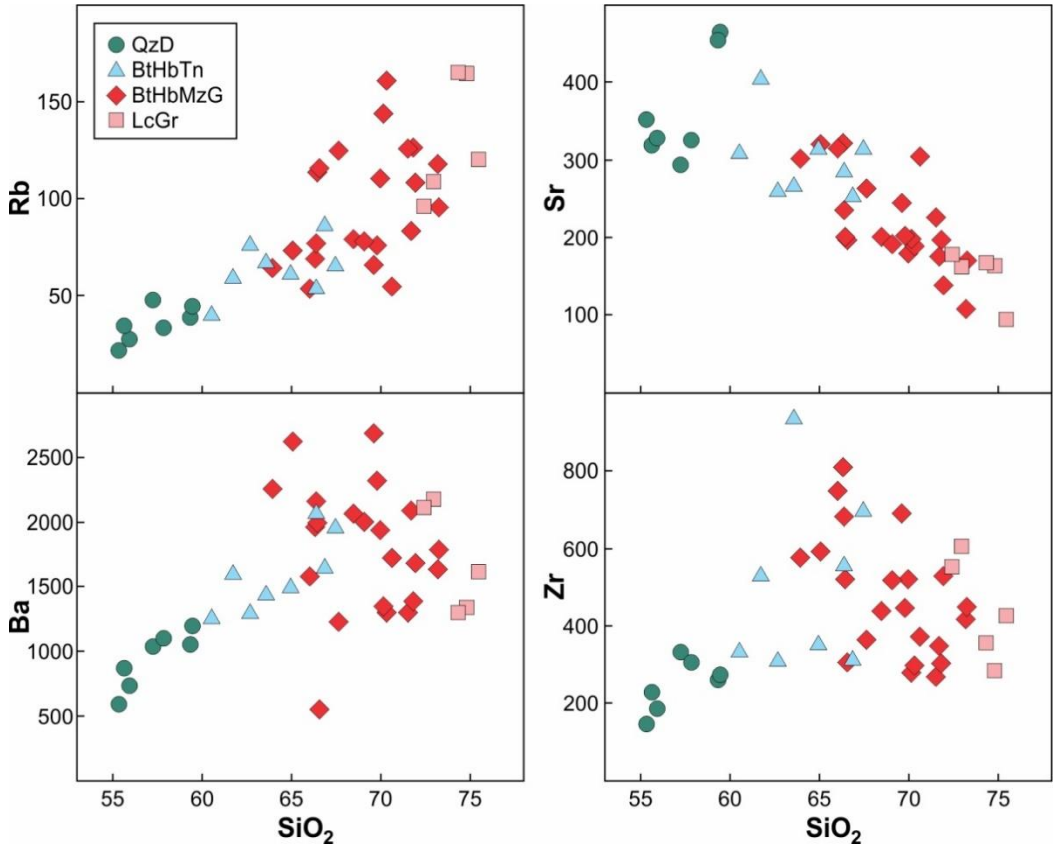

Figure 9. Harker diagrams for selected trace elements for granitoids from Vila União area. All trace elements are in ppm, and SiO_2 in wt.%. Abbreviations: QzD (quartz diorite), BtHbTn (biotite-hornblende tonalite), BtHbMzG (biotite-hornblende monzogranites) and LcGr (leucogranite).

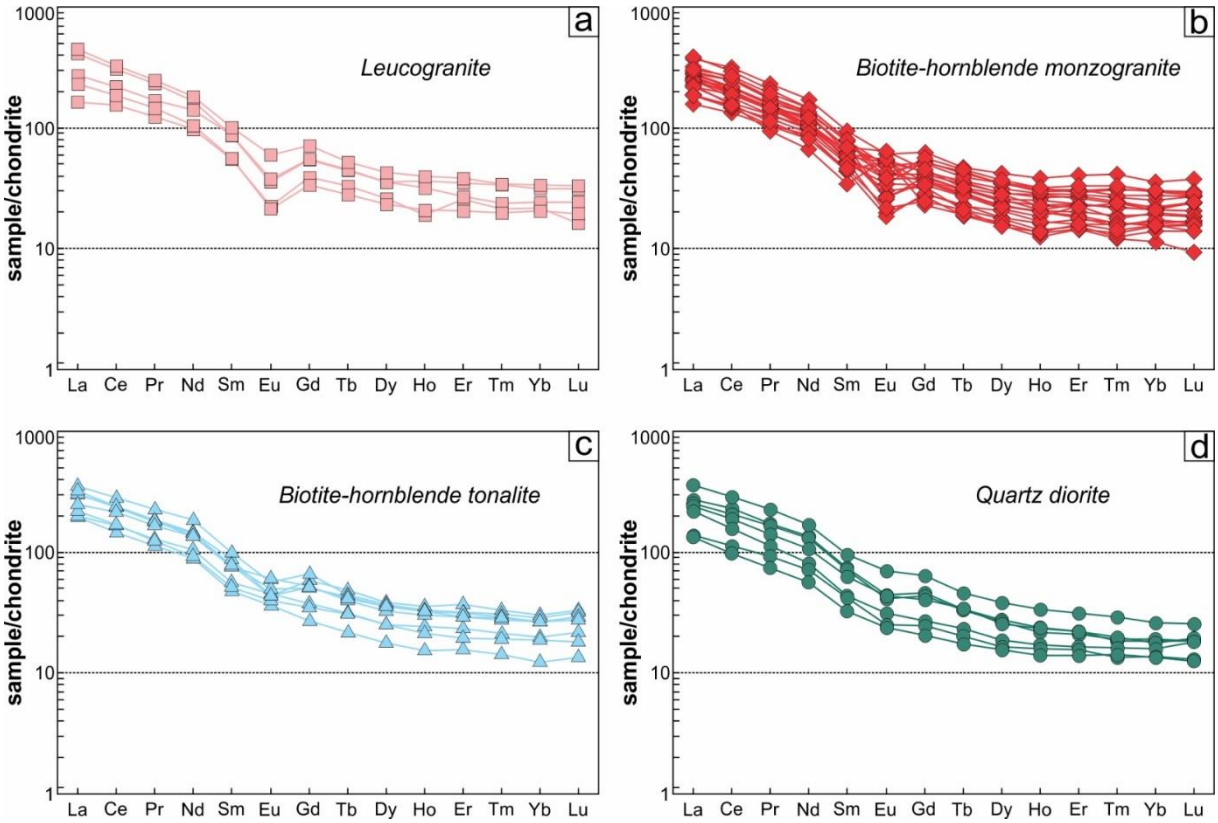

Figure 10. Rare earth elements patterns of the different varieties of the granitoids from Vila União area, with values normalized to C1 chondrite (McDonough and Sun, 1995).

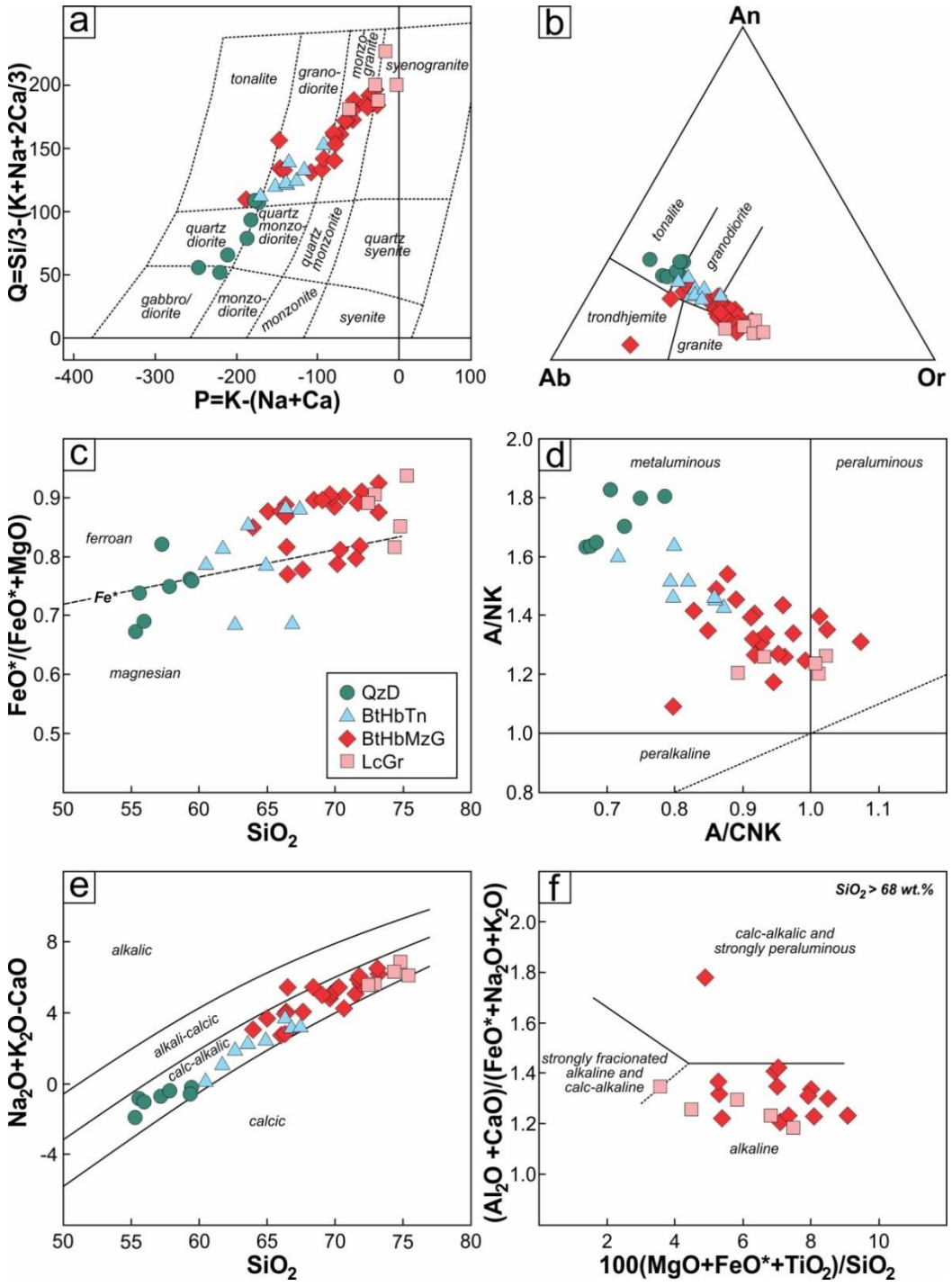

Figure 11. Geochemical diagrams for granitoids from Vila União area: (a) P-Q diagram from Debon and Le Fort (1988); (b) Normative feldspar triangle (O'Connor, 1965) with fields from Barker (1979); (c) FeO*/(FeO*+MgO) *vs.* SiO_2 after Frost et al. (2001) showing the ferroan character of the studied rocks; (d) A/CNK [$Al_2O_3/(CaO+Na_2O+K_2O)$] *vs.* A/NK [$Al_2O_3/(Na_2O+K_2O)$] diagram (Shand, 1950); (e) Na_2O+K_2O–CaO (MALI) *vs.* SiO_2 diagram (Frost et al., 2001); and (f) major element discrimination diagram for leucogranites (Sylvester, 1989). Abbreviations: QzD (quartz diorite), BtHbTn (biotite-hornblende tonalite), BtHbMzG (biotite-hornblende monzogranites) and LcGr (leucogranite).

According to Y *vs.* Nb tectonic diagram (Pearce et al., 1984; Figure 12a), the studied rocks show intraplate granites affinities, although a significant number of samples lie in volcanic arc and syn-collisional granites field. In the discrimination diagrams proposed by Whalen et al. (1987; Figure 12b) and Dall'Agnol and Oliveira (2007; Figure 12c), these rocks present an A-type affinity and, as shown by the Nb-Y-Ce ternary diagram as well (Eby, 1992; Figure 12d), they plot in the A2 type field, which suggests derivation from crustal source.

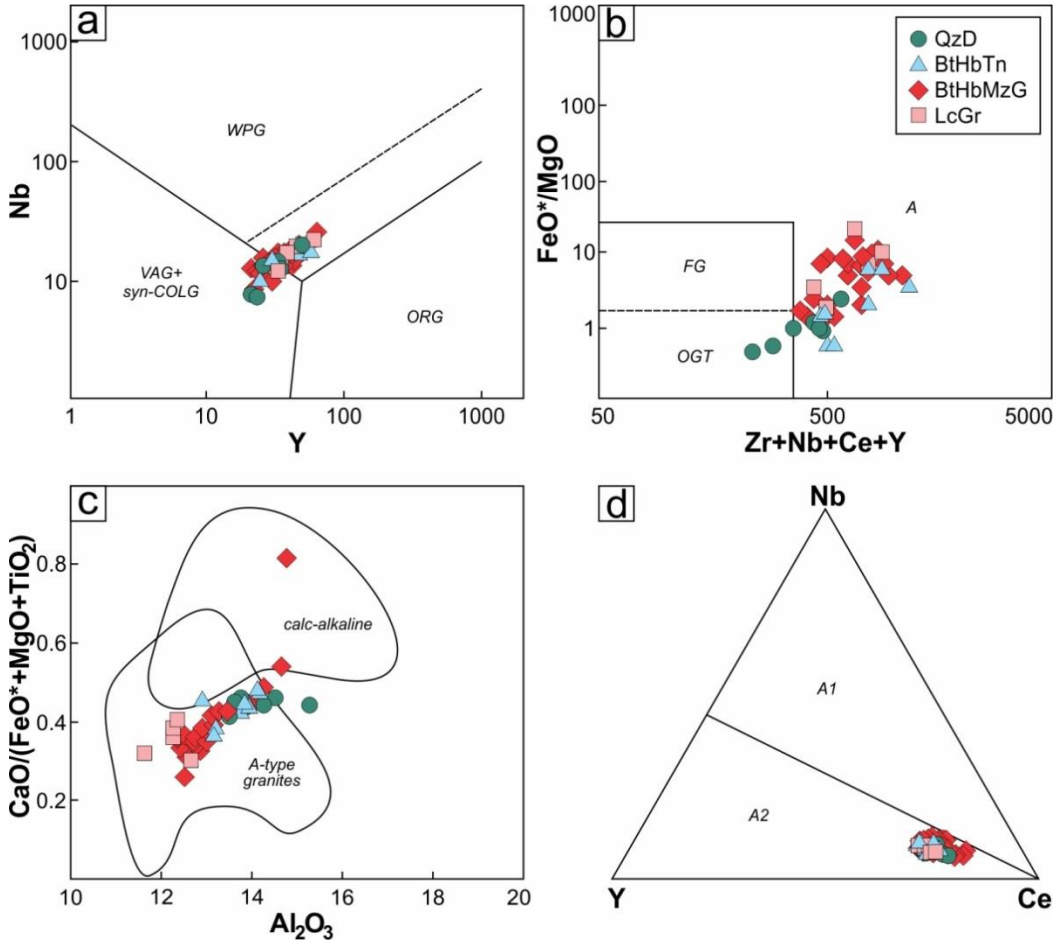

Figure 12. (a) Discrimination of tectonic environment diagram (Pearce et al., 1984); (b) discrimination diagram proposed by Whalen et al. (1987) showing the A-type affinities of the studied rocks; (c) $CaO/(FeO^*+MgO+TiO_2)$ *vs.* Al_2O_3 diagram (Dall'Agnol and Oliveira, 2007); and d) Nb-Y-Ce diagram. A1 and A2 fields after Eby (1992). Abbreviations: QzD (quartz diorite), BtHbTn (biotite-hornblende tonalite), BtHbMzG (biotite-hornblende monzogranites), LcGr (leucogranite), HFCA (highly fractionated calc-alkaline), WPG (within-plate granites), VAG (volcanic arc granites), syn-COLG (syn-collision granites), ORG (oceanic ridge granites), FG (fractionated granites) and OGT (unfractionated granites).

7. Isotopic data

7.1. U-Pb zircon dating

Four representative samples of different varieties from these granitoids were selected for geochronological analysis. Three of them were analyzed by the U-Pb SHRIMP method (leucogranite BVD 19-B, biotite-hornblende monzogranite AL 62-D and biotite-hornblende

tonalite BVD 42-C), and one by the U-Pb LA-MC-ICP-MS method (quartz diorite BVD 12-B). The location of the dated samples is shown in Figure 2 and their respective analytical data are summarized in the tables 4 and 5. The analytical techniques and data processing are described in section 4.2.

Table 4. Zircon U-Pb isotopic data obtained by SHRIMP for granitoids from Vila União area.

Spot	U	Th	Th/U	$^{206}Pb_c$	Isotopic ratios					Age		Discordance
	(ppm)	(ppm)		(%)	$^{207}Pb/^{235}U$	1σ (%)	$^{206}Pb/^{238}U$	1σ (%)	ρ	$^{207}Pb/^{206}Pb$	1σ (%)	(%)
BDE 19-B (Leucogranite)												
1.1	40	32	0.82	1.75	13.7470	1.4	0.5217	1.1	0.825	2751.7	12.6	2
2.1	61	71	1.20	5.54	13.6522	1.6	0.5260	1.0	0.606	2726.8	21.2	0
3.1	100	49	0.50	1.51	14.0034	1.0	0.5355	0.8	0.850	2739.3	8.4	-1
4.1	61	37	0.62	0.89	14.0997	1.2	0.5405	1.0	0.867	2735.2	9.9	-2
5.1	37	30	0.85	0.03	13.9701	1.4	0.5339	1.1	0.828	2740.4	12.6	-1
6.1	37	29	0.81	0.69	13.9122	1.4	0.5296	1.2	0.838	2746.6	12.3	0
7.1	45	38	0.86	0.02	13.7134	1.2	0.5208	1.0	0.846	2750.5	10.7	2
8.1	40	30	0.79	0.46	14.3742	1.5	0.5499	1.1	0.763	2738.5	15.7	-3
9.1	41	31	0.78	1.93	13.8725	1.4	0.5335	1.1	0.809	2729.9	13.4	-1
10.1	61	23	0.38	2.43	13.3443	1.2	0.5195	1.0	0.804	2709.8	11.9	0
11.1	52	42	0.83	0.35	14.1733	1.2	0.5410	1.0	0.856	2742.4	10.1	-2
12.1	557	347	0.64	-0.02	14.0176	0.6	0.5351	0.6	0.960	2742.0	3.0	-1
13.1	183	148	0.84	0.14	14.1240	0.8	0.5405	0.7	0.916	2738.0	5.2	-2
AL 62-D (Biotite-hornblende monzogranite)												
1.1	102	52	0.53	-0.98	13.9901	1.3	0.5313	1.2	0.926	2750.7	8.1	0
2.1	34	27	0.81	-2.18	14.1698	1.7	0.5280	1.5	0.856	2781.9	14.7	2
3.1	48	56	1.19	-1.47	14.0224	1.7	0.5230	1.5	0.850	2780.1	14.8	3
4.1	344	176	0.53	0.61	13.8953	1.2	0.5325	1.2	0.961	2735.5	5.5	-1
4.2	194	168	0.90	0.09	13.7350	1.2	0.5238	1.1	0.961	2743.7	5.4	1
5.1	100	90	0.93	0.41	13.1886	1.4	0.5030	1.2	0.879	2743.7	10.9	4
6.1	40	30	0.78	1.60	13.5247	1.8	0.5211	1.4	0.811	2727.0	17.2	1
7.1	597	719	1.24	0.56	13.8492	1.1	0.5293	1.1	0.983	2740.2	3.4	0
8.1	337	219	0.67	-0.22	14.0879	1.1	0.5321	1.1	0.975	2759.5	4.1	0
9.1	63	60	0.98	-1.37	14.0779	1.5	0.5300	1.3	0.890	2765.0	11.1	1
10.1	130	73	0.58	-0.50	13.8763	1.3	0.5299	1.2	0.943	2741.5	6.9	0
11.1	94	80	0.88	-0.06	14.0806	1.5	0.5354	1.4	0.914	2748.6	10.1	-1
BVD 42-C (Biotite-hornblende tonalite)												
1.1	86	52	0.62	0.11	14.1303	1.9	0.5387	1.6	0.851	2744.3	16.1	-2
2.1	83	34	0.42	2.30	13.3556	2.3	0.5088	1.6	0.712	2745.5	26.3	4
3.1	142	129	0.94	3.82	12.6672	2.4	0.4931	1.3	0.549	2709.8	33.3	6
4.1	131	59	0.47	1.65	13.3621	1.5	0.5114	1.3	0.902	2737.9	10.5	3
5.1	150	120	0.83	0.03	14.1137	1.4	0.5387	1.3	0.888	2742.2	10.9	-2
6.1	108	73	0.70	1.75	14.3831	2.8	0.5367	1.5	0.511	2779.5	40.1	0
7.1	91	43	0.49	0.83	13.7829	1.7	0.5271	1.5	0.869	2739.2	14.2	0
8.1	58	32	0.58	0.10	14.3873	2.5	0.5443	1.8	0.720	2756.9	28.5	-2
9.1	64	37	0.59	1.89	13.3724	2.0	0.5129	1.7	0.835	2734.3	18.5	3
10.1	42	22	0.54	2.28	13.7402	3.7	0.5232	2.1	0.559	2746.3	50.2	2
11.1	54	27	0.51	0.91	14.1970	3.4	0.5399	1.9	0.558	2748.2	45.8	-2
12.1	66	28	0.44	1.81	13.5992	2.3	0.5214	1.7	0.720	2734.8	26.6	1
13.1	34	19	0.59	2.33	13.4892	3.4	0.5156	2.3	0.671	2739.9	42.0	3
14.1	63	25	0.40	2.67	13.2956	2.2	0.5067	1.8	0.833	2745.0	20.0	5
15.1	192	180	0.97	0.64	14.0141	1.3	0.5303	1.2	0.918	2756.6	8.5	1
15.2	446	224	0.52	0.88	13.7426	1.3	0.5242	1.0	0.763	2743.3	13.9	1
16.1	35	21	0.62	3.82	13.7730	2.9	0.5094	2.4	0.821	2793.9	27.0	6
17.1	92	58	0.64	0.36	13.8281	1.9	0.5325	1.6	0.850	2727.7	16.2	-1

Pb_c: common Pb corrected using measured ^{204}Pb.

Table 5. Zircon U-Pb isotopic data obtained by LA-MC-ICP-MS for the granitoid sample BVD 12-B from Vila União area.

Spot	U	Th	Th/U	$^{206}Pb_c$	Isotopic ratios					Age		Discordance
	(ppm)	(ppm)		(%)	$^{207}Pb/^{235}U$	1σ (%)	$^{206}Pb/^{238}U$	1σ (%)	ρ	$^{207}Pb/^{206}Pb$	1σ (%)	(%)
1.1	4	3	0.80	0.35	15.3948	3.2	0.5976	2.0	0.619	2714.4	69.1	-6
2.1	12	12	1.02	0.21	14.2087	1.6	0.5532	1.3	0.802	2709.6	26.4	-3
3.1	54	57	1.06	0.12	12.6276	0.5	0.4770	0.4	0.731	2759.3	9.7	5
4.1	23	16	0.73	0.40	15.5870	2.5	0.6150	2.3	0.927	2687.7	25.4	-8
5.1	13	15	1.15	0.35	13.7508	1.4	0.5289	0.9	0.629	2729.6	30.6	0
6.1	11	10	0.93	0.37	14.5832	1.1	0.5629	0.5	0.456	2723.8	25.8	-3
7.1	5	4	0.76	0.16	15.7820	7.3	0.5752	4.3	0.588	2818.1	167.2	-2
8.1	50	25	0.52	0.12	13.5118	1.3	0.5256	0.8	0.599	2711.2	28.0	0
9.1	8	8	1.06	1.39	13.1417	2.7	0.5029	1.0	0.384	2738.0	67.4	2
10.1	18	16	0.91	0.47	14.4454	1.5	0.5452	1.3	0.866	2760.7	20.3	-1
11.1	13	13	1.02	0.39	15.7883	2.8	0.5805	1.2	0.438	2803.8	71.2	-3
12.1	26	20	0.78	0.23	14.7969	0.9	0.5669	0.6	0.619	2736.3	19.3	-3
13.1	12	8	0.66	0.48	16.9746	3.5	0.6132	2.3	0.665	2832.6	73.2	-5
14.1	15	16	1.11	0.40	14.6943	1.1	0.5663	0.8	0.706	2726.3	21.2	-3
15.1	17	14	0.83	0.37	15.3991	0.8	0.5835	0.4	0.500	2754.4	18.3	-4
16.1	16	15	0.91	0.28	14.8885	0.7	0.5681	0.5	0.732	2742.9	13.0	-3
17.1	30	51	1.71	0.52	13.9524	1.0	0.5326	0.9	0.931	2742.1	9.6	0
18.1	43	11	0.26	0.53	14.1648	3.0	0.5333	2.3	0.787	2764.9	50.8	0
19.1	120	18	0.16	0.43	8.7728	3.4	0.3864	3.3	0.971	2504.3	20.2	9
19.2	101	11	0.11	0.23	11.0678	1.4	0.4663	1.3	0.981	2578.6	6.9	2
20.1	12	10	0.87	0.38	13.2829	1.4	0.5027	0.8	0.570	2756.3	31.8	3
21.1	16	15	0.95	0.41	14.2941	0.8	0.5470	0.5	0.618	2738.0	17.3	-2
22.1	84	60	0.72	0.52	11.1455	1.3	0.4394	0.8	0.583	2689.1	29.3	7
23.1	14	13	0.89	0.31	14.9863	0.9	0.5889	0.5	0.523	2694.3	20.8	-6
24.1	61	29	0.49	0.32	14.0728	1.7	0.5539	1.6	0.979	2691.7	9.1	-3
25.1	65	9	0.14	0.12	15.3446	0.9	0.6136	0.9	0.928	2665.4	9.2	-9
26.1	19	13	0.66	0.34	13.8139	1.0	0.5273	0.6	0.616	2742.3	21.1	0
27.1	9	8	0.85	0.39	14.0254	2.1	0.5493	1.1	0.505	2700.0	49.0	-3
28.1	39	33	0.86	0.33	13.4486	0.6	0.5139	0.5	0.812	2740.3	9.7	1
29.1	13	14	1.05	0.30	14.4146	1.1	0.5617	0.7	0.625	2708.1	22.9	-3
30.1	12	11	0.91	1.32	13.7347	1.2	0.5219	0.7	0.526	2749.5	29.0	1
31.1	11	13	1.24	1.75	13.3305	1.4	0.5100	1.1	0.776	2738.3	23.8	2
32.1	24	24	1.00	0.28	13.4178	0.8	0.5080	0.6	0.658	2755.8	17.4	2
33.1	22	15	0.71	0.24	13.6670	1.2	0.5248	1.0	0.861	2732.3	16.7	0
34.1	22	26	1.21	0.21	13.5694	1.0	0.5202	0.7	0.672	2735.1	20.6	1
35.1	19	16	0.86	0.58	11.6072	2.6	0.4494	1.1	0.412	2718.7	65.3	7
36.1	32	31	0.99	0.57	13.2420	1.0	0.5100	0.6	0.536	2727.4	24.0	1
37.1	11	12	1.11	0.32	13.8377	1.8	0.5233	1.0	0.593	2757.6	39.3	1
38.1	13	15	1.09	0.34	13.1717	1.2	0.5168	0.7	0.572	2696.9	25.9	0
39.1	31	33	1.08	0.17	13.4024	0.5	0.5159	0.4	0.676	2728.2	10.8	1

Pb_c: common Pb corrected using measured ^{204}Pb.

In general, the zircon grains from these granitoids are colorless and transparent to dark brown or pink, euhedral to subhedral, long to shortly elongated with length varying from 150 to 300 μm, and an aspect ratio that ranges from 2 to 3. Backscattered electrons (BSE) images of zircon grains (Figure 13) reveal a regular oscillatory zoning, common but not systematic. Fractures are common and metamict portions are very restrict. Most grains contain small inclusions of opaque minerals and apatite. Moreover, they do not present inherited cores.

The SHRIMP analytical results in the sample BDE 19-B (Figure 14a) display that eleven spot analyses in different zircon grains gave an average $^{207}Pb/^{206}Pb$ age of 2744.1±5.5 Ma (MSWD = 0.15), whereas the four concordant spots yielded a Concordia age of 2744±11 Ma (MSWD = 1.6). In the sample AL 62-D (Figure 14b) eleven analyses define a Discordia with an upper intercept age of 2755±15 Ma (MSWD = 2.1), which is consistent with the

$^{207}Pb/^{206}Pb$ weighted average age of 2745.3±7.1 Ma (MSWD = 0.16) from eight concordant analyses. Sixteen spot analyses were obtained on zircon grains from the sample BVD 42-C, which defined an upper intercept age of 2745.9±4.8 Ma (MSWD = 1.3), and twelve concordant analyses yielded a Concordia age of 2745.8±9.9 Ma (MSWD = 0.0071; Figure 14c). A total of thirteen spot analyses were acquired in the sample BVD 12-B, carried out by the U-Pb LA-MC-ICP-MS method, which yielded an upper intercept age of 2738.8±7.9 Ma (MSWD = 0.64), and five concordant analyses defined a Concordia age of 2734.5±9 Ma (MSWD = 1.8; Figure 14d). All Th/U ratios are >0.1 and indicate magmatic origin. The ages presented above display a homogeneous pattern, about 2.75–2.73 Ga, and are interpreted as crystallization age.

7.2. Sm-Nd whole-rock isotope

Samarium-neodymium isotopic compositions were determined for nine samples, which comprise the different varieties of the granitoids from Vila União area. Full details regarding analytical procedures are given in the section 4.3. Sm-Nd data are listed in Table 6 and plotted in Figure 15. All samples display very close values, which $^{147}Sm/^{144}Nd$ ratios vary from 0.09627 to 0.11811. The initial εNd(t) values range between –1.69 and 0.72, and T_{DM} from 3.09 to 2.86 Ga. In spite of the similarities between them, we can realize the biggest εNd(t) values showed by the quartz dioritic samples, ranging from –0.51 to 0.72. Although this is a gentle difference, it could represent the mafic magma (end-member) without or, more likely, with low crustal contamination.

7.3. Lu-Hf zircon isotope

Hf-isotope data from zircon grains from four granitoids samples are presented in Table 7 and plotted in Figure 16, and reveal huge similarities between them. Thirteen zircon grains from the leucogranitic sample (BDE 19-B) show initial Hf isotopes ranging from 0.280912 and 0.280957, negative εHf(t) values of –3.8 to –2.2, and two-stage model ages (T_{DM2}) varying from 3.31 to 3.41 Ga. Twelve zircon grains from the sample AL 62-D (biotite-hornblende monzogranite) display a small range in initial $^{176}Hf/^{177}Hf$ ratios, ranging from 0.280931 to 0.280967. The εHf(t) values vary between –3.1 and –1.8 and T_{DM2} from 3.29 to 3.37 Ga. In the sample BVD 42-C (biotite-hornblende tonalite), analyses in sixteen zircon grains yielded negative εHf(t) values, from –4.4 to –2.5, T_{DM2} varying from 3.33 to 3.45 Ga, and initial $^{176}Hf/^{177}Hf$ ratios ranging between 0.280895 and 0.280948. Sixteen zircon grains from the quartz dioritic sample (BVD 12-B) present initial Hf isotopes ranging from 0.280895 to 0.280951, negative εHf(t) values of –4.6 to –2.6 and T_{DM2} of 3.33 to 3.46 Ga.

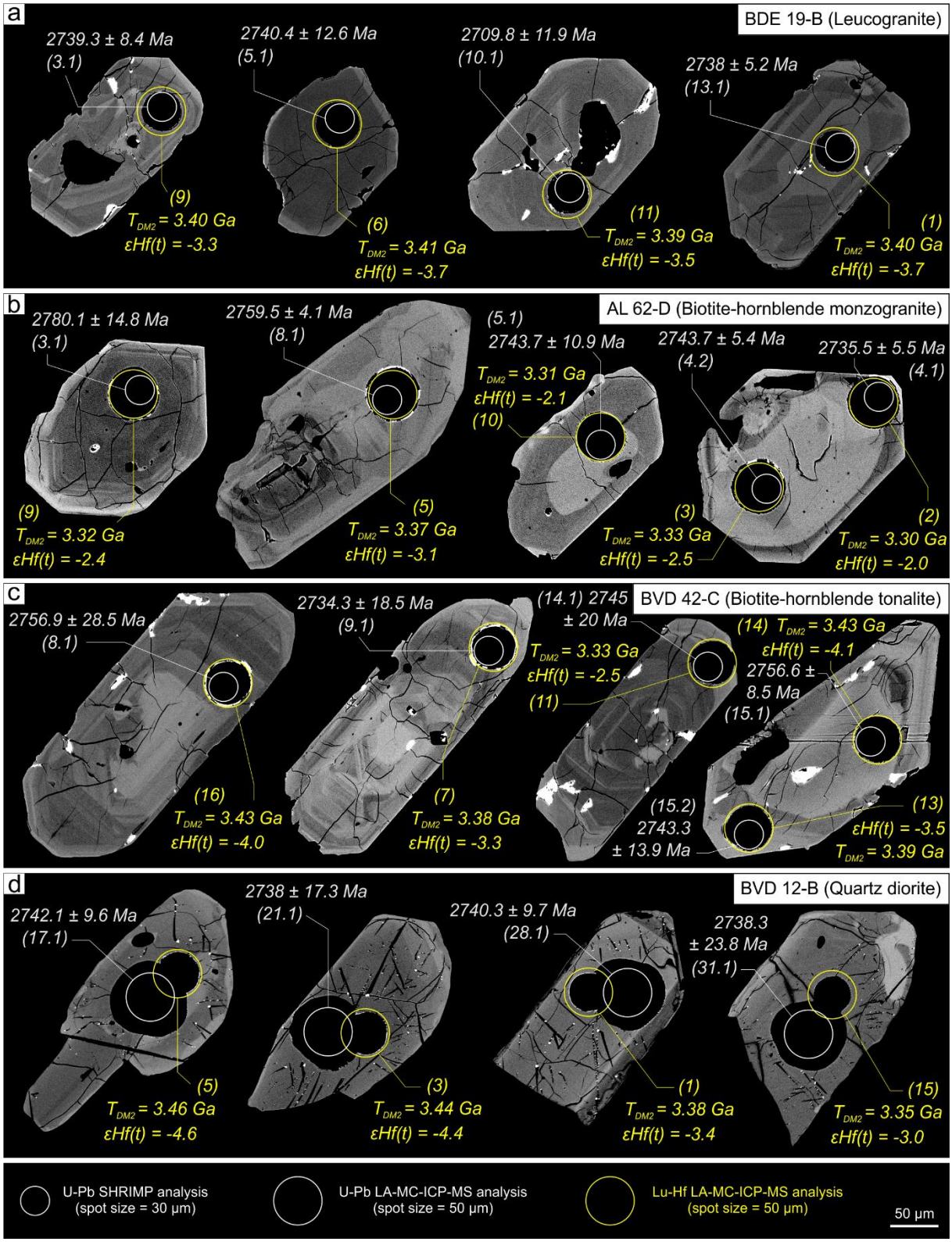

Figure 13. BSE images of representative zircon grains of the granitoids from Vila União area, with their respective *in situ* U-Pb ($^{207}Pb/^{206}Pb$ ages; white values) and Lu-Hf (εHf and T_{DM2}; yellow values) data. The numbers in parentheses correspond to the analyzed spot. The circles and their respective colors (see the legend) indicate the spot location.

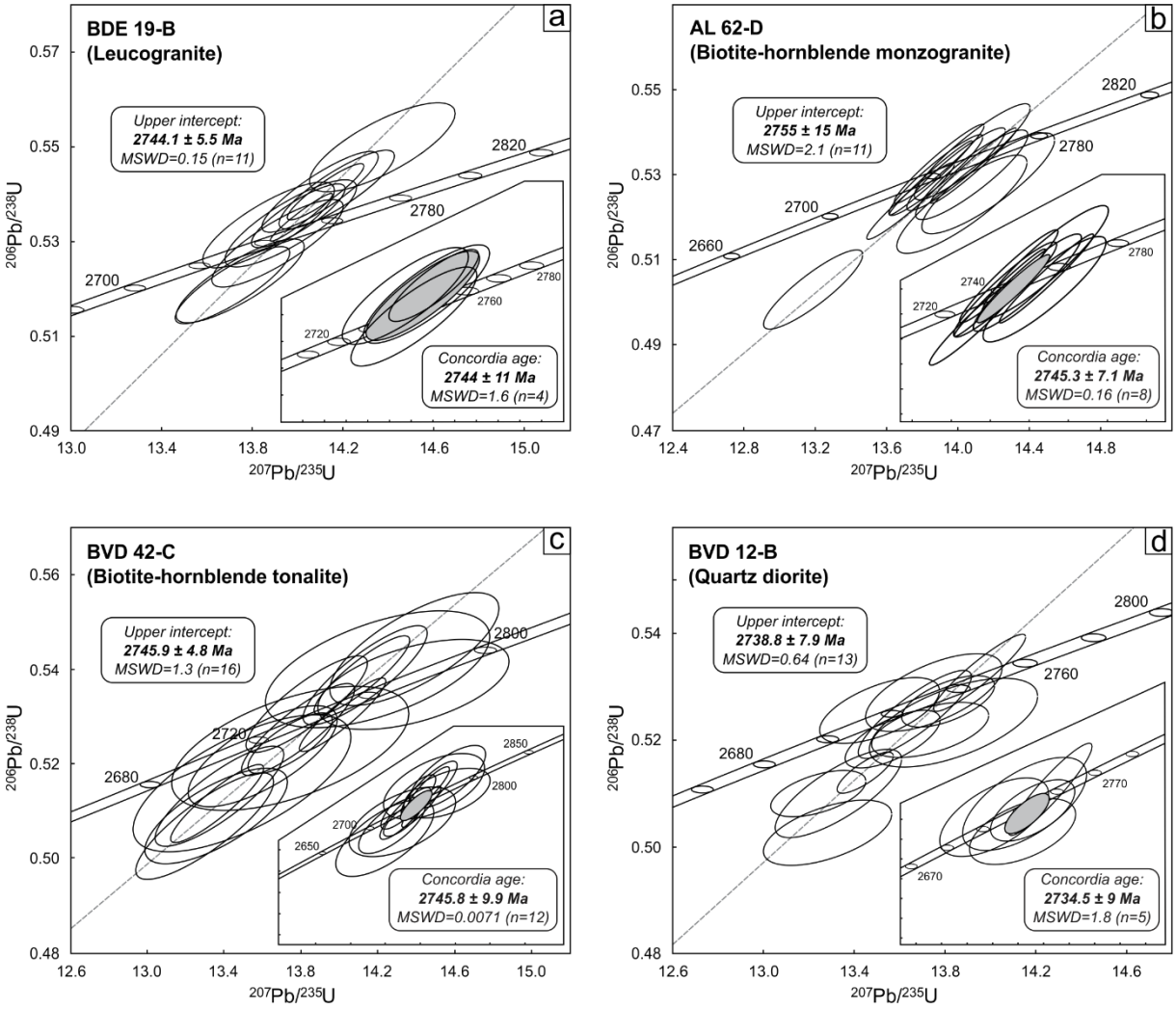

Figure 14. U-Pb concordia plots of the granitoids from Vila União area. Plots (a), (b) and (c) show results of SHRIMP U-Pb analyses, and plot (d) shows results of LA-MC-ICP-MS U-Pb analysis.

Table 6. Whole-rock Sm-Nd isotopic data for the granitoids from Vila União area.

Sample	Sm (ppm)	Nd (ppm)	$^{147}Sm/^{144}Nd$	2σ	$^{143}Nd/^{144}Nd$	2σ	$f_{(Sm/Nd)}$	t (Ma)	εNd(t)	T_{DM} (Ga)
Leucogranite										
BDE 19-B	6.49	38.16	0.10281	0.001386	0.51089	0.000013	-0.477	2744.0	-0.92	2.99
BVD 42-B	11.36	58.17	0.11811	0.000270	0.51115	0.000004	-0.400	2744.0	-1.31	3.06
Biotite-hornblende monzogranite										
BVD 15	6.39	34.47	0.11209	0.000170	0.51105	0.000007	-0.430	2745.3	-1.16	3.03
BVD 21	5.58	33.87	0.09962	0.000152	0.51080	0.000007	-0.494	2745.3	-1.62	3.04
BVD 42-H	8.05	45.10	0.10798	0.000125	0.51099	0.000004	-0.451	2745.3	-0.90	3.00
BVD 44	7.40	46.45	0.09627	0.000273	0.51079	0.000005	-0.511	2745.3	-0.54	2.95
Biotite-hornblende tonalite										
BVD 42-C	11.21	59.24	0.11440	0.000432	0.51106	0.000005	-0.418	2745.8	-1.69	3.09
Quartz diorite										
BVD 12-B	11.30	64.92	0.10521	0.000354	0.51096	0.000004	-0.465	2734.5	-0.51	2.96
BDE 38	8.89	51.77	0.10378	0.000313	0.51100	0.000006	-0.472	2734.5	0.72	2.86

T_{DM} and εNd(t) were calculated relative to CHUR and Depleted Mantle (DM) with present-day values of $^{143}Nd/^{144}Nd$ = 0.512638 and $^{147}Sm/^{144}Nd$ = 0.1967, following De Paolo and Wasserburg (1976) and De Paolo (1981) models, respectively, for Nd isotopic evolution of depleted mantle.

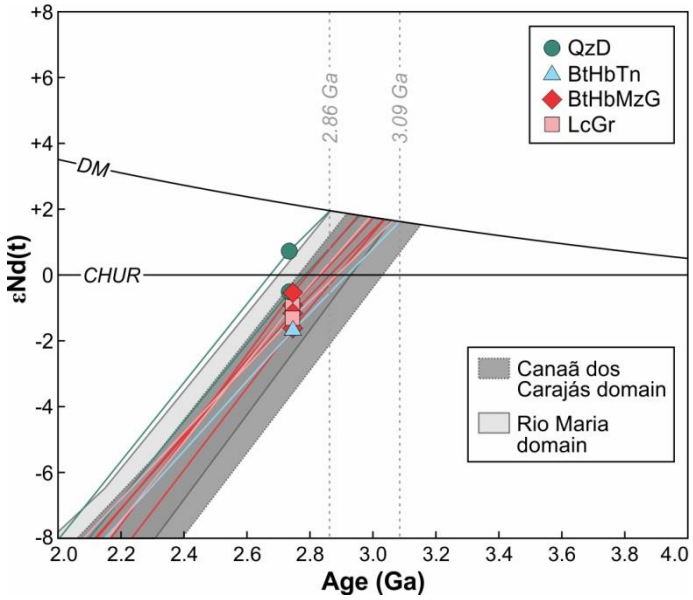

Figure 15. Plot of time *vs.* εNd values for the granitoids from Vila União area (dataset in Table 6). Abbreviations: QzD (quartz diorite), BtHbTn (biotite-hornblende tonalite), BtHbMzG (biotite-hornblende monzogranites) and LcGr (leucogranite).

8. Discussions

8.1. Petrogenetic processes

8.1.1. Introduction

Field, Petrographic and geochemical data clearly suggest that mingling (mixing) of felsic and mafic magmas in a deep plutonic environment is, at least in part, a suitable process involved in the origin of the Vila União granitoids, as showed in the section 3. Although this process has important participation in the formation of the studied rocks, it is worthwhile to make some considerations about other processes involved in the genesis of granite magmas. Partial melting from a single source was tested by Feio et al. (2012) in the Neoarchean plutons of the Planalto suite, which is composed strictly by syeno- and monzogranite, and shows textural and compositional affinities with those related to the more evolved varieties of the Vila União plutons (Oliveira et al., 2018; Marangoanha et al., unpublished results). These authors have stated that the granites from Planalto suite were derived by partial melting from a noritic source that could explain the generation of a magma with homogeneous composition and restrict SiO_2 contents (70.39–75.62 wt.%). Although a single mafic source is appropriate to explain the origin of the Planalto suite, it does not appear to be valid as the main process involved in the genesis of the Vila União granitoids. These plutons are formed by a wide variety of rocks whose mineralogical and chemical compositions do not admit a single process or source to clarify the origin of whole magma chamber (SiO_2 varying from 55.30 to 75.60 wt.%).

Table 7. LA-MC-ICP-MS Lu-Hf isotopic data of zircon grains for the granitoids from Vila União area.

Spot	$^{176}Yb/^{177}Hf$[a]	2σ	$^{176}Lu/^{177}Hf$[a]	2σ	$^{178}Hf/^{177}Hf$	$^{180}Hf/^{177}Hf$	SigHf[b]	$^{176}Hf/^{177}Hf$	2σ[c]	$^{176}Hf/^{177}Hf(t)$[d]	εHf(t)[d]	2σ[c]	T_{DM2}[e] (Ga)	Age[f] (Ma)	2σ
BDE 19-B (Leucogranite)															
1	0.0253	22	0.00094	6	1.46723	1.88675	10	0.280966	17	0.280916	-3.7	0.8285	3.40	2744	11
2	0.0156	14	0.00058	4	1.46721	1.88686	9	0.280942	18	0.280912	-3.8	0.8122	3.41	2744	11
3	0.0106	9	0.00042	3	1.46718	1.88673	9	0.280956	18	0.280935	-3.0	0.8048	3.36	2744	11
4	0.0192	26	0.00074	9	1.46720	1.88673	13	0.280950	18	0.280912	-3.8	0.8421	3.41	2744	11
5	0.0134	11	0.00051	3	1.46718	1.88681	9	0.280980	20	0.280953	-2.4	0.8074	3.32	2744	11
6	0.0122	11	0.00046	3	1.46722	1.88692	9	0.280938	19	0.280914	-3.7	0.8072	3.41	2744	11
7	0.0305	25	0.00114	7	1.46725	1.88678	9	0.280986	19	0.280926	-3.3	0.8382	3.38	2744	11
8	0.0129	11	0.00051	3	1.46723	1.88692	10	0.280945	19	0.280918	-3.6	0.8066	3.40	2744	11
9	0.0122	11	0.00049	3	1.46718	1.88691	10	0.280952	16	0.280926	-3.3	0.8067	3.40	2744	11
10	0.0107	9	0.00042	3	1.46722	1.88679	10	0.280937	24	0.280915	-3.7	0.8043	3.40	2744	11
11	0.0136	12	0.00055	4	1.46721	1.88672	7	0.280949	19	0.280920	-3.5	0.8083	3.39	2744	11
12	0.0087	8	0.00034	3	1.46719	1.88685	9	0.280975	19	0.280957	-2.2	0.8037	3.31	2744	11
13	0.0141	21	0.00053	7	1.46717	1.88689	9	0.280959	19	0.280931	-3.1	0.8271	3.37	2744	11
AL 62-D (Biotite-hornblende monzogranite)															
1	0.0089	8	0.00034	3	1.46716	1.88686	18	0.280963	19	0.280945	-2.6	0.7156	3.34	2745.3	7.1
2	0.0185	17	0.00070	5	1.46723	1.88683	16	0.280999	24	0.280963	-2.0	0.7157	3.30	2745.3	7.1
3	0.0154	13	0.00058	4	1.46717	1.88671	16	0.280979	33	0.280948	-2.5	0.7156	3.33	2745.3	7.1
4	0.0649	53	0.00235	14	1.46717	1.88682	16	0.281086	28	0.280962	-2.0	0.7157	3.30	2745.3	7.1
5	0.0172	14	0.00064	4	1.46722	1.88680	22	0.280964	26	0.280931	-3.1	0.7156	3.37	2745.3	7.1
6	0.0085	7	0.00032	2	1.46716	1.88674	17	0.280969	29	0.280952	-2.3	0.7157	3.32	2745.3	7.1
7	0.0130	11	0.00049	3	1.46718	1.88688	17	0.280970	28	0.280944	-2.6	0.7156	3.34	2745.3	7.1
8	0.0140	11	0.00052	3	1.46723	1.88680	15	0.280988	35	0.280961	-2.0	0.7157	3.30	2745.3	7.1
9	0.0151	12	0.00056	3	1.46723	1.88685	16	0.280981	24	0.280952	-2.4	0.7157	3.32	2745.3	7.1
10	0.0143	11	0.00053	3	1.46724	1.88677	15	0.280986	25	0.280958	-2.1	0.7157	3.31	2745.3	7.1
11	0.0144	12	0.00054	3	1.46723	1.88685	19	0.280995	44	0.280967	-1.8	0.7157	3.29	2745.3	7.1
12	0.0153	12	0.00057	3	1.46716	1.88684	15	0.280984	28	0.280954	-2.3	0.7157	3.32	2745.3	7.1
BVD 42-C (Biotite-hornblende tonalite)															
1	0.0184	15	0.00069	4	1.46723	1.88684	10	0.280965	24	0.280928	-3.2	0.8137	3.37	2745.8	9.9
2	0.0073	6	0.00029	2	1.46724	1.88682	11	0.280936	23	0.280921	-3.4	0.8018	3.39	2745.8	9.9
3	0.0077	8	0.00030	3	1.46724	1.88681	12	0.280947	22	0.280931	-3.1	0.8035	3.37	2745.8	9.9
4	0.0368	34	0.00140	10	1.46720	1.88684	9	0.280969	19	0.280895	-4.4	0.8677	3.45	2745.8	9.9
5	0.0091	7	0.00036	2	1.46720	1.88682	11	0.280953	24	0.280934	-3.0	0.8030	3.36	2745.8	9.9
6	0.0112	9	0.00044	3	1.46717	1.88668	10	0.280946	19	0.280922	-3.4	0.8046	3.39	2745.8	9.9
7	0.0110	9	0.00043	3	1.46718	1.88684	11	0.280948	20	0.280925	-3.3	0.8045	3.38	2745.8	9.9
8	0.0094	8	0.00037	2	1.46721	1.88678	10	0.280954	22	0.280934	-3.0	0.8032	3.36	2745.8	9.9
9	0.0173	14	0.00066	4	1.46720	1.88687	12	0.280947	21	0.280913	-3.7	0.8115	3.41	2745.8	9.9
10	0.0101	8	0.00039	2	1.46717	1.88685	10	0.280952	27	0.280931	-3.1	0.8037	3.37	2745.8	9.9
11	0.0078	6	0.00032	2	1.46723	1.88677	12	0.280965	19	0.280948	-2.5	0.8021	3.33	2745.8	9.9
12	0.0079	6	0.00032	2	1.46720	1.88695	9	0.280935	19	0.280918	-3.5	0.8022	3.40	2745.8	9.9
13	0.0115	9	0.00047	3	1.46718	1.88673	12	0.280945	23	0.280920	-3.5	0.8049	3.39	2745.8	9.9
14	0.0493	40	0.00180	11	1.46721	1.88679	10	0.280997	21	0.280903	-4.1	0.8926	3.43	2745.8	9.9
15	0.0141	11	0.00054	3	1.46720	1.88690	11	0.280959	20	0.280930	-3.1	0.8076	3.37	2745.8	9.9
16	0.0115	13	0.00044	4	1.46720	1.88688	11	0.280927	22	0.280904	-4.0	0.8095	3.43	2745.8	9.9
BVD 12-B (Quartz diorite)															
1	0.0200	18	0.00075	5	1.46718	1.88676	11	0.280970	18	0.280931	-3.4	0.8187	3.38	2734.5	9
2	0.0117	9	0.00045	3	1.46715	1.88686	12	0.280932	17	0.280909	-4.1	0.8052	3.43	2734.5	9
3	0.0212	18	0.00077	5	1.46720	1.88677	9	0.280942	18	0.280901	-4.4	0.8202	3.44	2734.5	9
4	0.0109	9	0.00042	3	1.46719	1.88669	10	0.280958	19	0.280937	-3.2	0.8047	3.36	2734.5	9
5	0.0152	14	0.00057	4	1.46724	1.88686	9	0.280925	21	0.280895	-4.6	0.8119	3.46	2734.5	9
6	0.0189	16	0.00070	5	1.46722	1.88681	11	0.280954	20	0.280917	-3.8	0.8150	3.41	2734.5	9
7	0.0220	22	0.00085	7	1.46721	1.88688	12	0.280943	18	0.280899	-4.5	0.8299	3.45	2734.5	9
8	0.0212	17	0.00077	5	1.46722	1.88669	9	0.280964	20	0.280924	-3.6	0.8183	3.39	2734.5	9
9	0.0133	11	0.00051	3	1.46718	1.88658	7	0.280932	17	0.280906	-4.2	0.8073	3.43	2734.5	9
10	0.0188	18	0.00069	6	1.46723	1.88681	10	0.280955	13	0.280918	-3.8	0.8204	3.40	2734.5	9
11	0.0154	13	0.00058	4	1.46713	1.88670	9	0.280982	17	0.280951	-2.6	0.8106	3.33	2734.5	9
12	0.0099	8	0.00039	2	1.46721	1.88665	10	0.280934	20	0.280914	-4.0	0.8036	3.41	2734.5	9
13	0.0234	19	0.00087	5	1.46719	1.88697	12	0.280951	16	0.280905	-4.3	0.8213	3.43	2734.5	9
14	0.0069	6	0.00029	2	1.46718	1.88694	14	0.280939	20	0.280924	-3.6	0.8015	3.39	2734.5	9
15	0.0180	14	0.00067	4	1.46718	1.88680	9	0.280977	26	0.280942	-3.0	0.8125	3.35	2734.5	9
16	0.0139	11	0.00055	3	1.46722	1.88693	10	0.280941	26	0.280912	-4.0	0.8073	3.42	2734.5	9

[a] $^{176}Yb/^{177}Hf = (^{176}Yb/^{173}Yb)_{true} \times (^{173}Yb/^{177}Hf)_{measured} \times (M_{173(Yb)}/M_{177(Hf)})^{\beta(Hf)}$, $\beta(Hf) = \ln(^{179}Hf/^{177}Hf_{true}/^{179}Hf/^{177}Hf_{measured})/\ln(M_{179(Hf)}/M_{177(Hf)})$, M = mass of respective isotope. The $^{176}Lu/^{177}Hf$ were calculated in a similar way by using the $^{175}Lu/^{177}Hf$ and β(Yb).

[b] Mean Hf signal in volt.

[c] Uncertainties are quadratic additions of the within-run precision and the daily reproducibility of the 40 ppb-JMC475 solution. Uncertainties for the JMC475 quoted at 2σ (2 standard deviation).

[d] Initial $^{176}Hf/^{177}Hf$ and εHf calculated using the Concordia age determined by SHRIMP and LA-ICP-MS dating (see column f), and the CHUR parameters: $^{176}Lu/^{177}Hf$ = 0.0336 and $^{176}Hf/^{177}Hf$ = 0.282785 (Bouvier et al., 2008).

[e] Two-stage model age in billion years using the measured $^{176}Lu/^{177}Hf$ of each spot (first stage = age of zircon), a value of 0.015 (Griffin et al., 2002) for the average continental crust (second stage), and average MORB (DM) $^{176}Lu/^{177}Hf$ and $^{176}Hf/^{177}Hf$ of 0.0388 and 0.283250 (Andersen et al., 2009), respectively.

[f] Concordia ages from tables 4 and 5.

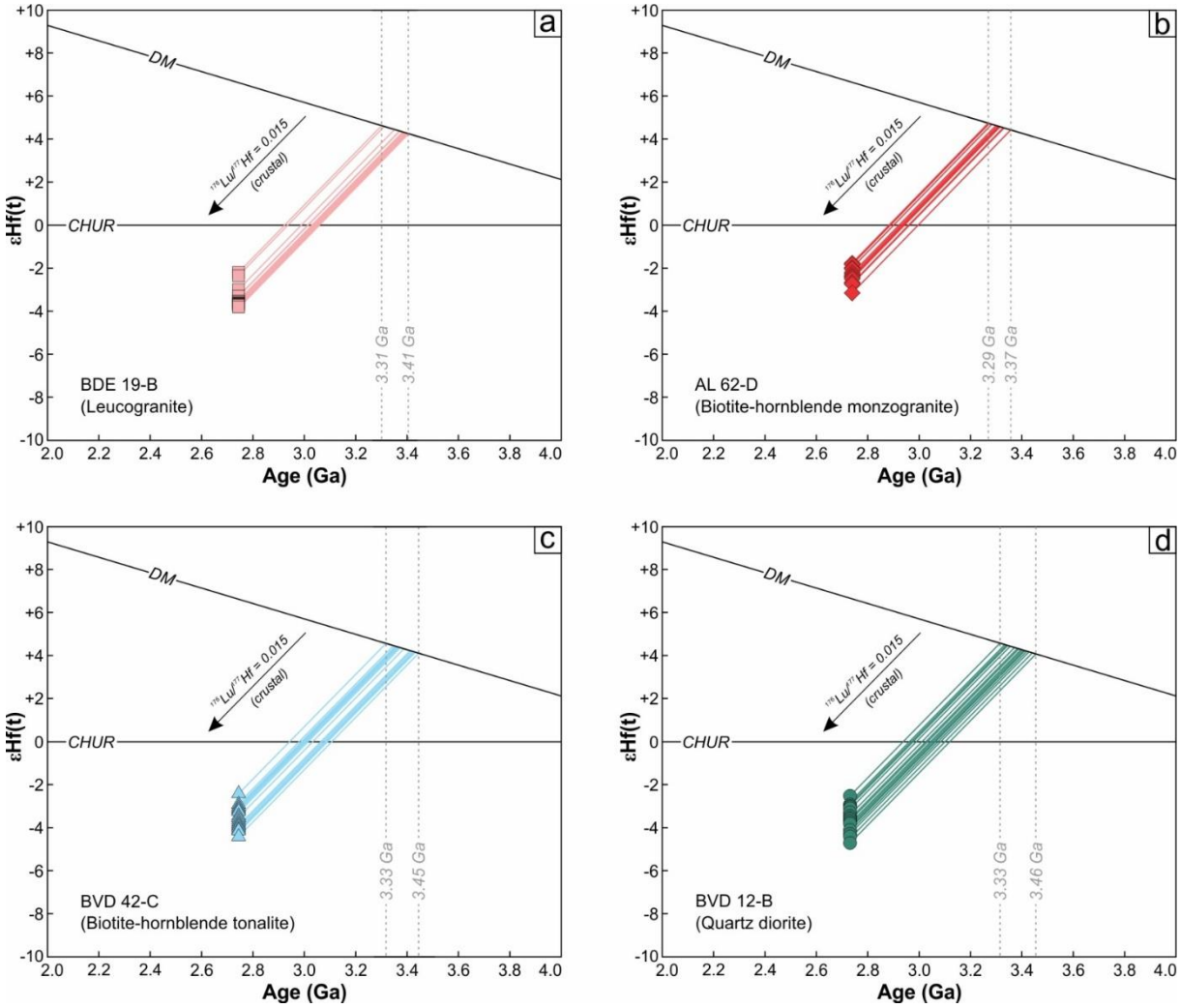

Figure 16. Plots of time *vs.* εHf values for the granitoids from Vila União area (dataset in Table 7).

Similarly, fractional crystallization seems to be an unlikely process responsible to have commanded the wide compositional variation identified in these granitoids. The discrete or null performance of this process can be indicated by the fact that the hornblende contents always prevail over those of biotite (see Table 2). In a fractional crystallization process would be expected that, in the more evolved varieties, biotite/hornblende ratios >1 and, consequently, in the less evolved ones, this ratios < 1. In the Vila União granitoids that ratio remains <1 in almost all samples.

8.1.2. Partial melting related to both mafic and felsic end-members

As stated above, the proposed petrogenetic model to generate the Neoarchean granitoids from Vila União area involves, initially, partial melting of two different sources to produce independent both felsic and mafic magmas, which define the two end-members. Therefore, in order to investigate and establish the parameters involved in these processes, the major elements mass balance calculations were performed using the software GENESIS 4.0

(Teixeira, 2005), which consists in adjusting the relative proportions of residual minerals (or whole-rock) from the source to reproduce the composition of the expected melt. The quality of the calculated data is reliable if the sum of the square residuals ($\sum R^2$) ≤1.2 (Wyers and Barton, 1986), and allows us to proceed to trace elements modeling, using Excel sheets created by the authors, which was based on the equilibrium partial melting equation (Wilson, 1989; Equation 1):

$$\frac{C_L}{C_0} = \frac{1}{F + D - FD} \quad (1)$$

where C_L and C_0 are the trace element concentrations in the melt (liquid) and in the source (solid), respectively, F is the weight fraction of melt formed and D is the bulk distribution coefficient for the residual solids at the moment when melt is removed from the system. The mineral/liquid partition coefficients (Kd) used in the modeling were obtained from Rollinson (1993) and the online database https://earthref.org/KDD/.

According to the evidences listed in the section 3 about the genesis of the studied granitoids, besides those in the literature about mafic rocks (Yoder and Tilley, 1962; Green and Ringwood, 1967; Kushiro, 1968; O'Hara, 1968; Stolper, 1980), partial melting is the more plausible process responsible for generate the mafic end-member. We have considered a generic model represented by partial melting of a depleted mantle (spinel lherzolite) to produce a diorite, and leaving a harzburgitic rock as residue. To test this model, the sample with the lowest silica content of the quartz dioritic variety, BVD 42-F, was assumed as the representative of the initial liquid produced by partial melting of a source represented by a spinel lherzolite from McDonough (1990). The results are presented in Table 8 and show that the major element compositions of the liquid gave excellent fits ($\sum R^2$ = 0.737) with a proportion melt:residue ratio of 8% to 92%, the latter represented by a harzburgite from Perkins and Anthony (2011; sample KH 25), consisting of olivine (75%), orthopyroxene (16%), clinopyroxene (8%) and spinel (1%). Thus, these same proportions of melt and residual mineral phases were tested in the trace elements modeling (Figure 17a), which also provided an excellent fit between the calculated melt (generated by partial melting from spinel lherzolite) and the representative mafic sample (BVD 42-F).

Table 8. Modeling major and trace elements compositions and residual mineral assemblages for generation of the mafic end-member by partial melting of spinel lherzolite.

	Source (C_0)[a]	Residue (C_S)[b]	Calculated	BVD 42-F
	Spinel lherzolite	Harzburgite	magma (C_L)	Diorite
Major elements (weight %) [c]				
SiO_2	44.14	43.04	54.84	54.65
TiO_2	0.09	0.08	1.09	1.17
Al_2O_3	2.28	1.80	14.50	15.07
Fe_2O_3*	9.38	8.78	11.77	11.37
MnO	0.14	0.12	0.19	0.17
MgO	41.52	44.72	4.86	4.94
CaO	2.16	1.30	7.63	7.24
Na_2O	0.24	0.14	4.06	4.28
K_2O	0.05	0.02	1.06	1.11
Trace elements (ppm)				
Ba	33		412.21	592
Rb	1.9		22.12	21.9
Sr	49		350.22	353
Y	4.4		21.87	20.7
Zr	21		155.95	147
Nb	4.8		14.10	7.5
La	2.6		30.60	31.7
Ce	6.29		58.46	59.4
Nd	2.67		25.31	25.6
Sm	0.47		4.61	4.83
Eu	0.16		1.29	1.34
Gd	0.6		3.97	4.09
Yb	0.26		2.15	2.15
Lu	0.043		0.298	0.310
Residual minerals (volume %) [b]				
Olivine		75		
Orthopyroxene		16		
Clinopyroxene		8		
Spinel		1		
$\sum R^2$		0.737		
Melt fraction (F)		8%		

[a] Values from McDonough (1990).

[b] Values from sample KH 25 (Perkins and Anthony, 2011).

[c] Original oxide values recast to 100%.

$\sum R^2$ = Sum of the squared residuals.

All iron is reported as Fe_2O_3.

Modelling of the felsic end-member, represented by the leucogranitic variety, was performed using the sample with the highest silica content (BVD 31), as the representative initial liquids. As already widespread in the literature, granitic melts could be produced by partial melting of TTG rocks – or metatonalites – (Rutter and Wyllie, 1988; Skjerlie and Johnston, 1992; Singh and Johannes, 1996; Gardien et al., 1995, 2000; Patiño Douce, 2005). In this context, it is worth noting that the area dominated by Neoarchean granites is surrounding by numerous occurrences of Na-granitoids akin to TTG rocks (see Figure 2). Considering the crustal level in which partial melting could occur, a sample representing the

composition of the middle crust was chosen as the probable source of such granites. Thus, the sample BVD 40 (Mesoarchean felsic granulite) was tested as source of the leucogranitic end-member from Vila União area. The best fit model for major elements was obtained with 5% of partial melting ($\sum R^2$ = 0.668; Table 9) and leaving a residue composed of plagioclase (68.83%), quartz (23.50%), biotite (6.31%), magnetite (1.10%) and orthopyroxene (0.26%). In terms of trace elements, the modeling yielded excellent result, as displayed in the Figure 17b, which shows a good fit between the calculated magma and the leucogranitic compositions.

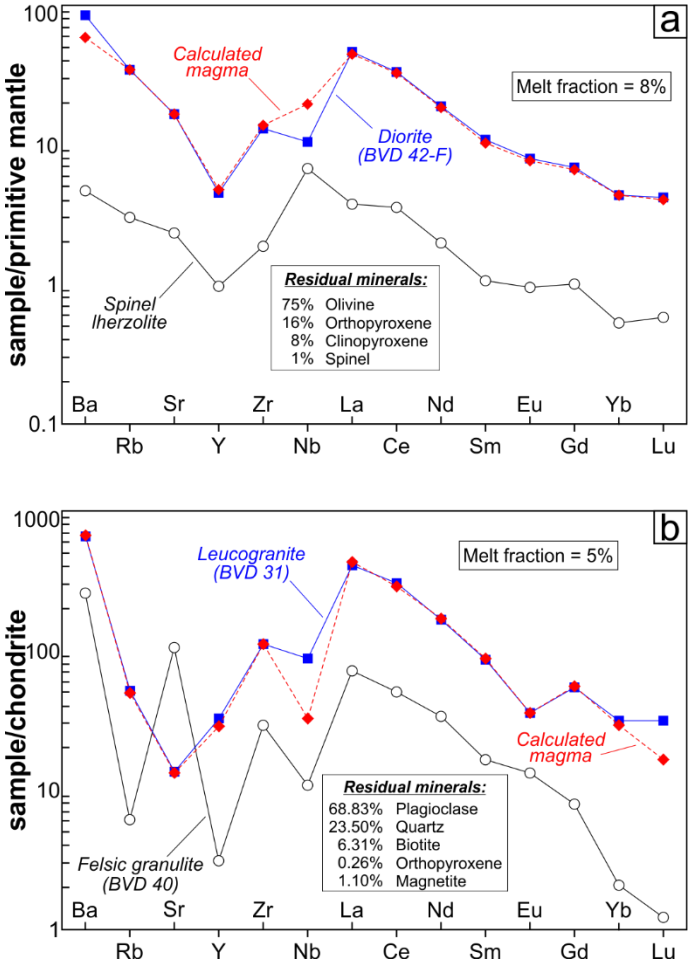

Figure 17. Trace elements models for generation of the (a) mafic and (b) felsic end-members by partial melting of spinel lherzolite and felsic granulite, respectively. Primitive mantle (PM) and chondrite (C1) normalization values are from Sun and McDonough (1989) and McDonough and Sun (1995), respectively.

8.1.3. Magma mixing related to granitoids from Vila União area

The mixing model was performed by using PETROMODELER (Ersoy, 2013), a Microsoft Excel spreadsheet program that models magmatic processes, including mixing, based on major and trace elements. This program consists in plot, firstly, two compositions in a binary diagram that would represent the mafic and felsic end-members, which are united by

a line called ‘mixing curve’ (generally a hyperbola-shaped curve), and spaced at 10% increments. Any point along the mixing curve would represent a hypothetic composition that is defined according to their respective position on the curve between the two end-members (for example, to a determined point, the felsic contribution in the mixing system is major as closer to felsic end-member on the hyperbola). Therefore, the geochemical analyses plotted on these diagrams will indicate their behavior in the mixing system. In other words, these diagrams will measure the contribution of each end-member in the mixing process to generate the hybrid granitoids.

Table 9. Modeling major and trace elements compositions and residual mineral assemblages for generation of the felsic end-member by partial melting of Mesoarchean felsic granulite.

	BVD 40 (C_0)[a]	Residue (C_S)	Composition of minerals					Calculated	BVD 31
	Felsic granulite[b]	Bulk	Pl[c]	Qz[d]	Bt[c]	Opx[c]	Mt[e]	magma (C_L)	Leucogranite[b]
			68.83%	23.50%	6.31%	0.26%	1.10%		
Major elements (weight %)									
SiO_2	69.68	69.40	63.02	100.00	37.78	51.80	0.00	76.29	76.39
TiO_2	0.29	0.39	0.09	0.00	5.12	0.00	0.00	0.21	0.30
Al_2O_3	16.58	17.09	23.56	0.00	13.86	0.52	0.00	11.45	11.67
FeO*	2.30	2.36	0.00	0.00	19.03	23.56	100.00	2.88	2.98
MnO	0.03	0.01	0.00	0.00	0.18	1.15	0.00	0.05	0.04
MgO	0.79	0.95	0.00	0.00	14.04	22.50	0.00	0.08	0.20
CaO	3.88	3.27	4.75	0.00	0.00	0.45	0.00	1.87	1.15
Na_2O	5.26	5.62	8.17	0.00	0.00	0.00	0.00	2.65	2.87
K_2O	1.19	0.90	0.40	0.00	9.87	0.00	0.00	4.50	4.40
Trace elements (ppm)									
Ba	625							1607.01	1585
Rb	14							114.22	118.5
Sr	765							95.09	97
Y	4.90							44.63	50.9
Zr	111			$\sum R^2$				422.12	424
Nb	2.60			0.668				7.84	21.1
La	17.00			Melt fraction (F)				102.13	96.0
Ce	30.80			5%				177.04	185.0
Nd	15.30							76.80	75.8
Sm	2.43							12.83	12.60
Eu	0.75							2.00	2.01
Gd	1.58							10.98	10.85
Yb	0.33							4.71	5.07
Lu	0.030							0.408	0.770

[a] Bulk composition from Marangoanha et al. (unpublished results).
[b] Original oxide values recast to 100%.
[c] Mineral composition values from Marangoanha et al. (unpublished results).
[d] Hypothetical composition, admitted as 100 wt.% of SiO_2.
[e] Mineral composition values from Deer et al. (1963).
$\sum R^2$ = sum of the squared residuals.
All iron is reported as FeO.

Accordingly, the studied granitoids analyses were plotted on the SiO_2 versus Fe_2O_3*/K_2O, K_2O/P_2O_5, Rb/Sr and Ti/Nb diagrams (Figure 18), which we consider the samples BVD 42-F and BVD 31 the mafic and felsic end-members, respectively, as modeled

previously in the section 8.1.2. These diagrams show that the studied granitoids fall into or very close to the mixing curve and form a continuous compositional spectrum between two contrasting end-members. The observed hyperbolic mixing array suggests that each sample represents a hybrid product generated from the mix in variable proportions between a mafic mantle-derived component (diorite) and a felsic crustal-derived one (leucogranite).

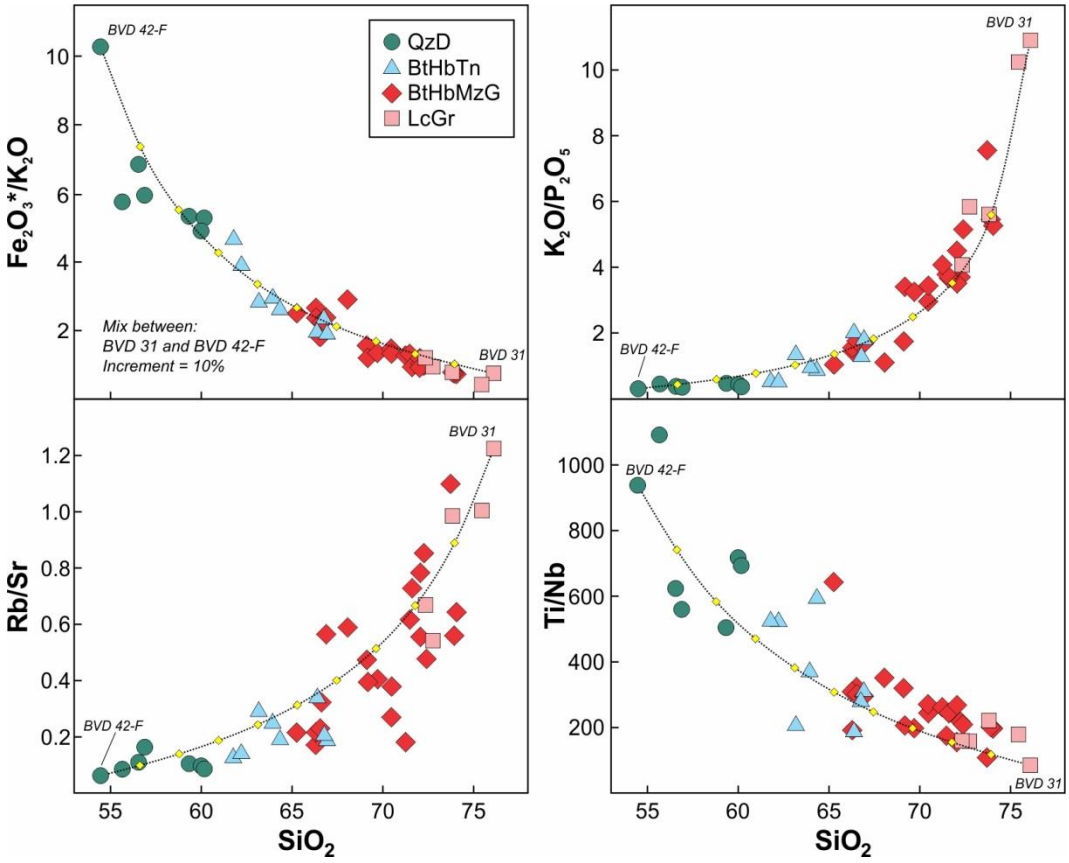

Figure 18. Major and trace elements *vs.* SiO_2 diagrams. Binary mixing curve (dotted line) between felsic and mafic end-members (BVD 31 and BVD 42-F, respectively), with 10% increments (yellow diamonds). The studied granitoids are plotted along the hyperbola. Abbreviations: QzD (quartz diorite), BtHbTn (biotite-hornblende tonalite), BtHbMzG (biotite-hornblende monzogranites) and LcGr (leucogranite).

In order to ratify the binary mixing process, we have also tested the REE modelling, based on the geochemical mass balance calculation (Rollinson, 1993) in equation (2):

$$C_M = X_A . C_A + X_B . C_B \quad (2)$$

where the poles A and B represent felsic and mafic end-members, respectively; C_M, C_A and C_B are the concentration of one element in the mixture, poles A and B, respectively; X_A and X_B are the weight fraction of A and B in the mixture, respectively, and $X_B = (1 - X_A)$. We have chosen the samples BVD 57 and BVD 42-F to represent the felsic and mafic end-members in the mixture, respectively, due to they show the more and less REE-enriched

patterns, respectively. We have also taken representative samples to represent each variety, as shown in Figure 19. According to the Figure 19a, the sample BDE 19-B (which represents the LcGr variety) is formed by a mix between 90% of the felsic and 10% of the mafic end-members. The BtHbMzG variety, represented by the sample BVD 47-H, shows a felsic:mafic end-members ratio of 60:40 (Figure 19b), while the sample BVD 47-E (BtHbTn variety) displays a ratio of 30:70 (Figure 19c). The less evolved variety, QzD, represented by the sample BVD 42-D, presents a mix between 10% of the felsic and 90% of the mafic end-members (Figure 19d). All these REE modelling have an excellent fit with the modelling in the Figure 18, and support the binary mixing hypothesis between two contrasting magmas responsible to generate the Neoarchean granitoids from Vila União area.

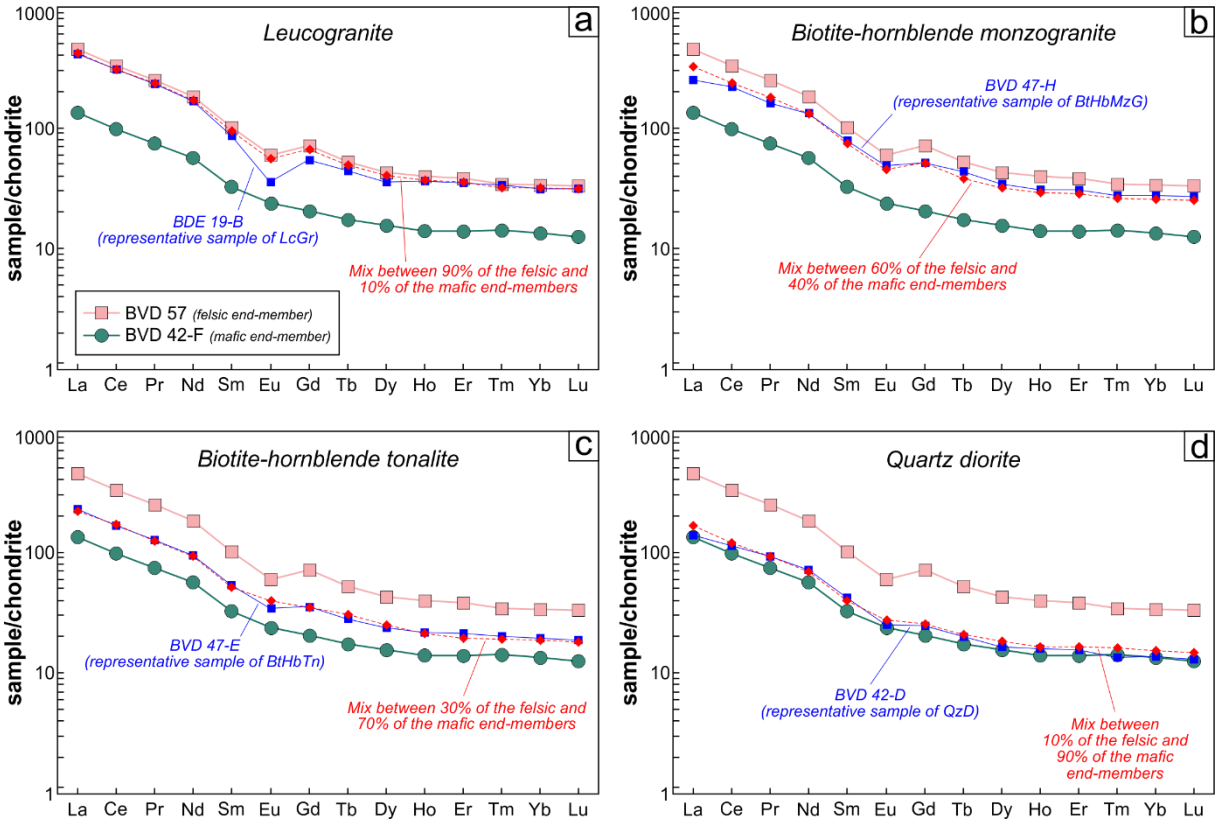

Figure 19. REE diagrams with concentration normalized to chondrite (C1) from McDonough and Sun (1995), showing the results of binary mixing models between felsic and mafic end-members (BVD 57 and BVD 42-F, respectively) in different proportion to generate the hybrid granitoids from Vila União area. Abbreviations: QzD (quartz diorite), BtHbTn (biotite-hornblende tonalite), BtHbMzG (biotite-hornblende monzogranites) and LcGr (leucogranite).

8.2. Implications of the isotopic signatures

One of the goals of this study is identify through isotopic data the hybridization process between both mafic and felsic end-members responsible to generate the Neoarchean granitoids from Vila União area. The Nd and Hf isotopic data in these rocks display some

peculiar features and can provide some different interpretations, which we consider to be crucial to draw a more precise geologic scenario related to the formation of these granitoids.

The Nd-isotopes data show that the LcGr, BtHbMzG and BtHbTn have very similar isotopic characteristics, with εNd(t) and T_{DM} values overlapped (ranging from –1.69 to –0.54, and from 3.09 to 2.95 Ga, respectively; cf. Table 6 and Figure 15), while the QzD variety – considered the mafic end-member in the mixing/mingling system studied – exhibits slightly high εNd(t) values, from –0.51 to 0.72, and T_{DM} from 2.96 to 2.86 Ga. It is expected that mafic magmas have εNd(t) values higher than felsic ones, as displayed in the studied rocks, although it is in a small order of magnitude (~2.4 epsilon units). But, we would also expect lower εNd(t) values to the felsic end-member (LcGr variety), as well as intermediate εNd(t) values – between $\varepsilon Nd(t)_{LcGr}$ and $\varepsilon Nd(t)_{QzD}$ – to the considered hybrid varieties (BtHbMzG and BtHbTn). However, it is quite common that Nd isotopic equilibrium is attained more rapidly than chemical equilibrium in the course of magma mixing/mingling (Lesher, 1990; Poli et al., 1996), which explains the overlapping between the LcGr (although this variety is composed by samples that represent the felsic end-member, we consider to have at least a minimum of mixing degree, as demonstrated in the sections 8.1.2 and 8.1.3) and the hybrid varieties (BtHbMzG and BtHbTn).

Concerning the zircon Hf isotopic data, all the varieties present isotopic signatures significantly similar between them, besides show homogeneous isotopic composition within each sample, as shown by the restricted variation in terms of initial $^{176}Hf/^{177}Hf$ ratios, εHf(t) and T_{DM2} (cf. Table 7 and Figure 16). The negative zircon εHf(t) values presented in all varieties (ranging from –4.6 to –1.8) suggest the involvement of an old crustal source. Moreover, the similarities in zircon Hf isotopic characteristics between mafic and felsic end-members (QzD and LcGr, respectively), besides their hybrid components (BtHbMzG and BtHbTn), require a more detailed explanation, mainly due to the felsic and mafic end-members were generated from two different sources, which we also would expect two different isotopic signatures. Thus, such similar Hf signatures between them could be explained by one of these processes: (i) the mafic and felsic magma sources had similar isotopic compositions, (ii) mafic and felsic granitoids reached isotopic equilibration during magma mixing/mingling, or (iii) zircon grains in the mafic and intermediaries rocks were transported from the host leucogranites during magma mixing. The geochemical modelling presented in the section 8.1.2 showed that partial melting of spinel lherzolite and enderbitic crust were responsible to generate both mafic and felsic magmas, respectively, which would be unlikely to think about these two different sources have the same Hf isotopic signature,

excluding the first situation. It is not so simple to reach isotopic equilibration in the zircon Hf isotopic system during mixing between felsic and mafic magmas. Zircon included in other mineral phases, mainly refractory ones, can be protected from isotopic re-equilibration in the mixed magma, which is plausible when two partially crystallized magmas are mixed (Bea, 1996; Zhang et al., 2016). Likewise, the high zircon Hf closure temperature (>1079 °C) indicates that Hf can remain isotopically closed during most thermal events (Cherniak et al., 1997; Wu et al., 2006; Hu et al., 2012). Therefore, the aforementioned arguments are significantly reasonable to not admit the zircon Hf isotopic re-equilibration in this case. Accordingly, if we admit that exists only one zircon population, with a well-defined Hf isotopic signature found in all varieties, it seems likely that occurred an effective interchange of zircon grains during the mixing process. The εHf(t) values from –4.6 to –1.8 recorded in the zircon grains point to a crustal source that, consequently, allow us to relate this isotopic signature to the LcGr magma. Therefore, these zircon grains could have been transferred from the felsic to the mafic magma during the mixing process. As the hybrid granitoids, and even the mafic microgranular enclaves (QzD variety), contain feldspar, quartz and other minerals that are considered to have originated from the LcGr (see section 3), it is likely that these zircons have a similar origin (Barbarin, 1990; Elburg, 1996). Thus, the "surviving" zircon grains incorporated into the mafic and hybrid granitoids retained the unmodified original Hf isotopic compositions from the leucogranitic magma (LcGr).

Based on the considerations on Nd and Hf isotopic data above raised, it is possible establish two significant constrains relative to the Neoarchean evolution in Vila União area:

(1) <u>The mafic end-member represents a juvenile component.</u> The Nd isotopic data do not reflect in fact a reliable conclusion about mafic end-member (neither felsic one) due to all analyzed samples represent a hybrid isotopic system between them. Nevertheless, we can extract an outstanding conclusion based on Sm-Nd data: even admitting the mafic samples being Nd-isotopically contaminated with crustal component, they show a slightly high εNd(t) and low T_{DM} (+0.72 epsilon units and 2.86 Ga, respectively), which means that their real T_{DM} (non-contaminated one) should have a lower value, probably a Neoarchean age (maybe the same as their crystallization age). If we consider this, it is possible conclude that the mafic magma (which represents the mafic end-member) was differentiated rapidly from its mantle source and had a very short residence in the crust. As well, the Sm-Nd data available really represent hybrid granitoids with different proportions of "juvenile + recycled components". As previously mentioned, the Hf

isotopic data represent the signature of the magmatic system related to the felsic end-member.

(2) The felsic end-member was derived from an old crustal source. Considering the zircon Hf isotopic data in all varieties as a non-contaminated isotopic data that reflect only the petrogenetic parameters from the felsic end-member, we conclude that this felsic magma represents pure crustal-derived component, with long crustal residence times, as recorded by the T_{DM2} ranging from 3.46 to 3.29 Ga.

8.2.1. Comparison with others Neoarchean granitoids from Carajás province

All isotopic data concerning Neoarchean granitoids in Carajás province are shown in Table 1, and only Canaã dos Carajás domain and Carajás basin record such information. It is important to highlight that practically all available parameters are related to Sm-Nd data, with only one Lu-Hf value. Therefore, the Neoarchean granitoids from Carajás province show a peculiar behavior: most of them have restricted negative εNd(t) values, ranging from –2.25 to –0.29, although rare wide values have been obtained (maximum of 0.30 and minimum of –4.11), and T_{DM} between 3.19 and 2.91 Ga (and a unique high T_{DM} value of 3.36 Ga). The authors have a consensus relating the homogeneous εNd(t) values to involvement/contamination of crustal source, even in the mafic rocks whose origin is related to partial melting of the peridotite mantle (Santos et al., 2013; Martins et al., 2017). The origin of the Neoarchean granitoids from Carajás province have been interpreted to most authors as partial melting of lower crust, composed by mafic granulite or intermediate meta-igneous rocks to generate the granites *stricto sensu* (Barros et al., 2009; Feio et al., 2012). The same Nd isotopic behavior shown by the Vila União granitoids, which is interpreted as a result of mixing between both mantle and crust-derived isotopic signatures, indicate a possible genesis common to other analogous plutons, not discarding the important participation of partial melting in their origins.

8.3. Integrated model of magmatic processes and geodynamic implications

Many authors have discussed about both the magma source and the tectonic regime related to the origin of Neoarchean granitoids from Carajás province. So far, there is a consensus on their genesis, which most of the authors (Barros et al., 2009; Feio et al., 2012; Cunha et al., 2016; Dall'Agnol et al., 2017) agree that they were generated by partial melting of a granulitic lower crust. Concerning tectonic regime, there are two hypothesis which explain the structural framework printed on these granites: (i) Barros et al. (2001, 2009), Feio et al. (2012), Cunha et al. (2016), Dall'Agnol et al. (2017) and Oliveira et al. (2018) state that

these granitoids were crystallized syn-tectonically, which imply that the opening and the subsequent inversion of the Carajás basin took place in a very short time span (between ~2.75–2.73 Ga); whereas (ii) Tavares (2015) proposes a pre-tectonic nature to them, and assumes that these granites were generated in an extensional regime, at 2.76–2.70 Ga, and after deformed and metamorphosed at 2.68–2.63 Ga.

Despite some similarities shared with the Neoarchean granitoids from Carajás province, the granitoids from Vila União area show particularities not discussed so far concerning Neoarchean magmatism in this province, especially with regard to the origin of their magmas. As demonstrated previously, it is believed that the studied granitoids were generated with the participation of hybridization processes from two contrasting magmas. The interactions between these two end-members (mafic and felsic ones) occurred in different degrees, resulting in a wide variety of rocks (cf. Figure 3) and compositions (mineralogical, geochemical and isotopic; cf. Figures 8–10 and Figure 15). The emplacement and construction of the Vila União plutons started during an extensional tectonic regime and, shortly afterward, the inversion of Carajás basin took place at a pure shear-dominated transpressional regime (justified by the E–W steeply inclined well-developed mylonitic foliation and steep-to-subvertically plunging mineral stretching lineation), which the magma crystallized under the latter tectonic regime condition, as evidenced by the microstructural features of syn-tectonic granitoids: presence of parallelism between magmatic and solid-state fabrics, and evidence of melt-present deformation.

According to the scenario described above, allied to the information available in the literature on Neoarchean granites of the Carajás province, a geodynamic model based on two stages is proposed to discuss the origin of the Neoarchean granitoids from Vila União area (Figure 20). This model involves, initially, mafic underplating in an N–S extensional tectonic regime (Figure 20a), which was responsible for generating the mantle-derived basic magma, which was injected in the lower and middle crusts. The heating generated by the intrusion of mafic magma induced the partial melting of middle crust (felsic granulite), producing felsic magma. The interaction between these two contrasting magmas occurs both by mixing – which this process took place in several degrees, as recorded by the wide range of granitoids – and by mingling, where the interaction between these two melts was incomplete or limited, most likely by their strong compositional contrasts, which was responsible for the development of MME, that could retain the identity of the mafic end-member.

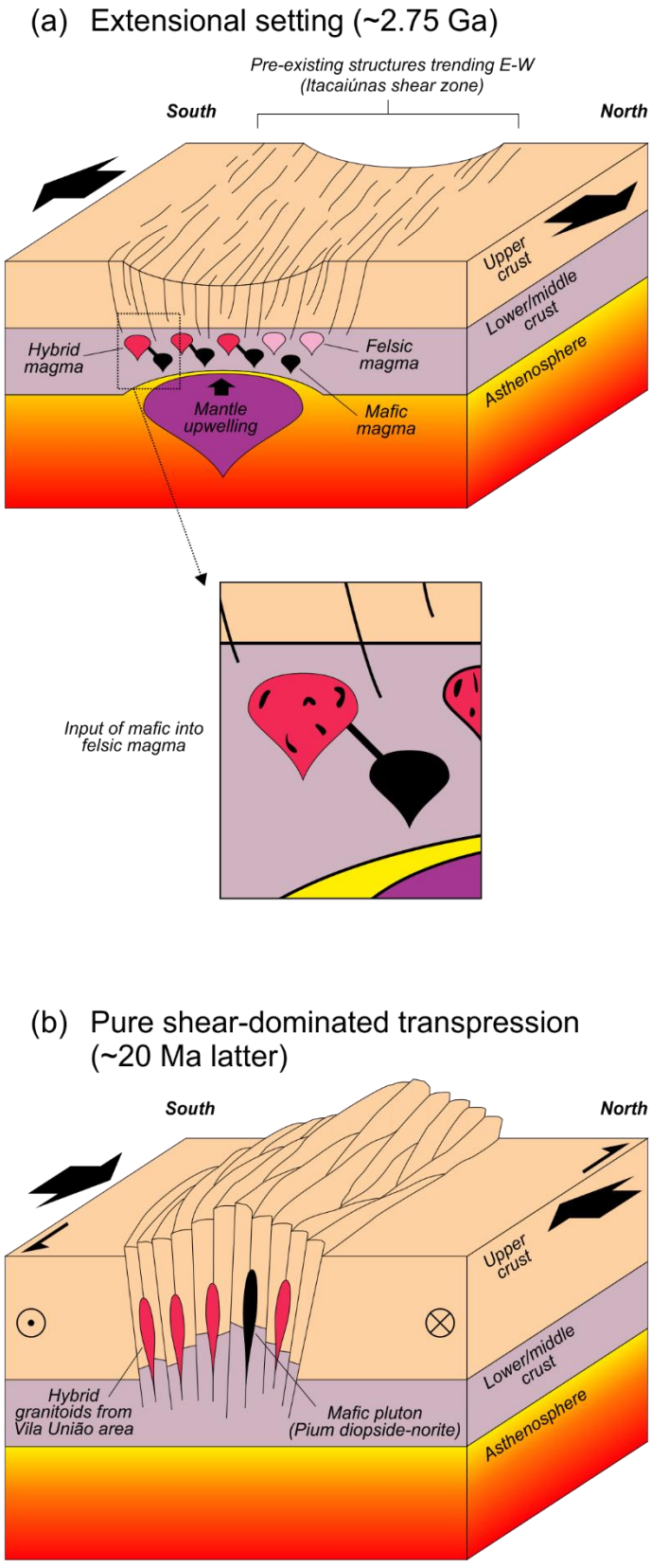

Figure 20. Simplified schematic illustration summarizing the petrogenetic/geodynamic model based on mixing/mingling process between both felsic and mafic melts to generate the granitoids of Vila União area that involved (a) extensional followed by (b) transpressional setting.

Santos et al. (2013) admitted that Pium diopside-norite was generated in an extensional setting, during the opening of Carajás basin. Mingling texture and Sm-Nd isotopic data indicate the involvement of a crustal component concerning its origin. Thus, it is assumed that the Neoarchean mafic pluton (Pium diopside-norite) represents the mafic magmatism generated by decompression melting of the mantle responsible by magmatic underplating.

The hybrid magma rising and emplacement were accompanied by the inversion of Carajás basin, described by a pure shear-dominated transpressional tectonic regime, with sinistral sense (Figure 20b; Marangoanha et al., unpublished results). Under this tectonic regime, the hybrid melt was channeled into pre-existing shear zones trending E–W (Itacaiúnas shear zone), formed during the Mesoarchean collision (Araújo et al., 1988; Tavares, 2015; Vasquez et al., 2008), to be emplaced in the ductile-brittle transition zone (middle crust) where the melt accumulates as plutons along the foliation (steep tabular sheeted intrusions). The transpressional tectonic regime played coevally with the hybrid magma cooling, giving rise to the Neoarchean deformed (and coalescent) A-type granitoids that resulted in the final terrane amalgamation at 2.75–2.73 Ga.

9. Conclusion

The main conclusion of this study can be summarized in the following and provide new insights on the Neoarchean evolution of the central portion from Canaã dos Carajás domain:

(1) Field and petrological observations combined with geochemical, geochronological and Nd-Hf isotopic dataset reveal that the wide compositional spectrum of the Vila União granitoids forms a continuous trend produced by mixing/mingling process between mantle- and crust-derived magmas.

(2) U-Pb SHRIMP and LA-MC-ICP-MS dating of zircon grains in all varieties yielded crystallization ages of 2.75–2.73 Ga, similar to those attributed to other Neoarchean granitoids from Carajás province. Combined Nd and Hf isotopes indicate that the felsic end-member in this hybrid system was produced by recycling of an old crustal source (felsic granulite), whose Hf-T_{DM2} is between 3.46 and 3.29 Ga, and the mafic end-member represents a juvenile component. It points to an older crust in the Canaã dos Carajás domain, rather than of 3.2 Ga previously recorded.

(3) The drawn geologic scenario revels that at ~2.75 Ga, this crust segment was submitted initially by an N–S extensional tectonic regime driven by underplate that was

responsible to generate mafic magma related to Pium diopside-norite. Immediately, this mafic magma intrusion provides heat in the middle crust to form felsic magma, which both were hybridized during ascent. ~20 Ma later, the hybrid magma rising and emplacement were accompanied by the inversion of Carajás basin under a pure shear-dominated transpressional tectonic regime that resulted in amalgamation of coalescent A-type plutons.

Acknowledgements

The authors are grateful for the support in geological mapping provided by J.R.M. Mesquita, E.O. Gabriel, M.N.S. dos Santos and P.J.L. dos Santos, and to the Laboratório de Geologia Isotópica from Federal University of Pará (Pará-Iso/UFPA) staffs for Sm-Nd data. C.N. Lamarão is acknowledged for his support with the acquisition of the BSE images conducted at the Laboratório de Microanálises from UFPA. One of the authors (BM) thanks the Conselho Nacional de Desenvolvimento Científico e Tecnológico (CNPq) for a doctor thesis scholarship (Proc. 163874/2014-0). Funding for this project has come from CNPq (D.C. Oliveira – Proc. 311388/2016-7 and 485806/2013-4), Fundo de Amparo à Pesquisa do Estado do Pará (FAPESPA; Proc. 133/2008-0), Vale/FAPESPA (ICAAF n. 053/2011) and INCT program (CNPq/FAPESPA/CAPES/PETROBRAS; Proc. 573733/2008-2).

References

Afonso, J.M.L., Oliveira, D.C., Silva, F.F., 2017. Novas ocorrências de granitos tipo A na Província Carajás, in: Lima, A.M.M., Gorayeb, P.S.S. (Eds.), Contribuições à Geologia da Amazônia, vol. 10. Sociedade Brasileira de Geologia – Núcleo Norte. Belém, pp. 209–224 (in Portuguese).

Almeida, J.A.C., Dall'Agnol, R., Oliveira, M.A., Macambira, M.J.B., Pimentel, M.M., Rämö, O.T., Guimarães, F.V., Leite, A.A.S., 2011. Zircon geochronology and geochemistry of the TTG suites of the Rio Maria granite-greenstone terrane: implications for the growth of the Archean crust of Carajás Province, Brazil. Precambrian Research 187, 201–221.

Althoff, F.J., Barbey, P., Boullier, A.M., 2000. 2.8–3.0 Ga plutonism and deformation in the SE Amazonian craton: the Archean granitoids of Marajoara (Carajás Mineral Province, Brazil). Precambrian Research 104, 187–206.

Andersen, T., Andersson, U.B., Graham, S., Aberg, G., and Simonsen, S.L., 2009. Granitic magmatism by melting of juvenile continental crust: new constraints on the source of Paleoproterozoic granitoids in Fennoscandia from Hf isotopes in zircon. Journal of the Geological Society 166, 233–247.

Annen, C., Blundy, J., Sparks, R., 2006. The genesis of intermediate and silicic magmas in deep crustal hot zones. Journal of Petrology 47(3), 505–539.

Annen, C., Sparks, R.S.J., 2002. Effects of repetitive emplacement of basaltic intrusions on thermal evolution and melt generation in the crust. Earth and Planetary Science Letters 203, 937–955.

Araújo, O.J.B, Maia, R.G.N, João, X.S.J., Costa, J.B.S., 1988. A megaestruturação arqueana da Folha da Serra dos Carajás, in: Congresso Latino Americano de Geologia, vol. 7. Anais do 35º Simpósio Brasileiro de Geologia. SBG, Belém, pp. 324–338 (in Portuguese).

Avelar, V.G., Lafon, J.M., Correia Jr., F.C., Macambira, E.M.B., 1999. O Magmatismo arqueano da região de Tucumã – Província Mineral de Carajás: novos resultados geocronológicos. Revista Brasileira de Geociências 29, 454–460 (in Portuguese).

Barbarin, B., 1990. Plagioclase xenocrysts and mafic magmatic enclaves in some granitoids of the Sierra Nevada batholith, California. Journal of Geophysical Research 95, 17747–17756.

Barbarin, B., Didier, J., 1992. Genesis and evolution of mafic microgranular enclaves through various types of interaction between coexisting felsic and mafic magmas. Transactions of the Royal Society of Edinburgh Earth Sciences 83, 145–153.

Barker, F., 1979. Trondhjemite: a definition, environment and hypotheses of origin, in: Barker, F. (Ed.), Trondhjemites, Dacites and Related Rocks. Elsevier, Amsterdam, pp. 1–12.

Barros, C.E.M., Barbey, P., 1998. A importância da granitogênese tardi-arqueana (2,5 Ga) na evolução tectono-metamórfica da Província Mineral de Carajás – Complexo Granítico Estrela e sua auréola de contato. Revista Brasileira de Geociências 28, 513–522.

Barros, C.E.M., Barbey, P., Boullier, A.M., 2001. Role of magma pressure, tectonic stress and crystallization progress in the emplacement of the syntectonic A-type Estrela Granite Complex (Carajás Mineral Province, Brazil). Tectonophysics 343, 93–109.

Barros, C.E.M., Sardinha, A.S., Barbosa, J.P.O., Macambira, M.J.B., 2009. Structure, petrology, geochemistry and zircon U-Pb and Pb-Pb geochronology of the synkinematic Archean (2.7 Ga) A-type granites from the Carajás Metallogenic Province, northern Brazil. Canadian Mineralogist 47, 1423–1440.

Baxter, S., Feely, M., 2002. Magma mixing and mingling textures in granitoids: examples from the Galway Granite, Connemara, Ireland. Mineralogy and Petrology 76, 63–74.

Bea, F., 1996. Residence of REE, Y, Th, and U in granites and crustal protoliths, implications for the chemistry of crustal melts. Journal of Petrology 37, 521–552.

Black, L.P., Kamo, S.L., Williams, I.S., Mundil, R., Davis, D.W., Korsch, R.J., Foudoulis, C., 2003. The application of SHRIMP to Phanerozoic geochronology: A critical application of four zircon standards, Chem. Geol., 200, 171–188.

Bouchez, J.L., Delas, C., Gleizes, G., Nédélec, A., Cuney, M., 1992. Submagmatic microfractures in granites. Geology 20, 35–38.

Bouvier, A., Vervoort, J.D., Patchett, P.J., 2008. The Lu-Hf and Sm-Nd isotopic composition of CHUR: constraints from unequilibrated chondrites and implications for the bulk composition of terrestrial planets. Earth and Planetary Science Letters 273, 48–57.

Bowden, P., Batchelor, R.A., Chapell, B.W., Didier, J., Lameyre, J., 1984. Petrological, geochemical and source criteria for the classification of granitic rocks: a discussion. Physics of the Earth and Planetary Interiors 35, 1–11.

Burda, J., Gaweda, A., Klötzli, U., 2011. Magma hybridization in the Western Tatra Mts. granitoid intrusion (S-Poland, Western Carpathians). Mineralogy and Petrology 103, 19–36.

Cherniak, D.J., Hanchar, J.M., Watson, E.B., 1997. Diffusion of tetravalent cations in zircon. Contributions to Mineralogy and Petrology 127, 383–390.

Chu, N.C., Taylor, R.N., Chavagnac, V., Nesbitt, R.W., Boella, R.M., Milton, J.A., German, C.R., Bayon, G., Burton, K., 2002. Hf isotope ratio analysis using multi-collector inductively coupled plasma mass spectrometry: an evaluation of isobaric interference corrections. Journal of Analytical Atomic Spectrometry 17, 1567–1574.

Cunha, I.R.V., Dall'Agnol, R., Feio, G.R.L., 2016. Mineral chemistry and magnetic petrology of the Archean Planalto Suite, Carajás Province – Amazonian Craton: Implications for the evolution of ferroan Archean granites. Journal of South American Earth Sciences 67, 100–121.

Dall'Agnol, R., Cunha, I.R.V, Guimarães, F.V, Oliveira, D.C., Teixeira, M.F.B., Feio, G.R.L., Lamarão, C.N., 2017. Mineralogy, geochemistry, and petrology of Neoarchean ferroan to magnesian granites of Carajás Province, Amazonian Craton: The origin of hydrated granites associated with charnockites. Lithos 277, 3–32.

Dall'Agnol, R., Oliveira, D.C., 2007. Oxidized, magnetite-series, rapakivi-type granites of Carajás, Brazil: implications for classification and petrogenesis of A-type granites. Lithos 93, 215–233.

Dall'Agnol, R., Oliveira, D.C., Guimarães, F.V., Gabriel, E.O., Feio, G.R.L., Lamarão, C.N., Althoff, F.J., Santos, P.A., Teixeira, M.F.B., Silva, A.C., Rodrigues, D.S., Santos, M.J.P., Silva, C.R.P., Santos, R.D., Santos, P.J.L., 2013. Geologia do Subdomínio de Transição do Domínio Carajás – Implicações para a evolução arqueana da Província Carajás - Pará. Anais do 13º Simpósio de Geologia da Amazônia. SBG, Belém, CD-rom (in Portuguese).

Dall'Agnol, R., Oliveira, M.A., Almeida, J.A.C., Althoff, F.J., Leite, A.A.S., Oliveira, D.C., Barros, C.E.M., 2006. Archean and Paleoproterozoic granitoids of the Carajás metallogenetic province, eastern Amazonian craton, in: Dall'Agnol, R., Rosa-Costa, L.T., Klein, E.L. (Eds.), Symposium on Magmatism: Crustal Evolution, and Metallogenesis of the Amazonian Craton. Abstracts Volume and Field Trips Guide. Belém, PRONEX-UFPA/SBG-NO, pp. 99–150.

Dall'Agnol, R., Teixeira, N.P., Rämö, O.T., Moura, C.A.V., Macambira, M.J. B., Oliveira, D.C., 2005. Petrogenesis of the Paleoproterozoic, rapakivi, A-type grantites of the Archean Carajás Metallogenic Province, Brazil. Lithos 80, 101–129.

Dan, W., Wang, Q., Wang, X.C., Liu, Y., Wyman, D.A., Liu, Y.S., 2015. Overlapping Sr-Nd-Hf-O isotopic compositions in Permian mafic enclaves and host granitoids in Alxa Block, NW China: Evidence for crust–mantle interaction and implications for the generation of silicic igneous provinces. Lithos 230, 133–145.

De Paolo, D.J., 1981. Neodymium isotope in the Colorado Front Range and crust–mantle evolution in the Proterozoic. Nature 291,193–196.

De Paolo, D.J., Wasserburg, G.J., 1976. Nd isotope variations and petrogenetic models. Geophysical Research Letters 3, 249–252.

Debon, F., Le Fort, P., 1988. A cationic classification of common plutonic rocks and their magmatic associations: principles, method, applications. Bulletin of Mineralogy 111, 493–510.

Deer, W.A., Howie, R.A., Zussman, J., 1963. Rock-Forming Minerals, vol. 4. Longmans, London.

Delinardo, M.A.S., Monteiro, L.V.S., Moreto, C.P.N., Sousa, S.D., Melo, G.H.C., 2014. Complexo Xingu: Uma secção da crosta inferior exumada durante a evolução do Domínio Carajás, PA. Anais do 47º Congresso Brasileiro de Geologia. SBG, Salvador, CD-rom (in Portuguese).

Delinardo, M.A.S., Monteiro, L.V.S., Santos, T.J.S., Moreto, C.P.N., Sousa, S.D., 2015. Partial melting and magma generation in the Mesoarchean (ca. 3.0 Ga) TTG gneisses of

the Xingu Complex, Carajás Province, Amazon Craton. 8th Hutton Symposium on granites and related rocks. Florianópolis, CD-rom.

DOCEGEO (Rio Doce Geologia e Mineração – Distrito Amazônia), 1988. Revisão litoestratigráfica da Província Mineral de Carajás, Pará. 35º Congresso Brasileiro de Geologia. SBG, Belém, pp. 11–54 (in Portuguese).

Donaire, T., Pascual, E., Pin, C., Duthou, J.L., (2005) Microgranular enclaves as evidence rapid cooling in granitoid rocks: the case of the Los Pedroches granodiorite, Iberian Massif, Spain. Contributions to Mineralogy and Petrology 149, 247–265.

Dorais, M.J., Whitney, J.A., Roden, M.F., 1990. The origin of mafic enclaves from the Dinkey Creek pluton, central Sierra Nevada Batholith. Journal of Petrology 31, 853–881.

Eby, G.N., 1992. Chemical subdivision of the A-type granitoids: petrogenesis and tectonic implications. Geology 20, 641–644.

Elburg, M.A., 1996. U-Pb ages and morphologies of zircon in micrograniteoid enclaves and peraluminous host granites: evidence for magma mingling. Contributions to Mineralogy and Petrology 123, 177–189.

Ersoy, E.Y., 2013. PETROMODELER (Petrological Modeler): a Microsof Excel spreadsheet program for modelling melting, mixing, crystallization and assimilation processes in magmatic systems. Turkish Journal of Earth Sciences 22, 115–125.

Feio, G.R.L., Dall'Agnol, R., Dantas, E.L., Macambira, M.J.B., Gomes, A.C.B., Sardinha, A.S., Oliveira, D.C, Santos, R.D., Santos, P.A., 2012. Geochemistry, geochronology and origin of the Neoarchean Planalto Granite suite, Carajás, Amazonian craton: A-type or hydrated charnockitic granites? Lithos 151, 57–73.

Feio, G.R.L., Dall'Agnol, R., Dantas, E.L., Macambira, M.J.B., Santos, J.O.S., Althoff, F.J., Soares, J.E.B., 2013. Archean granitoid magmatism in the Canaã dos Carajás area: implications for crustal evolution of the Carajás province, Amazonian craton, Brazil. Precambrian Research 227, 157–185.

Frost, B.R., Barnes, C., Collins, W., Arculus, R., Ellis, D., Frost, C., 2001. A chemical classification for granitic rocks. Journal of Petrology 42, 2033–2048.

Gabriel, E.O., Oliveira, D.C., 2014. Geologia, petrografia e geoquímica dos granitoides arqueanos de alto magnésio da região de Água Azul do Norte, porção sul do Domínio Carajás, Pará. Boletim do Museu Paraense Emílio Goeldi, Ciências Naturais, 9(3), 533–564 (in Portuguese).

Galarza, M.A., Oliveira, D.C., Rodrigues, E.A., Santos, A.N., Martins, A.C., Marangoanha, B., 2017. Neoarchean granitoids (2.73–2.74 Ga) intrusive and associated with the Pium

Diopside-Norite, Canaã dos Carajás, Carajás Province (PA). Contribuições à Geologia da Amazônia 10, 225–246.

Gardien, V., Thompson, A.B., Grujic, D., Ulmer, P., 1995. Experimental melting of biotite + plagioclase + quartz ± muscovite assemblages and implications for crustal melting. Journal of Geophysical Research – Solid Earth 100, 15581–15591.

Gardien, V., Thompson, A.B., Ulmer, P., 2000. Melting of biotite + plagioclase + quartz gneisses: the role of H_2O in the stability of amphibole. Journal of Petrology 41, 651–666.

Gerdes, A., Zeh, A., 2006. Combined U-Pb and Hf isotope LA-MC-ICP-MS analyses of detrital zircons: Comparison with SHRIMP and new constraints for the provenance and age of an Armorican metasediment in Central Germany. Earth and Planetary Science Letters 249, 47–62.

Gerdes, A., Zeh, A., 2009. Zircon formation versus zircon alteration – New insights from combined U-Pb and Lu-Hf in-situ LA-ICP-MS analyses, and consequences for the interpretation of Archean zircon from the Central Zone of the Limpopo Belt. Chemical Geology 261, 230–243.

Green, D.H., Ringwood, A.E., 1967. An experimental investigation of the gabbro to eclogite transformation and its petrological applications: Geochimica et Cosmochimica Acta 31, 767–833.

Griffin, W.L., Wang, X., Jackson, S.E., Pearson, N.J., O'Reilly, S.Y., 2002. Zircon geochemistry and magma mixing, SE China: in-situ analysis of Hf isotopes, Tonglu and Pingtan igneous complexes. Lithos 61, 237–269.

Guimarães, F.V.G., Dall'Agnol, R., Almeida, J.A.C., Oliveira, M.A., 2010. Caracterização geológica, petrográfica e geoquímica do trondhjemito Mogno e tonalito Mariazinha, terreno granito-greenstone de Rio Maria e Pará. Revista Brasileira de Geociências 40 (2), 196–211.

Hibbard, M.J., 1991. Textural anatomy of twelve magma-mixed granitoid systems, in: Didier, J., Barbarin, B. (Eds.), Enclaves and Granite Petrology, Developments in Petrology, vol. 13. Elsevier, Amsterdam, pp. 431–444.

Hu, Z.C., Liu, Y.S., Gao, S., Liu, W.G., Zhang, W., Tong, X.R., Lin, L., Zong, K.Q., Li, M., Chen, H.H., Zhou, L., Yang, L., 2012. Improved in situ Hf isotope ratio analysis of zircon using newly designed X skimmer cone and jet sample cone in combination with the addition of nitrogen by laser ablation multiple collector ICP-MS. Journal of Analytical Atomic Spectrometry 27, 1391–1399.

Hühn, S.R.B., Macambira, M.J.B, Dall'Agnol, R., 1999. Geologia e Geocronologia Pb–Pb do Granito Alcalino Arqueano Planalto, Região da Serra do Rabo – Carajás – PA, in: Resumos Expandidos do 6º Simpósio de Geologia da Amazônia. SBG, Manaus, 463–466 (in Portuguese).

Janoušek, V., Farrow, C.M., Erban, V., 2003. GCDkit: new PC software for interpretation of whole-rock geochemical data from igneous rocks. Geochimica et Cosmochimica Acta 67, 186.

Kushiro, I., 1968. Compositions of magmas formed by partial zone melting of the earth's upper mantle. Journal of Geophysical Research 73, 619–634.

Lafon, J.M., Macambira, M.J.B., Pidgeon, R.T., 2000. Zircon U-Pb SHRIMP dating of Neoarchean magmatism in the southwestern part of the Carajás Province (eastern Amazonian Craton, Brazil). 31st International Geological Congress, Rio de Janeiro, CD-rom.

Lameyre, J., Bowden, P., 1982. Plutonic rock type series: discrimination of various granitoid series and related rocks. Journal of Volcanology and Geothermal Research 14, 169–186.

Le Maître, R.W., Streckeisen, A., Zanettin, B., Le Bas, M.J., Bonin, B., Bateman, P., Bellieni, G., Dudek, A., Efremova, J., Keller, J., Lameyre, J., Sabine, P.A., Schmidt, R., Sørensen, H., Woolley, A.R., 2002. Igneous rocks. A classification and glossary of terms. Recommendations of the International Union of Geological Sciences Subcommission on the Systematics of Igneous Rocks. Cambridge University Press, Cambridge, 252 pp.

Leite, A.A.S., Dall'Agnol, R., Macambira, M.J.B., Althoff, F.J., 2004. Geologia e geocronologia dos granitóides arqueanos da região de Xinguara (PA) e suas implicações na evolução do terreno granito–greenstone de Rio Maria. Revista Brasileira de Geociências 34, 447–458 (in Portuguese).

Lesher, C.E., 1990. Decoupling of chemical and isotopic exchange during magma mixing. Nature 344, 235–237.

Ludwig, K.R., 2008. User's Manual for Isoplot 3.6: a Geochronological Toolkit for Microsoft Excel. Berkeley Geochronology Center Special Publication, Berkeley.

Machado, N., Lindenmayer, Z.G., Krogh, T.E., Lindenmayer, D., 1991. U–Pb geochronology of Archean magmatism and basement reactivation in the Carajás area, Amazon shield, Brazil. Precambrian Research 49, 329–354.

Martins, P.L.G., Toledo, C.L.B., Silva, A.M., Chemale Jr, F., Santos, J.O.S., Assis, L.M., 2017. Neoarchean magmatism in the southeastern Amazonian Craton, Brazil:

Petrography, geochemistry and tectonic significance of basalts from the Carajás Basin. Precambrian Research 302, 340–357.

McDonough, W.F., 1990. Constraints on the composition of the continental lithospheric mantle. Earth and Planetary Science Letters 101, 1–18.

McDonough, W.F., Sun, S.S., 1995. The composition of the Earth. Chemical Geology 120(3–4), 223–253.

Melo, G.H.C., Monteiro, L.V.S., Xavier, R.P., Santiago, E.B.S., 2014. Geocronologia U–Pb e uma nova perspectiva sobre a evolução do depósito IOCG de classe mundial Salobo, Província Carajás, Brasil. Anais do 47º Congresso Brasileiro de Geologia. SBG, Salvador, CD-rom (in Portuguese).

Moreto, C.P.N, Monteiro, L.V.S., Xavier, R.P., Creaser, R.A., DuFrane, S.A., Tassinari, C.C.G., Sato, K., Kemp, A.I.S., Amaral, W.S., 2015. Neoarchean and Paleoproterozoic Iron Oxide-Copper-Gold Events at the Sossego Deposit, Carajás Province, Brazil: Re-Os and U-Pb Geochronological Evidence. Economic Geology 110, 809–835.

Moreto, C.P.N., Monteiro, L.V.S., Xavier, R.P., Amaral, W.S., Santos, T.J.S., Juliani, C., Souza Filho, C.R., 2011. Mesoarchean (3.0 and 2.86 Ga) host rocks of the iron oxide–Cu–Au Bacaba deposit, Carajás Mineral Province: U–Pb geochronology and metallogenetic implications. Mineralium Deposita 46, 789–811.

Nogueira, A.C.R., Truckenbrodt, W., Pinheiro, R.V.L., 1995. Formação Águas Claras, Pré-Cambriano da Serra dos Carajás: redescrição e redefinição litoestratigráfica. Boletim do Museu Paraense Emílio Goeldi 7, 177–277 (in Portuguese).

O'Connor, J.T., 1965. A classification for quartz-rich igneous rocks based on feldspar rations. US Geological Survey Professional Papers 525, 79–84.

O'hara, M.J., 1968.The bearing of phase equilibria studies in synthetic and natural systems on the origin and evolution of basic and ultrabasic rocks. Earth-Science Reviews 4, 69–133.

Oliveira, D.C., Macambira, M.J.B., Santos, P.J.L., Gabriel, E.O., Rodrigues, D.S., Silva, A.C., Silva, M.L.T., Sousa, S.D., Santos, R.D., Galarza, M.A.T., 2011. Archean granitoids of the Transition Domain Carajás Province (Brazil): geological, geochemical and geochronological aspects. Colloquium African Geology 23, 320.

Oliveira, E.C., Lafon, J.M., Gioia, S.M.C.L., Pimentel, M.M., 2008. Datação Sm-Nd em rocha total e granada do metamorfismo granulítico da região de Tartarugal Grande, Amapá Central. Revista Brasileira de Geociências 38, 114–127.

Oliveira, M.A., Dall'Agnol, R., Althoff, F.J., Leite, A.A.S., 2009. Mesoarchean sanukitoid rocks of the Rio Maria Granite-Greenstone Terrane, Amazonian Craton, Brazil. Journal of South American Earth Sciences 27, 146–160.

Oliveira, V.E.S., Oliveira, D.C., Marangoanha, B., Lamarão, C.N., 2018. Geology, mineralogy and petrological affinities of the Neoarchean granitoids from the central portion of the Canaã dos Carajás domain, Amazonian craton, Brazil. Journal of South American Earth Sciences 85, 135–159.

Palivcová, M., Waldhausrová, J., Ledvinková, V., 1995. Occeli in mafic rocks of granitic complexes. Krystalinikum 22, 149–186.

Passchier, C.W., Trouw, R.A.J., 2005. Microtectonics, second ed. Springer-Verlag, Berlin–Heidelberg–New York.

Patchett, P.J., Tatsumoto, M., 1980. A routine high-precision method for Lu-Hf isotope geochemistry and chronology. Contributions to Mineralogy and Petrology 75, 263–267.

Patiño Douce, A.E., 2005. Vapor-absent melting of tonalite at 15-32 kbar. Journal of Petrology 46, 275–290.

Pearce, J.A., Harris, N.B.W., Tindle, A.G., 1984. Trace element discrimination diagrams for the tectonic interpretation of granitic rocks. Journal of Petrology 25, 956–983.

Perkins, D., Anthony, E.Y., 2011. The evolution of spinel lherzolite xenoliths and the nature of the mantle at Kilbourne Hole, New Mexico. Contributions to Mineralogy and Petrology 162, 1139–1157.

Pidgeon, R., Macambira, M.J.B., Lafon, J.M., 2000. Th–U–Pb isotopic systems and internal structures of complex zircons from an enderbite from the Pium Complex, Carajás Province, Brazil: evidence for the ages of granulite facies metamorphism and the source of the enderbite. Chemical Geology 166, 159–171.

Poli, G., Tommasini, S., Halliday, A.N., 1996. Trace elements and isotopic exchange during acid-basic magma interaction processes. Transactions of the Royal Society of Edinburgh Earth Sciences 87, 225– 232.

Rodrigues, D.S., Oliveira, D.C., Macambira, M.J.B., 2014. Geologia, geoquímica e geocronologia do Granito Mesoarqueano Boa Sorte, município de Água Azul do Norte, Pará – Província Carajás. Boletim do Museu Paraense Emílio Goeldi. Série Ciências da Terra 9(3), 597–633 (in Portuguese).

Rollinson, H., 1993. Using Geochemical Data. Longman, London.

Rutter, M.J., Wyllie, P.J., 1988. Melting of vapour-absent tonalite at 10 kbar to simulate dehydration-melting in the deep crust. Nature 331, 159–160.

Santos, P.J.L., Oliveira, D.C., Galarza, M.A., Macambira, M.J.B., 2010. Geologia, petrografia e geocronologia das rochas granitoides do Complexo Xingu da região de Nova Canadá, município de Água Azul do Norte – Província mineral de Carajás, in 45° Congresso Brasileiro de Geologia, Belém, CD-rom.

Santos, R.D., Galarza, M.A., Oliveira, D.C., 2013. Geologia, geoquímica e geocronologia do Diopsídio-Norito Pium, Província Carajás. Boletim do Museu Paraense Emílio Goeldi, Série Ciências da Terra 8, 355–382 (in Portuguese).

Sardinha, A.S., Barros, C.E.M., Krymsky, R., 2006. Geology, geochemistry, and U–Pb geochronology of the Archean (2.74 Ga) Serra do Rabo granite stocks, Carajás Metallogenetic Province, northern Brazil. Journal South American Earth Science 20, 327–339.

Sato, K., Basei, M.A.S., Siga Jr., O., Sproesser, W.M., Passarelli, C.R., 2008. Novas técnicas aplicadas ao método U-Pb no CPGeo – IGc/USP: avanços na digestão química, espectrometria de massa (TIMS) e exemplos de aplicação integrada com SHRIMP. Geologia USP: Série Científica 7, 77–99.

Sato, K., Tassinari, C.C.G., Basei, M.A.S., Siga Júnior, O., Onoe, A.T., Souza, M.D., 2014. Sensitive High Resolution Ion Microprobe (SHRIMP IIe/MC) of the Institute of Geosciences of the University of São Paulo, Brazil: analytical method and first results. Geologia USP, Série Científica 14(3), 3–18.

Scherer, E.E., Münker, C., Mezger, K., 2001. Calibration of the lutetium-hafnium clock. Science 293, 683–687.

Shand, S.J., 1950. Eruptive rocks their genesis, composition, classification and their relation to ore deposit, fourth ed. Murby, London, 488 pp.

Singh, J., Johannes, W., 1996. Dehydration melting of tonalites. Part II. Compositions of melts and solids. Contributions to Mineralogy and Petrology 125, 26–44.

Skjerlie, K.P., Johnston, A.D., 1992. Vapor-absent melting at 10 kbar of a biotite-bearing and amphibole bearing tonalitic gneiss – implications for the generation of A-type granites. Geology 20, 263–266.

Souza, Z.S., Potrel, H., Lafon, J.M., Althoff, F.J., Pimentel, M.M., Dall'Agnol, R., Oliveira, C.G., 2001. Nd, Pb and Sr isotopes of the Identidade Belt, an Archaean greenstone belt of the Rio Maria region (Carajás Province, Brazil): implications for the Archaean geodynamic evolution of the Amazonian Craton. Precambrian Research 109, 293–315.

Stacey, J.S., Kramers, J.D., 1975. Approximation of terrestrial lead isotope evolution by a two-stage model. Earth and Planetary Science Letters 26, 207–221.

Stern, R.A., 1998. High resolution SIMS determination of radiogenic trace isotope ratios in minerals, in: Cabri, L.J., Vaughan, D.J. (Eds.), Modern approaches to ore and environmental mineralogy, Ottawa, v. 27, pp. 241–268.

Stolper, E., 1980. A phase diagram for mid-ocean ridge basalts: Preliminary results and implications for petrogenesis. Contributions to Mineralogy and Petrology 74, 13–27.

Sun, S.S., McDonough, W.F., 1989. Chemical and isotopic systematics of oceanic basalts: Implications for mantle composition and processes, in: Saunders, A.D., Norry, M.J. (Eds.), Magmatism in the Ocean Basins. Journal of the Geological Society 42, 313–345.

Sylvester, P.J., 1989. Post-collisional alkaline granites. Journal of Geology 97, 261–280.

Tassinari, C.C.G., Macambira, M., 2004. A evolução tectônica do Craton Amazônico, in: Mantesso-Neto, V., Bartorelli, A., Carneiro, C.D.R., Brito Neves, B.B. (Eds.), Geologia do Continente Sul Americano: Evolução da obra de Fernando Flávio Marques Almeida, São Paulo, pp. 471–486.

Tavares, F.M., 2015. Evolução geotectônica do nordeste da Província Carajás. Tese de Doutorado – Universidade Federal do Rio de Janeiro, Rio de Janeiro, 115 pp. (in Portuguese).

Teixeira, L.R., 2005. GENESIS 4.0 – Software de Modelamento Geoquímico.

Teixeira, M.F.B., Dall'Agnol, R., Santos, J.O.S., Sousa, L.A.M., Lafon, J.-M., 2017. Geochemistry, geochronology and Nd isotopes of the Gogó da Onça Granite: A new Paleoproterozoic A-type granite of Carajás Province, Brazil. Journal of South American Earth Sciences 80 (2017) 47–65.

Trouw, R.A.J., Passchier, C.W., Wiersma, D.J., 2010. Atlas of Mylonites- and related microstructures. Springer-Verlag, Berlin–Heidelberg.

Vasquez, L.V., Rosa-Costa, L.R., Silva, C.G., Ricci, P.F., Barbosa, J.O., Klein, E.L., Lopes, E.S., Macambira, E.B., Chaves, C.L., Carvalho, J.M., Oliveira, J.G., Anjos, G.C., Silva, H.R., 2008. Escala 1:1.000.000, in: Vasquez, M.L., Rosa-Costa, L.T. (Eds.), Geologia e Recursos Minerais do Estado do Pará: Sistema de Informações Geográficas e SIG: texto explicativo dos mapas Geológico e Tectônico e de Recursos Minerais do Estado do Pará. CPRM, Belém, 328 pp. (in Portuguese).

Vernon, R.H., 1990. Crystallization and hybridism in microgranitoid enclave magmas: microstructural evidence. Journal of Geophysical Research 95, 17849–17859.

Vernon, R.H., 2010. Granites really are magmatic: using structural evidence to refute some obstinate hypotheses, in: Forster, M.A., FitzGerald, J.D., Lister, G.S. (Eds.), The Science of Microstructure. Journal of the Virtual Explorer 35, 1–36.

Whalen, J.W., Currie, K.L., Chappel, B.W., 1987. A-type granites: geochemical characteristics, discrimination and petrogenesis. Contribution to Mineralogy and Petrology 95, 407–419.

Wiebe, R.A., 1968. Plagioclase stratigraphy: a record of magmatic conditions and events in a granite stock. American Journal of Science 266, 690–703.

Williams, I.S., 1998. U-Th-Pb Geochronology by Ion Microprobe, in: McKibben, M.A., Shanks III, W.C., Ridley, W.I. (Eds.), Applications of Microanalytical Techniques to Understanding Mineralizing Processes. Society of Economic Geologists, v. 7, pp. 1–35.

Wilson, M., 1989. Igneous Petrogenesis – A Global Tectonic Approach, Springer, Dordrecht.

Wu, F.-Y., Yang, Y.-H., Xie, L.-W., Yang, J.-H., Xu, P., 2006. Hf isotopic compositions of the standard zircons and baddeleyites used in U-Pb geochronology. Chemical Geology 234, 105–126.

Wyers, G.P., Barton, M., 1986. Petrology and evolution of transitional alkaline-subalkaline lavas from Patmos, Dodecanesos, Greece: evidence for fractional crystallization, magma mixing, and assimilation. Contributions to Mineralogy and Petrology 93, 297–311.

Wyllie, P., Cox, K., Biggar, G., 1962. The habit of apatite in synthetic systems and igneous rocks. Journal of Petrology 3, 238–243.

Yoder, H.S., Tilley, C.E., 1962. Origin of basalt magmas: an experimental study of natural and synthetic rock systems. Journal of Petrology 3, 341–532.

Zhang, J., Wang, T., Castro, A., Zhang, L., Shi, X., Tong, Y., Zhang, Z., Guo, L., Yang, Q., Iaccheri, L.M., 2016. Multiple Mixing and Hybridization from Magma Source to Final Emplacement in the Permian Yamatu Pluton, the Northern Alxa Block, China. Journal of Petrology 57, 933–980.

4 ZIRCON U-Pb, Lu-Hf ISOTOPIC AND GEOCHEMICAL CONSTRAINTS ON THE ORIGIN AND TECTONIC SIGNIFICANCE OF THE FELSIC GRANULITES AND Na-GRANITOIDS OF THE NORTHERN ARCHEAN CARAJÁS PROVINCE, BRAZIL

Autores:
Bhrenno Marangoanha
Davis Carvalho de Oliveira

Artigo a ser submetido para publicação à revista A (*Qualis* CAPES)

Zircon U-Pb, Lu-Hf isotopic and geochemical constraints on the origin and tectonic significance of the felsic granulites and Na-granitoids of the northern Archean Carajás province, Brazil

Bhrenno Marangoanha [a,b], Davis Carvalho de Oliveira [a,b]

[a] Grupo de Pesquisa Petrologia de Granitoides (GPPG), Instituto de Geociências (IG), Universidade Federal do Pará (UFPA), Rua Augusto Corrêa, 01, CEP 66075-110, Belém, Pará, Brazil

[b] Programa de Pós-graduação em Geologia e Geoquímica (PPGG), IG-UFPA, Belém, Pará, Brazil

ABSTRACT

The central portion of the Canaã dos Carajás domain (Ouro Verde area) exhibits such a peculiar scenario that involves two units of orthopyroxene-bearing sodic rocks: (i) the Mesoarchean Ouro Verde felsic granulite, with protolith crystallization and metamorphism ages of 3.05–2.93 Ga and 2.89–2.84 Ga, respectively, and (ii) the Neoarchean enderbite, composed by tonalites, trondhjemites and scarce quartz diorites, crystallized at 2.75–2.73 Ga, and shows syn-tectonic character. While the orthopyroxene in the felsic granulite was formed by the primary biotite breakdown during metamorphism, in the enderbitic rocks this mineral was formed by crystallization of a hot and anhydrous magma at deep crustal levels. This terrane evolved in three important geodynamic stages: (1) at 3.0–2.93 Ga, TTG crust was generated by partial melting of LILE-enriched basalts in a N–S subduction setting; (2) between 2.89–2.84 Ga, in collisional setting, large volume of anatectic granites was formed e contributed to crustal thickening, which triggered granulite-facies ultrahigh temperature metamorphism in the TTG crust, forming the Ouro Verde felsic granulite; and (3) in the Neoarchean, at 2.75–2.73 Ga, the lowermost mafic crust was delaminated during crustal thickening, causing crustal underplating followed by partial melting of the Mesoarchean mafic granulite which is responsible by origin of the enderbitic magma. This area was submitted to a transpressional/transtensional tectonic regime, leading to the development of plutons linearly (E–W-trending) amalgamated and emplaced along of ancient suture zones (ductile-brittle transition). Lu-Hf isotope data of magmatic cores of the zircons from the Mesoarchean felsic granulite show Hf-T_{DM2} of 3.44–3.15 Ga and εHf(t) values between -1.7 and 3.0, which suggest juvenile source. The Neoarchean enderbite presents Hf-T_{DM2} of 3.46–3.29 Ga and lower εHf(t) values (between -4.8 and -1.9), and points to a longer crustal

residence time to these rocks. All these findings led us to consider the central portion of the Canaã dos Carajás domain as an exhumed lower crust, and the tectonic juxtaposition of anatectic granites, enderbites and high-grade metamorphic rocks suggest that Ouro Verde area represent shallow and deep exposure levels of the same crust.

Keywords: Orthopyroxene; Mesoarchean granulite; Neoarchean enderbite; Exhumation; Metamorphism; Carajás province.

1. Introduction

The geodynamic processes that shaped the early continental crust are still somewhat enigmatic and controversial (De Wit, 1998; Moyen et al., 2006; Hamilton, 2011; Bédard et al., 2013), mainly due to the typical strong reworking of the Archean crust by subsequent tectono-thermal events. However, there appears to be an emerging consensus that lateral, accretionary plate tectonic processes began in the Meso- or Neoarchean (Moyen et al., 2006; Nutman and Friend, 2007; Brown, 2010; Almeida et al., 2011; Dziggel et al., 2014; Laurent et al., 2014; Martin et al., 2014), although some authors argue that the observed bulk crustal shortening in many Archaean cratons can be equally explained by mantle convection currents in the absence of lateral plate tectonics (Bédard et al., 2013). In most Archean cores, their rocks have variable field aspects ranging from homogeneous gneisses to highly heterogeneous migmatites as a result of post-magmatic metamorphic overprinting (Martin, 1994), whose thermal evolution and structures are still poorly constrained due to the scarcity of appropriate geological records and to the metamorphic studies are still comparatively rare. For the Proterozoic and Phanerozoic, metamorphic signature of accretionary tectonics is recognized as a thermal duality, where rocks with contrasting metamorphic histories are juxtaposed against one another (Brown, 2010).

It has long been recognized that high-grade gneiss terranes and low-grade granite-greenstone terranes represent distinct types of Archean crust, identified on the basis of distinct rock types, structural styles, and metamorphic grade (Windley and Bridgwater, 1971). Condie (1981) suggested that the two types of crust represent different structural levels of the same crust whose models fall into three categories: (i) both differ in age and tectonic setting; (ii) high-grade terranes represent the uplifted and eroded root-zones of low-grade terranes; or (iii) high- and low-grade terranes record the same ranges of age but reflect different tectonic settings.

The present work has recognized in the central part of Canaã dos Carajás domain, (the northern portion of the Carajás province) such a peculiar geological-structural scenario, with

both orthopyroxene-bearing magmatic and metamorphic rocks, spatially associated, but petrologically distinct. The area investigated in this study is situated around the Ouro Verde village that represents a well-preserved section through mid- to lower Archean continental crust. Additionally, it is one of the type localities to study the mechanisms of crust formation and terrane accretion in high-grade Archean gneiss terrains. Previous studies showed that the area is dominated by Na-high rocks (TTG, enderbite and felsic granulite), anatectic granites, hybrid granites (A-type), mafic rocks, and numerous enclaves mafic, mainly granulites, which were amalgamated during the Neoarchean at ca. 2.75–2.73 Ga.

Based on the strong structural-metamorphic evidence for regional-scale crustal shortening during the Mesoarchean (~2.87 Ga), Delinardo et al. (2014) presented a new model of metamorphic evolution, which the felsic granulite (Chicrim-Cateté orthogranulite) were submitted to an ultra-high temperature (UHT) granulite metamorphism (T = 907–1128 ºC and P = 8.1–13.7 kbar), whereas the TTG granitoids (Xingu complex) reach the upper amphibolite facies metamorphism (T = 785 ºC and P = 8.8 kbar). However, the age, origin and tectonic significance of this gneiss and Na-granitoids are currently unknown due to the lack of detailed geochronological, kinematic and petrological data. Thus, the goal of this paper is to characterize these contrasting orthopyroxene-bearing sodic rocks, in order to stablish some parameters related to their respective genesis. In this study, petrography, whole-rock major and trace elements and zircon U-Pb-Hf isotopic results for both magmatic and metamorphic rocks are reported to constrain their respective petrogenesis. Furthermore, Modelling of melt and residue compositions allows us to draw conclusions on the extent of melt formation and demonstrate the role of these rocks during the crustal evolution of the Carajás province.

2. Geological setting

According to the most recent geologic framework, established by Dall'Agnol et al. (2013), the Carajás province comprises three domains: Rio Maria, Sapucaia and Canaã dos Carajás (Figure 1), and these authors consider the last one as the basement of the Carajás basin. The Rio Maria domain, located in the southern part of the province, represents a typical granite-greenstone terrane. It is formed by greenstone belts (2.97–2.90 Ga; Souza et al., 2001), TTG suites (2.98–2.92 Ga; DOCEGEO, 1998; Althoff et al., 2000; Souza et al., 2001; Leite et al., 2004; Dall'Agnol et al., 2006; Almeida et al., 2011), sanukitoid suite (2.87 Ga; Oliveira et al., 2009) and leucogranites (2.87–2.86 Ga; Althoff et al., 2000; Souza et al., 2001; Leite et al., 2004; Almeida et al., 2010). The Sapucaia domain shows strong lithologic

similarity to the Rio Maria domain, however, their rocks were intensely affected by Neoarchean events, represented by deformed A-types granitoids (Dall'Agnol et al., 2013, 2017).

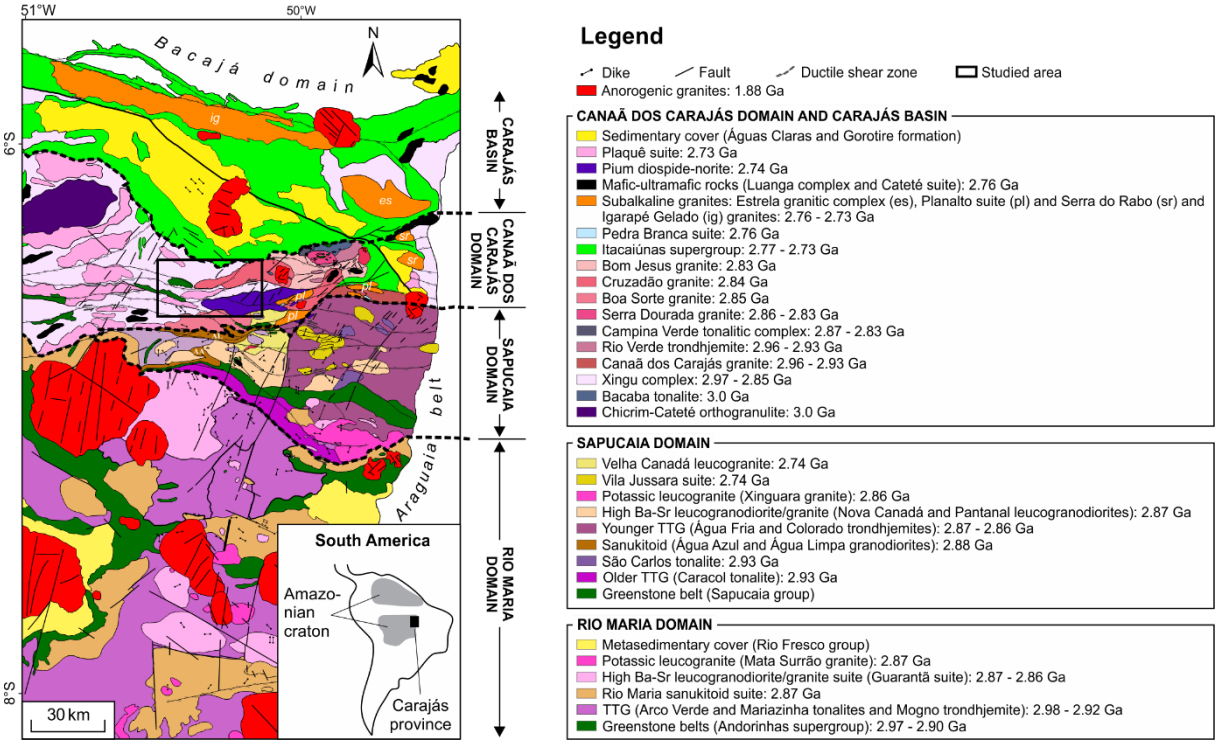

Figure 1. Geological map of the Carajás province, showing the limits between the Rio Maria, Sapucaia and Canaã dos Carajás domains, besides Carajás basin (dashed lines; modified from Gabriel et al., 2014).

The Canaã dos Carajás domain is interpreted as the basement of Carajás basin and shows a more reworked crust compared with Rio Maria and Sapucaia ones (Dall'Agnol et al., 2013). The Mesoarchean units are Chicrim-Cateté orthogranulite, with crystallization and metamorphism age of 3.0 and 2.85, respectively (Pidgeon et al., 2000; Vasquez et al., 2008), Bacaba tonalite (3.0 Ga; Moreto et al., 2011), Xingu complex – an heterogeneous lithologic association formed mainly by gneiss, migmatites and granitoids –, with crystallization age varying from 2.97 to 2.85 Ga (Machado et al., 1991; Avelar et al., 1999; Delinardo et al., 2014; Melo et al., 2014), Canaã dos Carajás granite and Rio Verde trondhjemite, both formed between 2.96 and 2.93 Ga (Feio et al., 2013), and Campina Verde tonalitic complex, Rio Verde trondhjemite, and Bom Jesus, Serra Dourada, Cruzadão and Boa Sorte granites, all with crystallization age ranging from 2.87 to 2.83 Ga (Feio et al., 2013; Rodrigues et al., 2014). This domain was intensely affected by Neoarchean events, more specifically between 2.77 and 2.70 Ga, as recorded by granitic and mafic-ultramafic magmatism, as well as greenstone belts and sedimentary rocks (Nogueira et al., 1995; Vasquez et al., 2008; Dall'Agnol et al., 2013). A summary of ages distribution for the Meso- and Neoarchean geologic units from

Canaã dos Carajás domain is shown in the Figure 2. Around 1.88 Ga, the entire Carajás province was affected by the emplacement of anorogenic granites and associated dikes (Dall'Agnol et al., 2005; Teixeira et al., 2017).

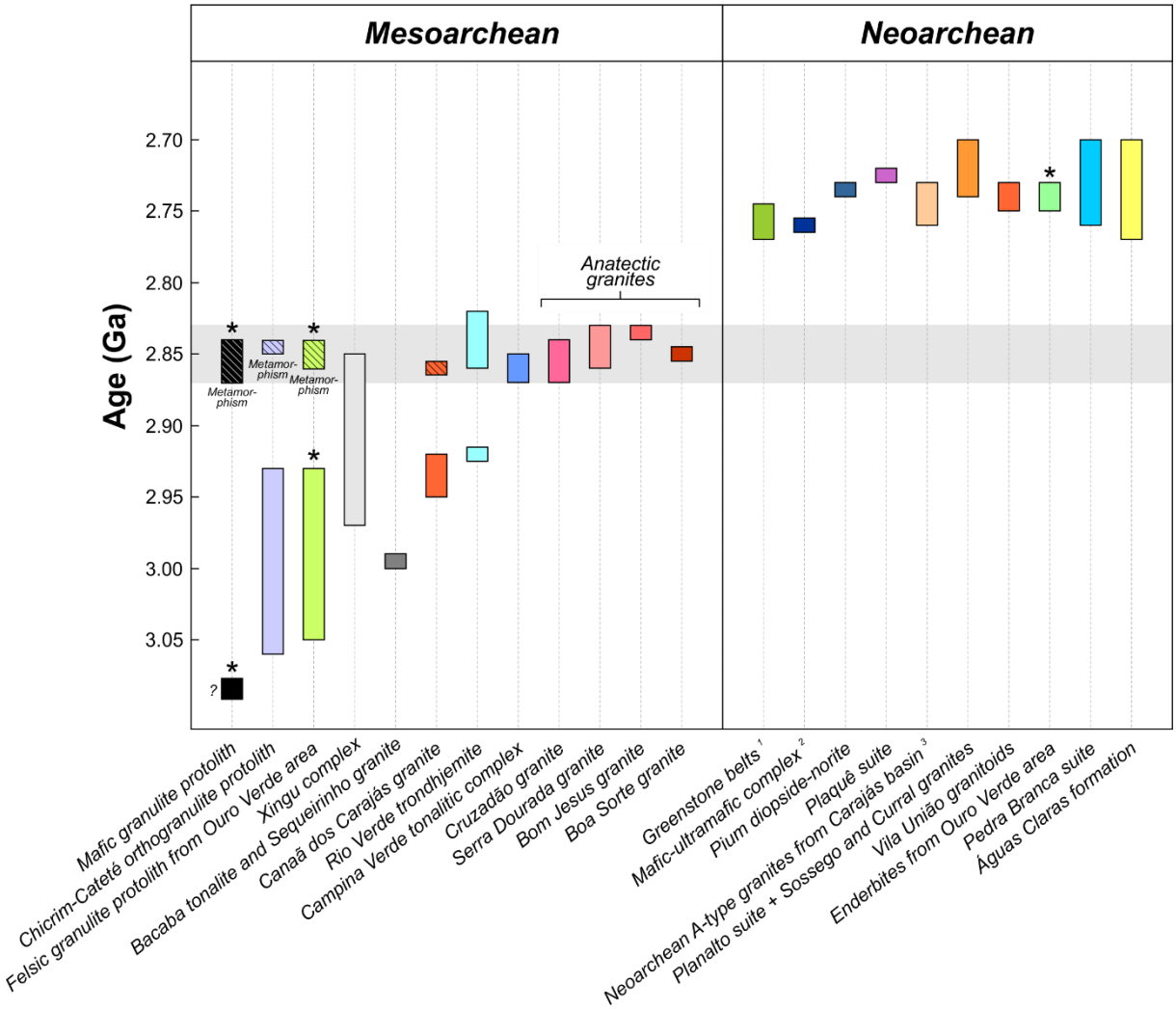

Figure 2. Summary of ages distribution for the Meso- and Neoarchean geologic units from Canaã dos Carajás domain, Carajás province. (1) Rio Novo, Igarapé Pojuca, Igarapé Bahia, Grão-Pará and Igarapé Salobo groups; (2) Cateté suite and Luanga complex; (3) Igarapé Gelado and Serra do Rabo granites, and Estrela granitic complex. The grey field represents the Mesoarchean anatectic granites crystallization age range (between 2.87–2.83 Ga). The asterisk symbol indicates the geochronological data obtained in this work. All references are in the text.

3. Previous studies about orthopyroxene-bearing granitic and felsic orthogranulitic rocks from Carajás province

The first orthopyroxene-bearing rock recorded in Carajás province was mafic granulites mapped immediately to south of Serra dos Carajás by Hirata et al. (1982), which DOCEGEO (1987) grouped these granulites into the Pium complex unit. Additionally, the high-grade metamorphism and migmatization were locally dated in ca. 2.86 Ga (Machado et al., 1991). Pidgeon et al. (2000) dated an enderbite (felsic granulite), attributed as a variety of

Pium complex, and obtained two ages of 3.0 and 2.85 Ga, interpreted by these authors as protolith crystallization and granulite-facies metamorphism ages, respectively. Concerning the mafic rocks, Ricci and Carvalho (2006) verified that in this area occur only gabbros – and not mafic granulites as stated by the previous authors –, which form an E–W elongated pluton, and these authors interpret the enderbite dated by Pidgeon et al. (2000) as a xenolith from the Chicrim-Cateté orthogranulite hosted in the Pium complex.

In a more updated geological setting related to this area, the Geological Survey of Brazil (CPRM) confirms the Ricci and Carvalho (2006) interpretation, besides also redefines the 'igneous' Pium complex unit as Pium diopside-norite (Vasquez et al., 2008), which was later corroborated by Santos et al. (2013) that obtained Neoarchean age to gabbronorites and diorites related to Pium diopside-norite of 2.74 Ga. Recently, Delinardo et al. (2014) studied the basement of Pium diopside-norite and identified both felsic (enderbitic and opdalitic granulitic gneisses) and mafic (granulites) rocks, which grouped them into the Chicrim-Cateté orthogranulite unit. Concerning the felsic gneisses, these authors obtained two age patterns: between 3.06 and 2.95, attributed as protolith crystallization ages, and 2.86–2.85 Ga, interpreted as metamorphic event (granutilization), while the mafic granulites yielded ages of 2.89 Ga, considered as crystallization ages.

4. Geological and structural aspects of the Ouro Verde area

It was identified from this work expressive occurrences of orthopyroxene-bearing sodic rocks in the central portion of Canaã dos Carajás domain that include both metamorphic and magmatic types (Figure 3), which had been initially considered as part of the undifferentiated gneissic basement rocks (Xingu complex). These rocks are inserted in the context of a kilometer-scale Mesoarchean (ca. 2.8 Ga) E–W-trending Itacaiúnas shear zone (Holdsworth and Pinheiro, 2000). The metamorphic rocks are composed essentially by felsic granulites with tonalitic/trondhjemitic compositions (Figure 4a), besides small volume of associated mafic granulites is also recorded as enclave (Figures 4b and c). They are exposed close to Ouro Verde village and consist of two bodies elongated in the E–W direction, located in the northern and southern limits of Pium diopside-norite (cf. Figure 3). The north body has a lenticular shape up to ~25 km long, whereas the south one presents ~13 km in length. It is important to highlight that both granulitic bodies are in contact with extensive Mesoarchean leucogranitic plutons, represented by Cruzadão granite in the north, and Boa Sorte granite in the south, which define a huge thermic anomaly caused by this magmatism at 2.89–2.83 Ga. The igneous sodic rock occurrences are represented by tonalitic/trondhjemitic rocks (Figure

4d) with subordinate quartz diorites, which outcrop as three E–W-trending lenticular plutons (up to ~5 km long) in the central and southern parts of the area (cf. Figure 3). Some outcrops show that this tonalitic/trondhjemitic granitoid seems to be accompanied by migmatization process, suggesting that this rock could be originated by partial melting from a mafic granulitic rock (Figures 4e and f).

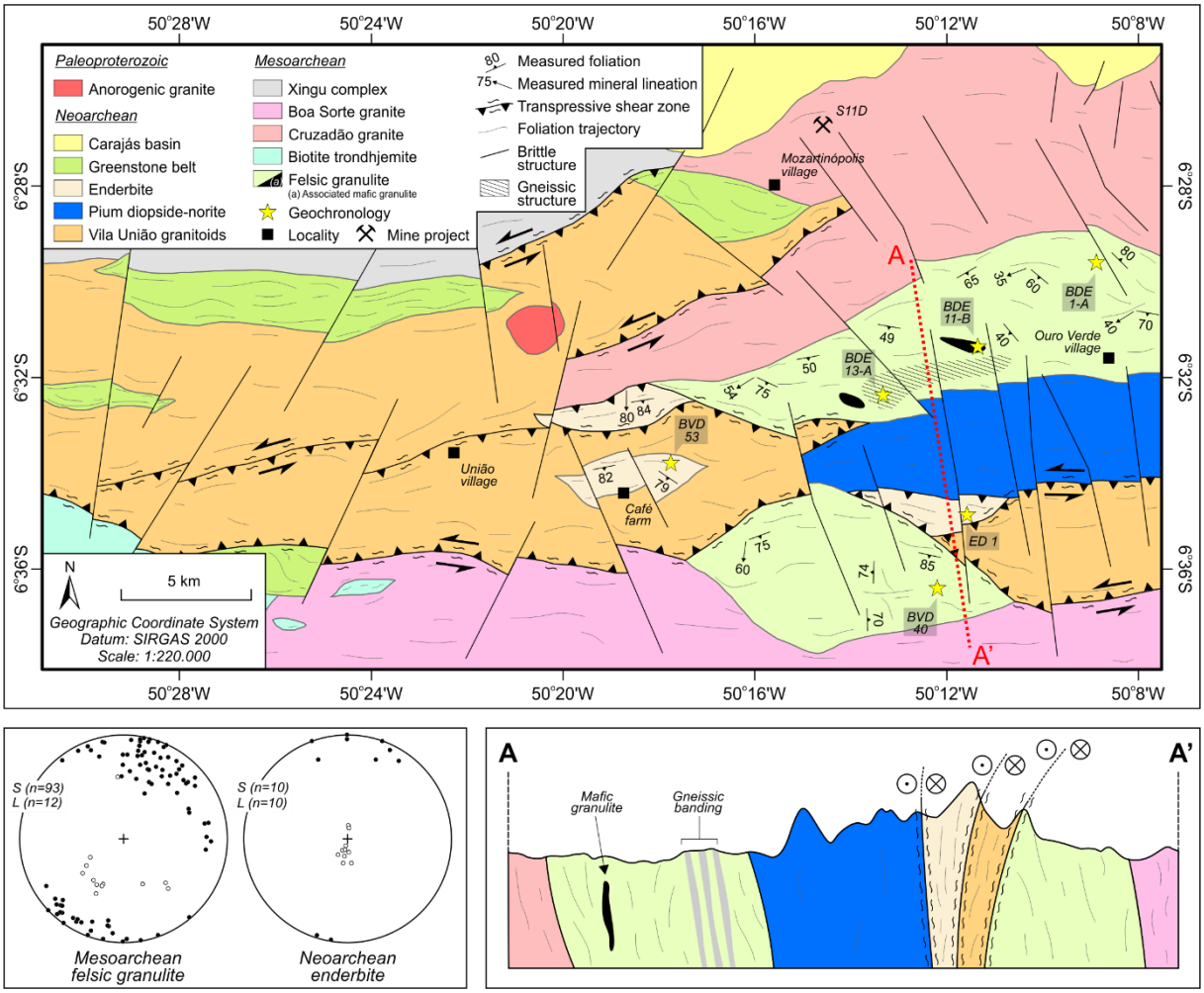

Figure 3. Geological sketch map of the studied area, showing lower hemisphere equal-area (Schmidt-Lambert) stereographic plots of poles to foliation and mineral lineation of both Mesoarchean and Neoarchean orthopyroxene-bearing sodic rocks from the studied area. Detailed interpretative cross-section A–A' is shown (see map for location).

On the map scale, foliation trajectory of the orthopyroxene-bearing granulitic rocks form a main E–W to NW–SE trends, with rare N–S occurrences, while foliation trajectory and shear zones that affect the enderbitic rocks display a main E–W trend, with sigmoidal and anastomosing array. These shear zones also mark the contact between the enderbitic rocks with both coeval hybrid granitoids from Vila União area and Pium diopside-norite, and the Mesoarchean wall rocks (cf. Figure 3). The plutons of enderbitic affinities may grow through amalgamation of sequentially intruded sheets or relatively small magma pulses

emplaced along the shear structure of Neoarchean age (reactivation of ancient suture zones), resulting in elongated bodies parallel to the major E–W-trending compressional.

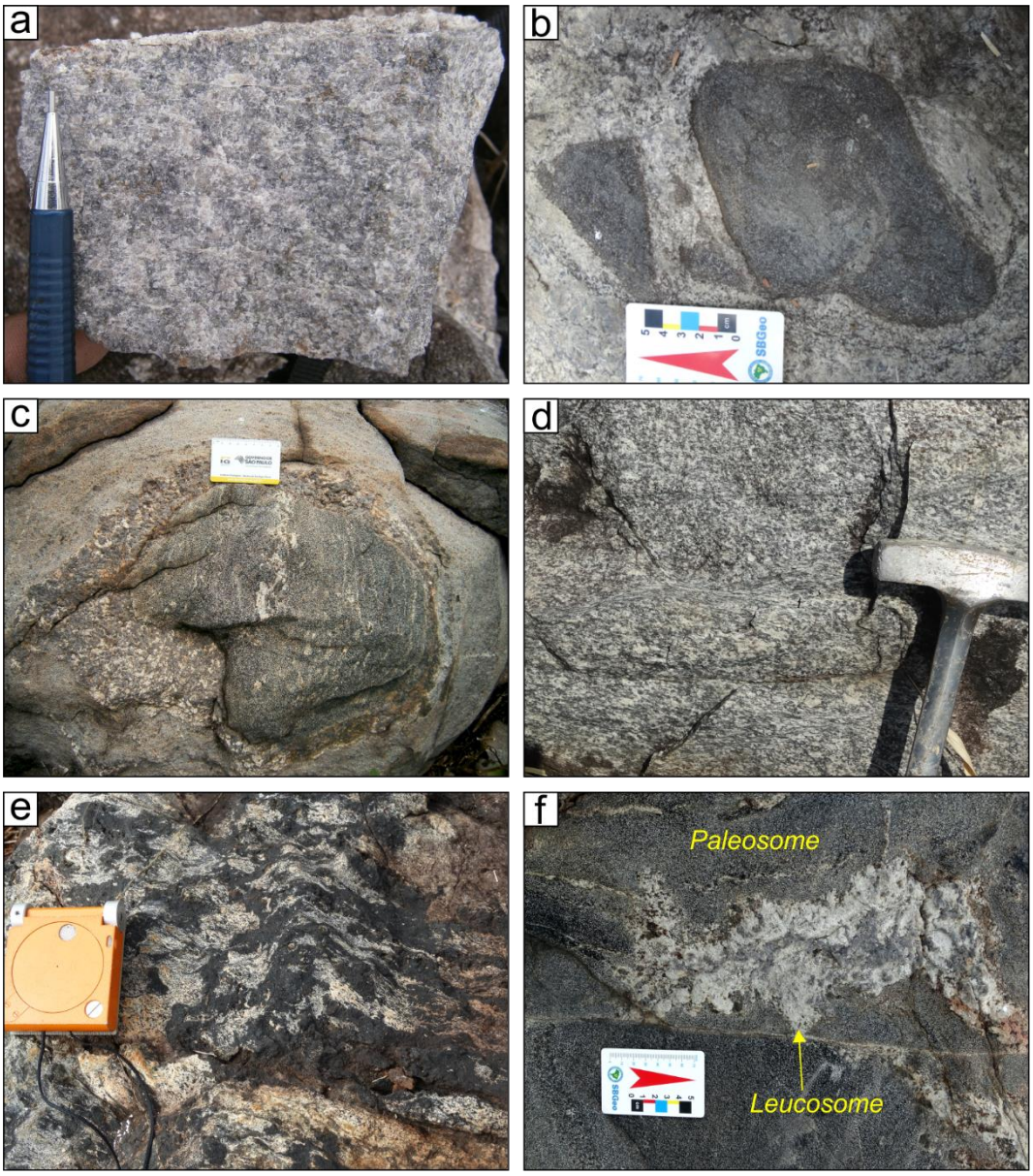

Figure 4. Mesoscopic aspects of the sodic rocks from Ouro Verde area. (a) Felsic granulite with tonalitic to trondhjemitic compositions, brownish greyish colored and greasy looking; (b) and (c) mafic granulite enclave hosted by felsic granulite; (d) tonalitic granitoid showing moderate mylonitic foliation; and (e) and (f) relation between the tonalitic granitoids (leucosome) and mafic rock (paleosome), suggesting migmatization process (metatexite).

Fieldwork observations allow us identify two different structural domains on the sodic rocks: (1) an E–W to WNW–ESE steeply inclined foliation – with rare N–S occurrences – towards mostly the S, associated with shallow-to-moderately plunging mineral stretching lineation, present in the Mesoarchean felsic granulites; and (2) an E–W steeply inclined well-developed foliation towards both the N and S, and steep-to-subvertically plunging mineral

stretching lineation, printed on Neoarchean enderbites (see stereoplots in Figure 3). It is worth noting that the structural pattern of the studied enderbitic rocks is quite similar to those of coeval hybrid granitoids from Vila União area (Oliveira et al., 2018; Marangoanha et al., unpublished results).

Outcrop-scale analyses reveal significant differences between both orthopyroxene-bearing metamorphic and magmatic rocks. The structures present in the metamorphic rocks are well-developed foliations, defined mainly by mineral foliation – marked by the preferred orientation of platy mineral grains and aggregates (Figure 5a), and a planar shape fabric defined by the flattened crystals, like quartz ribbons (Figure 5b), and flattened mafic enclaves (Figure 5c) – accompanied by occasional gneissic banding (Figure 5d) and folded mafic enclaves (Figure 5e). All these types of foliation trends E–W to NW–SE with moderate (40–69°) to subvertical (70–89°) dips towards mostly the S, and the mineral stretching lineation plunges are moderate (35–60°), towards predominantly the S (cf. Figure 3). Besides these structural data, it was also identified a not typical structural pattern, defined by a uniform N–S-trending foliation with steep dips towards the W (69–74°). This N–S pattern has a restrict occurrence, and is clearly crosscut (or overprinted) by the E–W to NW–SE pattern (Figure 5f). High thermal event is also recorded by scarce migmatization observed on a small scale, although some portions of the granulitic bodies still preserve original igneous texture.

On the other hand, the orthopyroxene-bearing magmatic rocks (enderbite) present a simpler structural pattern, described basically by moderate mylonitic foliation (Figure 5h and i), which trends E–W, associated with subvertical dips toward mostly the S, and mineral lineation plunging steep-to-subvertically towards the S (70–84°). This structural pattern rarely affects the felsic granulitic rocks as evidenced by Neoarchean shear zones dislocating N–S-trending Mesoarchean fabrics (Figure 5i).

5. Methods

5.1. Mineral chemistry

Orthopyroxene of three representative samples from the felsic granulites were submitted to wavelength dispersive spectroscopy (WDS) quantitative analyses at the Laboratório de Microanálises da Universidade Federal do Pará (UFPA) using a JEOL JXA-8230 microprobe, aiming to obtain the main compositional features of this mineral, in order to define the metamorphic or igneous nature. Operating conditions were 15 kV for the column acceleration voltage, 20 nA for beam current and analysis time of 10 seconds. The standards

used for instrument calibration were microcline (Si, Al and K), albite (Na), andradite (Fe and Ca), pyrophanite (Ti and Mn), vanadinite (Cl and V), forsterite (Mg) and topaz (F).

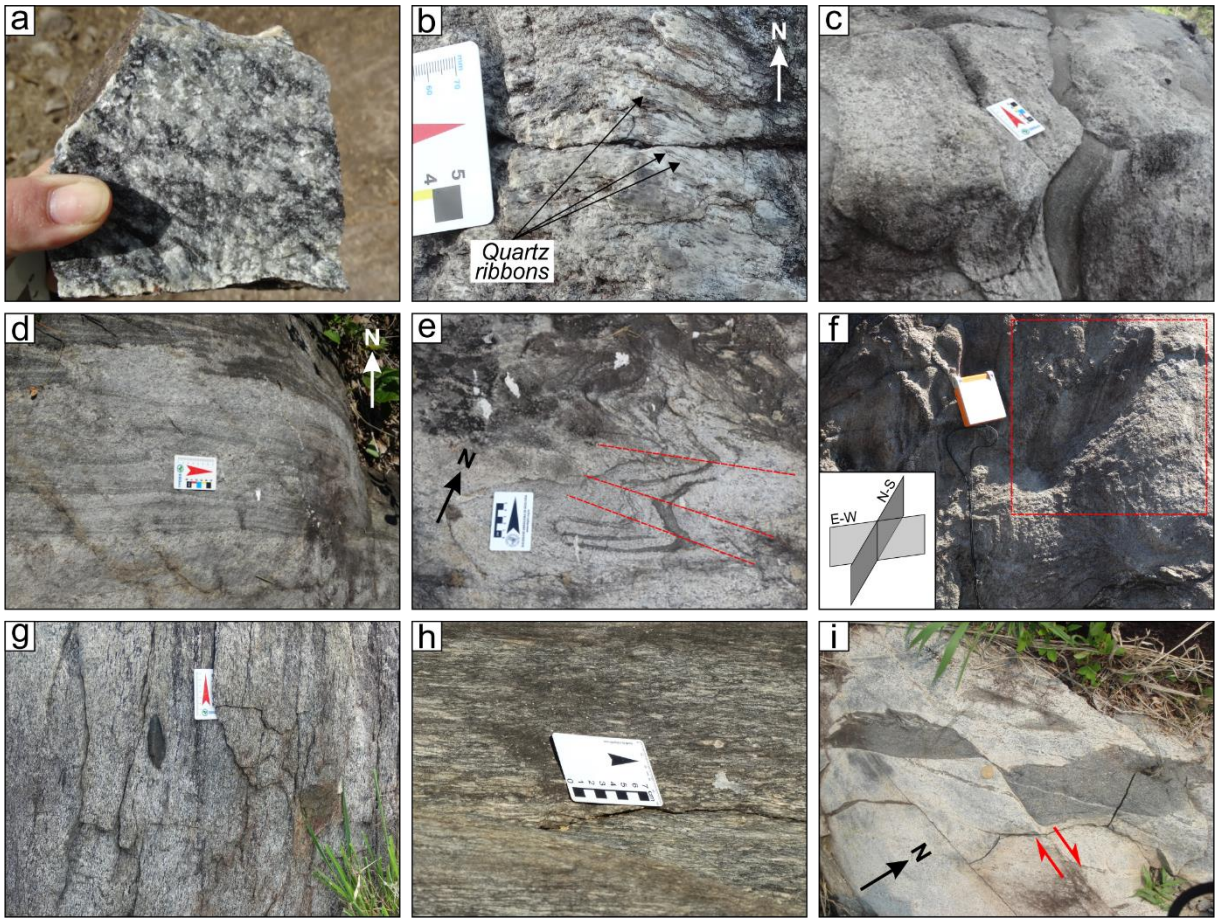

Figure 5. Structural aspects of the Meso- and Neoarchean orthopyroxene-bearing sodic rocks from the studied area. (a) rock showing preferred orientation of platy mineral grains and aggregates; (b) planar shape fabric defined by the flattened quartz aggregates (ribbons); (c) flattened mafic enclaves; (d) gneissic banding; (e) folded mafic enclaves (the dashed lines represent the axial traces); (f) N–S-trending foliation crosscut by the E–W one; (g) and (h) moderate mylonitic foliation, associated with subvertical dips; and (i) Neoarchean shear band dislocating Mesoarchean fabrics (the earlier structure: N–S-trending) represented by the felsic granulite and the mafic enclave.

5.2. Geochemistry

Around 0.5–5 kg fresh samples for whole-rock chemical analysis were crushed at the Oficina de Preparação de Amostras, Federal University of Pará (OPA/UFPA), Brazil, by using both primary and secondary jaw crushers, until the particles reach between 0.1 to 0.3 mm in size, and then this material was powdered in an agate swing mill until reaches a particle size <10 µm. Twenty analyses were obtained at ACME Analytical Laboratory, performed by ICP-AES for major elements and ICP-MS for trace elements (including the rare-earth elements). Geochemical diagrams were generated by using GCDkit software

(Janoušek et al., 2003). More detailed information about analytical procedures can be found at www.acmelab.com.

5.3. Geochronology

Zircon grains from three representative felsic granulites, one mafic granulite and two intrusive orthopyroxene tonalites (enderbites) were separated at the Isotopic Geology Laboratory, Federal University of Pará (Pará-Iso/UFPA). Around 10–20 kg rock for each sample were crushed, grinded and sieving into fractions between 125–175 μm, and then processed using isodynamic magnetic separator and heavy-liquid (bromoform), followed by hand picking under a binocular microscope.

To carry out both the SHRIMP (Sensitive High-Resolution Ion Microprobe) and LA-SF-ICP-MS (Laser Ablation – Sector Field – Ion Coupled Plasma Mass Spectrometer) U-Pb dating methods, representative zircon grains were mounted in epoxy resin and polished down to expose the grain centers. Internal morphology of the zircon grains was examined using cathodoluminescence (CL) and backscattered electron (BSE) imaging in order to choose potential target sites for U-Pb analyses. CL and BSE were collected using a JEOL JXA-8230 scanning electron microprobe (SEM) working at 15 kV, 20 μA and 11 mm working distance, equipped at Laboratório de Microanálises, Federal University of Pará (Brazil).

Four U-Pb zircon analyses were performed using a SHRIMP IIe system installed at the Laboratório de Geologia de Alta Resolução, University of São Paulo, Brazil (GeoLab/USP), whose instrumental performance and analytical procedures are documented by Stern (1998), Williams (1998) and Sato et al. (2008, 2014). The standards used were SL 13 for U composition reference (238 ppm; Sato et al., 2014), and TEMORA-2 zircon (416.78±0.33 Ma; Black et al., 2003) as isotope ratios standard. The spot size of the primary ion beam was 30μm. Isoplot 4.15 software of Ludwig (2008) was used to calculate the $^{207}Pb/^{206}Pb$ ages and build Concordia plots. Errors quoted in tables and figures are at the 1σ levels.

Two U-Pb analyses were conducted by *in situ* LA-SF-ICP-MS at the Laboratório de Geoquímica Isotópica of Federal University of Ouro Preto (UFOP), Brazil, with a ThermoScientific Element 2 Sector Field (SF) ICP-MS coupled to a CETAC LSX-213 G2+ (λ = 213 nm) Nd:YAG laser following the method described in Gerdes and Zeh (2006, 2009) and Frei and Gerdes (2009). Helium was used as the carrier gas to enhance the transport efficiency of ablated material. Individual analytical spots were typically of 20 μm in diameter. U-Th-Pb ratios and absolute abundances were determined relative to the GJ-1 (608.5±1.5 Ma; Jackson et al., 2004), BB (564±33 Ma; Santos et al., 2017) and Plešovice (337±1 Ma; Sláma

et al., 2008) zircon standards. The analytical data were calculated and plotted using the Isoplot 4.15 software (Ludwig, 2008). Error ellipses on Concordia plots are shown at the 95% confidence level (2σ). The analytical uncertainty in all grouped age data is quoted at the 95% confidence level (2σ).

One sample was analyzed by single zircon Pb-evaporation method, which was carried out on a Finnigan MAT 262 TIMS (Thermal Ionization Mass Spectrometry) at Pará-Iso/UFPA, following the method stablished by Kober (1986, 1987), and according to the detailed technical procedure described by Costi et al. (2000) and Noce et al. (2000). Whole zircon grains were analyzed using a rhenium filament configuration. Three evaporation steps were performed, at 1450, 1500 and 1550°C, during 5 minutes each one. After each step the Pb isotopic composition was measured using the ion counting collector, and then each step provides an age from the average of the $^{207}Pb/^{206}Pb$ ratios. The age of the sample is calculated from the results of the highest temperature step of all crystals. Steps with lower ages probably reflect Pb loss after crystallization and were not used to sample age calculation. Weighted mean and errors on the ages were calculated following Gaudette et al. (1998). Common Pb correction was performed using the model of Stacey and Kramer (1975). Analyses with $^{204}Pb/^{206}Pb$ ratios higher than 0.0004 were rejected in order to avoid significant errors caused by inaccurate common Pb correction. Errors quoted in tables and figures are at the 2σ levels.

5.4.Lu-Hf isotopic data

Lu–Hf isotopic analyses were carried out at the Isotope Laboratory of Ouro Preto Federal University (UFOP), Brazil, using a multi-collector ICP-MS Thermo-Scientific Neptune Plus system coupled to a Photon-Machines 193 ArF Excimer laser ablation system, following the methods suggesting by Gerdes and Zeh (2006, 2009). Hf isotopic data reported in this study were obtained from the zircon grains with U–Pb data. Laser spots for Lu–Hf analyses were drilled on or immediately beside the previous U–Pb spots, but always within the same zircon domain characterized by CL and BSE imaging.

Data were collected in static mode during 60 seconds of ablation with a spot size of 50 µm. Nitrogen (~0.080 l/min) was introduced into the Ar sample carrier gas. Typical signal intensity was ca. 10 V for ^{180}Hf. The isotopes ^{172}Yb, ^{173}Yb and ^{175}Lu were simultaneously monitored during each analysis step to allow for correction of isobaric interferences of Lu and Yb isotopes on mass 176. The ^{176}Yb and ^{176}Lu were calculated using a $^{176}Yb/^{173}Yb$ of 0.796218 (Chu et al., 2002) and $^{176}Lu/^{175}Lu$ of 0.02658 (JWG in-house value). The correction for instrumental mass bias utilized an exponential law and a $^{179}Hf/^{177}Hf$ value of 0.7325

(Patchett and Tatsumoto, 1980) for correction of Hf isotopic ratios. The mass bias of Yb isotopes generally differs slightly from that of the Hf isotopes with a typical offset of the βHf/βYb of ca. 1.04 to 1.06 when using the $^{172}Yb/^{173}Yb$ value of 1.35274 from Chu et al. (2002). This offset was determined for each analytical session by averaging the βHf/βYb of multiple analyses of the JMC 475 solution doped with variable Yb amounts and all laser ablation analyses (typically n > 50) of zircon with a ^{173}Yb signal intensity of > 60 mV. The mass bias behavior of Lu was assumed to follow that of Yb. The Yb and Lu isotopic ratios were corrected using the βHf of the individual integration steps (n = 60) of each analysis divided by the average offset factor of the complete analytical session. The results were calibrated with the standard zircon Temora (415 Ma; Hf = 0.282680), Mud Tank (730 Ma; Hf = 0.282501) and 91500 (1065 Ma; Hf = 0.282307). Initial epsilon hafnium value εHf(t) was calculated using a decay constant of 1.865×10^{-11} yr^{-1} (Scherer et al., 2001). The average MORB (DM) $^{176}Lu/^{177}Hf$ and $^{176}Hf/^{177}Hf$ of 0.0384 and 0.283165, respectively, and a value of 0.0113 for the average continental crust (Taylor and McLennan, 1985; Wedepohl, 1995), $^{176}Lu/^{177}Hf = 0.0336$, and $^{176}Hf/^{177}Hf = 0.282785$ for CHUR (Bouvier et al., 2008).

6. Petrography

6.1. Felsic granulites

In general, the felsic granulites are mostly leucocratic, brownish greyish colored (cf. Figure 4a and 5a), greasy looking and inequigranular, characterized by a typical porphyroclastic texture (medium- to coarse-grained) with granoblastic matrix (fine-grained). The porphyroclasts are composed exclusively by plagioclase, whereas the granoblastic matrix is made up mainly by plagioclase, quartz, biotite, ortho- and clinopyroxene, and amphibole. These rocks display slight to well-developed preferred orientation, defined by oriented both biotite flakes and quartz ribbons (or eventually forming large lenses-like aggregates) alternating with bands composed mostly of fine-grained plagioclase neoblasts developing polygonal array. Oriented plagioclase porphyroclasts also describe the foliation printed in these rocks. These granulites are characterized by homogeneous variation in modal mineralogy and are composed basically of plagioclase (59.00–71.55 vol.%), quartz (25.45–36.65 vol.%), biotite (0.15–10.85 vol.%), orthopyroxene (0.05–7.50 vol.%) and amphibole (up to 1.50 vol.%). Accessory phases include opaque minerals, clinopyroxene, K-feldspar, zircon and apatite. Secondary minerals are chlorite, epidote and sericite.

Plagioclase occurs as relicts (Pl_1), mostly up to 2.5 mm, but eventually can reach up 4.2 mm, represented by anhedral to subhedral porphyroclasts, produced by the crushing or

fragmentation of large grains from the protolith, and are parallel to the foliation (Figure 6a); as very fine crystals (Pl_2), made up when smaller fragments around Pl_1 are further crushed to finer and finer sizes (sometimes close to becoming powders), which both occurs associated (Pl_1 surrounded by Pl_2) and describe the core-mantle texture (cf. Figure 6a); and forming mosaics of polygonal-shaped recrystallized plagioclase (Pl_3) in the granoblastic fabric, up to 0.1 mm, with ~120° dihedral angles (Figure 6b). Pl_1 and eventual Pl_2 display undulose extinction, kink bands and tapering twins (Figure 6c) induced by the deformation, whereas Pl_3 shows strain-free aspects. Concerning quartz, it was recognized Qz_1, corresponding to fine aggregates as ribbons (Figure 6d) and lenses (Figure 6e), up to 0.6 mm, with undulose extinction, which wrap around Pl_1 (cf. Figure 6d); fine-grained neoblasts (Qz_2), up to 0.1 mm, which display strain-free aspects and coexist with Pl_3 (cf. Figure 6b); and very fine-grained crystals (Qz_3) present along cleavage planes (describing symplectite texture) of retrograde biotite (Figure 6f) and amphibole. Brownish relict biotite (Bt_1; Figure 6g) is up to 1 mm, occur mainly along grain boundaries of Pl_1 and Qz_1, and exhibits strong preferred orientation, aligned along the rock foliation (cf. Figure 6e). Late biotite (Bt_2) represents a retrograde product formed at the expense of the orthopyroxene (cf. Figure 6f). Orthopyroxene (Opx) displays subhedral to anhedral crystal shape, which textural evidences strongly suggest their metamorphic origin by Bt_1 breakdown (Figures 6g and h). In order to ratify the nature of these orthopyroxenes, it was performed mineral chemistry analyses and plotted in the discrimination diagram from Rietmeijer (1983; Figure 7) that confirm their metamorphic origin. It can also occur totally or partially replaced by Bt_2 – or less common by amphibole (Amp) – especially along fractures (cf. Figure 6f). The first appearance of K-feldspar (Kfs_1) is in the interiors of deformed plagioclase porphyroclasts, forming small islands (‘blebs’; Figure 6i) or as antiperthitic cores. Subordinate fine K-feldspar crystals (Kfs_2) are also present close to Opx, Qz_3, Bt_1 and/or Amp, formed during the prograde metamorphism at expenses of the Bt_1 breakdown (cf. Figure 6h).

6.2. Enderbites

Although these rocks display remarkable mylonitization – that will be detailed below – they still exhibit considerable original magmatic texture, and we consider that their original mineralogy assemblage remains unchanged. Therefore, modal analyses were performed on 11 representative samples by counting between 1,500 and 2,000 points/sample, with a Stageledge (Endeeper) point counter. The modal compositions are presented in Table 1. These rocks mainly comprise plagioclase (51.27–67.01 vol.%), quartz (7.33–37.80 vol.%), clinopyroxene

(up to 22.27 vol.%), amphibole (up to 15.07 vol.%), biotite (up to 14.65 vol.%) and orthopyroxene (up to 11.73 vol.%) as essential minerals. The varietals and accessory phases are opaque minerals, primary epidote, titanite, allanite and zircon. Secondary phases include chlorite and secondary epidote.

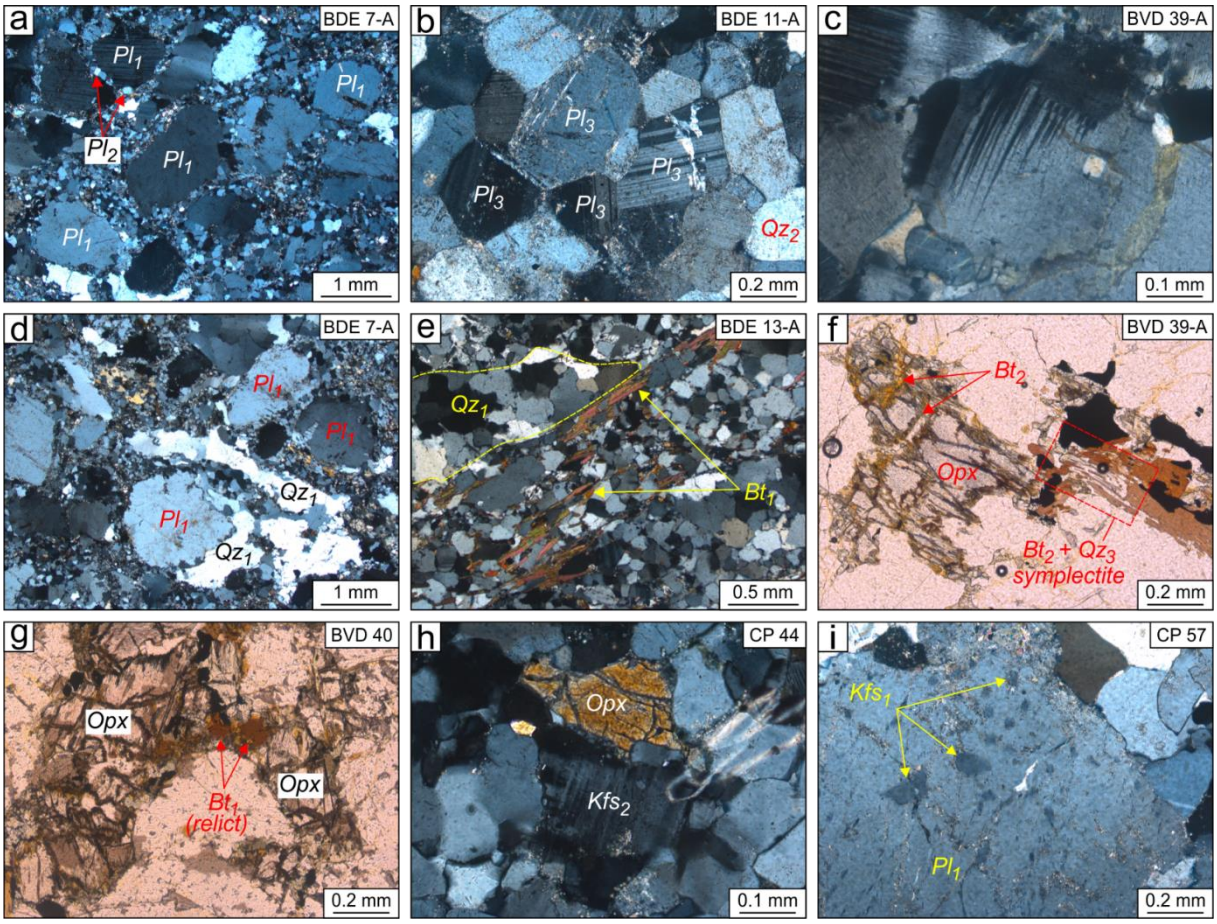

Figure 6. Representative photomicrographs of the felsic granulite. (a) General aspect of this unit, showing a typical porphyroclastic texture (medium- to coarse-grained) represented by plagioclase (Pl_1), with granoblastic matrix (fine-grained), composed mostly by plagioclase (Pl_2 and Pl_3) and quartz (Qz_1 and Qz_2); (b) fine-grained plagioclase (Pl_3) and quartz (Qz_2) neoblasts developing polygonal array in a granoblastic fabric, with strain-free aspects and forming ~120° dihedral angles between them; (c) plagioclase (Pl_1) displaying tapering twins; (d) ribbon-like quartz (Qz_1) with undulose extinction wrapping around plagioclase porphyroclast (Pl_1); (e) lens-like quartz (Qz_1) and biotite flakes (Bt_1) displaying well-developed preferred orientation; (f) detail of orthopyroxene (Opx) rimmed by symplectitic biotite-quartz (Bt_2 + Qz_3), and biotite (Bt_2) occurring along orthopyroxene fractures, both textures suggesting retrometamorphic path; (g) relict biotite (Bt_1) almost completely replaced by orthopyroxene in a prograde metamorphism; (h) orthopyroxene (Opx) + K-feldspar (Kfs_2) formed at the expense of the biotie (Bt_1) breakdown (prograde metamorphism); and (i) K-feldspar (Kfs_1) occurring in the interiors of deformed plagioclase porphyroclasts, forming small islands ('blebs'). Photomicrographs (a), (b), (c), (d), (e), (h) and (i) under crossed nicols, and (f) and (g) under parallel nicols.

When plotted in the Q-A-P diagram (Le Maître et al., 2002; Figure 8), these rocks fall mostly into the tonalitic/trondhjemitic field, while two samples in the quartz dioritic field. In general, they are locally homogeneous in appearance, gray-white in color, equigranular, medium-grained, predominantly hololeucocratic and leucocratic (M' = 1.80–25.66 vol.%),

with subordinate mesocratic occurrences (M' up to 39.40 vol.%; cf. Figure 8). The IUGS classification for orthopyroxene-bearing granitoids (Streckeisen, 1974) classifies these rocks as enderbites.

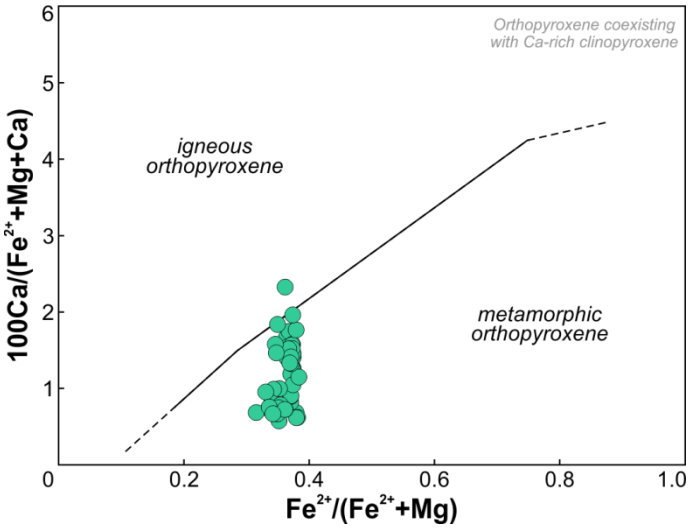

Figure 7. Genetic discriminative diagram for orthopyroxene (Rietmeijer, 1983).

Table 1. Modal compositions of the enderbites from the central portion of Canaã dos Carajás domain, Carajás province.

Sample	BVD 51	BVD 35-A	CP 89	BVD 41-B	CP 88	BVD 36-B	BVD 41-A	BVD 52-A	BVD 36-A	BVD 53	BVD 52-B
Variety	Quartz diorite		Trondhjemite			Tonalite					
Minerals (vol.%)											
Quartz	7.33	9.33	33.60	34.80	37.80	21.47	21.67	22.67	26.35	29.20	30.33
Plagioclase	67.01	51.27	62.50	58.81	54.00	64.32	57.73	58.79	51.40	59.26	58.33
Alkali feldspar	-	-	-	-	-	-	-	<0.01	<0.01	-	<0.01
Biotite	-	-	-	1.60	5.10	5.40	13.40	0.67	14.65	0.07	-
Amphibole	5.73	4.13	-	4.40	0.50	5.00	4.33	15.07	4.40	5.20	4.40
Clinopyroxene	9.93	22.27	-	0.13	-	0.27	0.80	0.40	-	0.47	2.67
Orthopyroxene	5.20	11.73	-	0.13	-	2.67	1.60	1.00	1.95	1.73	2.73
Opaque minerals	4.73	1.27	1.50	-	2.20	0.87	0.40	1.40	0.95	3.87	1.47
Titanite	-	-	0.30	0.13	-	-	-	-	-	0.13	-
Epidote	0.07	-	-	-	-	-	-	-	-	0.07	0.07
Allannite	-	-	-	-	-	-	-	-	-	<0.01	-
Zircon	-	-	<0.01	-	0.20	-	0.07	-	<0.01	<0.01	<0.01
Chlorite	-	-	2.10	-	0.20	-	-	-	0.30	-	-
A+P	67.01	51.27	62.50	58.81	54.00	64.32	57.73	58.79	51.40	59.26	58.33
Colour index (M')	25.66	39.40	3.90	6.39	8.20	14.21	20.60	18.54	22.25	11.54	11.34

Abbreviations: <0.01 (mineral present but not counted), A+P (alkali-feldspar + plagioclase sum).

Plagioclase occurs predominantly as subhedral porphyroclasts (mostly between 2.0 and 4.5 mm, but eventually can reach up to 7.0 mm) with undulose extinction and partially recrystallized, mantled by fine-grained aggregate of new grains, induced by bulging (BLG-recrystallization) and subgrain rotation recrystallization (SGR-recrystallization), which define a core-mantle structure (Figures 9a and b). These porphyroclasts develop a preferred orientation, concordantly to the dominant E–W regional trend, which sometimes can present

strain shadows of quartz and biotite (Figure 9c). Deformation twinning (tapering twins) and by kinking (Figure 9d) in plagioclase porphyroclasts are also common. Subordinate crystals with brittle fracturing may present submagmatic microfractures filled with quartz-feldspar aggregates optically continuous with the immediately adjacent primary quartz (Figure 9e), which is a good evidence of melt-present deformation (Bouchez et al., 1992). Some euhedral to subeuhedral crystals mantled by mafic minerals (orthopyroxene, clinopyroxene and amphibole) display free-strain aspects (Figure 9f), suggesting that these mafic aggregates had acted as a 'shield' during the melt-present deformation, and protected plagioclase crystals from this deformation. Quartz forms anhedral crystals, up to 0.6 mm, and is almost fully recrystallized, mainly by both bulging (BLG-recrystallization; Figure 9g) and SGR-recrystallization (Figure 9h), whereas some occurrences show undulose extinction with subgrains formation induced by recovery process. Clino- and orthopyroxene and amphibole present subhedral crystals, with anhedral occurrences, up to 2.2 mm, and are practically preserved from deformation process (cf. Figure 9f), whereas rare BLG-recrystallization is recognized. Biotite is brownish-red, up to 0.7 mm, and occurs aligned with the plagioclase porphyroclasts, defining preferred mineral orientation (cf. Figure 9c). Eventually, it develops smooth kink bands. Peritectic reactions have been observed in the mafic phases, as defined by amphibole (±biotite) rimming ortho- and clinopyroxene (Figure 9i).

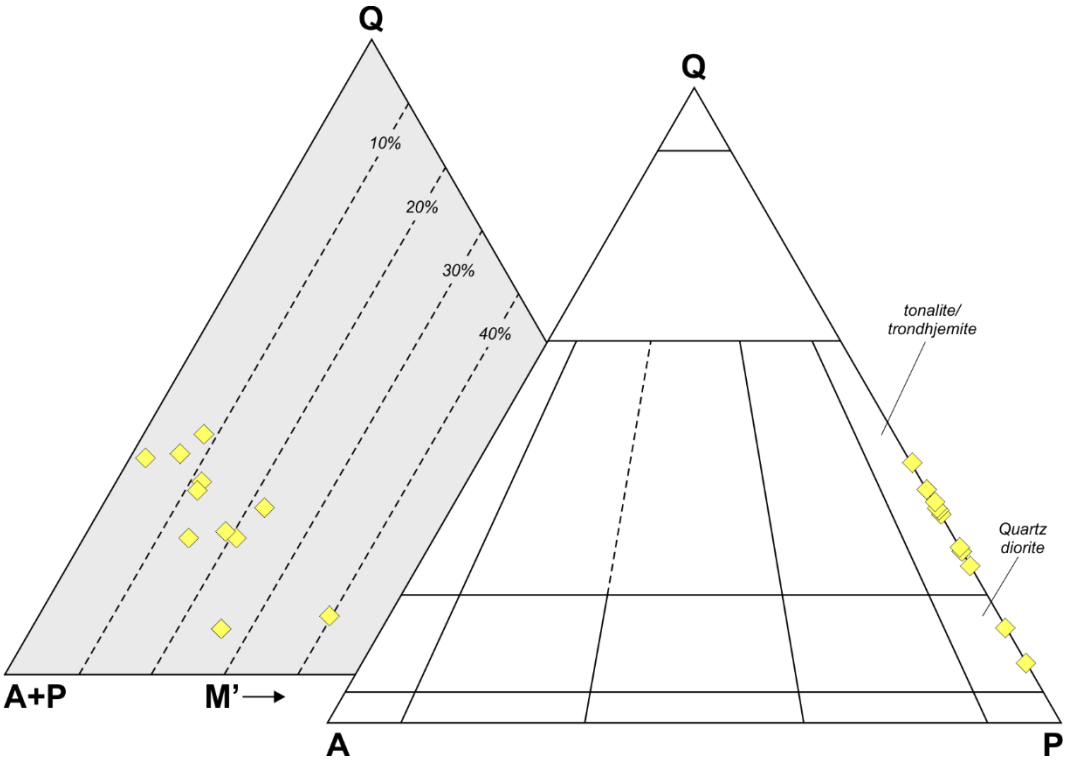

Figure 8. Q-A-P and Q-(A+P)-M plots for the enderbites from the studied area (Le Maître et al., 2002).

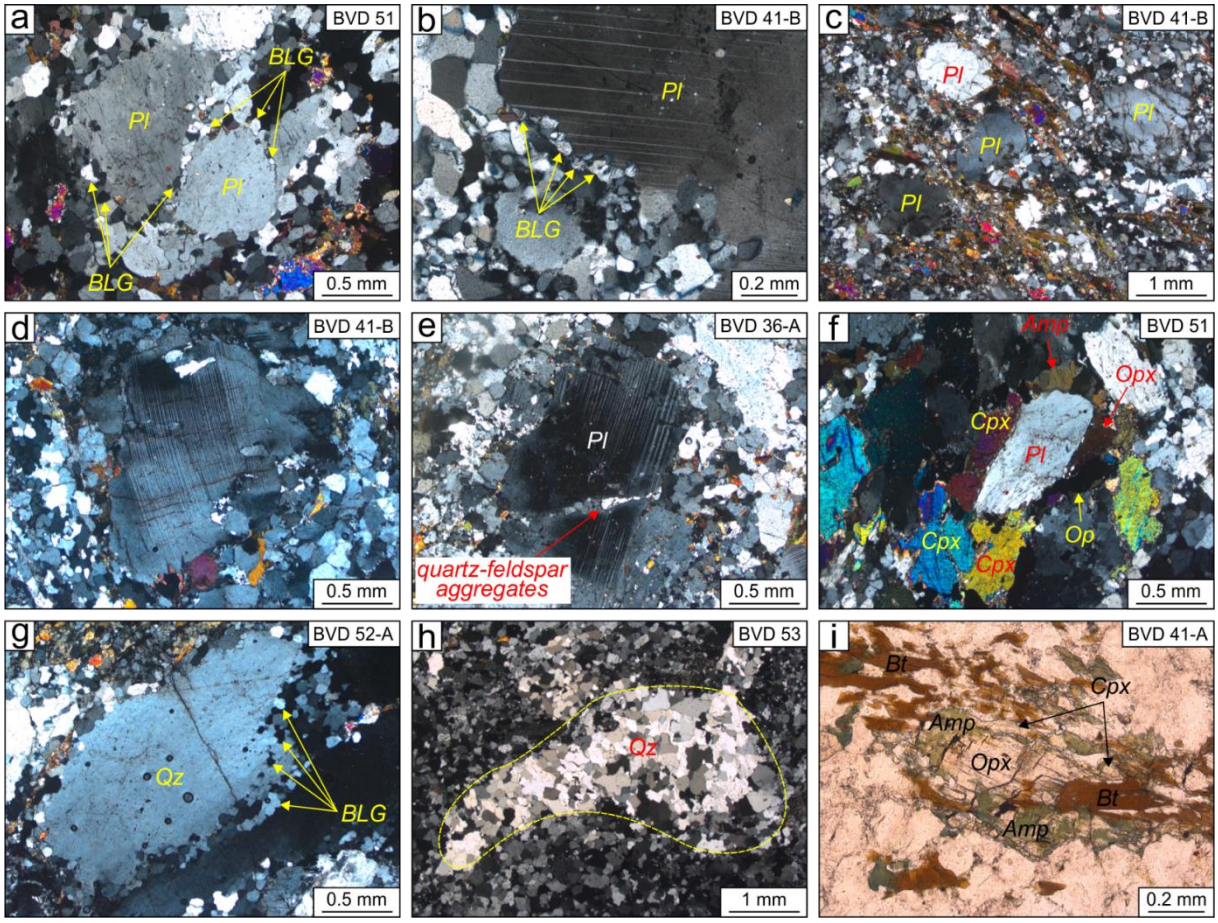

Figure 9. Representative photomicrographs of the enderbite. (a) and (b) core-mantle structures in plagioclase porphyroclasts formed by bulging recrystallization (BLG); (c) general aspect of this unit, defined by the mylonitic foliation, which plagioclase porphyroclasts develop a preferred orientation with strain shadows of quartz and biotite; (d) deformation by kinking in plagioclase porphyroclast; (e) submagmatic microfractures in subhedral plagioclase porphyroclast filled with quartz-feldspar aggregates; (f) subhedral plagioclase porphyroclast mantled by mafic minerals displaying free-strain aspects; (g) incipient to moderate recrystallization to small new grains by BLG in quartz; (h) quartz entirely recrystallized by subgrain rotation recrystallization (SGR); and (i) peritectic reactions in the mafic phases defined by ortho- and clinopyroxene rimmed by amphibole and biotite. Photomicrographs (a), (b), (c), (d), (e), (f), (g) and (h) under crossed nicols, and (i) under parallel nicols. Abbreviations: Amp (amphibole); Bt (biotite), Cpx (clinopyroxene); Op (opaque minerals); Opx (orthopyroxene); Pl (plagioclase) and Qz (quartz).

7. Geochemistry

7.1. Introduction

Eight fresh samples of the felsic granulite and twelve ones of the enderbite were selected for geochemical analyses, whose results are given in Table 2, and the analytical methods are described in the section 5.1.

7.2. Major and minor elements

The felsic granulites and the enderbite present distinct chemical behavior between each other. The first one comprises a narrow range of SiO_2 content, between 68.40 and 71.57 wt.%, whereas the second one shows a wider variation, ranging from 53.00 to 80.40 wt.%. In

Harker diagrams (Figure 10), TiO_2, Al_2O_3, Fe_2O_3*, CaO, MgO and Na_2O display a negative correlation with SiO_2 related to both felsic granulites and the enderbite. The enderbite display the higher TiO_2 (0.15–2.17 wt.%), Fe_2O_3* (1.20–6.23 wt.%), CaO (2.09–10.45 wt.%), MgO (0.34–4.39 wt.%) and Na_2O (4.53–7.11 wt.%), and the lower Al_2O_3 (11.15–15.65 wt.%) contents compared to the felsic granulites [TiO_2 (0.20–X0.33 wt.%), Fe_2O_3* (1.15–2.77 wt.%), CaO (2.96–4.09 wt.%), MgO (0.49–1.49 wt.%), Na_2O (4.73–6.14 wt.%) and Al_2O_3 (15.04–16.35 wt.%)].

7.3. Trace elements

Both felsic granulites and the enderbites display different behavior concerning trace element in Harker diagrams (Figure 11), and both do not show any clear correlation with SiO_2 content. In general, the Ba and Sr contents are higher in the felsic granulites (111–931 ppm and 554.3–765.0 ppm, respectively) than in the enderbite [71.1–334 ppm (with an isolated sample showing 780 ppm) and 274.5–371.0 ppm (with only one sample displaying 655.0 ppm), respectively]. The Rb values from these two groups of sodic rocks are almost overlapped, which the enderbites exhibit values ranging from 3.4 to 35.7 ppm, while the felsic granulites show contents between 4.0 and 29.7 ppm. Concerning HFSE (high field strength elements), the enderbites are enriched in Y, Nb and Zr compared to the felsic granulites. The first one shows contents varying between 8.6–35.6 ppm, 3.9–32.1 ppm and 33.0–775.0 ppm, respectively, while the second one exhibits values ranging from 1.0–10.1 ppm, 1.1–8.1 ppm and 90.7–274.6 ppm, respectively.

In the chondrite-normalized REE diagrams (Figure 12a), the felsic granulites show enrichment in LREE over HREE, resulting in a moderate to high fractionated REE pattern (La_N/Yb_N ratio between 9.62 and 143.08). It is recorded the predominance of positive Eu anomaly (Eu/Eu* = 1.09–3.01), whereas subordinate slightly negative Eu anomaly is also present (Eu/Eu* = 0.57–0.95). The enderbites show moderate REE contents and a low fractionated REE pattern (Figure 12b), with La_N/Yb_N ratio varying between 1.51 and 33.56. The Eu anomaly varies from slightly negative to positive (Eu/Eu* = 0.49–1.98).

Table 2. Geochemical compositions of the felsic granulites and enderbites from the central portion of Canaã dos Carajás domain, Carajás province.

Sample	BVD 39-A	BVD 40	CP 57	BDE 7-A	BDE 13-A	CP 44	BDE 1-A	BDE 11-A	BVD 51	BVD 35-A	BVD 53	BVD 41-A	BVD 52-A	CP 88	BVD 36-B	BVD 52-B	BVD 36-A	ED 1	CP 40	BVD 41-B
Unit	Felsic granulite								Enderbite											
Major elements (wt.%)																				
SiO_2	68.40	68.50	70.12	70.53	70.64	71.02	71.09	71.57	53.00	56.60	65.80	66.50	68.50	69.34	69.80	70.50	70.90	77.10	77.15	80.40
TiO_2	0.30	0.29	0.26	0.33	0.24	0.26	0.29	0.20	2.17	0.44	1.07	0.28	0.75	0.76	0.77	0.78	0.78	0.18	0.19	0.15
Al_2O_3	16.35	16.30	16.08	15.04	15.72	15.55	15.45	15.96	13.60	15.65	14.35	14.90	13.60	13.98	13.65	13.50	13.60	11.25	11.80	11.15
Fe_2O_3*	2.77	2.51	2.40	2.15	2.15	2.38	1.15	1.16	6.23	4.15	5.33	4.32	2.96	3.86	4.01	2.82	3.72	1.90	1.93	1.20
MnO	0.03	0.03	0.02	0.03	0.02	0.03	0.02	0.01	0.05	0.05	0.03	0.04	0.03	0.06	0.06	0.04	0.03	0.01	0.02	0.01
MgO	0.90	0.78	0.77	1.49	0.75	0.77	0.72	0.49	4.39	3.60	0.78	2.85	1.73	1.87	2.09	1.31	2.09	0.60	0.63	0.34
CaO	4.09	3.81	3.42	2.96	3.51	3.50	3.84	3.34	10.45	10.00	3.90	3.56	5.20	4.13	3.76	4.70	3.50	2.40	2.44	2.09
Na_2O	4.83	5.17	5.06	6.14	5.31	4.73	6.14	4.77	6.31	7.11	6.24	5.16	5.25	5.00	4.69	4.89	4.60	4.53	4.71	4.54
K_2O	1.09	1.17	1.28	0.26	0.90	1.04	0.23	1.51	0.59	0.74	0.68	1.69	0.48	0.58	0.83	0.47	0.85	0.57	0.56	0.54
P_2O_5	0.10	0.11	0.08	0.10	0.08	0.08	0.09	0.04	0.02	<0.01	0.01	0.24	<0.01	0.01	<0.01	0.04	0.01	<0.01	0.01	<0.01
LOI	0.37	0.46	0.30	0.80	0.50	0.40	0.80	0.70	0.78	0.81	0.91	0.41	0.35	0.20	0.71	0.71	0.58	0.49	0.40	0.54
Total	99.23	99.13	99.79	99.83	99.82	99.76	99.82	99.75	97.59	99.15	99.10	99.95	98.85	99.79	100.37	99.76	100.66	99.03	99.84	100.96
Trace elements (ppm)																				
Ba	682	625	616	137	536	484	111	931	71.1	96.3	111	780	250	270	334	305	298	191.5	176	207
Sr	697.0	765.0	601.9	572.3	606.8	554.3	614.2	732.1	306.0	371.0	288.0	655.0	317.0	324.0	284.0	318.0	299.0	291.0	274.5	284.0
Rb	8.8	14.0	16.9	6.7	14.8	8.9	4.0	29.7	3.4	4.1	5.3	35.7	9.0	12.4	31.5	6.2	28.3	8.4	7.2	8.2
Zr	128.0	111.0	93.8	137.1	124.9	161.1	274.6	90.7	173.0	33.0	775.0	46.0	324.0	323.1	328.0	378.0	380.0	307.0	243.2	332.0
Y	2.5	4.9	1.9	3.1	2.4	2.3	10.1	1.0	23.9	35.6	8.6	15.5	16.5	12.1	15.0	14.8	16.5	30.0	28.9	19.0
Hf	3.7	3.0	2.3	4.1	3.0	4.5	6.5	2.4	4.6	1.0	18.7	1.2	8.5	8.3	9.5	10.5	9.3	10.5	7.3	10.5
Nb	2.6	2.6	1.6	5.9	1.1	4.9	8.1	1.6	32.1	8.8	20.4	3.9	12.0	12.2	15.0	12.8	13.3	14.4	15.6	13.1
Ta	0.4	0.4	0.1	0.9	0.3	0.1	1.3	0.3	1.2	0.6	1.5	0.4	1.0	0.7	1.3	1.1	1.3	1.1	0.9	2.4
Th	0.4	0.5	0.3	15.6	0.2	4.9	28.2	1.0	1.4	0.2	7.7	2.0	10.3	10.8	13.8	12.6	10.8	10.3	10.5	17.4
La	21.4	17.0	15.4	7.0	19.7	33.7	10.9	13.2	16.5	9.3	49.9	25.8	14.4	10.4	14.7	12.9	14.4	8.0	6.8	8.8
Ce	34.0	30.8	26.9	14.4	32.4	62.3	31.0	18.8	32.5	20.0	80.5	52.8	23.1	17.2	22.6	22.0	23.4	19.0	17.4	18.6
Pr	3.34	4.10	2.59	1.56	3.23	6.36	4.79	1.82	3.72	3.17	8.70	5.86	2.53	1.81	2.59	2.67	2.48	2.80	2.65	2.36
Nd	11.4	15.3	8.5	5.7	10.5	20.8	21.2	6.0	15.6	15.5	26.2	22.4	10.2	6.8	9.6	11.4	9.4	13.1	12.3	10.8
Sm	1.51	2.43	1.09	1.22	1.46	2.66	4.53	0.74	4.22	5.26	2.88	4.60	2.91	1.65	2.26	2.78	2.35	3.43	2.99	2.28
Eu	0.68	0.75	0.61	0.42	0.62	0.67	0.74	0.61	0.87	0.92	0.79	1.06	0.95	1.10	1.13	0.98	1.19	1.25	1.11	1.01
Gd	1.08	1.58	0.73	0.95	1.02	1.41	3.14	0.44	4.63	6.12	1.90	3.61	3.29	1.70	2.68	2.56	2.66	4.35	3.27	2.87
Tb	0.13	0.21	0.09	0.12	0.11	0.16	0.44	0.03	0.74	1.02	0.27	0.55	0.52	0.34	0.40	0.41	0.46	0.62	0.65	0.49
Dy	0.56	0.94	0.36	0.53	0.39	0.61	2.11	0.15	4.52	6.29	1.38	2.96	3.07	2.03	2.60	2.70	3.15	4.20	3.91	3.09
Ho	0.07	0.16	0.06	0.13	0.08	0.07	0.39	0.03	0.86	1.30	0.31	0.57	0.57	0.42	0.56	0.54	0.63	0.97	0.89	0.65
Er	0.30	0.45	0.16	0.27	0.18	0.22	0.91	0.07	2.79	3.76	0.87	1.58	1.79	1.38	1.75	1.55	1.91	3.31	2.87	2.30
Tm	0.03	0.08	0.02	0.03	0.02	0.03	0.13	0.01	0.41	0.50	0.17	0.22	0.27	0.22	0.29	0.27	0.26	0.49	0.46	0.38
Yb	0.23	0.33	0.12	0.30	0.16	0.16	0.77	0.11	2.73	3.21	1.01	1.31	1.74	1.38	1.98	1.69	1.92	3.44	3.05	2.57
Lu	0.05	0.03	0.02	0.04	0.02	0.03	0.12	0.01	0.46	0.56	0.20	0.18	0.33	0.24	0.32	0.24	0.27	0.64	0.50	0.44
Eu/Eu*	1.55	1.09	1.96	1.15	1.47	0.95	0.57	3.01	0.60	0.49	0.97	0.77	0.93	1.98	1.40	1.10	1.45	0.99	1.08	1.20
La_N/Yb_N	63.21	35.00	87.18	15.85	83.64	143.08	9.62	81.52	4.11	1.97	33.56	13.38	5.62	5.12	5.04	5.19	5.09	1.58	1.51	2.33
Sr/Y	278.80	156.12	316.79	184.61	252.83	241.00	60.81	732.10	12.80	10.42	33.49	42.26	19.21	26.78	18.93	21.49	18.12	9.70	9.50	14.95

Fe_2O_3* = total iron recalculated as Fe_2O_3. LOI = loss on ignition. Eu/Eu* = $Eu_N/[(Sm_N + Gd_N)/2]$. La_N, Yb_N, Eu_N, Sm_N and Gd_N normalized to C1 chondrite (McDonough and Sun, 1995).

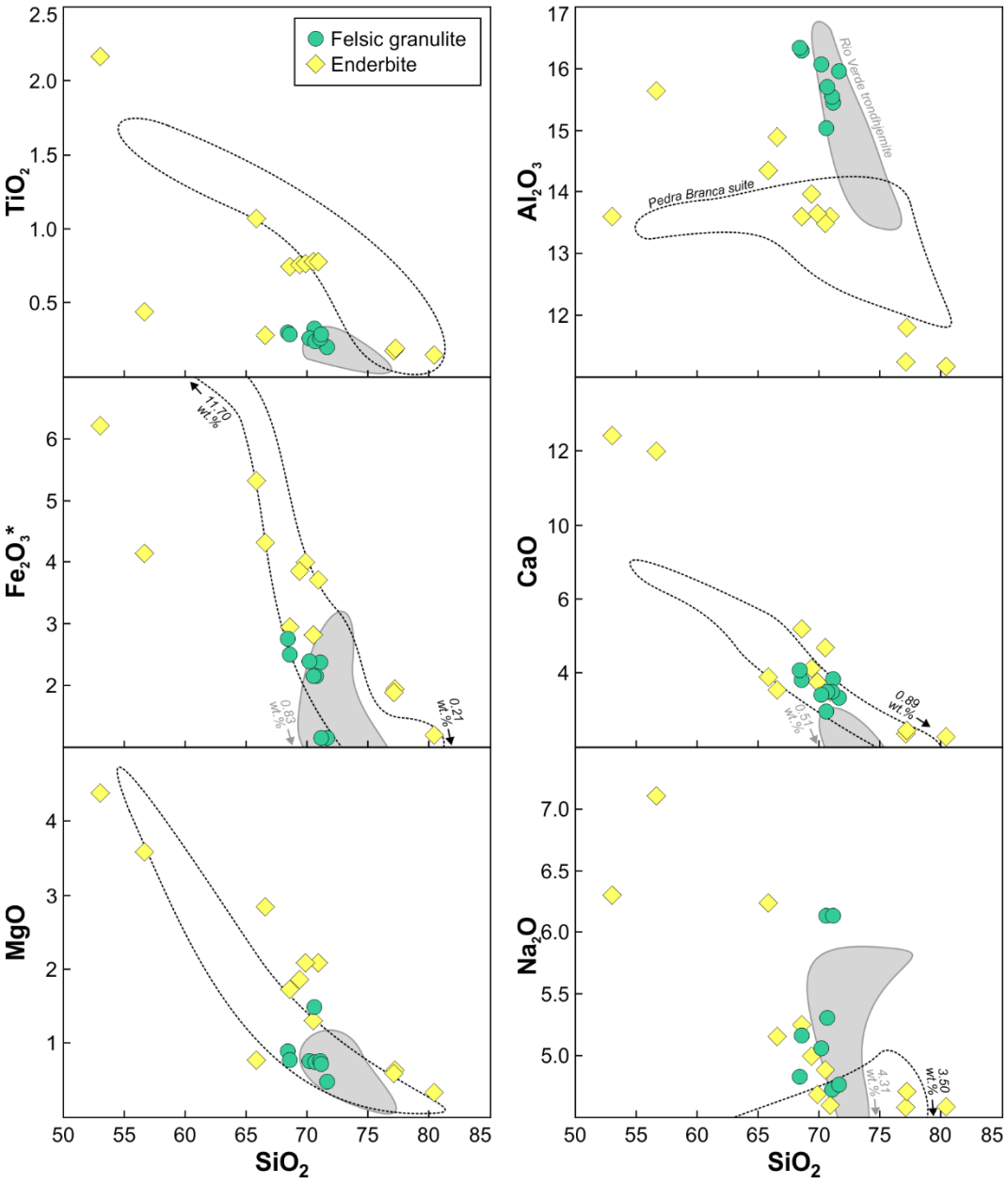

Figure 10. Harker diagrams (in wt.%) for the felsic granulites and enderbites from the studied area, compared with Mesoarchean Rio Verde TTG and Neoarchean Pedra Branca suite (Feio et al., 2013).

The primitive mantle-normalized multi-element diagrams for incompatible elements show, in general, that the felsic granulites (Figure 12c) are moderately LILE-enriched, with most Rb, Ba, Th and K values between 3 and 100 times higher than the primitive mantle values, and exhibit a notable negative Nb-Ta and positive Sr and Ti anomalies, and absence of P anomaly. The enderbites (Figure 12d) are slightly more LILE-enriched, with most Rb, Ba, Th and K values between 10 and 200 times higher than the primitive mantle values, with absence of Nb-Ta anomaly, slight positive Sr anomaly and pronounced negative P and Ti anomalies.

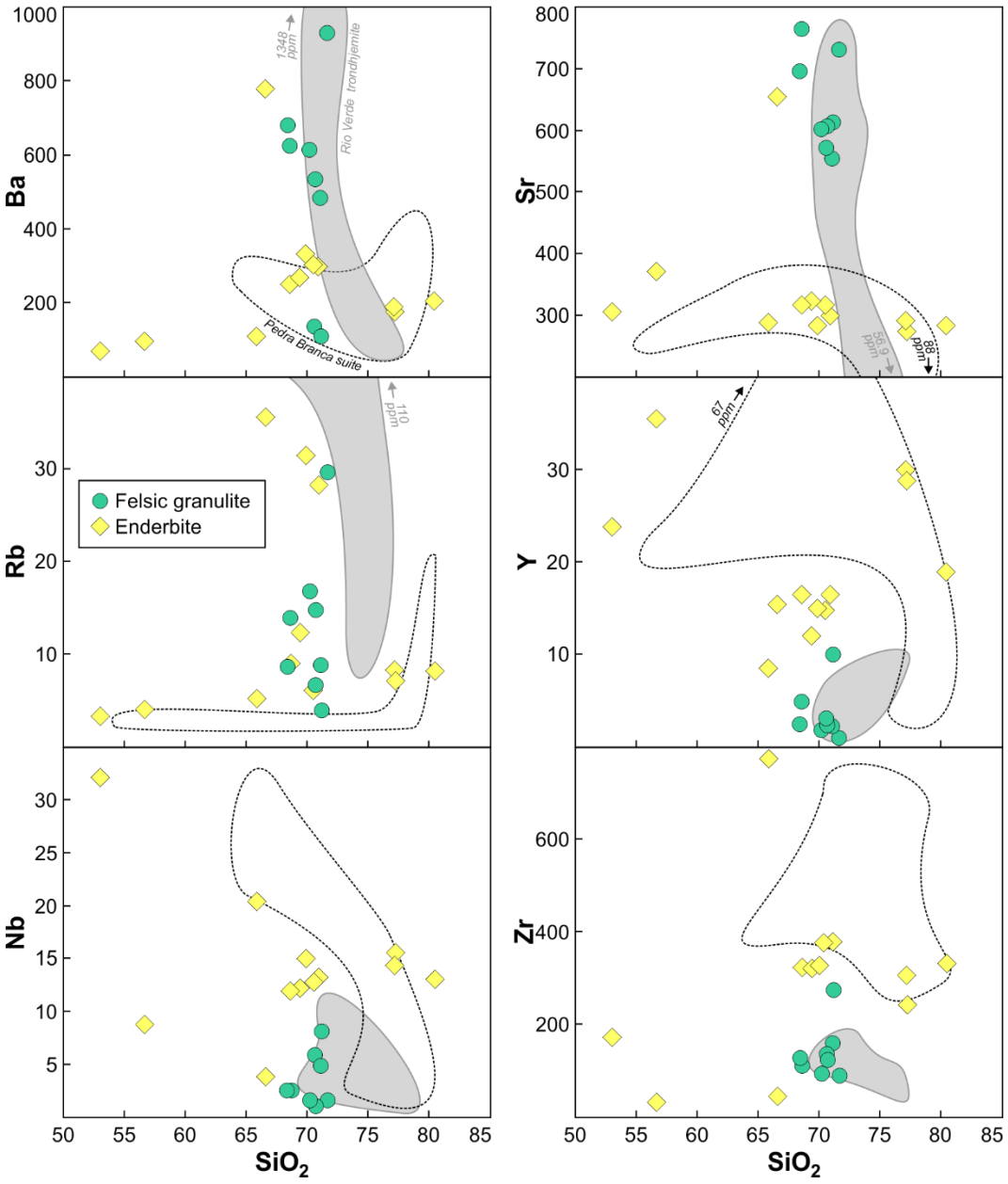

Figure 11. Harker diagrams for selected trace elements for the felsic granulite and enderbites from the studied area, compared with Mesoarchean Rio Verde TTG and Neoarchean Pedra Branca suite (Feio et al., 2013).

7.4. Classification

Apart from few exceptions, both felsic granulites and enderbites share the same classification. In the P-Q diagram (Debon and Le Fort, 1988; Figure 13a) both rock groups plot in the tonalite field. In the normative Ab-An-Or diagram (O'Connor, 1965, with fields from Barker, 1979; Figure 13b) the felsic granulites plot both in the tonalite and trondhjemite fields, whereas the enderbites plot only in the trondhjemite field. According to SiO_2 *vs.* FeO*/(FeO*+MgO) diagram (Frost et al., 2001; Figure 13c), the low Fe-number from both rock groups classifies them as magnesian granitoids. Regarding Shand's (1950) parameters (Figure 13d), the felsic granulites are slightly both metaluminous to peraluminous, while the

enderbites are purely metaluminous. When plotted in the SiO_2 *vs.* Na_2O+K_2O-CaO diagram (Frost et al., 2001; Figure 13e), the felsic granulites fall in the calcic field, while the enderbitic samples lie mostly in the calcic field, although few samples fall in the calc-alkalic field. The sodic character of both felsic granulites and enderbites is demonstrated in the K-Na-Ca diagram (Barker and Arth, 1976, with field of Archean TTG from Martin, 1994; Figure 13f). The AFM diagram (Irvine and Baragar, 1971; Figure 13g) shows that both rock groups have geochemical affinities with rocks of the calc-alkaline series, although they plot in distinct areas of the diagram. According to SiO_2 *vs.* K_2O diagram (fields of Peccerillo and Taylor, 1976; Figure 13h), both felsic granulites and enderbites plot mostly in the tholeiite series field, whereas subordinate samples fall in the calc-alkaline series field and, in the [2(A/CNK)]-(Na_2O/K_2O)-[2(FMSB)] diagram from Laurent et al. (2014; Figure 13i), both rocks groups lie in the TTG field.

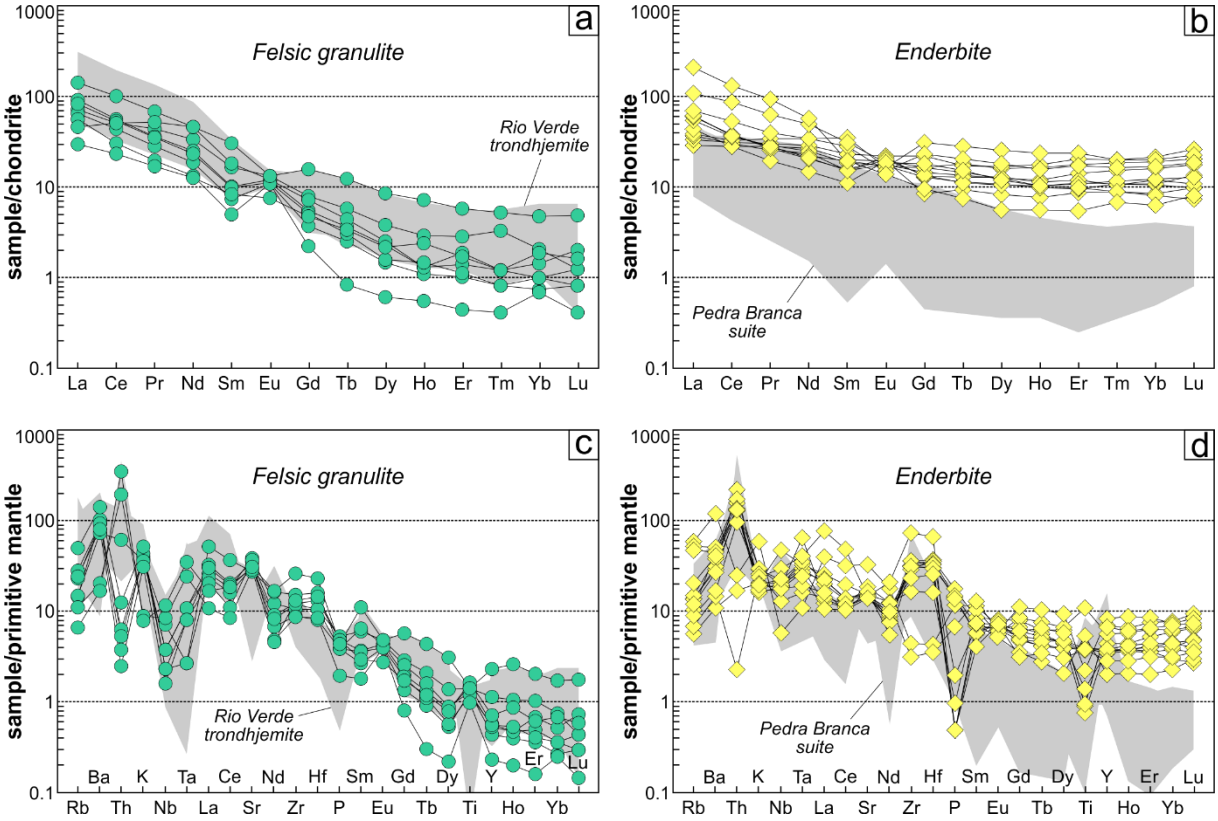

Figure 12. (a and b) REE and (c and d) multi-element patterns of the Meso- and Neoarchean sodic rocks from the studied area, with values normalized to C1 chondrite and pyrolite (McDonough and Sun, 1995), respectively, compared with Mesoarchean Rio Verde TTG and Neoarchean Pedra Branca suite (Feio et al., 2013).

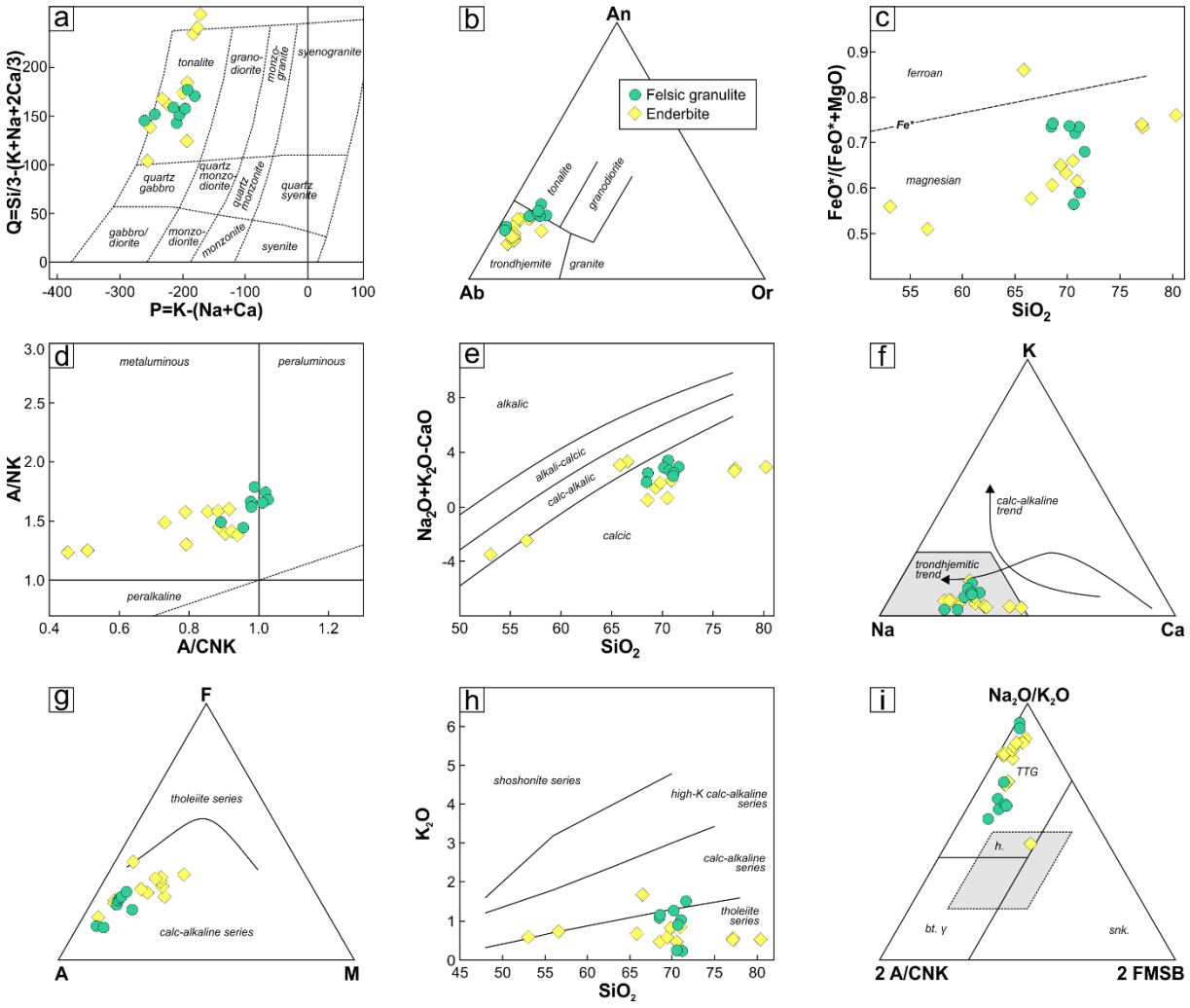

Figure 13. Geochemical diagrams for the felsic granulites and enderbites from the studied area: (a) P-Q diagram from Debon and Le Fort (1988); (b) Normative feldspar triangle (O'Connor, 1965) with fields from Barker (1979); (c) FeO*/(FeO*+MgO) *vs.* SiO_2 after Frost et al. (2001) showing the ferroan character of the studied rocks; (d) A/CNK [$Al_2O_3/(CaO+Na_2O+K_2O)$] *vs.* A/NK [$Al_2O_3/(Na_2O+K_2O)$] diagram (Shand, 1943); (e) Na_2O+K_2O-CaO (MALI) *vs.* SiO_2 diagram (Frost et al., 2001); and (f) K-Na-Ca diagram, with trends for calc-alkaline and trondhjemite series as defined by Barker and Arth (1976), and grey field of Archean TTG (Martin, 1994); (g) AFM diagram, with fields of tholeiite and calc-alkaline series of Irvine and Baragar, 1971); (h) SiO_2 *vs.* K_2O diagram, with fields of Peccerillo and Taylor (1976); (i) ternary classification diagram proposed by Laurent et al. (2014).

8. Isotopic data

8.1. Introduction

Concerning geochronological data, three samples of the felsic granulite, one of the mafic granulitic enclave and two of the enderbite were selected for geochronological analysis. Two samples of the felsic granulite were analyzed by the U-Pb SHRIMP method (samples BDE 1-A and BDE 13-A) and one by the U-Pb LA-MC-ICP-MS method (BVD 40). The mafic granulite (sample BDE 11-B) was analyzed by the U-Pb SHRIMP method. One sample of the enderbite (ED 1) was analyzed by both U-Pb SHRIMP and Pb-evaporation methods, and another was analyzed by the U-Pb LA-MC-ICP-MS method (BVD 53).

Two samples of the felsic granulite (BDE 13-A and BVD 40) and two of the enderbite (BVD 53 and ED 1) were selected to perform *in situ* zircon Lu-Hf isotopic analysis. The localization of the analyzed samples is shown in Figure 3 and their respective isotopic dataset are summarized in the tables 3–11. The analytical techniques and data processing are described in sections 5.3 and 5.4.

8.2. Pb-evaporation and U-Pb zircon dating

8.2.1. Mesoarchean felsic granulite

The Mesoarchean felsic granulite are located in the Ouro Verde area, and their rocks display different zircons grains in terms of external morphology and internal texture (Figure 14), which were separated into two groups: (i) zircon grains from sample BDE 1-A are euhedral to subhedral, long to shortly elongated with length varying from 250 to 400 μm, an aspect ratio that ranges from 2 to 4, and are characterized by the presence of well-developed growth zoning with rare local resorption, and (ii) zircon grains from the samples BDE 13-A and BVD 40, composed by prismatic crystals with rounded terminations, up to 320 μm in length and elongation ratios ranging from 2 to 4, which present two well-defined domains, one with concentric oscillatory-zoned core and other with homogeneous unzoned rim. Analyses performed in the first group are interpreted as magmatic age of the protolith. Concerning the second group, analyses from the domain with concentric oscillatory zoning are interpreted as magmatic age of the protolith (population 1), and those in the unzoned domain is reported as metamorphic overgrowth (population 2). Both groups do not present inherited cores.

Table 3. Zircon U-Pb isotopic data obtained by SHRIMP for the Mesoarchean felsic granulite (BDE 1-A).

Spot	U	Th	Th/U	$^{206}Pb_c$	Isotopic ratios					Age		Discordance
	(ppm)	(ppm)		(%)	$^{207}Pb/^{235}U$	1σ (%)	$^{206}Pb/^{238}U$	1σ (%)	ρ	$^{207}Pb/^{206}Pb$	1σ (%)	(%)
1.1	92.59	36.43	0.39	0.11	19.1888	1.1	0.6068	1.0	0.932	3047.6	6.3	0
2.1	113.38	42.53	0.38	0.32	19.7458	1.1	0.6112	1.0	0.946	3081.8	5.5	0
3.1	124.14	81.06	0.65	0.01	19.3448	1.0	0.6046	1.0	0.943	3066.3	5.4	1
4.1	95.45	49.69	0.52	1.51	18.9769	1.1	0.5936	1.0	0.919	3064.9	6.8	2
4.2	114.56	68.61	0.60	0.16	18.6581	1.0	0.5827	1.0	0.935	3067.6	5.9	4
5.1	92.35	53.31	0.58	11.98	19.9596	1.8	0.6336	1.0	0.566	3041.3	24.2	-4
6.1	92.58	54.84	0.59	0.78	19.1853	1.1	0.6044	1.0	0.929	3053.6	6.4	0
7.1	139.53	113.93	0.82	0.09	16.0541	1.0	0.5246	0.9	0.942	2994.9	5.4	10
8.1	101.41	47.13	0.46	7.45	18.6753	1.4	0.6004	1.0	0.733	3021.0	14.8	0
9.1	199.46	194.90	0.98	0.49	20.5164	1.9	0.6440	1.7	0.917	3059.3	11.8	-5
10.1	386.19	444.38	1.15	0.20	18.1879	0.9	0.5791	0.8	0.973	3036.6	3.2	3
12.1	105.22	65.88	0.63	1.52	19.3854	1.3	0.6131	1.2	0.944	3047.4	6.7	-1
13.1	110.85	81.90	0.74	0.79	19.7160	1.1	0.6207	1.0	0.887	3054.6	7.9	-2
14.1	417.54	577.83	1.38	1.78	16.0583	0.9	0.5304	0.8	0.952	2977.5	4.3	9
15.1	158.25	94.20	0.60	0.49	16.0717	1.0	0.5139	0.9	0.929	3029.7	5.9	13

Pb_c: common Pb corrected using measured ^{204}Pb.

Table 4. Zircon U-Pb isotopic data obtained by SHRIMP for the Mesoarchean felsic granulite (BDE 13-A).

Spot	U	Th	Th/U	$^{206}Pb_c$	Isotopic ratios					Age		Discordance
	(ppm)	(ppm)		(%)	$^{207}Pb/^{235}U$	1σ (%)	$^{206}Pb/^{238}U$	1σ (%)	ρ	$^{207}Pb/^{206}Pb$	1σ (%)	(%)
Magmatic domain (core)												
1.1	331.66	285.21	0.86	0.35	15.6701	0.7	0.5404	0.7	0.945	2908.0	3.8	4
2.1	126.36	63.14	0.50	-0.01	17.2166	0.9	0.5810	0.8	0.913	2943.1	5.6	0
4.1	141.25	68.66	0.49	0.12	17.1602	0.9	0.5755	0.8	0.864	2953.2	7.2	1
5.1	151.52	63.02	0.42	0.29	17.4595	0.8	0.5869	0.7	0.917	2949.2	5.2	-1
6.1	56.41	23.92	0.42	1.81	18.6467	4.6	0.5805	1.0	0.212	3072.6	72.0	4
6.2	326.86	41.91	0.13	1.12	13.3639	0.7	0.4629	0.7	0.911	2900.7	4.9	18
7.1	166.96	107.04	0.64	0.22	16.9093	0.8	0.5765	0.7	0.923	2926.5	5.0	0
8.1	140.20	68.04	0.49	0.17	17.7563	0.8	0.5913	0.8	0.917	2964.4	5.4	-1
9.1	146.13	99.23	0.68	-0.09	17.5408	0.8	0.5922	0.8	0.921	2942.2	5.2	-2
10.1	138.00	55.02	0.40	0.42	17.6283	0.9	0.5888	0.8	0.903	2959.6	5.9	-1
11.1	232.69	121.57	0.52	0.06	17.5087	0.7	0.5876	0.7	0.938	2951.8	4.1	-1
12.1	154.84	62.81	0.41	2.91	16.6918	0.9	0.5669	0.7	0.849	2932.7	7.4	1
14.1	107.90	46.32	0.43	0.31	16.9008	1.2	0.5755	1.1	0.941	2928.5	6.4	0
15.1	150.93	53.51	0.35	0.37	16.4438	1.4	0.5500	1.3	0.950	2957.3	6.9	6
16.1	128.30	67.59	0.53	0.00	17.1645	1.4	0.5733	1.4	0.950	2959.5	7.2	2
17.1	124.62	49.84	0.40	0.63	17.2524	1.5	0.5748	1.4	0.946	2963.7	7.7	2
19.1	166.27	117.37	0.71	2.70	17.2214	1.5	0.5663	1.4	0.949	2984.9	7.4	4
20.1	119.34	72.70	0.61	1.82	16.6065	1.5	0.5601	1.4	0.940	2943.8	8.2	3
21.1	166.99	69.85	0.42	0.55	16.2836	1.4	0.5591	1.3	0.951	2915.1	6.8	2
22.1	89.59	41.49	0.46	1.74	16.1408	2.0	0.5540	1.5	0.768	2915.7	20.8	3
23.1	108.72	45.35	0.42	1.33	16.7509	1.6	0.5619	1.5	0.939	2952.6	8.6	3
25.1	54.74	23.48	0.43	1.68	17.6540	2.0	0.5826	1.9	0.923	2979.0	12.4	1
25.2	176.45	86.36	0.49	3.14	14.3414	1.4	0.4930	1.3	0.923	2913.0	8.8	14
26.1	148.98	111.92	0.75	0.67	16.7195	1.4	0.5595	1.3	0.950	2956.6	7.1	4
Metamorphic domain (rim)												
1.2	87.27	75.48	0.86	0.25	15.4328	1.0	0.5460	0.9	0.894	2866.4	7.1	2
3.1	82.56	96.53	1.17	10.63	15.7452	1.6	0.5612	0.9	0.578	2854.2	20.8	-1
8.2	74.93	70.43	0.94	7.19	15.0318	1.4	0.5443	0.9	0.678	2828.7	16.6	1
9.2	95.92	82.26	0.86	0.15	16.0148	0.9	0.5677	0.8	0.897	2863.3	6.7	-1
13.1	91.28	92.09	1.01	1.41	15.7849	1.0	0.5608	0.8	0.865	2859.5	7.9	0
15.2	81.85	71.17	0.87	2.32	14.3344	1.7	0.5070	1.6	0.914	2866.9	11.2	9
18.1	72.84	55.56	0.76	8.06	15.8936	2.5	0.5526	1.6	0.649	2894.7	30.9	3
20.2	79.57	67.62	0.85	2.34	14.6703	1.7	0.5211	1.6	0.914	2859.8	11.3	7
21.2	92.61	84.05	0.91	10.61	15.5819	2.1	0.5412	1.5	0.744	2896.2	22.4	5
24.1	159.5	60.97	0.38	1.36	15.9188	1.4	0.5527	1.3	0.947	2897.0	7.4	3
24.2	72.01	70.31	0.98	2.17	15.0095	1.9	0.5370	1.7	0.914	2848.2	12.3	3

Pb_c: common Pb corrected using measured ^{204}Pb.

Table 5. Zircon U-Pb isotopic data obtained by LA-SF-ICP-MS for the Mesoarchean felsic granulite (BVD 40).

Spot	U	Th	Th/U	$^{206}Pb_c$	Isotopic ratios					Age		Discordance
	(ppm)	(ppm)		(%)	$^{207}Pb/^{235}U$	2σ (%)	$^{206}Pb/^{238}U$	2σ (%)	ρ	$^{207}Pb/^{206}Pb$	2σ (%)	(%)
Magmatic domain (core)												
1.1	363.60	565.89	1.56	1.50	12.2577	1.7	0.4450	1.4	0.796	2824.5	16.9	-10
2.1	228.63	134.70	0.59	0.00	13.4199	1.9	0.4776	1.3	0.666	2856.8	23.2	-7
3.1	68.75	52.25	0.76	0.75	14.9451	1.6	0.5159	1.3	0.770	2906.2	17.0	-5
4.1	223.22	126.23	0.57	0.26	15.6768	1.6	0.5369	1.2	0.760	2919.1	16.8	-3
5.1	329.46	10.70	0.03	0.00	14.5574	1.9	0.5099	1.3	0.674	2882.6	23.0	-5
6.1	21.72	10.84	0.50	0.02	18.6799	2.3	0.5713	1.6	0.712	3100.9	25.3	-4
6.2	106.40	51.14	0.48	0.34	15.6725	1.6	0.5353	1.3	0.773	2923.7	16.7	-3
7.1	170.99	33.76	0.20	0.14	14.9551	1.7	0.5153	1.3	0.780	2909.3	17.4	-5
8.1	225.88	145.81	0.65	0.12	14.0395	1.7	0.4953	1.3	0.745	2871.1	18.8	-6
9.1	718.34	291.84	0.41	0.47	14.9473	1.6	0.5172	1.2	0.746	2902.7	17.1	-4
10.1	691.77	261.81	0.38	0.59	16.7879	1.8	0.5636	1.4	0.794	2951.5	17.5	-1
11.1	120.59	63.03	0.52	0.00	16.1027	1.9	0.5489	1.3	0.661	2926.7	23.1	-2
12.1	55.49	30.41	0.55	0.50	16.8164	1.7	0.5639	1.3	0.787	2953.4	17.0	-1
12.2	37.42	104.16	2.78	0.00	15.7033	2.1	0.5361	1.5	0.728	2924.3	23.5	-3
13.1	142.23	58.03	0.41	0.79	14.9711	1.6	0.5169	1.2	0.756	2905.9	17.1	-5
15.1	231.91	192.52	0.83	0.00	13.4271	1.7	0.4772	1.2	0.742	2859.0	18.1	-7
16.1	163.83	116.80	0.71	0.00	15.6793	1.7	0.5377	1.3	0.761	2917.1	18.3	-3
17.1	193.54	68.24	0.35	0.00	15.0546	1.7	0.5155	1.3	0.773	2919.4	17.3	-5
18.1	139.92	61.32	0.44	0.00	14.5530	2.0	0.5073	1.3	0.663	2890.5	23.9	-5
19.1	199.79	28.59	0.14	0.00	15.6262	1.8	0.5401	1.4	0.775	2904.2	18.6	-2
20.1	112.08	3.99	0.04	0.33	14.5257	1.7	0.5084	1.3	0.744	2883.9	18.3	-5
21.1	139.78	30.56	0.22	0.00	14.5356	1.6	0.5073	1.2	0.754	2888.7	17.5	-5
23.1	48.98	20.61	0.42	0.00	14.5487	2.5	0.5071	2.1	0.849	2890.8	21.1	-5
24.1	204.02	201.69	0.99	0.46	17.3424	2.0	0.5856	1.7	0.828	2942.1	18.4	1
25.1	398.93	405.95	1.02	0.30	17.1162	2.4	0.5783	1.9	0.803	2941.1	22.7	0
26.1	136.55	32.25	0.24	0.41	17.0881	2.3	0.5780	1.9	0.828	2939.3	21.1	0
28.1	516.50	6.18	0.01	0.19	8.9035	2.0	0.3513	1.6	0.824	2687.7	18.5	-17
29.1	94.00	47.76	0.51	0.00	17.3679	2.1	0.5843	1.8	0.835	2947.9	18.7	0
30.1	255.69	94.85	0.37	0.28	13.2577	2.1	0.4724	1.7	0.826	2854.8	19.1	-8
31.1	43.15	3.21	0.07	0.00	15.9730	2.5	0.5422	2.1	0.854	2933.4	21.2	-3
32.1	211.96	42.94	0.20	0.08	10.0529	2.1	0.3844	1.7	0.809	2739.5	20.4	-14
Metamorphic domain (rim)												
1.2	407.5	77.67	0.19	0.57	14.4315	1.7	0.5263	1.3	0.787	2817.1	16.9	-2
5.2	54.77	32.02	0.58	0.09	14.7625	1.9	0.5383	1.5	0.774	2817.3	19.5	-1
14.1	321.4	21.98	0.07	0.00	13.7354	1.6	0.5103	1.2	0.748	2786.6	17.3	-3
17.2	32.78	68.6	2.09	0.00	14.6352	2.1	0.5314	1.5	0.701	2824.1	24.2	-2
19.2	32.44	82.39	2.54	0.03	14.3559	2.6	0.5100	1.9	0.713	2859.8	29.9	-4
20.2	4.063	10.58	2.6	0.01	17.2717	5.7	0.6724	3.7	0.653	2709.7	71.2	12
21.2	6.498	10.06	1.55	0.01	9.9766	8.0	0.4051	4.8	0.603	2640.3	106.1	-10
22.1	41.89	111.8	2.67	0.00	14.2147	2.0	0.5199	1.6	0.792	2812.2	20.2	-2
27.1	121.7	83.27	0.68	0.38	16.0892	2.1	0.5951	1.8	0.835	2793.8	18.9	4

Pb_c: common Pb corrected using measured ^{204}Pb.

Table 6. Zircon U-Pb isotopic data obtained by SHRIMP for the Mesoarchean mafic granulite (BDE 11-B).

Spot	U	Th	Th/U	$^{206}Pb_c$	Isotopic ratios					Age		Discordance
	(ppm)	(ppm)		(%)	$^{207}Pb/^{235}U$	1σ (%)	$^{206}Pb/^{238}U$	1σ (%)	ρ	$^{207}Pb/^{206}Pb$	1σ (%)	(%)
1.1	130.27	26.58	0.20	21.37	15.4624	2.1	0.5282	1.2	0.571	2923.3	28.1	8
2.1	449.60	68.01	0.15	0.28	15.9343	1.0	0.5623	0.9	0.891	2870.6	7.5	0
3.1	407.16	136.00	0.33	1.32	13.7781	1.1	0.5256	0.9	0.834	2743.2	9.9	1
4.1	184.78	74.77	0.40	0.35	15.6048	1.4	0.5542	1.1	0.744	2860.1	15.4	1
5.1	492.64	75.79	0.15	0.11	15.7159	1.1	0.5589	0.9	0.838	2857.9	9.5	0
6.1	190.10	47.31	0.25	2.00	14.3210	1.1	0.5156	1.0	0.928	2838.0	6.8	7
7.1	399.59	58.70	0.15	0.19	16.1370	1.2	0.5678	1.2	0.980	2875.2	3.9	-1
7.2	189.90	72.02	0.38	0.35	15.0562	1.1	0.5418	1.0	0.943	2838.8	5.9	2
8.1	101.32	18.22	0.18	2.53	14.9878	1.3	0.5438	1.2	0.904	2825.2	9.4	1
9.1	442.46	185.86	0.42	0.15	15.3930	0.9	0.5517	0.9	0.968	2845.4	3.9	1
10.1	387.53	54.15	0.14	0.78	15.4071	1.3	0.5371	1.3	0.977	2890.5	4.4	5
11.1	396.58	140.85	0.36	0.70	15.5709	1.0	0.5569	0.9	0.963	2848.8	4.2	0
12.1	1155.48	624.15	0.54	0.89	2.3940	1.1	0.1563	0.9	0.743	1817.2	14.0	52
13.1	917.48	279.42	0.30	0.68	4.5738	0.9	0.2220	0.9	0.932	2339.5	5.8	49
14.1	499.19	112.06	0.22	0.27	15.8777	1.0	0.5646	0.9	0.904	2858.1	7.2	-1

Pb_c: common Pb corrected using measured ^{204}Pb.

Table 7. Zircon U-Pb isotopic data obtained by LA-SF-ICP-MS for the Neoarchean enderbite (BVD 53).

Spot	U	Th	Th/U	$^{206}Pb_c$	Isotopic ratios					Age		Discordance
	(ppm)	(ppm)		(%)	$^{207}Pb/^{235}U$	2σ (%)	$^{206}Pb/^{238}U$	2σ (%)	ρ	$^{207}Pb/^{206}Pb$	2σ (%)	(%)
1.1	1.23	0.95	0.77	0.00	13.3687	6.6	0.5151	5.8	0.887	2726.8	50.1	1
2.1	11.35	2.45	0.22	0.03	13.9140	2.2	0.5325	1.5	0.680	2738.0	26.6	0
2.2	10.56	7.35	0.70	0.04	13.9359	2.1	0.5392	1.5	0.736	2719.9	23.1	-1
3.1	42.63	13.72	0.32	0.20	13.3352	1.8	0.5220	1.4	0.795	2700.8	18.2	0
4.1	25.31	24.05	0.95	0.00	13.4411	2.0	0.5141	1.3	0.662	2738.9	24.9	1
5.1	95.91	96.15	1.00	1.73	13.3811	1.7	0.5181	1.3	0.776	2718.6	17.5	1
5.2	58.56	28.95	0.49	0.00	13.3449	2.0	0.5182	1.4	0.680	2714.0	24.8	0
5.3	51.52	34.41	0.67	0.28	14.0298	1.6	0.5366	1.2	0.748	2739.0	17.3	-1
6.1	21.65	33.65	1.55	0.11	13.9760	2.0	0.5331	1.6	0.790	2743.3	20.6	0
7.1	53.81	21.36	0.40	0.13	13.9989	1.8	0.5327	1.4	0.785	2747.4	18.0	0
8.1	95.48	42.47	0.44	0.44	13.3537	1.6	0.5207	1.2	0.744	2707.2	17.3	0
8.2	34.09	38.72	1.14	0.00	13.3688	2.0	0.5177	1.4	0.672	2718.6	24.7	1
8.3	229.52	412.01	1.80	0.39	14.0179	1.6	0.5328	1.1	0.738	2749.3	17.2	0
9.1	53.89	24.16	0.45	0.09	13.3376	1.7	0.5140	1.3	0.755	2726.5	18.3	1
9.2	17.77	28.46	1.60	0.00	14.1634	2.3	0.5311	1.7	0.741	2771.4	25.5	1
10.1	25.58	24.76	0.97	0.00	14.0723	2.2	0.5318	1.6	0.721	2758.6	25.4	1
10.2	56.94	48.20	0.85	0.00	14.0466	2.0	0.5391	1.4	0.672	2733.4	24.6	-1
10.3	71.44	51.18	0.72	0.14	14.0575	1.9	0.5367	1.4	0.767	2741.8	19.7	-1
11.1	37.24	50.27	1.35	0.24	14.0876	1.7	0.5296	1.3	0.770	2767.3	17.8	1
11.2	7.30	1.42	0.19	0.00	13.5931	2.4	0.5147	1.8	0.745	2755.3	25.8	2
12.1	12.64	9.64	0.76	0.02	13.7750	3.0	0.5312	1.6	0.532	2725.4	41.3	0
12.2	61.32	32.96	0.54	0.21	13.3740	1.7	0.5134	1.3	0.760	2732.8	17.8	1
13.1	19.85	29.21	1.47	0.48	14.0319	1.8	0.5295	1.4	0.787	2761.1	17.9	0
14.1	15.58	3.55	0.23	0.22	13.9860	1.8	0.5393	1.4	0.777	2725.5	18.7	-1
14.2	9.97	1.80	0.18	0.02	13.9210	2.6	0.5318	1.7	0.646	2741.0	32.1	0
15.1	69.99	114.49	1.64	0.11	14.0225	1.8	0.5295	1.4	0.774	2759.9	18.6	0
15.2	67.36	53.00	0.79	0.14	14.0226	1.8	0.5289	1.4	0.779	2761.9	18.4	1
15.3	9.10	2.48	0.27	0.05	13.9500	2.1	0.5363	1.6	0.758	2730.5	22.4	-1
16.1	73.82	65.13	0.88	0.00	13.3808	1.8	0.5138	1.4	0.782	2732.4	18.4	1
17.1	13.28	12.12	0.91	0.04	13.9399	2.0	0.5279	1.5	0.719	2755.2	23.3	0
18.1	84.26	36.75	0.44	0.00	13.3531	2.4	0.5233	1.9	0.809	2698.7	23.3	0
19.1	119.49	162.89	1.36	0.17	13.7322	2.7	0.5250	2.1	0.793	2739.6	27.1	0
20.1	26.68	32.58	1.22	0.00	15.3361	3.1	0.5768	2.5	0.806	2766.5	30.3	-4
21.1	369.58	448.72	1.21	0.23	9.7418	2.6	0.4064	2.0	0.780	2595.3	27.2	9
22.1	13.17	17.37	1.32	0.00	19.1253	4.4	0.6948	3.9	0.891	2823.3	32.4	-12
23.1	33.15	37.40	1.13	0.00	12.9416	3.1	0.5053	2.5	0.828	2704.9	28.3	1
24.1	186.03	51.19	0.28	0.00	13.8139	3.0	0.5271	2.3	0.768	2742.8	31.8	0
25.1	69.35	106.17	1.53	0.03	16.2929	3.0	0.6160	2.2	0.736	2757.9	33.4	-7
26.1	13.07	14.48	1.11	0.04	15.8213	4.4	0.5957	3.9	0.900	2764.7	31.3	-5
27.1	195.56	266.22	1.36	0.00	12.3287	2.0	0.4829	1.3	0.661	2699.6	24.6	3
28.1	30.91	51.43	1.66	0.00	11.3745	2.2	0.4492	1.5	0.695	2686.1	26.1	6
29.1	135.75	250.40	1.84	0.00	12.9570	1.6	0.5018	1.2	0.762	2718.5	17.2	2
30.1	18.10	23.96	1.32	0.00	13.6119	2.2	0.5218	1.6	0.720	2735.1	25.1	1
31.1	27.47	44.43	1.62	0.14	12.7473	2.0	0.4999	1.6	0.792	2697.8	20.5	2
32.1	29.42	52.82	1.80	0.00	13.5323	1.9	0.5255	1.5	0.812	2714.0	18.2	0
33.1	17.53	20.94	1.19	0.00	15.0463	2.4	0.5687	2.1	0.850	2758.3	21.1	-3
34.1	20.88	34.05	1.63	0.00	14.0007	2.2	0.5372	1.5	0.708	2733.7	25.4	-1
35.1	60.37	105.16	1.74	0.06	13.5013	1.8	0.5270	1.3	0.742	2705.4	19.8	0
36.1	22.24	18.70	0.84	0.10	13.2129	1.9	0.5127	1.5	0.788	2715.1	19.1	1

Pb_c: common Pb corrected using measured ^{204}Pb.

Table 8. Zircon U-Pb isotopic data obtained by SHRIMP for the Neoarchean enderbite (ED 1).

Spot	U	Th	Th/U	$^{206}Pb_c$	Isotopic ratios					Age		Discordance
	(ppm)	(ppm)		(%)	$^{207}Pb/^{235}U$	1σ (%)	$^{206}Pb/^{238}U$	1σ (%)	ρ	$^{207}Pb/^{206}Pb$	1σ (%)	(%)
1.1	455.03	431.68	0.95	1.96	13.4741	1.1	0.5223	1.1	0.958	2716.7	5.4	0
1.2	286.02	173.88	0.61	1.01	13.5500	1.2	0.5163	1.1	0.961	2745.2	5.3	2
2.1	236.32	401.02	1.70	0.04	13.9126	1.2	0.5320	1.1	0.967	2739.2	4.9	0
3.1	259.89	136.04	0.52	3.70	11.8318	1.3	0.4617	1.1	0.893	2705.8	9.4	11
4.1	150.25	89.93	0.60	2.84	13.2995	1.3	0.5078	1.2	0.891	2741.6	9.8	4
5.1	475.12	281.55	0.59	6.81	8.6007	1.4	0.3584	1.1	0.763	2596.9	15.5	32
6.1	37.38	21.31	0.57	1.34	13.8437	1.7	0.5315	1.4	0.866	2732.6	13.7	-1
7.1	85.62	38.45	0.45	-0.42	14.0187	1.4	0.5327	1.2	0.920	2749.6	8.7	0
8.1	169.88	193.84	1.14	8.95	12.8251	1.8	0.4877	1.2	0.655	2748.6	22.0	7
9.1	113.07	65.95	0.58	2.37	13.4433	1.3	0.5116	1.2	0.905	2747.2	9.2	3
10.1	237.31	305.27	1.29	8.05	13.4193	1.5	0.5076	1.1	0.766	2757.1	15.7	4
11.1	472.25	373.54	0.79	0.62	13.6971	1.1	0.5236	1.1	0.978	2739.9	3.9	1
12.1	301.13	176.77	0.59	1.08	13.4078	1.2	0.5160	1.1	0.962	2728.7	5.2	2

Pb_c: common Pb corrected using measured ^{204}Pb.

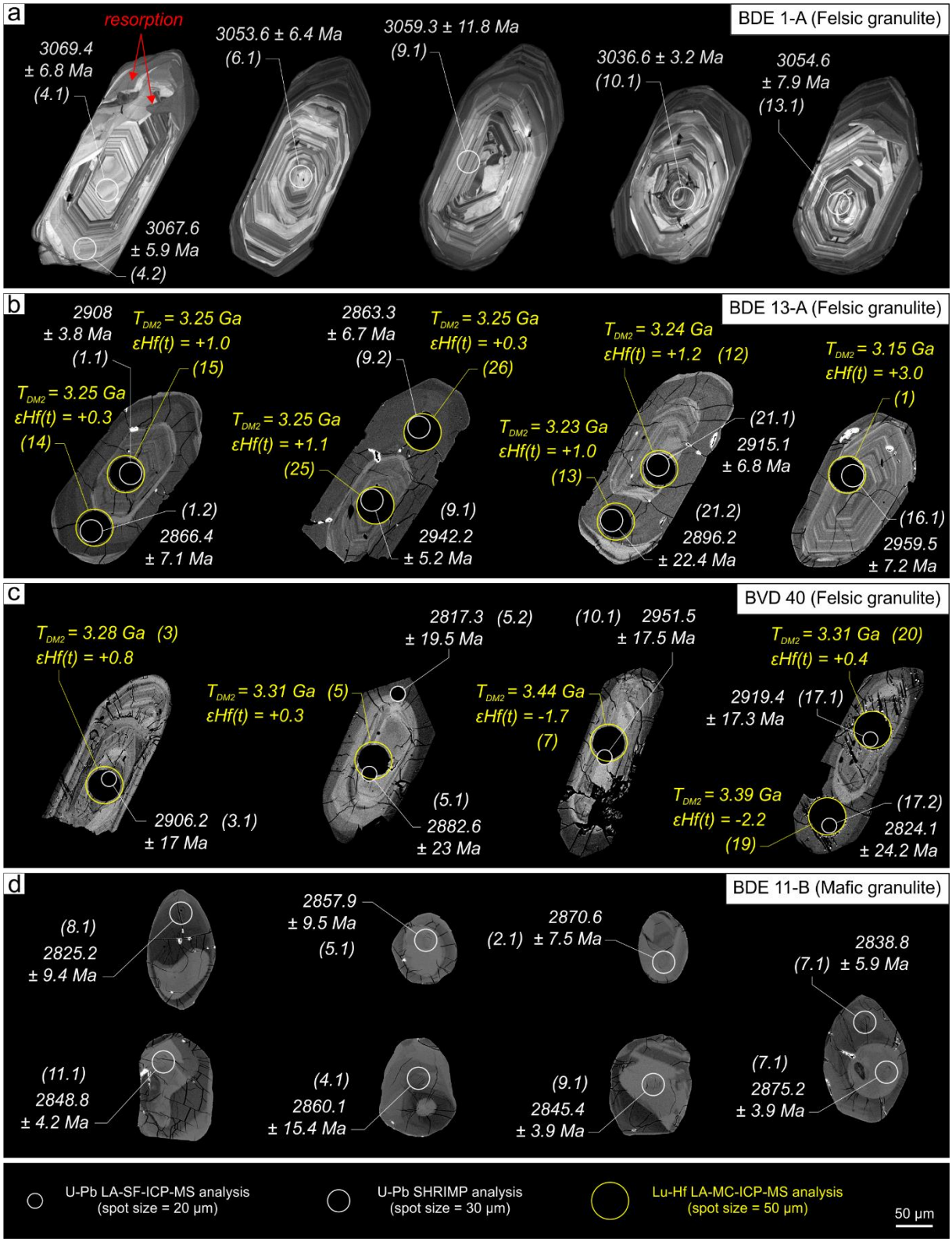

Figure 14. CL and BSE images of representative zircon grains of the felsic (a, b and c) and mafic (d) granulites from the studied area, with their respective in situ U-Pb ($^{207}Pb/^{206}Pb$ ages; white values) and Lu-Hf (εHf and T_{DM2}; yellow values) data. The numbers in parentheses correspond to the analyzed spot. The circles (see the legend) mark the position of the laser spot (scaled to size).

Table 9. Summary of zircon single-crystal evaporation Pb isotopic data of the Neoarchean enderbite (ED 1).

Zircon	Evaporation temperature (°C)	Number of ratios	$^{204}Pb/^{206}Pb$	2σ	$(^{208}Pb/^{206}Pb)_c$	2σ	$(^{207}Pb/^{206}Pb)_c$	2σ	Age (Ma)	2σ
1	1550	38/38	0.000030	0.000004	0.37217	0.00089	0.19123	0.00030	2753	3
3	1500	18/26	0.000134	0.000025	0.34946	0.00206	0.19131	0.00083	2753	7
13	1500	36/36	0.000122	0.000004	0.37449	0.00087	0.19160	0.00043	2756	4
13	1550	38/38	0.000150	0.000010	0.37775	0.00085	0.19143	0.00024	2755	2
15	1500	32/40	0.000023	0.000003	0.20369	0.00060	0.19122	0.00026	2753	2
Mean age (Ma)									*2753.8*	*1.2*

The SHRIMP analytical results in the sample BDE 1-A (Figure 15a) display that nine spot analyses in different zircon grains gave an average $^{207}Pb/^{206}Pb$ age of 3056.8±6.7 Ma (MSWD=4.2), whereas the four concordant spots yielded a concordia age of 3055.1±8.8 Ma (MSWD=0.0066). A total of thirty-five spot analyses have been made on twenty-six zircon grains in the sample BVD 13-A (Figure 15b). Data for zircon cores record two distinct age groups. A first group of core domains (population 1a) records an upper intercept age of 2955.7±5.1 Ma (MSWD=5.3), defined by eleven discordant spot analyses, and four concordant analyzes yielded a Concordia age of 2950.5±8.4 Ma (MSWD=0.00062). Seven discordant analyses of slightly younger core domains (population 1b) yielded a Discordia with an upper intercept age of 2930.2±3.3 Ma (MSWD=1.7). Two analyses populations of unzoned overgrowths on the magmatic grains were recorded. Three discordant spot analyses from the population 2a define a Discordia with an upper intercept age of 2898±32 Ma (MSWD=0.021). The population 2b yielded an average $^{207}Pb/^{206}Pb$ age of 2862.5±3.9 Ma (MSWD=0.73) defined by six discordant spot analyses, while three concordant spot analyses gave a concordia age of 2865±11 Ma (MSWD=2.1).

Forty analyses carried out on thirty-two zircon grains were performed in the sample BVD 40 by the U-Pb LA-MC-ICP-MS method (Figure 15c). The core analyses (population 1) provided a Discordia with an upper intercept age of 2950.4±6.8 Ma (MSWD=0.83) defined by twenty-eight discordant spot analyses, whereas four spot analyses yielded a concordia age of 2946±19 Ma (MSWD=0.32). The rim analyses (population 2) yielded a discordant $^{207}Pb/^{206}Pb$ age of 2847±39 Ma (MSWD=0.65) defined by five discordant spot analyses.

The sample BDE 11-B represents a mafic granulite that occurs as enclave in the felsic granulite. In summary, their zircon grains are anhedral, rounded to shortly elongated, ranging in size from 80 to 120 μm, and an aspect ratio that ranges from 1 to 2. They are formed by a unique domain, with unzoned and completely homogeneous aspects, as the rim domain from the felsic granulite, which will have the same interpretation, describing a metamorphic event. It was analyzed by the U-Pb SHRIMP method, which fifteen spots on fourteen grains have been analyzed (Figure 15d). The data are discordant and two distinct groups were identified.

Four spot analyses from one group (population 2a) provided discordant $^{207}Pb/^{206}Pb$ age of 2870±4.9 Ma (MSWD=0.28), while the second group (population 2b) yielded a Discordia with an upper intercept age of 2850.2±4.3 Ma (MSWD=0.58) defined by five discordant spot analyses, and four spot analyses gave a concordia age of 2844.8±7.8 Ma (MSWD=0.62).

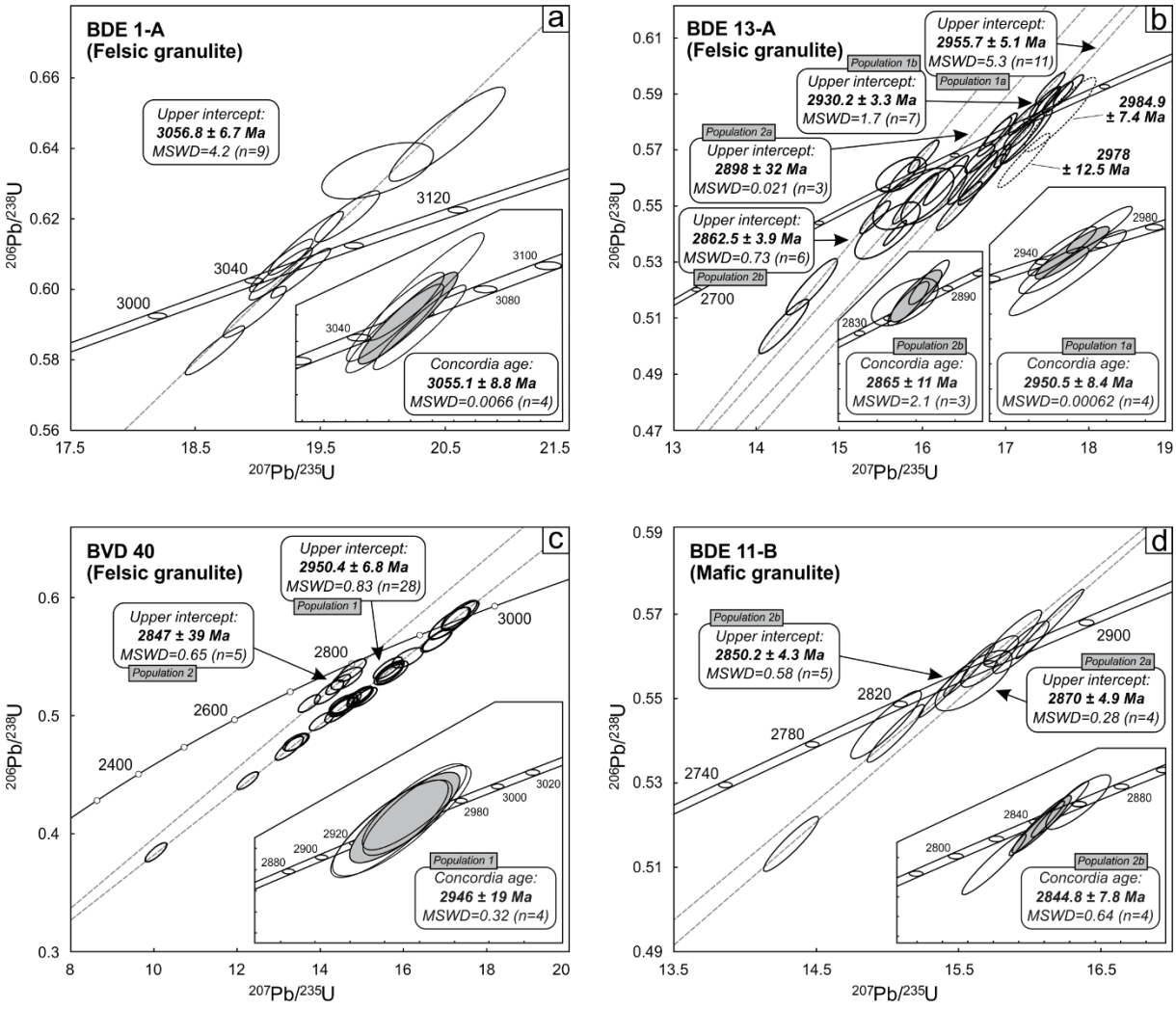

Figure 15. U-Pb concordia plots of the felsic (a, b and c) and mafic (d) granulites from the studied area. Plots (a), (b) and (d) show results of SHRIMP U-Pb analyses, and plot (c) shows results of LA-SF-ICP-MS U-Pb analysis.

8.2.2. Neoarchean enderbite

The zircon grains from the Neoarchean enderbites (Figure 16) display a typical feature of preserved well-developed concentric oscillatory zoning, interpreted as magmatic origin. Sometimes, these concentric oscillatory zoning are locally penetrated by convolute zoning. In general, their zircon grains are doubly-terminated prismatic crystals, with elongation ratios ranging between 2 and 4, and varying from 180 to 320 μm in size. The domain with convolute zoning was not analyzed due to its metamict aspect.

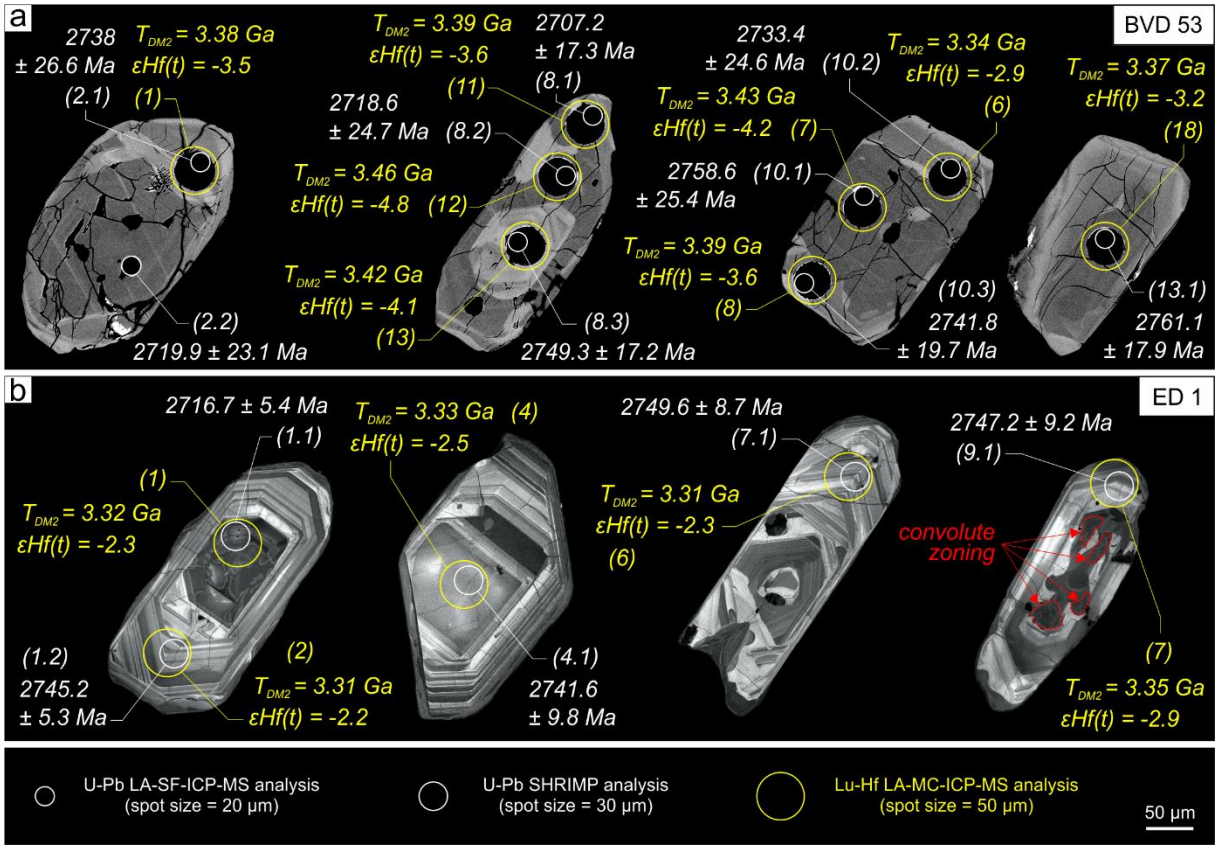

Figure 16. BSE and CL images of representative zircon grains of the enderbites from the studied area, with their respective in situ U-Pb ($^{207}Pb/^{206}Pb$ ages; white values) and Lu-Hf (εHf and T_{DM2}; yellow values) data. The numbers in parentheses correspond to the analyzed spot. The circles (see the legend) mark the position of the laser spot (scaled to size).

The U-Pb LA-MC-ICP-MS analytical results in the sample BVD 53 (Figure 17a) show that thirty-six spot analyses yielded a concordia age of 2734.5±5.9 Ma (MSWD=2.4), while twenty-nine concordant spots defined a concordia age of 2730.4±7.1 Ma (MSWD=1.3).

The sample ED 1 was analyzed by both U-Pb SHRIMP and Pb-evaporation methods. Concerning the U-Pb SHRIMP method (Figure 17b), eleven spot analyzes defined a Discordia with an upper intercept age of 2743±13 Ma (MSWD=10.5), whereas four concordant analyses defined a concordia age of 2740.2±8.3 Ma (MSWD=0.0089). Eleven zircon grains have been analyzed by the Pb-evaporation method, which four grains yielded an age of 2753.8±1.2 Ma (MSWD=0.81; Figure 18).

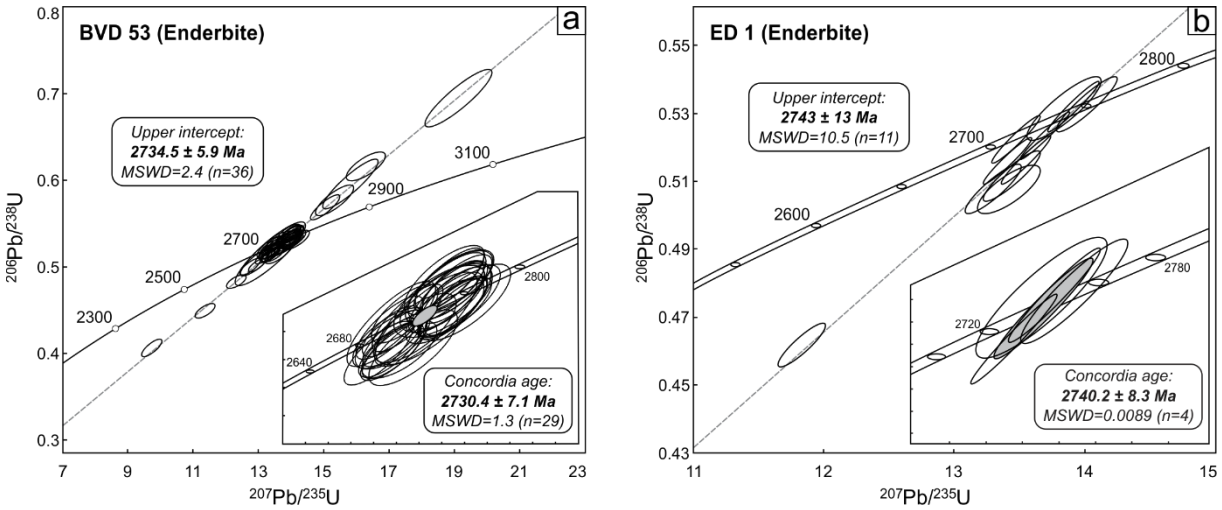

Figure 17. U-Pb concordia plots of the enderbites from the studied area. Plot (a) shows results of LA-SF-ICP-MS U-Pb analysis, and plot (b) shows results of SHRIMP U-Pb analyses.

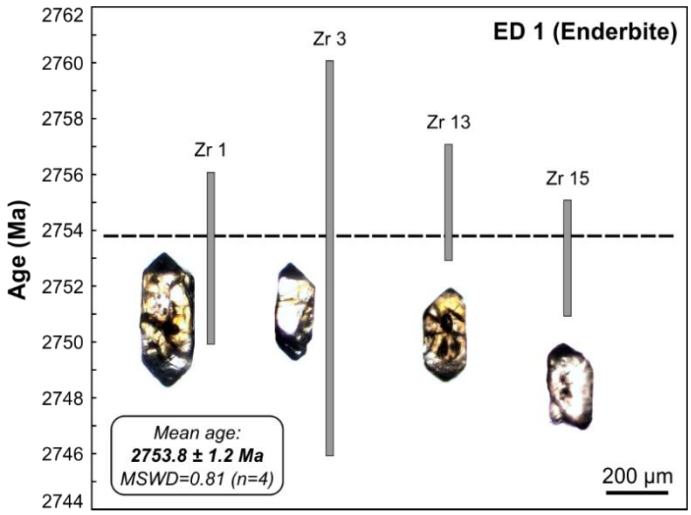

Figure 18. Single zircon Pb-evaporation age plot for the sample ED 1 from studied area. The vertical gray bars correspond the error for each zircon grain and horizontal dashed black line represents to the mean age for sample. Each analysis (gray bar) is accompanied by its respective zircon image (photomicrograph). Abbreviation: Zr (zircon).

8.3. Lu-Hf zircon isotope

8.3.1. Mesoarchean felsic granulite

Zircon grains from the felsic granulite present two domains: the magmatic core and the metamorphic rim. Concerning the magmatic domain, twenty zircon grains from the sample BDE 13-A present initial Hf isotopes ranging from 0.280906 and 0.280966, slightly positive εHf(t) values of 0.8 to 3.0, and two-stage model ages (T_{DM2}) varying from 3.15 to 3.28 Ga, while nine analyses from the metamorphic domain show initial $^{176}Hf/^{177}Hf$ ratios ranging from 0.280907 to 0.280948, negative to positive εHf(t) values, varying between -1.1 and 1.0, and T_{DM2} from 3.23 to 3.34 Ga. In the sample BVD 40, analyses in seventeen zircon grains from the magmatic domain yielded negative to positive εHf(t) values, from -1.7 to 1.4, T_{DM2} varying from 3.24 to 3.44 Ga, and initial $^{176}Hf/^{177}Hf$ ratios ranging between 0.280837

and 0.280926. Five analyses in its metamorphic domain display initial Hf isotopes ranging from 0.280888 to 0.280916, negative εHf(t) values of -2.2 to -1.2 and T_{DM2} of 3.33 to 3.39 Ga (Figure 19).

Table 10. LA-MC-ICP-MS Lu-Hf isotopic data of zircon grains for the Mesoarchean felsic granulite. Ages from U-Pb SHRIMP (Table 4) and U-Pb LA-SF-ICP-MS (Table 5).

Spot	Domain	$^{176}Yb/^{177}Hf$[a]	2σ	$^{176}Lu/^{177}Hf$[a]	2σ	$^{178}Hf/^{177}Hf$	$^{180}Hf/^{177}Hf$	SigHf[b]	$^{176}Hf/^{177}Hf$	2σ[c]	$^{176}Hf/^{177}Hf(t)$[d]	εHf(t)[d]	2σ[c]	T_{DM2}[e] (Ga)	Age[f] (Ma)	2σ
BDE 13-A																
1	core	0.0097	8	0.00039	2	1.46722	1.88681	11	0.280988	27	0.280966	3.0	0.8041	3.15	2950.5	8.4
2	core	0.0119	10	0.00048	3	1.46721	1.88682	10	0.280957	21	0.280930	1.7	0.8060	3.23	2950.5	8.4
3	core	0.0121	10	0.00048	3	1.46721	1.88680	11	0.280969	24	0.280941	2.1	0.8062	3.20	2950.5	8.4
4	core	0.0130	11	0.00050	3	1.46720	1.88684	11	0.280943	24	0.280915	1.2	0.8070	3.26	2950.5	8.4
5	core	0.0103	10	0.00042	3	1.46715	1.88675	10	0.280972	18	0.280948	1.9	0.8060	3.20	2930,2*	3.3
6	rim	0.0112	9	0.00045	3	1.46720	1.88693	11	0.280968	16	0.280944	0.9	0.8050	3.23	2898*	32
7	rim	0.0070	6	0.00028	2	1.46713	1.88690	12	0.280922	18	0.280907	-1.1	0.8022	3.34	2865	11
8	rim	0.0076	7	0.00030	2	1.46718	1.88680	11	0.280957	22	0.280940	0.8	0.8028	3.24	2898*	32
9	core	0.0080	7	0.00032	2	1.46720	1.88679	11	0.280955	21	0.280937	2.8	0.8029	3.19	2984,9**	7
10	core	0.0153	12	0.00060	4	1.46714	1.88687	10	0.280959	19	0.280924	2.2	0.8095	3.22	2979**	12
11	core	0.0082	7	0.00033	2	1.46717	1.88681	11	0.280946	20	0.280927	1.6	0.8028	3.23	2950.5	8.4
12	core	0.0099	11	0.00040	4	1.46722	1.88701	10	0.280951	18	0.280928	1.2	0.8076	3.24	2930,2*	3.3
13	rim	0.0058	6	0.00023	2	1.46714	1.88677	11	0.280957	20	0.280945	1.0	0.8020	3.23	2898*	32
14	rim	0.0069	5	0.00028	2	1.46719	1.88677	12	0.280963	19	0.280947	0.3	0.8018	3.25	2865	11
15	core	0.0111	9	0.00044	3	1.46726	1.88689	11	0.280948	19	0.280924	1.0	0.8050	3.25	2930,2*	3.3
16	core	0.0224	18	0.00081	5	1.46719	1.88681	10	0.280952	18	0.280906	0.8	0.8198	3.28	2950.5	8.4
17	core	0.0112	9	0.00044	3	1.46716	1.88679	10	0.280974	22	0.280949	1.9	0.8051	3.20	2930,2*	3.3
18	core	0.0103	8	0.00040	2	1.46720	1.88691	11	0.280963	26	0.280940	1.6	0.8043	3.22	2930,2*	3.3
19	core	0.0128	10	0.00050	3	1.46714	1.88682	11	0.280950	22	0.280922	1.4	0.8065	3.24	2950.5	8.4
20	rim	0.0070	6	0.00027	2	1.46714	1.88678	12	0.280952	15	0.280937	0.0	0.8019	3.27	2865	11
21	core	0.0119	10	0.00046	3	1.46717	1.88686	11	0.280969	19	0.280943	2.2	0.8058	3.20	2950.5	8.4
22	core	0.0060	5	0.00025	1	1.46721	1.88672	10	0.280945	21	0.280931	1.3	0.8014	3.24	2930,2*	3.3
23	rim	0.0104	8	0.00040	2	1.46717	1.88689	11	0.280935	16	0.280912	-0.9	0.8043	3.33	2865	11
24	core	0.0100	9	0.00040	3	1.46716	1.88685	11	0.280985	21	0.280962	2.9	0.8054	3.15	2950.5	8.4
25	core	0.0097	8	0.00039	2	1.46721	1.88694	11	0.280948	17	0.280927	1.1	0.8038	3.25	2930,2*	3.3
26	rim	0.0083	7	0.00032	2	1.46722	1.88687	12	0.280965	21	0.280948	0.3	0.8027	3.25	2865	11
27	rim	0.0075	6	0.00029	2	1.46719	1.88681	12	0.280936	21	0.280920	-0.7	0.8021	3.31	2865	11
28	core	0.0104	8	0.00042	3	1.46722	1.88690	11	0.280973	18	0.280949	2.4	0.8044	3.18	2950.5	8.4
29	core	0.0108	9	0.00043	3	1.46726	1.88676	11	0.280967	21	0.280943	2.2	0.8047	3.20	2950.5	8.4
BVD 40																
1	rim	0.0081	6	0.00035	2	1.46724	1.88685	12	0.280910	17	0.280891	-2.1	0.8024	3.39	2847*	39
2	core	0.0189	15	0.00080	5	1.46719	1.88673	10	0.280915	19	0.280870	-0.5	0.8140	3.36	2946	19
3	core	0.0142	11	0.00057	3	1.46721	1.88680	11	0.280939	18	0.280907	0.8	0.8080	3.28	2946	19
4	core	0.0170	16	0.00067	5	1.46720	1.88689	12	0.280906	24	0.280868	-0.6	0.8161	3.37	2946	19
5	core	0.0115	9	0.00049	3	1.46723	1.88677	13	0.280920	18	0.280893	0.3	0.8052	3.31	2946	19
6	core	0.0200	16	0.00076	5	1.46718	1.88681	12	0.280913	18	0.280870	-0.5	0.8161	3.36	2946	19
7	core	0.0266	21	0.00093	6	1.46717	1.88673	15	0.280890	21	0.280837	-1.7	0.8276	3.44	2946	19
8	core	0.0358	29	0.00129	8	1.46724	1.88693	13	0.280913	15	0.280840	-1.6	0.8496	3.43	2946	19
9	core	0.0219	18	0.00087	5	1.46719	1.88681	11	0.280929	19	0.280880	-0.2	0.8189	3.34	2946	19
10	core	0.0088	7	0.00035	2	1.46721	1.88681	13	0.280929	24	0.280910	0.9	0.8031	3.27	2946	19
11	core	0.0115	9	0.00034	2	1.46718	1.88701	11	0.280914	20	0.280894	0.3	0.8053	3.31	2946	19
12	core	0.0047	4	0.00020	1	1.46719	1.88689	12	0.280937	23	0.280926	1.4	0.8009	3.24	2946	19
13	core	0.0088	7	0.00039	2	1.46712	1.88670	10	0.280885	22	0.280862	-0.8	0.8030	3.38	2946	19
14	core	0.0085	7	0.00035	2	1.46721	1.88681	15	0.280925	22	0.280905	0.7	0.8028	3.29	2946	19
15	rim	0.0080	6	0.00034	2	1.46719	1.88690	15	0.280931	25	0.280912	-1.4	0.8024	3.34	2847*	39
16	rim	0.0105	8	0.00039	2	1.46722	1.88681	14	0.280938	17	0.280916	-1.2	0.8042	3.33	2847*	39
17	core	0.0080	6	0.00032	2	1.46720	1.88686	14	0.280926	17	0.280908	0.8	0.8026	3.28	2946	19
18	core	0.0097	8	0.00042	3	1.46716	1.88690	14	0.280914	19	0.280891	0.2	0.8037	3.32	2946	19
19	rim	0.0074	7	0.00029	2	1.46714	1.88687	14	0.280904	19	0.280888	-2.2	0.8025	3.39	2847*	39
20	core	0.0170	14	0.00067	4	1.46723	1.88687	15	0.280933	20	0.280896	0.4	0.8123	3.31	2946	19
21	core	0.0095	8	0.00040	3	1.46717	1.88680	16	0.280920	17	0.280897	0.4	0.8038	3.30	2946	19
22	rim	0.0082	7	0.00032	2	1.46721	1.88690	15	0.280920	21	0.280902	-1.7	0.8027	3.36	2847*	39

[a] $^{176}Yb/^{177}Hf = (^{176}Yb/^{173}Yb)_{true} \times (^{173}Yb/^{177}Hf)_{measured} \times (M_{173(Yb)}/M_{177(Hf)})^{\beta(Hf)}$, $\beta(Hf) = \ln(^{179}Hf/^{177}Hf_{true}/^{179}Hf/^{177}Hf_{measured})/\ln(M_{179(Hf)}/M_{177(Hf)})$, M = mass of respective isotope. The $^{176}Lu/^{177}Hf$ were calculated in a similar way by using the $^{175}Lu/^{177}Hf$ and β(Yb).

[b] Mean Hf signal in volt.

[c] Uncertainties are quadratic additions of the within-run precision and the daily reproducibility of the 40 ppb-JMC475 solution. Uncertainties for the JMC475 quoted at 2σ (2 standard deviation).

[d] Initial $^{176}Hf/^{177}Hf$ and εHf calculated using the Concordia age determined by SHRIMP and LA-ICP-MS dating (see column f), and the CHUR parameters: $^{176}Lu/^{177}Hf$ = 0.0336 and $^{176}Hf/^{177}Hf$ = 0.282785 (Bouvier et al., 2008).

[e] Two-stage model age in billion years using the measured $^{176}Lu/^{177}Hf$ of each spot (first stage = age of zircon), a value of 0.015 (Griffin et al., 2002) for the average continental crust (second stage), and average MORB (DM) $^{176}Lu/^{177}Hf$ and $^{176}Hf/^{177}Hf$ of 0.0388 and 0.283250 (Andersen et al., 2009), respectively.

[f] Concordia ages from tables 4 and 5; * Discordia age; ** Individual $^{207}Pb/^{206}Pb$ age.

8.3.2. Neoarchean enderbite

Twenty-three analyses from the sample BVD 53 yielded negative εHf(t) values of -4.8 to -2.8, T_{DM2} varying from 3.34 to 3.46 Ga, and initial Hf isotopes ranging from 0.280894 and 0.280950. The sample ED 1 shows quite similar isotopic behavior when compared to the previous sample, displaying a narrower initial $^{176}Hf/^{177}Hf$ ratios, ranging between 0.280932 and 0.280967, negative εHf(t) values of -3.2 to -1.9, and T_{DM2} of 3.29 to 3.37 Ga (Figure 19).

Table 11. LA-MC-ICP-MS Lu-Hf isotopic data of zircon grains for the Neoarchean enderbite. Ages from U- U-Pb LA-SF-ICP-MS (Table 7) and Pb SHRIMP (Table 8).

Spot	$^{176}Yb/^{177}Hf$[a]	2σ	$^{176}Lu/^{177}Hf$[a]	2σ	$^{178}Hf/^{177}Hf$	$^{180}Hf/^{177}Hf$	SigHf[b]	$^{176}Hf/^{177}Hf$	2σ[c]	$^{176}Hf/^{177}Hf(t)$[d]	εHf(t)[d]	2σ[c]	T_{DM2}[e] (Ga)	Age[f] (Ma)	2σ
BVD 53															
1	0.0091	7	0.00043	3	1.46719	1.88677	17	0.280951	21	0.280928	-3.5	0.8029	3.38	2730.4	7.1
2	0.0116	9	0.00045	3	1.46722	1.88683	9	0.280971	20	0.280947	-2.9	0.8052	3.34	2730.4	7.1
3	0.0072	8	0.00029	3	1.46723	1.88679	10	0.280941	16	0.280925	-3.6	0.8033	3.39	2730.4	7.1
4	0.0327	26	0.00127	8	1.46721	1.88672	9	0.280984	18	0.280917	-3.9	0.8415	3.41	2730.4	7.1
5	0.0146	12	0.00056	3	1.46719	1.88668	10	0.280979	23	0.280950	-2.8	0.8082	3.34	2730.4	7.1
6	0.0076	6	0.00031	2	1.46720	1.88682	9	0.280963	20	0.280946	-2.9	0.8020	3.34	2730.4	7.1
7	0.0173	14	0.00066	4	1.46720	1.88677	9	0.280944	22	0.280910	-4.2	0.8114	3.43	2730.4	7.1
8	0.0080	6	0.00033	2	1.46721	1.88680	10	0.280944	24	0.280927	-3.6	0.8022	3.39	2730.4	7.1
9	0.0181	14	0.00068	4	1.46722	1.88672	8	0.280957	24	0.280921	-3.8	0.8126	3.40	2730.4	7.1
10	0.0089	7	0.00037	2	1.46721	1.88690	11	0.280946	24	0.280927	-3.6	0.8028	3.39	2730.4	7.1
11	0.0096	8	0.00039	2	1.46722	1.88687	10	0.280947	22	0.280927	-3.6	0.8033	3.39	2730.4	7.1
12	0.0110	9	0.00043	3	1.46721	1.88700	9	0.280917	31	0.280894	-4.8	0.8044	3.46	2730.4	7.1
13	0.0390	31	0.00147	9	1.46722	1.88679	9	0.280989	20	0.280912	-4.1	0.8589	3.42	2730.4	7.1
14	0.0165	13	0.00063	4	1.46720	1.88688	9	0.280961	20	0.280928	-3.5	0.8105	3.38	2730.4	7.1
15	0.0244	20	0.00092	6	1.46720	1.88688	11	0.280958	19	0.280910	-4.2	0.8233	3.42	2730.4	7.1
16	0.0162	14	0.00062	4	1.46719	1.88684	9	0.280949	20	0.280916	-4.0	0.8113	3.41	2730.4	7.1
17	0.0125	10	0.00049	3	1.46719	1.88683	10	0.280971	19	0.280945	-2.9	0.8060	3.35	2730.4	7.1
18	0.0152	12	0.00057	4	1.46716	1.88682	9	0.280966	17	0.280936	-3.2	0.8092	3.37	2730.4	7.1
19	0.0174	14	0.00067	4	1.46719	1.88672	10	0.280965	20	0.280930	-3.5	0.8117	3.38	2730.4	7.1
20	0.0128	15	0.00050	5	1.46729	1.88688	10	0.280943	18	0.280917	-3.9	0.8137	3.41	2730.4	7.1
21	0.0199	16	0.00079	5	1.46722	1.88679	10	0.280974	20	0.280932	-3.4	0.8164	3.38	2730.4	7.1
22	0.0119	12	0.00052	4	1.46719	1.88685	11	0.280942	19	0.280915	-4.0	0.8080	3.41	2730.4	7.1
23	0.0152	16	0.00058	5	1.46719	1.88695	8	0.280931	20	0.280901	-4.5	0.8161	3.45	2730.4	7.1
ED 1															
1	0.0137	11	0.00048	3	1.46720	1.88679	18	0.280981	24	0.280956	-2.3	0.7157	3.32	2740.2	8.3
2	0.0707	57	0.00245	15	1.46720	1.88671	17	0.281087	24	0.280958	-2.2	0.7157	3.31	2740.2	8.3
3	0.0192	15	0.00070	4	1.46721	1.88678	18	0.280969	21	0.280932	-3.2	0.7156	3.37	2740.2	8.3
4	0.0216	20	0.00079	6	1.46725	1.88688	25	0.280992	19	0.280950	-2.5	0.7156	3.33	2740.2	8.3
5	0.0263	25	0.00094	7	1.46712	1.88676	16	0.280997	24	0.280947	-2.6	0.7156	3.34	2740.2	8.3
6	0.0094	8	0.00036	2	1.46719	1.88684	14	0.280976	33	0.280958	-2.3	0.7157	3.31	2740.2	8.3
7	0.0097	8	0.00036	2	1.46718	1.88684	15	0.280960	28	0.280941	-2.9	0.7156	3.35	2740.2	8.3
8	0.0124	10	0.00046	3	1.46717	1.88672	15	0.280981	26	0.280957	-2.3	0.7157	3.31	2740.2	8.3
9	0.0141	11	0.00053	3	1.46717	1.88676	21	0.280995	29	0.280967	-1.9	0.7157	3.29	2740.2	8.3
10	0.0305	25	0.00107	7	1.46714	1.88680	17	0.281013	28	0.280957	-2.3	0.7157	3.31	2740.2	8.3

[a] $^{176}Yb/^{177}Hf = (^{176}Yb/^{173}Yb)_{true} \times (^{173}Yb/^{177}Hf)_{measured} \times (M_{173(Yb)}/M_{177(Hf)})^{\beta(Hf)}$, $\beta(Hf) = \ln(^{179}Hf/^{177}Hf_{true}/^{179}Hf/^{177}Hf_{measured})/\ln(M_{179(Hf)}/M_{177(Hf)})$, M = mass of respective isotope. The $^{176}Lu/^{177}Hf$ were calculated in a similar way by using the $^{175}Lu/^{177}Hf$ and β(Yb).

[b] Mean Hf signal in volt.

[c] Uncertainties are quadratic additions of the within-run precision and the daily reproducibility of the 40 ppb-JMC475 solution. Uncertainties for the JMC475 quoted at 2σ (2 standard deviation).

[d] Initial $^{176}Hf/^{177}Hf$ and εHf calculated using the Concordia age determined by SHRIMP and LA-ICP-MS dating (see column f), and the CHUR parameters: $^{176}Lu/^{177}Hf$ = 0.0336 and $^{176}Hf/^{177}Hf$ = 0.282785 (Bouvier et al., 2008).

[e] Two-stage model age in billion years using the measured $^{176}Lu/^{177}Hf$ of each spot (first stage = age of zircon), a value of 0.015 (Griffin et al., 2002) for the average continental crust (second stage), and average MORB (DM) $^{176}Lu/^{177}Hf$ and $^{176}Hf/^{177}Hf$ of 0.0388 and 0.283250 (Andersen et al., 2009), respectively.

[f] Concordia ages from tables 7 and 8.

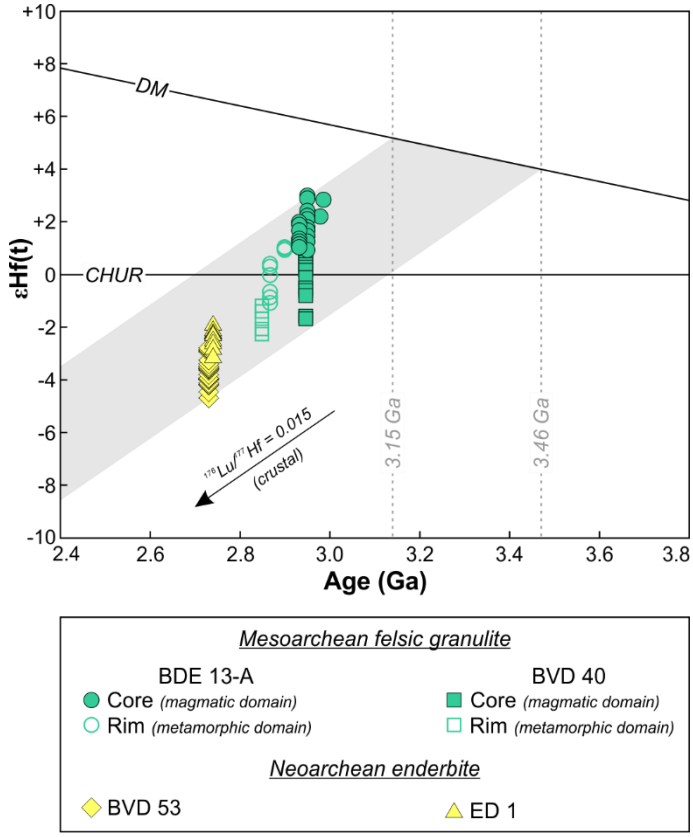

Figure 19. Plots of time *vs.* εHf for the Meso- and Neoarchean sodic rocks from the studied area (dataset in Tables 10 and 11).

9. Discussions

9.1. Affinities and origin of the Meso- and Neoarchean sodic magmas from Ouro Verde area

Concerning the studied Mesoarchean felsic granulites, there is no geochemical data available in the literature related to akin rocks in Carajás province. However, there are two exposures of Mesoarchean Na-granitoids close to the studied area that display crystallization ages coincident with those of felsic granulite protolith crystallization: 3.0 Ga Bacaba tonalite (Moreto et al., 2011) and 2.93 Ga Rio Verde TTG (Feio et al., 2013). However, the first was not geochemically discriminated, then the comparisons will be constrained to Rio Verde TTG. The results show that the felsic granulite protoliths share accentuated similarities with the Rio Verde TTG, although slight differences are also identified. Concerning SiO_2 contents, both rocks present nearly coincident values, although the felsic granulites display slight lower contents and a narrower range of SiO_2 compared to Rio Verde TTG. In counterpart, the Rio Verde TTG presents lower CaO and higher Ba and Rb contents, negative Sr and Ti anomalies, and a slightly more prominent Nb-Ta anomaly. Al_2O_3 and Sr contents are wider and superimpose the felsic granulites values (cf. Figures 10–12).

Regarding the enderbite plutons, granitoids from Pedra Branca suite (Feio et al., 2013) had been the only Neoarchean granitoids of sodic affinity identified in the Carajás province. However, this suite presents lower CaO, Na_2O and Rb, and higher Y contents, wider range of FeO* and narrower range of Al_2O_3 when compared with those of the Ouro Verde area. In addition, the REE patterns between these lithologies are completely different, whose studied rocks present all values between 10–15 times higher than those from Pedra Branca suite (cf. Figure 10–12).

9.1.1. Mesoarchean felsic granulite protolith

The geochemical data previously presented demonstrate that the Mesoarchean felsic granulites from Ouro Verde area display strong affinities with typical Archean TTG: Al_2O_3 content ≥ 15 wt.% at 70 wt.% SiO_2, sodic nature (high Na_2O content) and correlated low K_2O/Na_2O ratio (< 0.5), ferromagnesian oxide-poor (Fe_2O_3 + MgO + MnO + TiO_2 ≤ 5 wt.%), A/CNK index between about 0.9 and 1.1, moderate to low Mg#, negative Nb-Ta anomalies, fractionated REE patterns (high La_N/Yb_N), high Sr, and low HREE and Y (Martin, 1994, 1999; Martin et al., 2005; Moyen, 2009). Several models have been hypothesized to account for Archean TTG genesis (Martin, 1999; Drummond and Defant, 1990; Foley et al., 2002; Rapp et al., 2003; Condie, 2005; Almeida et al., 2011), which it is assumed that the protolith of the felsic granulite (TTG-like) was generated through partial melting of LILE-enriched basaltic source (oceanic plateau basalts) in subduction zones (Martin et al., 2014). However, some aspects must be considered concerning the nature of the residue. Firstly, the high both La_N/Yb_N and Sr/Y ratios and the affinity to the low-HREE TTG from Heilimo et al. (2010; Figures 20a, b and c, respectively) point to a garnet-bearing and plagioclase-free amphibolite residue, although the presence of slight both positive to negative Eu anomaly (cf. Figure 12a), accompanied by predominant positive Sr anomaly (cf. Figure 12c) could reflect absence of plagioclase in the source or also admits minor plagioclase fractionation. Similarly, although these rocks present moderate negative Nb-Ta anomaly, it is accompanied by positive Ti anomaly, which could suggest that rutile was either absent or had a minor participation in the residue.

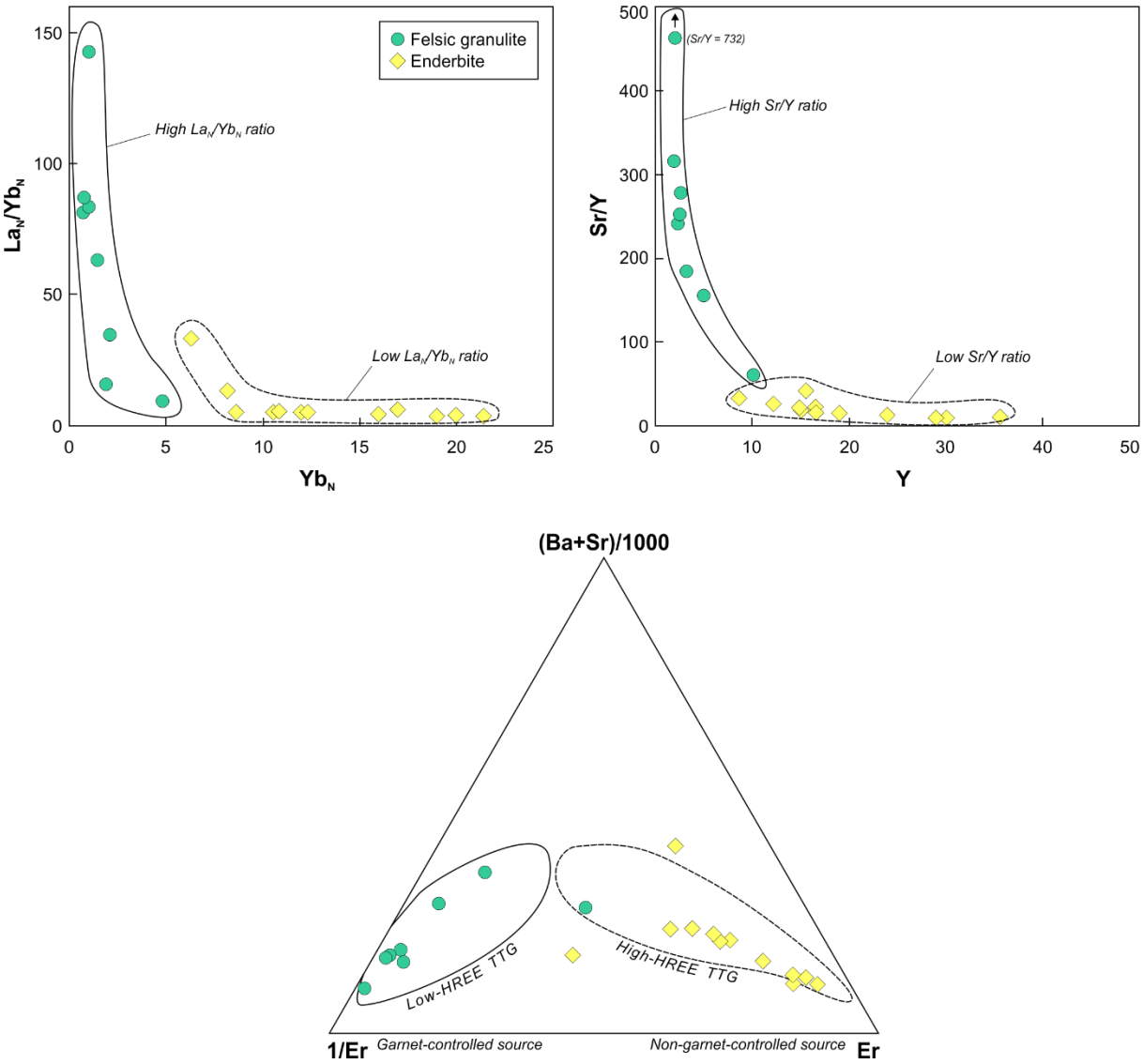

Figure 20. (a) La_N/Yb_N *vs.* Yb_N, (b) Sr/Y *vs.* Y and (c) [1/Er]-[(Ba+Sr)/1000]-[Er] (Heilimo et al., 2010) diagrams.

Considering all the aforementioned information, we have proposed a petrogenetic model to generate the protolith of the felsic granulites from Ouro Verde area – admitted as a TTG – that would involve partial melting of LILE-enriched basaltic source. In order to investigate the parameters involved in these processes, the major elements mass balance calculations were performed using the software GENESIS 4.0 (Teixeira, 2005), that consists in adjusting the relative proportions of residual minerals from the source to reproduce the composition of the expected melt. The quality of the calculated data is reliable if the sum of the square residuals ($\sum R^2$) ≤1.2 (Wyers and Barton, 1986), and allows us to proceed to trace elements modeling, using Excel sheets created by the authors, which was based on the equilibrium partial melting equation (Wilson, 1989; Equation 1):

$$\frac{C_L}{C_0} = \frac{1}{F + D - FD} \quad (1)$$

where C_L and C_0 are the trace element concentrations in the melt (liquid) and in the source (solid), respectively, F is the weight fraction of melt formed and D is the bulk distribution coefficient for the residual solids at the moment when melt is removed from the system. The mineral/liquid partition coefficients (Kd) used in the modeling were obtained from Rollinson (1993), Martin et al. (2014) and from the online database https://earthref.org/KDD/.

The ambiguous Eu-Sr pair behavior is not clear concerning if plagioclase is present or not in the residue, which allowed to test two models of partial melting of LILE-enriched hydrous metabasalt producing TTG melts in equilibrium with: (1) a plagioclase-free and (2) a plagioclase-bearing garnet amphibolite residue. Therefore, the sample CP 44 was taken to represent the initial liquid, while a LILE-enriched Archean basalt sample from Pilbara craton (sample F2 from Smithies et al., 2009) was used as source. The results show that in the partial melting assuming a plagioclase-free garnet amphibolite residue, the best models provided $\sum R^2$ relatively high to be statistically acceptable ($\sum R^2 > 4$), although gave a reasonable fit for the trace elements modeling. On the other hand, the modeling assuming the TTG melt in equilibrium with a plagioclase-bearing garnet amphibolite residue provided good fits ($\sum R^2 < 1$), which the lowest $\sum R^2$ were reached when rutile was replaced by ilmenite in the residue ($\sum R^2 = 0.597$; Table 12), that was obtained with 15% of partial melting, leaving a residue composed of amphibole (62.49%), garnet (17.63%), plagioclase (14.89%), ilmenite (3.30%) and clinopyroxene (1.69%). Thus, these same proportions of melt and residual mineral phases (proportion melt:residue ratio of 15% to 85%) were tested in the trace elements modeling (Figure 21a), which also yielded an excellent fit between the calculated melt (generated by partial melting of LILE-enriched metabasalts) and the representative TTG-like rock sample (protolith of the felsic granulite; sample CP 44).

Table 12. Modeling major and trace elements compositions and residual mineral assemblages for generation of the Mesoarchean felsic granulite protolith by partial melting of enriched metabasalt.

	F2 (C_0)[a]	Residue (C_S)	Composition of minerals					Calculated magma (C_L)	CP 44
	Enriched metabasalt[b]	Bulk	Amp[c]	Grt[c]	Pl[c]	Ilm[d]	Cpx[c]		Felsic granulite protolith (TTG-like)[b]
			62.49%	17.63%	14.89%	3.30%	1.69%		
Major elements (weight %)									
SiO_2	47.83	43.94	44.98	38.84	50.24	0.00	50.56	71.53	71.71
TiO_2	2.06	2.61	1.49	0.03	0.00	50.00	0.27	0.05	0.26
Al_2O_3	15.41	15.55	11.19	21.51	30.46	0.00	2.52	15.54	15.70
FeO*	14.21	16.36	15.29	27.15	0.00	50.00	12.15	2.09	2.16
MnO	0.25	0.35	0.14	1.45	0.00	0.00	0.23	-0.02	0.03
MgO	7.43	8.80	12.01	5.51	0.00	0.00	10.04	0.59	0.78
CaO	9.51	10.60	10.88	6.31	14.39	0.00	22.59	3.47	3.53
Na_2O	2.37	1.54	1.60	0.00	3.42	0.00	0.42	5.13	4.78
K_2O	0.94	0.25	0.39	0.00	0.04	0.00	0.00	1.62	1.05
Trace elements (ppm)									
Ba	94.0							512.1	484.0
K	7555							10971	8634
Sr	135.1							441.2	554.3
Y	27.4							3.3	2.3
Zr	108.7			$\sum R^2$				157.7	161.1
Nb	8.6			0.597				4.8	4.9
La	7.62			Melt fraction (F)				34.42	33.70
Ce	19.91			15%				60.69	62.30
Nd	16.45							20.92	20.80
Sm	4.69							2.57	2.66
Eu	1.71							0.67	0.67
Gd	4.98							1.39	1.41
Yb	2.40							0.19	0.16
Lu	0.400							0.033	0.030

[a] 3.5 Ga enriched basalt from Pilbara craton (Smithies et al., 2009).

[b] Original oxide values recast to 100%.

[c] Values from Weaver et al. (1982).

[d] Values from Martin (1987).

$\sum R^2$ = sum of the squared residuals.

All iron is reported as FeO.

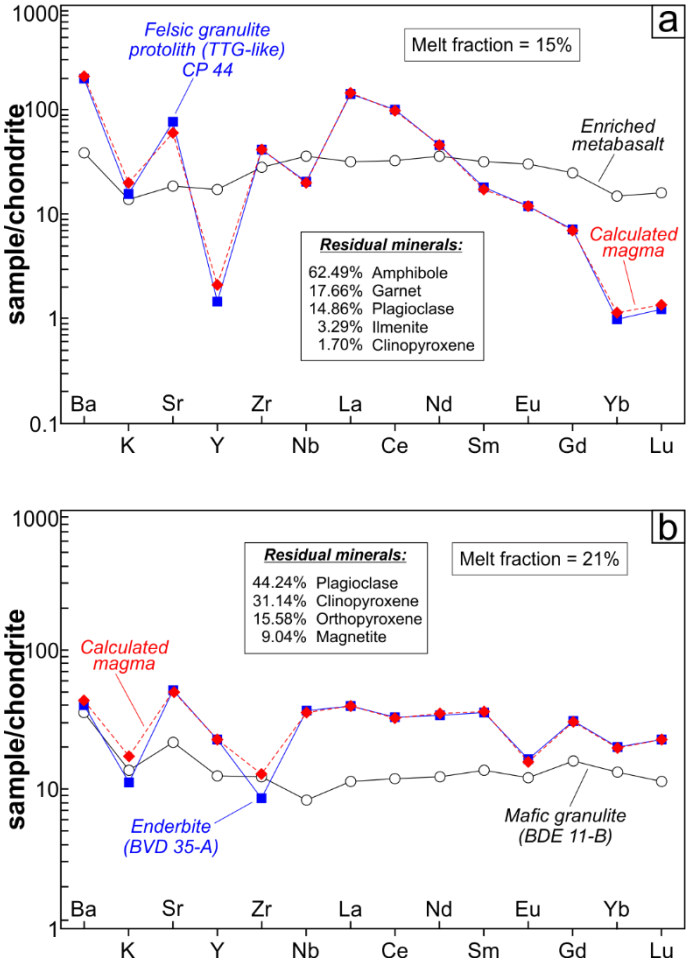

Figure 21. Trace elements models for generation of the (a) Mesoarchean felsic granulite protolith (TTG-like) and (b) the Neoarchean enderbite, both by partial melting. Chondrite (C1) normalization values are from Sun McDonough and Sun (1995).

9.1.2. Neoarchean enderbite

As stated in the section 4, the genesis of the enderbite plutons is associated to the Neoarchean granitogenesis in the Canaã dos Carajás domain, which are coeval with Pium diopside-norite. The presence of mafic magma coeval with those of felsic nature (A-type granites) seems to indicate a petrogenetic model invoking underplating of the lower crust (Marangoanha et al., unpublished results), which adds mass and heat to the continental crust and can cause, among other effects, regional-scale granulite- to amphibolite- facies metamorphism, anatexis, and surface uplift. However, the choice of an adequate petrogenetic model able to give rise to A-type magmas depends on the tectonic regimes during which the magmas were emplaced. Thus, considering the consistent within plate affinity and overall transtensional/transpressional regime during emplacement (syntectonic) of the Neoarchean granitoids from Carajás region, one can conclude that granite generation (2.75 Ga) does not seem to be related neither to an environment of magmatic arc nor to continent rift, as assumed by Barros et al. (2009) and Tavares (2015), respectively. Alternatively, to assume another

hypothesis, it is worth noting that as crust thickens during shortening, the lowermost crust may undergo metamorphic eclogitization, which increases its density promoting the development of thick lithosphere which is then prone to gravitational removal (Krystopowicz and Currie, 2013; Thybo and Artemieva, 2013). In this case, lower crust (eclogitic root) and mantle lithosphere could have been removed through delamination (detachment from the weak lower crust) during crustal thickening, followed by widespread crustal deformation and magmatism (mafic magmas generated beneath continental areas are frequently emplaced at the Moho and in the lowermost crust).

A petrogenetically coherent model to clarify the origin of the Neoarchean enderbite is presented considering a tectono-magmatic scenario related to crustal thickening in a transpressional regime at 2.75 Ga, with subsequent inversion of the Carajás basin ~20 Ma latter (at 2.73 Ga), and crustal heating caused by underplated mafic crust delaminated after transforming into eclogite. In this case, partial melting of the lower crust (Mesoarchean mafic granulite) appears to be the main mechanism accounted to generate orthopyroxene-bearing Na-granitoid plutons, as indicated by their Hf-T_{DM2} of 3.46–3.29 (cf. Table 11 and Figure 19). Major elements mass balance calculations and trace elements modeling were performed having as representative of the initial liquid the sample BVD 35-A, and of Mesoarchean lower crust, the sample BDE 11-B (mafic granulite) considered as a potential source. The nature of the residue was defined according to the low La_N/Yb_N and Sr/Y ratios (Figure 20a and b, respectively), and the affinity to the high-HREE TTG from Heilimo (2010; Figure 20c) which stablish a garnet+amphibole-free and plagioclase-bearing granulitic restite in equilibrium with the produced melt (orthopyroxene-bearing tonalite). Also, the absence of negative Nb-Ta anomaly (cf. Figure 12d) points to a rutile-free residue. The major elements model obtained gave excellent results, which the best fit model ($\sum R^2$ = 0.881; Table 13) was achieved to generate the enderbite from Ouro Verde area by 21% melting of the lower crust, leaving a residue composed by plagioclase (44.24%), clinopyroxene (31.14%), orthopyroxene (15.58%) and magnetite (9.04%). This model yielded an excellent fit for trace elements modeling (Figure 21b).

Table 13. Modeling major and trace elements compositions and residual mineral assemblages for generation of the Neoarchean enderbite by partial melting of Mesoarchean mafic granulite.

	BDE 11-B (C_0)[a]	Residue (C_S)	Composition of minerals				Calculated	BVD 35-A
	Mafic granulite[b]	Bulk	Pl[c]	Cpx[c]	Opx[c]	Mt[c]	magma (C_L)	Enderbite[b]
			44.24%	31.14%	15.58%	9.04%		
Major elements (weight %)								
SiO_2	49.90	48.10	53.02	51.54	54.11	0.04	57.60	57.87
TiO_2	0.82	0.45	0.02	0.63	0.17	2.30	0.73	0.34
Al_2O_3	14.34	14.09	29.44	2.56	1.05	0.91	15.84	16.00
FeO*	11.56	13.94	0.29	8.47	15.63	92.38	3.57	3.81
MnO	0.21	0.18	0.00	0.34	0.40	0.07	0.11	0.05
MgO	7.42	8.58	0.23	13.97	26.05	0.16	3.56	3.68
CaO	11.86	12.54	12.46	21.69	1.59	0.00	10.03	10.22
Na_2O	2.96	2.02	4.20	0.49	0.03	0.05	7.10	7.27
K_2O	0.93	0.09	0.19	0.02	0.01	0.00	1.46	0.76
Trace elements (ppm)								
Ba	85.2						105.1	96.3
K	7472						9479	6144
Sr	156.0						364.4	371.0
Y	19.5						35.6	35.6
Zr	47.0		$\sum R^2$				48.6	33.0
Nb	2.0		0.881				8.5	8.8
La	2.70		Melt fraction (F)				9.42	9.30
Ce	7.30		21%				19.92	20.00
Nd	5.60						15.90	15.50
Sm	2.03						5.34	5.26
Eu	0.68						0.88	0.92
Gd	3.18						6.09	6.12
Yb	2.12						3.19	3.21
Lu	0.280						0.561	0.560

[a] Data from the authors.

[b] Original oxide values recast to 100%.

[c] Values from Shao and Wei (2011).

$\sum R^2$ = sum of the squared residuals.

All iron is reported as FeO.

9.2. Metamorphism and deformation parameters

9.2.1. Deformational domains

Based on cross-cutting relationships, and macro- and microscopic analyses, allied to geochronologic/isotopic data, two events of Archean deformation, designated D_1 and D_2, have been identified on the rocks from the studied area. D_1 deformational event is observed in the felsic and mafic orthogranulite, while D_2 is recorded in the tonalitic enderbite. It is noteworthy to mention that D_2 event is also well-recorded in the Vila União hybrid granitoids (Marangoanha et al., unpublished results), however, these rocks are not the aim in this work.

D_1 event is defined by a dominant pattern, characterized by the development of a well-defined E–W to WNW–ESE-striking foliation (S_1), with moderate to subvertical dips towards mostly the S, and moderate plunging mineral stretching lineation (L_1; see stereoplots from the Figure 3). Folding structures (F_1) are quite common and are marked by subvertical folds (subvertical fold hinges) with axes plane striking E–W to WNW–ESE, parallel to S_1 (cf. Figure 5e). It is important to mention that are recorded rare N–S-striking foliation, which

appears to be transposed by S_1 (cf. Figure 5f) and could suggest the earliest structural frame recorded in the Carajás province. This deformational domain gathers the following magmatic, tectonic and metamorphic episodes: (i) at 3.05 to 2.93 Ga was generated the felsic granulite protolith (typical TTG-like) in an arc-related setting; and (ii) at 2.89 to 2.84 Ga (peak at ~2.86 Ga) this crust was submitted by a ultrahigh temperature (UHT) metamorphism, in a granulitic facies, triggered by crustal thickening (crustal reworking) during the generation of large bulk of anatectic granites (e.g. Boa Sorte and Cruzadão granites; cf. Figures 2 and 3) in a collisional setting. In summary, the arc-related setting followed by collision is supported by shortening strain events printed on the rocks from this deformational domain, which are related to a convergent system, and defined as contraction-dominated tectonic regime.

In contrast, the D2 event displays a simpler structural pattern, comprised by an E–W steeply inclined well-developed mylonitic foliation (S2) towards both the N and S, and steep-to-subvertically plunging mineral stretching lineation (L2). Shear bands (C2) is recorded crosscutting rare N–S-striking foliation (related to the Mesoarchean; cf. Figure 5i). As stated before, the generation of the enderbite and others Neoarchean granitoids involves initially a detachment of the lowermost crust during crustal thickening at 2.75 Ga, followed by mafic underplating. Consolidation of their magmas occurred under pure shear-dominated transpressional tectonic regime at 2.73 Ga, characterized by combined ductile shear (less expressive) and compressional movements (dominant). Thus, the syn-tectonic nature of the enderbite, associated to the structural pattern printed on this rock, stablish the pure shear-dominated transpressional tectonic regime played during the D2 event.

9.2.2. Mesoarchean metamorphism

Petrographic analysis performed on the Mesoarchean felsic granulites combined to structural and geochronological data allowed to make some considerations concerning the metamorphic history in this portion of crust. Firstly, the highly coincident both anatectic granites crystallization (e.g. Cruzadão, Boa Sorte, Bom Jesus e Serra Dourada granites) and metamorphic ages (recorded by zircon rims in the felsic granulites; see section 8.2.1), spanning 2.89–2.84 Ga (see Figure 2) indicate the crustal thickening (related to a collisional regime) as the main source of heat to promote regional high-temperature metamorphism in the pre-existing TTG crust – although other minor heat source could also be considered, as those related to the anatectic granites magmatism/emplacement. In this case, prograde and retrograde reaction textures that can be used to elucidate changes in P-T conditions during the metamorphic history. The prograde reaction texture observed in these rocks are dehydration

reactions, resulting in the orthopyroxene formed at expense of biotite breakdown, according to the reaction Bt + Qz → Opx + Kfs + melt (cf. Figures 6g and h), which correspond to the time of peak metamorphic conditions. Although less common, orthopyroxene is also formed by the reaction Amp + Qz → Opx + Cpx + melt. The retrograde metamorphic condition is evident from the formation of Bt-Qz symplectite replacing peak-metamorphic orthopyroxene by the reaction Opx + Kfs + melt → Bt + Qz (cf. Figure 6f). This retrograde condition is also supported by the granoblastic fabric observed in some plagioclase crystals with strain-free aspects (cf. Figure 6b), which can be associated to static recrystallization (Passchier and Trouw, 2005).

All these observations are reinforced by Delinardo et al. (2014) findings, which performed P-T calculations from conventional geothermobarometry on these rocks and obtained results of peak-metamorphic P-T conditions of 13.7–8.1 kbar and 1128–907°C, and retrograde metamorphic conditions of 5.5–4.4 kbar and 905–893°C, and defines ultra-high temperature metamorphism (UHT) for these granulites.

9.2.3. Partial melting and lower crust exhumation model

The onset of partial melting has a profound effect on the structures and strain rates in the continental crust, which will lead to heterogeneous deformation in the crust with increasing melt flow (Brown, 2010). In residual crust (granulite), evidence of melt extraction pathways at mesoscale is recorded by leucosome networks that allow the transfer of melt to ascent conduits at the initiation of the melt-extraction event. Differential stress in anisotropic rocks results in the formation of many different types of dilatant structures (i.e. boudins) to which the melt migrates during the deformation. In this case, the melt ascent starts via ductile fracture (propagates from dilation or shear bands) that allows transport of melt along the crustal-scale ascent conduits. Anatectic systems become more ordered by decreasing the number and increasing the width of ascent conduits from the anatectic zone through the overlying *subsolidus* crust to the ductile-brittle transition zone, where the melt accumulates in plutons along the foliation as sills (emplacement of laccoliths or steep tabular sheeted intrusions). The melt storage in the base of the upper crust can lead to both the upper-lower crust detachment and the development of large scale shear zones (Brown, 2013). Such scenario juxtaposes different structural levels of the crust by crustal shortening along the major regional-scale structures.

Crustal thickening and exhumation during transpression (foliation steeply dipping) and transtension (dilatant structures) in highly oblique zones characterize many crust segments

that suffered crustal shortening in the Precambrian terrains. The tectonic exhumation model of the Carajás domain in a regional imbricated system (Araújo and Maia, 1991) related to the development of the Itacaiúnas shear belt (Costa et al., 1995; Holdsworth and Pinheiro, 2000) can be attributed to the aforementioned process. In this context, the high-grade metamorphic rocks (granulite core) of the Rio Verde area was deformed, intruded, and exhumed in an oblique tectonic regime involving a switch from transpression to transtension (exhumation). A ~50 Ma history of transpression and transtension is recorded in Neoarchean massifs and Carajás basin deposits (Figure 2). The granitic and enderbitic rocks record a high temperature syn-transpression ductile fabric that was overprinted by lower-grade syn-transtension ductile shear zones. In the Mesoarchean granulite, the sinistral shear bands overprinted the N-S earlier fabrics during exhumation cycle (cf. Figure 5i). Extension occurred in concert with lateral motion along shortening-parallel structures, and is a major mechanism by which lower to middle crust is exhumed, and that triggered emplacement of crustal and mantle derived magmas (Vila União hybrid granitoids and Pium diopside-norite, respectively).

The tectonic history of the Rio Verde area involved a protracted history of high-grade metamorphism and crustal melting, consistent with models for prograde metamorphism in collisional settings (pure shear strain) in 2.87 Ga. In addition, exhumation of the granulite core provides a remarkably complete view into the mid-crust of a highly oblique system, and, it permits to stablish the reconstruction of the tectonic and thermal history of the upper 25 km of continental crust during ~50 Ma of tectonism.

The tectonic juxtaposition of Archean TTG-greenstone and high-grade terrains is a common feature of Archaean orogens worldwide, e.g., the SW Greenland, the Napier complex in Antarctica, Siberian craton, the Limpopo belt in southern Africa and the southern part of the Dharwar craton, India (Harley, 1989; Kolb et al., 2012). The similarity in chemical compositions and lithologic proportion (greenstone belt/TTG ratios in low grade areas and mafic granulite/enderbite ratios in high grade areas) suggest that many of these Archean terrains represent shallow and deep exposure levels of the same crust (juxtaposed).

9.3. Geodynamic reconstruction

The dataset presented so far provide new insight on the Archean evolution for the Canaã dos Carajás domain (Carajás province), whose proposed evolution can be divided into three stages: (i) between 3.05 and 2.93 Ga (Figure 22a), TTG crust was formed through partial melting of a subducted LILE-rich basaltic crust (e.g. oceanic plateau basalts), whose Lu-Hf zircon isotopic data (magmatic core values) with T_{DM2} ranging from 3.44–3.15 Ga and

εHf(t) between -1.7 and 3.0, suggest juvenile character to these rocks (cf. Table 10 and Figure 19); (ii) in the period between 2.89 and 2.84 Ga (Figure 22b), this crustal segment has experienced a large volume of anatectic granites emplacement, represented by Boa Sorte, Cruzadão and other related granites, accompanied by crustal thickening (N–S crustal shortening), which induced UHT granulite-facies metamorphism in the lower-middle portion of the pre-existing TTG crust. This condition was responsible for forming the felsic granulite from the TTG protolith, as also indicated by their metamorphic zircon rims ages (cf. Figure 14b and c, and Figure 15b and c – population 2). The interval of age (2.87–2.84 Ga) obtained to the mafic granulite (cf. Figure 14d), which is subordinated and commonly occurs as enclave hosted in the felsic granulite, can be interpreted as metamorphic event (see section 8.2.1). Accordingly, the spatial relation between mafic and felsic granulites in the Ouro Verde area indicates that their respective protoliths were affected simultaneously by granulite-facies metamorphism. Although the felsic granulite zircon grains display both preserved magmatic core and metamorphic rim, zircon grains from the mafic granulite have overprinted entirely their magmatic data during the metamorphism, probably due to the smaller size of its grains (see Figure 14d) has facilitated the diffusional resetting rate (Moser et al., 2017); and (iii) in the Neoarchean, at ~2.75 Ga (Figure 22c), this area was submitted to a N–S transtensional/transpressional tectonic regime, where the lowermost mafic crust was delaminated during crustal thickening, causing crustal underplating by mantle-derived mafic magma followed by partial melting of the Mesoarchean mafic granulite which is solely responsible by the origin of the enderbite. In consequence of this process, also is attributed the formation of the Vila União hybrid granitoids, which indicates the coexistence of both felsic and mafic magmas through mixing and mingling evidences, and whose origins are related to partial melting of the Mesoarchean felsic granulite and the mantle, respectively, producing magmas akin to leucogranitic melt (A-type granites) and the Pium diopside-norite, respectively (Marangoanha et al., unpublished results). These magmas were channeled through of the crust via pre-existing Mesoarchean shear zones trending E–W (Itacaiúnas shear zone) as constrained by analysis of field structures and whose emplacement occurred under pure shear-dominated transpression, with E–W sinistral sense of tectonic movement (syn-tectonic nature; Figure 22d). The crustal thickening and shortening has lasted about 20 Ma, when at 2.73 Ga the complete Carajás basin inversion would have occurred. The main mechanisms and processes involved in the origin of the granitoids and metamorphic rocks from Ouro Verde area are schematically illustrated in the flowchart of Figure 23.

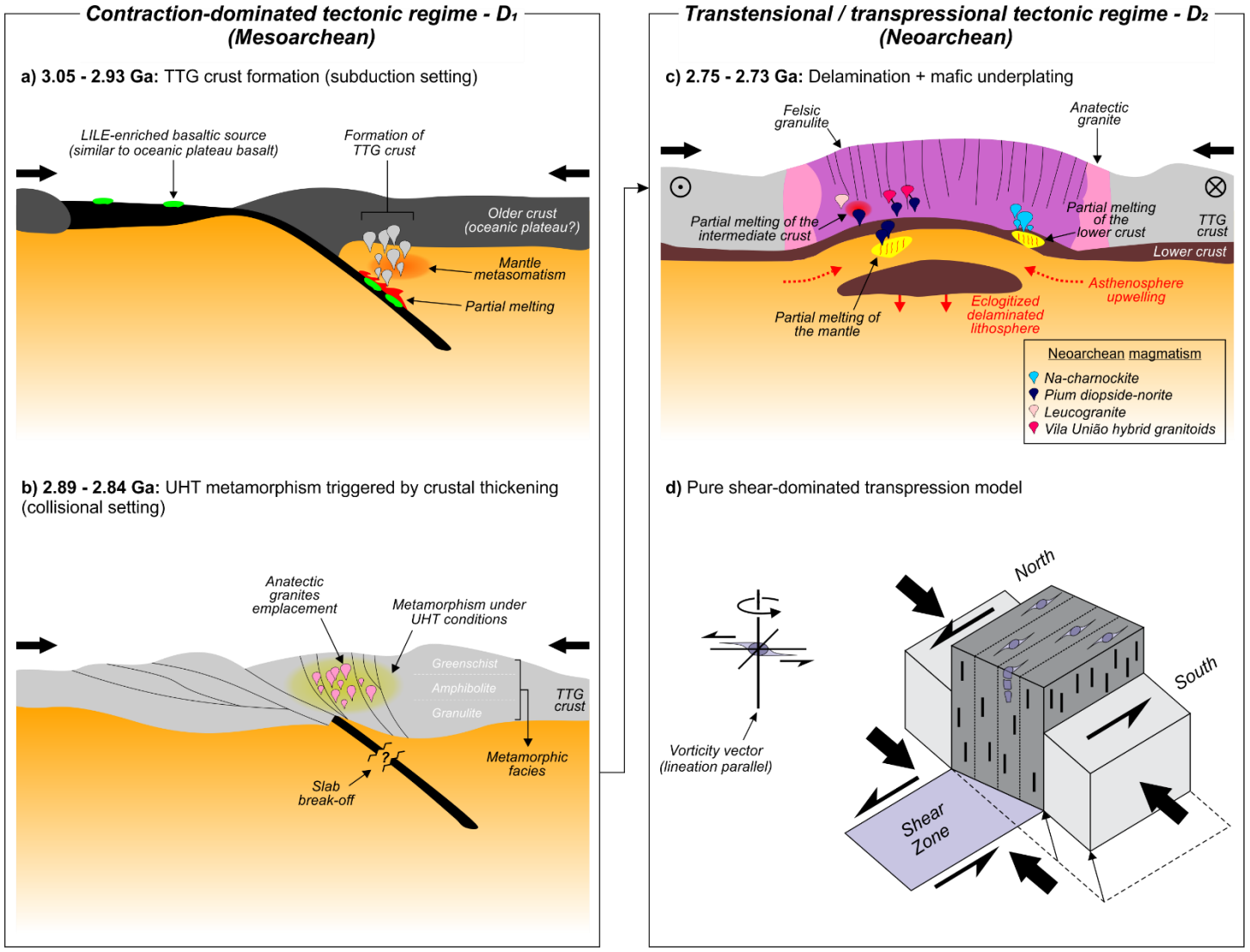

Figure 22. Simplified schematic illustration summarizing the proposed petrogenetic/geodynamic model corresponding to the generation of both Meso- and Neoarchean orthopyroxene-bearing sodic rocks from Canaã dos Carajás domain, Carajás province. See text for discussion.

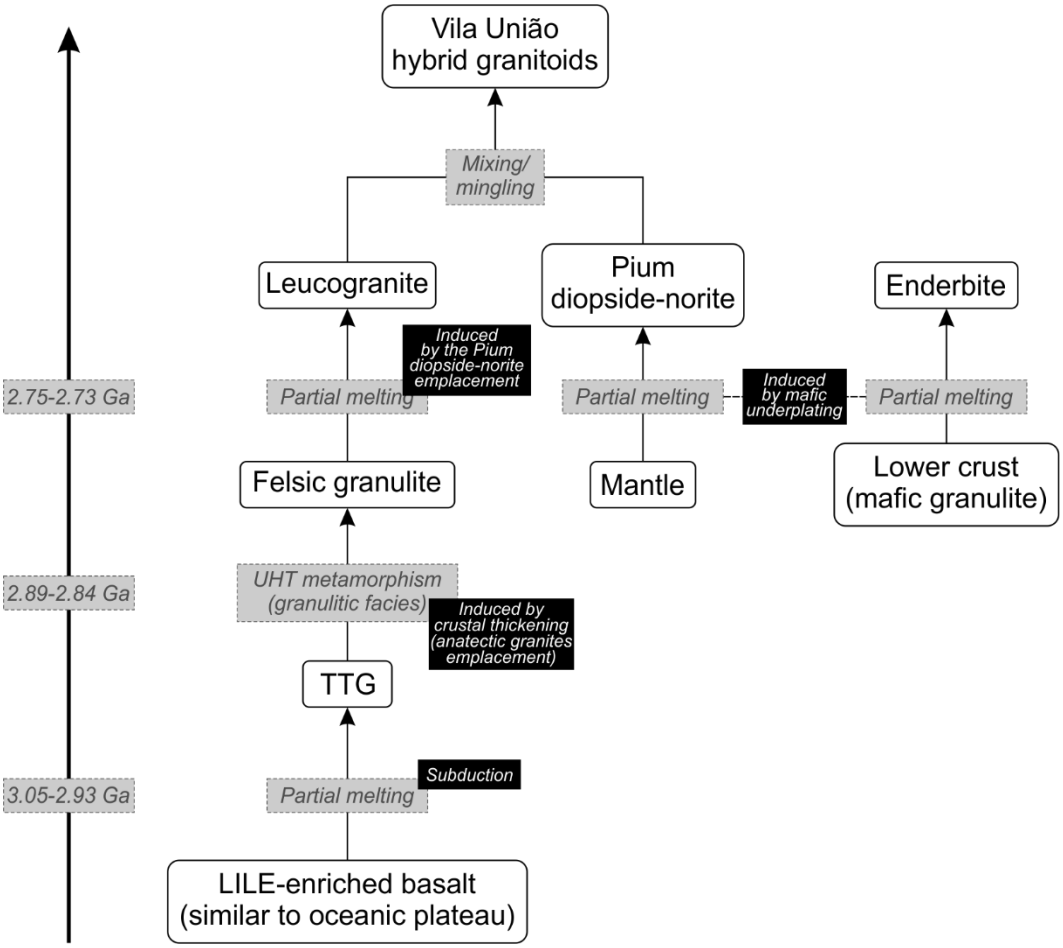

Figure 23. Sketch summarizing the proposed petrogenetic/geodynamic model in the Figure 22.

10. Conclusions

(1) The Mesoarchean Ouro Verde felsic granulite has as protolith a TTG formed between 3.05 to 2.93 Ga in a N–S subduction related-setting, from partial melting of LILE-enriched metabasalts, and then metamorphosed in granulite-facies at 2.89–2.84 Ga during a N–S collisional regime. The Hf-T_{DM2} of 3.44–3.15 Ga and the clear positive to slight negative εHf(t) values (between -1.7 and 3.0) of the magmatic zircon cores from the Mesoarchean Ouro Verde felsic granulite suggest magma derivation from juvenile sources.

(2) The Neoarchean enderbite has crystallization age of 2.75–2.73 Ga and was formed by partial melting of mafic granulite at lower crust level. The origin of the Neoarchean magmatism of the Carajás province is related to a transpressional/transtensional tectonic regime at 2.75 Ga, with subsequent inversion of the Carajás basin ~20 Ma latter (at 2.73 Ga), and crustal heating caused by underplated mafic crust. The Neoarchean enderbite displays Hf-T_{DM2} of 3.46–3.29 Ga and lower εHf(t) values, between -4.8 and -1.9, that reflects longer crustal residence time to these rocks.

(3) The tectonic history of the Rio Verde area involved high-grade metamorphism and crustal melting, consistent with models for prograde metamorphism in collisional settings. The high-grade metamorphic rocks (granulite core) were intruded and exhumed in an oblique tectonic regime involving a switch from transpression to transtension during the development of the Itacaiúnas shear belt, which mark the transition between the lower and upper crustal zones of the Carajás domain. Deformation and magma emplacement were assisted by partial melts (widespread occurrence of leucosomes in mafic granulite), that resulted in the final terrane amalgamation at 2.75–2.73 Ga.

Acknowledgements

We would like to thank C.N. Lamarão and G.T. Marques for providing BSE and CL images conducted at the Laboratório de Microanálises (UFPA). We are also grateful to K. Sato and A.T. Onoe for the assistance during the acquisition of U-Pb SHRIMP data at the Laboratório de Geologia de Alta Resolução (USP), and A.R. Alkmim for the help provided during the acquisition of U-Pb LA-SF-ICP-MS and Lu-Hf data at the Laboratório de Geoquímica Isotópica (UFOP). The first author (BM) thanks Conselho Nacional de Desenvolvimento Científico e Tecnológico (CNPq) for a doctor thesis scholarship (Proc. 163874/2014-0). Funding for this project has come from CNPq (D.C. Oliveira – Proc. 311388/2016-7 and 485806/2013-4), Fundo de Amparo à Pesquisa do Estado do Pará (FAPESPA; Proc. 133/2008-0), Vale/FAPESPA (ICAAF n. 053/2011) and INCT program (CNPq/FAPESPA/CAPES/PETROBRAS; Proc. 573733/2008-2).

References

Almeida, J.A.C., Dall'Agnol, R., Dias, S.B., Althoff, F.J., 2010. Origin of the Archean Leucogranodiorite-granite suites: evidence from the Rio Maria terrane and implications for granite magmatism in the Archean. Lithos 120, 235–257.

Almeida, J.A.C., Dall'Agnol, R., Oliveira, M.A., Macambira, M.J.B., Pimentel, M.M., Rämö, O.T., Guimarães, F.V., Leite, A.A.S., 2011. Zircon geochronology and geochemistry of the TTG suites of the Rio Maria granite-greenstone terrane: implications for the growth of the Archean crust of Carajás Province, Brazil. Precambrian Research, 187, 201–221.

Althoff, F.J., Barbey, P., Boullier, A.M., 2000. 2.8–3.0 Ga plutonism and deformation in the SE Amazonian craton: the Archean granitoids of Marajoara (Carajás Mineral Province, Brazil). Precambrian Research, 104, 187–206.

Andersen, T., Andersson, U.B., Graham, S., Aberg, G., Simonsen, S.L., 2009. Granitic magmatism by melting of juvenile continental crust: new constraints on the source of Paleoproterozoic granitoids in Fennoscandia from Hf isotopes in zircon. Journal of the Geological Society, 166, 233–247.

Araújo, O.J.B., Maia, R.G.N., 1991. Projeto especial mapas de recursos minerais, de solos e de vegetação para a área do Programa Grande Carajás; Subprojeto Recursos Minerais; Folha SB.22-Z-A: Serra dos Carajás – Estado do Pará. DNPM/CPRM, Brasília, 164 pp. (in Portuguese).

Avelar, V.G., Lafon, J.M., Correia Jr., F.C., Macambira, E.M.B., 1999. O Magmatismo arqueano da região de Tucumã – Província Mineral de Carajás: novos resultados geocronológicos. Revista Brasileira de Geociências 29, 454–460 (in Portuguese).

Barker, F., 1979. Trondhjemite: a definition, environment and hypotheses of origin, in: Barker, F. (Ed.), Trondhjemites, Dacites and Related Rocks. Elsevier, Amsterdam, pp. 1–12.

Barker, F., Arth, J.G., 1976. Generation of trondhjemite-tonalite liquids and Archean bimodal trondhjemite-basalt suites. Geology 4, 596–600.

Barros, C.E.M., Sardinha, A.S., Barbosa, J.P.O., Macambira, M.J.B., 2009. Structure, petrology, geochemistry and zircon U-Pb and Pb-Pb geochronology of the synkinematic Archean (2.7 Ga) A-type granites from the Carajás Metallogenic Province, northern Brazil. Canadian Mineralogist 47, 1423–1440.

Bédard, J.H., Harris, L.B., Thrurston, P.C., 2013. The hunting of the snArc. Precambrian Research 229, 20–48.

Black, L.P., Kamo, S.L., Williams, I.S., Mundil, R., Davis, D.W., Korsch, R.J., Foudoulis, C., 2003. The application of SHRIMP to Phanerozoic geochronology: A critical application of four zircon standards, Chem. Geol., 200, 171–188.

Bouchez, J.L., Delas, C., Gleizes, G., Nédélec, A., Cuney, M., 1992. Submagmatic microfractures in granites. Geology 20, 35–38.

Bouvier, A., Vervoort, J.D., Patchett, P.J., 2008. The Lu-Hf and Sm-Nd isotopic composition of CHUR: constraints from unequilibrated chondrites and implications for the bulk composition of terrestrial planets. Earth and Planetary Science Letters 273, 48–57.

Brown, M., 2010. Melting of the continental crust during orogenesis: the thermal, rheological and compositional consequences of melt transport from lower to upper continental crust. Canadian Journal of Earth Sciences 47, 655–694.

Brown, M., 2013. Granite: from genesis to emplacement. Geological Society of America Bulletin 125, 1079–1113.

Chu, N.C., Taylor, R.N., Chavagnac, V., Nesbitt, R.W., Boella, R.M., Milton, J.A., German, C.R., Bayon, G., Burton, K., 2002. Hf isotope ratio analysis using multi-collector inductively coupled plasma mass spectrometry: an evaluation of isobaric interference corrections. Journal of Analytical Atomic Spectrometry 17, 1567–1574.

Condie, K.C., 1981. Archaean greenstone belts. Elsevier, Amsterdam.

Condie, K.C., 2005. TTGs and adakites: are they both slab melts? Lithos 80, 33–44.

Costa, J.B.S., Araújo, O.J.B., João, X.S.J., Macambira, M.J.B., Lafon, J.M., 1995. A Província Mineral de Carajás: Aspectos tectono-estruturais, estratigráficos e geocronológicos. Boletim do Museu Paraense Emílio Goeldi (Série Ciências da Terra) 7, 199–235.

Costi, H.T., Dall'Agnol, R., Moura, C.A.V., 2000. Geology and Pb–Pb geochronology of Paleoproterozoic volcanic and granitic rocks of Pitinga Province, Amazonian craton, northern Brazil. International Geology Review 42, 832–849.

Dall'Agnol, R., Cunha, I.R.V, Guimarães, F.V, Oliveira, D.C., Teixeira, M.F.B., Feio, G.R.L., Lamarão, C.N., 2017. Mineralogy, geochemistry, and petrology of Neoarchean ferroan to magnesian granites of Carajás Province, Amazonian Craton: The origin of hydrated granites associated with charnockites. Lithos 277, 3–32.

Dall'Agnol, R., Oliveira, D.C., Guimarães, F.V., Gabriel, E.O., Feio, G.R.L., Lamarão, C.N., Althoff, F.J., Santos, P.A., Teixeira, M.F.B., Silva, A.C., Rodrigues, D.S., Santos, M.J.P., Silva, C.R.P., Santos, R.D., Santos, P.J.L., 2013. Geologia do Subdomínio de Transição do Domínio Carajás – Implicações para a evolução arqueana da Província Carajás - Pará. Anais do 13º Simpósio de Geologia da Amazônia. SBG, Belém, CD-rom (in Portuguese).

Dall'Agnol, R., Oliveira, M.A., Almeida, J.A.C., Althoff, F.J., Leite, A.A.S., Oliveira, D.C., Barros, C.E.M., 2006. Archean and Paleoproterozoic granitoids of the Carajás metallogenetic province, eastern Amazonian craton, in: Dall'Agnol, R., Rosa-Costa, L.T., Klein, E.L. (Eds.), Symposium on Magmatism: Crustal Evolution, and Metallogenesis of the Amazonian Craton. Abstracts Volume and Field Trips Guide. Belém, PRONEX-UFPA/SBG-NO, pp. 99–150.

Dall'Agnol, R., Teixeira, N.P., Rämö, O.T., Moura, C.A.V., Macambira, M.J. B., Oliveira, D.C., 2005. Petrogenesis of the Paleoproterozoic, rapakivi, A-type grantites of the Archean Carajás Metallogenic Province, Brazil. Lithos 80, 101–129.

De Wit, M.J., 1998. On Archean granites, greenstones, cratons and tectonics: does the evidence demand a verdict? Precambrian Research 91, 181–226.

Debon, F., Le Fort, P., 1988. A cationic classification of common plutonic rocks and their magmatic associations: principles, method, applications. Bulletin of Mineralogy 111, 493–510.

Delinardo, M.A.S., Monteiro, L.V.S., Moreto, C.P.N., Sousa, S.D., Melo, G.H.C., 2014. Complexo Xingu: Uma secção da crosta inferior exumada durante a evolução do Domínio Carajás, PA. Anais do 47º Congresso Brasileiro de Geologia. SBG, Salvador, CD-rom (in Portuguese).

DOCEGEO (Rio Doce Geologia e Mineração – Distrito Amazônia), 1987. Lithostratigraphic review of the Carajás District and Southern Pará – Brazil, in: Final Meeting of The Working Group, Carajás (PA). Extended abstract, IUGS-UNESCO, p. 32–39.

DOCEGEO (Rio Doce Geologia e Mineração – Distrito Amazônia), 1988. Revisão litoestratigráfica da Província Mineral de Carajás, Pará. 35º Congresso Brasileiro de Geologia. SBG, Belém, pp. 11–54 (in Portuguese).

Drummond, M.S., Defant, M.J., 1990. A model for trondhjemite-tonalite-dacite genesis and crustal growth via slab melting: Archean to modern comparisons. Journal of Geophysics Research 95, 21503–21521.

Dziggel, A., Diener, J.F.A., Kolb, J., Kokfelt, T.F., 2014. Metamorphic record of accretionary processes during the Neoarchean: The Nuuk region, southern West Greenland. Precambrian Research 242, 22–38.

Feio, G.R.L., Dall'Agnol, R., Dantas, E.L., Macambira, M.J.B., Santos, J.O.S., Althoff, F.J., Soares, J.E.B., 2013. Archean granitoid magmatism in the Canaã dos Carajás area: implications for crustal evolution of the Carajás province, Amazonian craton, Brazil. Precambrian Research 227, 157–185.

Foley, S.F., Tiepolo, M., Vannucci, R., 2002. Growth of early continental crust controlled by melting of amphibolite in subduction zones. Nature 417, 837–840.

Frei, D., Gerdes, A., 2009. Accurate and precise in-situ zircon U-Pb age dating with high spatial resolution and high sample throughput by automated LA-SF-ICP-MS. Chemical Geology 261 (3–4), 261–270.

Frost, B.R., Barnes, C., Collins, W., Arculus, R., Ellis, D., Frost, C., 2001. A chemical classification for granitic rocks. Journal of Petrology 42, 2033–2048.

Frost, B.R., Frost, C.D., 2008. On charnockites. Gondwana Research 13, 30–44.

Frost, B.R., Lindsley, D.H., 1992. Equilibria among Fe-Ti oxides, pyroxenes, olivine, and quartz: Part II. Application. American Mineralogist 77, 1004–1020.

Frost, B.R., Lindsley, D.H., Andersen, D.J., 1988. Fe-Ti oxide-silicate equilibria: assemblages with fayalitic olivine. American Mineralogist 73, 727–740.

Frost, R.B., Frost, C.D., Hulsebosch, T.P., Swapp, S.M., 2000. Origin of the charnockites of the Louis Lake Batholith, Wind River Range, Wyoming. Journal of Petrology 41, 1759–1776.

Gabriel, E.O., Oliveira, D.C., 2014. Geologia, petrografia e geoquímica dos granitoides arqueanos de alto magnésio da região de Água Azul do Norte, porção sul do Domínio Carajás, Pará. Boletim do Museu Paraense Emílio Goeldi, Ciências Naturais, 9(3), 533–564 (in Portuguese).

Gaudette, H.E., Lafon, J.M., Macambira, M.J.B., Moura, C.A.V., Scheller, T., 1998. Comparison of single filament Pb evaporation/ionization zircon ages with conventional U-/Pb results: examples from the Precambrian of Brazil. Journal South American Earth Science 11, 351–363.

Gerdes, A., Zeh, A., 2006. Combined U-Pb and Hf isotope LA-MC-ICP-MS analyses of detrital zircons: Comparison with SHRIMP and new constraints for the provenance and age of an Armorican metasediment in Central Germany. Earth and Planetary Science Letters 249, 47–62.

Gerdes, A., Zeh, A., 2009. Zircon formation versus zircon alteration – New insights from combined U-Pb and Lu-Hf in-situ LA-ICP-MS analyses, and consequences for the interpretation of Archean zircon from the Central Zone of the Limpopo Belt. Chemical Geology 261, 230–243.

Grantham, G.H., Mendonidis, P., Thomas, R.J., Satish-Kumar, M., 2012. Multiple origins of charnockite in the Mesoproterozoic Natal belt, Kwazulu-Natal, South Africa. Geoscience Frontiers 3(6), 755–771.

Griffin, W.L., Wang, X., Jackson, S.E., Pearson, N.J., O'Reilly, S.Y., 2002. Zircon geochemistry and magma mixing, SE China: in-situ analysis of Hf isotopes, Tonglu and Pingtan igneous complexes. Lithos 61, 237–269.

Hamilton, W.B., 2011. Plate tectonics began in Neoproterozoic time, and plumes from deep mantle have never operated. Lithos 123, 1–20.

Harley, S.L., 1989. The origin of granulites: A metamorphic perspective: Geological Magazine 126, 215–247.

Heilimo, E., Halla, J., Hölttä, P., 2010. Discrimination and origin of the sanukitoid series: Geochemical constraints from the Neoarchean western Karelian Province (Finland). Lithos 115, 27–39.

Hirata, W.K., Rigon, J.C., Kadekaru, K., Cordeiro, A.A.C., Meireles, E.A., 1982. Geologia Regional da Província Mineral de Carajás. In: 1st Simpósio de Geologia da Amazônia, Belém (in Portuguese).

Holdsworth, R.E., Pinheiro, R.V.L., 2000. The anatomy of shallow-crustal transpressional structures: insights from the Archaean Carajás fault zone, Amazon, Brazil. Journal of Structural Geology 22, 1105–1123.

Holland, T.H., 1900. The charnockite series, a group of Archean hypersthenic rocks in peninsular India. Memoirs of the Geological Survey of India 28, 119–249.

Irvine, T.N., Baragar, W.R.A., 1971. A guide to the chemical classification of the common volcanic rocks. Canadian of Journal Earth Sciences 8, 523–547.

Jackson, S.E., Pearson, N.J., Griffin, W.L., Belousova, E.A., 2004. The application of laser ablation-inductively coupled plasma-mass spectrometry to in situ U-Pb zircon geochronology. Chemical Geology 211, 47–69.

Janardhan, A.S., Newton, R.C., Hansen, E.C., 1982. The transformation of amphibolite facies gneiss to charnockite in Southern Karnataka and Northern Tamil Nadu, India. Contributions to Mineralogy and Petrology 79, 130–149.

Janoušek, V., Farrow, C.M., Erban, V., 2003. GCDkit: new PC software for interpretation of whole-rock geochemical data from igneous rocks. Geochimica et Cosmochimica Acta 67, 186.

Köber, B., 1986. Whole-grain evaporation for 207Pb/206Pb-age-investigations on single zircons using a double-filament thermal ion source. Contributions to Mineralogy and Petrology 93, 482–490.

Köber, B., 1987. Single-zircon evaporation combined with Pb+-emitter bedding for 207Pb/206Pb-age investigations using thermal ion mass spectroscopy, and implications to zirconology. Contributions to Mineralogy and Petrology 96, 63–71.

Kolb, J., Kokfelt, T.F., Dziggel, A., 2012. Geodynamic setting and deformation history of an Archaean terrane at mid-crustal level: The Tasiusarsuaq terrane of southern West Greenland. Precambrian Research 212–213, 34–56.

Krystopowicz, N.J, Currie, C.A., 2013. Crustal eclogitization and lithosphere delamination in orogens. Earth and Planetary Science Letters 361, 195–207.

Laurent, O., Rapopo, M., Stevens, G., Moyen, J.F., Martin, H., Doucelance, R., Bosq, C., 2014. Contrasting petrogenesis of Mg-K and Fe-K granitoids and implications for post-collisional magmatism: case study from the Late-Archean Matok pluton (Pietersburg block, South Africa). Lithos 196–197, 131–149.

Le Maître, R.W., Streckeisen, A., Zanettin, B., Le Bas, M.J., Bonin, B., Bateman, P., Bellieni, G., Dudek, A., Efremova, J., Keller, J., Lameyre, J., Sabine, P.A., Schmidt, R., Sørensen, H., Woolley, A.R., 2002. Igneous rocks. A classification and glossary of terms. Recommendations of the International Union of Geological Sciences Subcommission on the Systematics of Igneous Rocks. Cambridge University Press, Cambridge, 252 pp.

Leite, A.A.S., Dall'Agnol, R., Macambira, M.J.B., Althoff, F.J., 2004. Geologia e geocronologia dos granitóides arqueanos da região de Xinguara (PA) e suas implicações na evolução do terreno granito–greenstone de Rio Maria. Revista Brasileira de Geociências 34, 447–458 (in Portuguese).

Lindsley, D.H., Frost, B.R., 1992. Equilibria among Fe-Ti oxides, pyroxenes, olivine, and quartz: Part I. Theory. American Mineralogist 77, 987–1003.

Ludwig, K.R., 2008. User's Manual for Isoplot 3.6: a Geochronological Toolkit for Microsoft Excel. Berkeley Geochronology Center Special Publication, Berkeley.

Machado, N., Lindenmayer, Z.G., Krogh, T.E., Lindenmayer, D., 1991. U–Pb geochronology of Archean magmatism and basement reactivation in the Carajás area, Amazon shield, Brazil. Precambrian Research 49, 329–354.

Martin, H., 1987. Petrogenesis of Archaean trondhjemites, tonalites and granodiorites from eastern Finland: major and trace element geochemistry. Journal of Petrology 28, 921–953.

Martin, H., 1994. The Archean grey gneisses and the gneisses of continental crust, in: Condie, K.C. (Ed.), Developments in Precambrian Geology. Archean Crustal Evolution, vol. 11, Elsevier, Amsterdam, pp. 205–259.

Martin, H., 1999. Adakitic magmas: modern analogues of Archaean granitoids. Lithos 46, 411–429.

Martin, H., Moyen, J.-F., Guitreau, M., Blichert-Toft, J., Le Pennec, J.-L., 2014. Why Archaean TTG cannot be generated by MORB melting in subduction zones 198–199, 1–13.

Martin, H., Smithies, R.H., Rapp, R., Moyen, J.-F., Champion, D., 2005. An overview of adakite, tonalite–trondhjemite–granodiorite (TTG) and sanukitoid: relationships and some implications for crustal evolution. Lithos 79, 1–24.

McDonough, W.F., Sun, S.S., 1995. The composition of the Earth. Chemical Geology 120(3–4), 223–253.

Melo, G.H.C., Monteiro, L.V.S., Xavier, R.P., Santiago, E.B.S., 2014. Geocronologia U–Pb e uma nova perspectiva sobre a evolução do depósito IOCG de classe mundial Salobo, Província Carajás, Brasil. Anais do 47º Congresso Brasileiro de Geologia. SBG, Salvador, CD-rom (in Portuguese).

Moreto, C.P.N., Monteiro, L.V.S., Xavier, R.P., Amaral, W.S., Santos, T.J.S., Juliani, C., Souza Filho, C.R., 2011. Mesoarchean (3.0 and 2.86 Ga) host rocks of the iron oxide–Cu–Au Bacaba deposit, Carajás Mineral Province: U–Pb geochronology and metallogenetic implications. Mineralium Deposita 46, 789–811.

Moser, D.E., Corfu, F., Darling, J.R., Reddy, S.M., Tait, K., 2017. Microstructural Geochronology: Planetary Records Down to Atom Scale, American Geophysical Union, Washington.

Moyen, J.F., 2009. High Sr/Y and La/Y ratios: the meaning of the "adakitic signature". Lithos 112, 556–574.

Moyen, J.F., Stevens, G., Kirsters, A., 2006. Record of mid-Archean subduction from metamorphism in the Barberton terrain, South Africa. Nature 422, 559–562, doi:10.1038/nature04972.

Newton, R.C., 1992. An overview of charnockites. Precambrian Research 55, 299–405.

Noce, C.M., Macambira, M.J.B., Soares, A.C.P., 2000. Chronology of Neoproterozoic-Cambrian granite magmatism in the Araçuai Belt, eastern Brazil, based on single zircon evaporation dating. Revista Brasileira de Geociências 30, 25–29.

Nogueira, A.C.R., Truckenbrodt, W., Pinheiro, R.V.L., 1995. Formação Águas Claras, Pré-Cambriano da Serra dos Carajás: redescrição e redefinição litoestratigráfica. Boletim do Museu Paraense Emílio Goeldi 7, 177–277 (in Portuguese).

Nutman, A.P., Friend, C.R.L., 2007. Adjacent terranes with ca. 2715 and 2650 Ma high-pressure metamorphic assemblages in the Nuuk region of the North Atlantic Craton, southern West Greenland: Complexities of Neoarchean collisional orogeny. Precambrian Research 155, 159–203.

O'Connor, J.T., 1965. A classification for quartz-rich igneous rocks based on feldspar rations. US Geological Survey Professional Papers 525, 79–84.

Oliveira, M.A., Dall'Agnol, R., Althoff, F.J., Leite, A.A.S., 2009. Mesoarchean sanukitoid rocks of the Rio Maria Granite-Greenstone Terrane, Amazonian Craton, Brazil. Journal of South American Earth Sciences 27, 146–160.

Oliveira, V.E.S., Oliveira, D.C., Marangoanha, B., Lamarão, C.N., 2018. Geology, mineralogy and petrological affinities of the Neoarchean granitoids from the central portion of the Canaã dos Carajás domain, Amazonian craton, Brazil. Journal of South American Earth Sciences 85, 135–159.

Passchier, C.W., Trouw, R.A.J., 2005. Microtectonics, second ed. Springer-Verlag, Berlin–Heidelberg–New York.

Patchett, P.J., Tatsumoto, M., 1980. A routine high-precision method for Lu-Hf isotope geochemistry and chronology. Contributions to Mineralogy and Petrology 75, 263–267.

Peccerillo, A., Taylor, S.R., 1976. Geochemistry of Eocene calc-alkaline volcanic rocks from the Kastamonu area, Northern Turkey. Contribution to Mineralogy and Petrology 58, 63–81.

Pichamuthu, C.S., 1969. Nomenclature of charnockites. Indian Mineralogist 10, 23–55.

Pidgeon, R., Macambira, M.J.B., Lafon, J.M., 2000. Th–U–Pb isotopic systems and internal structures of complex zircons from an enderbite from the Pium Complex, Carajás Province, Brazil: evidence for the ages of granulite facies metamorphism and the source of the enderbite. Chemical Geology 166, 159–171.

Rapp, R.P., Shimizu, N., Norman, M.D., 2003. Growth of early continental crust by partial melting of eclogite. Nature 425, 605–609

Ricci, P.S.F., Carvalho, M.A., 2006. Rocks of the Pium-Area, Carajás Block, Brazil – A deep seated high-T gabbroic pluton (charnockitoid-like) with xenoliths of enderbitic gneisses dated at 3002 Ma – the basement problem revisited, in: Anais do 8º Simpósio de Geologia da Amazônia. SBG, Manaus, CD-rom (in Portuguese).

Rietmeijer, F.J.M., 1983. Chemical distinction between igneous and metamorphic orthopyroxenes especially those coexisting with Ca-rich clinopyroxenes: a re-evaluation. Mineralogical Magazine 47, 143–151.

Rodrigues, D.S., Oliveira, D.C., Macambira, M.J.B., 2014. Geologia, geoquímica e geocronologia do Granito Mesoarqueano Boa Sorte, município de Água Azul do Norte, Pará – Província Carajás. Boletim do Museu Paraense Emílio Goeldi. Série Ciências da Terra 9(3), 597–633 (in Portuguese).

Rollinson, H., 1993. Using Geochemical Data. Longman, London.

Santos, M.M., Lana, C., Scholz, R., Buick, I., Schmitz, M.D., Kamo, S.L., Gerdes, A., Corfu, F., Tapster, S., Lancaster, P., Storey, C.D., Basei, M.A.S., Tohver, E., Alkmim, A., Nalini, H., Krambrock, K., Fantini, C., Wiedenbeck, M., 2017. A new appraisal of Sri

Lankan BB zircon as a reference material for LA-ICP-MS U-Pb geochronology and Lu-Hf isotope tracing. Geostandards & Geoanalytical Research doi: 10.1111/ggr.12167.

Santos, R.D., Galarza, M.A., Oliveira, D.C., 2013. Geologia, geoquímica e geocronologia do Diopsídio-Norito Pium, Província Carajás. Boletim do Museu Paraense Emílio Goeldi, Série Ciências da Terra 8, 355–382 (in Portuguese).

Sato, K., Basei, M.A.S., Siga Jr., O., Sproesser, W.M., Passarelli, C.R., 2008. Novas técnicas aplicadas ao método U-Pb no CPGeo – IGc/USP: avanços na digestão química, espectrometria de massa (TIMS) e exemplos de aplicação integrada com SHRIMP. Geologia USP: Série Científica 7, 77–99.

Sato, K., Tassinari, C.C.G.T., Basei, M.A.S., Siga Júnior, O., Onoe, A.T., Souza, M.D., 2014. Sensitive high resolution, ion microprobe (SHRIMP IIe/MC) of the Institute of Geoscience of University of São Paulo, Brazil: analytical method and frst results. Geologia USP: Série Científica 14(3), 3–18.

Scherer, E.E., Münker, C., Mezger, K., 2001. Calibration of the lutetium-hafnium clock. Science 293, 683–687.

Shand, S.J., 1950. Eruptive rocks their genesis, composition, classification and their relation to ore deposit, fourth ed. Murby, London, 488 pp.

Shao, J.A., Wei, C.J., 2011. Petrology and tectonic significance of the early Mesozoic granulite xenoliths from the eastern Inner Mongolia, China. Science China Earth Sciences 54, 1484–1491.

Sláma, J., Košler, J., Condon, D.J., Crowley, J.L., Gerdes, A., Hanchar, J.M.,Horstwood, M.S.A., Morris, G.A., Nasdala, L., Norberg, N., Schaltegger, U.,Schoene, B., Tubrett, M.N., Whitehouse, M.J., 2008. Plešovice zircon d a new natural reference material for U-Pb and Hf isotopic microanalysis. Chemical Geology 249, 1–35.

Smithies, R.H., Champion, D.C., Van Kranendonk, M.J., 2009. Formation of Paleoarchean continental crust through infracrustal melting of enriched basalt. Earth and Planetary Science Letters 281, 298–306.

Souza, Z.S., Potrel, H., Lafon, J.M., Althoff, F.J., Pimentel, M.M., Dall'Agnol, R., Oliveira, C.G., 2001. Nd, Pb and Sr isotopes of the Identidade Belt, an Archaean greenstone belt of the Rio Maria region (Carajás Province, Brazil): implications for the Archaean geodynamic evolution of the Amazonian Craton. Precambrian Research 109, 293–315.

Stacey, J.S., Kramers, J.D., 1975. Approximation of terrestrial lead isotope evolution by a two-stage model. Earth and Planetary Science Letters 26, 207–221.

Stern, R.A., 1998. High resolution SIMS determination of radiogenic trace isotope ratios in minerals, in: Cabri, L.J., Vaughan, D.J. (Eds.), Modern approaches to ore and environmental mineralogy, Ottawa, v. 27, pp. 241–268.

Streckeisen, A., 1974. Classification and nomenclature of plutonic rocks: Recommendations of the IUGS subcommission on the systematics of igneous rocks. Geologische Rundschau, 63, 773–786.

Tavares, F.M., 2015. Evolução geotectônica do nordeste da Província Carajás. Tese de Doutorado – Universidade Federal do Rio de Janeiro, Rio de Janeiro, 115 pp. (in Portuguese).

Taylor, S.R., McLennan, S.M., 1985. The Continental Crust: Its Composition and Evolution. Blackwell, Oxford.

Teixeira, L.R., 2005. GENESIS 4.0 – Software de Modelamento Geoquímico.

Teixeira, M.F.B., Dall'Agnol, R., Santos, J.O.S., Sousa, L.A.M., Lafon, J. M., 2017. Geochemistry, geochronology and Nd isotopes of the Gogó da Onça Granite: A new Paleoproterozoic A-type granite of Carajás Province, Brazil. Journal of South American Earth Sciences 80 (2017) 47–65.

Thybo, H., Artemieva, I.M., 2013. Moho and magmatic underplating in continental lithosphere. Tectonophysics 609, 605–619.

Vasquez, L.V., Rosa-Costa, L.R., Silva, C.G., Ricci, P.F., Barbosa, J.O., Klein, E.L., Lopes, E.S., Macambira, E.B., Chaves, C.L., Carvalho, J.M., Oliveira, J.G., Anjos, G.C., Silva, H.R., 2008. Escala 1:1.000.000, in: Vasquez, M.L., Rosa-Costa, L.T. (Eds.), Geologia e Recursos Minerais do Estado do Pará: Sistema de Informações Geográficas e SIG: texto explicativo dos mapas Geológico e Tectônico e de Recursos Minerais do Estado do Pará. CPRM, Belém, 328 pp. (in Portuguese).

Weaver, B.L., Tarney, J., Windley, B. F., Leake, B.E., 1982. Geochemistry and petrogenesis of Archaean metavolcanic amphibolites from Fiskenæsset, S. W. Greenland. Geochimica et Cosmochimica Acta 46, 2203–2215.

Wedepohl, K.H., 1995. The compositions of the continental crust. Geochimica et Cosmochimica Acta 59, 1217–1232.

Williams, I.S., 1998. U-Th-Pb Geochronology by Ion Microprobe, in: McKibben, M.A., Shanks III, W.C., Ridley, W.I. (Eds.), Applications of Microanalytical Techniques to Understanding Mineralizing Processes. Society of Economic Geologists, v. 7, pp. 1–35.

Wilson, M., 1989. Igneous Petrogenesis – A Global Tectonic Approach, Springer, Dordrecht.

Windley, B.F., Bridgwater, D., 1971. The evolution of Archaean low- and high-grade terrains. Geological Society of Australia: Special Publications 3, 33–46.

Winther, K.T., 1996. An experimentally based model for the origin of tonalitic and trondhjemitic melts. Chemical Geology 127, 43–59.

Wyers, G.P., Barton, M., 1986. Petrology and evolution of transitional alkaline-subalkaline lavas from Patmos, Dodecanesos, Greece: evidence for fractional crystallization, magma mixing, and assimilation. Contributions to Mineralogy and Petrology 93, 297–311.

5 CONCLUSÕES E CONSIDERAÇÕES FINAIS

- A região de Ouro Verde, porção central do Domínio Canaã dos Carajás (Província Carajás), representa um segmento da crosta de evolução complexa, formada por eventos tectono-magmático-metamórfico durante o Meso- e Neoarqueano.
- Entre 3,05 e 2,93 Ga, houve a formação de crosta TTG a partir de fusão parcial de basaltos enriquecidos (platôs oceânicos) previamente transformada em granada anfibolito, em ambiente de subducção.
- Entre 2,89 a 2,84 Ga, com a evolução tectônica para regime colisional, houve a geração de granitos anatéticos e espessamento crustal, provocando metamorfismo regional da crosta TTG sob fácies granulito de ultra-alta temperatura e que seria responsável pela formação dos ortogranulitos félsicos da área de Ouro Verde.
- No Neoarqueano, entre 2,75 a 2,73 Ga, essa porção da crosta sofreu processo de delaminação, provocado pelo "descolamento" da base da crosta (altamente densa e refratária), que induziu *underplating* máfico. Esse processo promoveu a fusão parcial da crosta granulítica máfica mesoarqueana, que gerou líquidos de natureza sódica em níveis crustais profundos, condicionando a cristalização/estabilização de ortopiroxênio, formando, dessa forma, os enderbitos.
- Esta anomalia térmica também foi responsável pela fusão parcial do manto, gerando líquidos máficos que formam o Diopsídio-Norito Pium. A colocação desse líquido máfico no embasamento mesoarqueano, de composição granulítica félsica, induziu sua fusão, gerando líquidos leucogranítico. Ambos os líquidos – de origem mantélica e crustal – sofreram processos de mistura e *mingling*, dando origem às rochas híbridas de Vila União.
- Os magmas neoarqueanos tiveram sua ascensão e colocação facilitadas por estruturas E–W pré-existentes, de idade mesoarqueana (Cinturão de Cisalhamento Itacaiúnas), que serviram de condutos. A geração e a consolidação desses magmas neoarqueanos ocorreu sob regime tectônico transpressional dominado por cisalhamento puro, atribuindo uma natureza sin-tectônica a essas rochas. Esse regime tectônico foi o responsável pela exumação da crosta granulítica mesoarqueana da área de Ouro Verde através de sistemas imbricados.
- Dados isotópicos de Hf em zircão atribuem fonte juvenil ao protólitos dos granulitos félsicos mesoarqueanos, enquanto que os enderbitos e o membro leucogranítico formador dos granitoides de Vila União apontam para participação de uma fonte com maior tempo

de residência crustal. Dados isotópicos de Sm-Nd sugerem fonte juvenil para as rochas do Diopsídio-Norito Pium.

REFERÊNCIAS

Almeida F.F.M., Hasui Y., Brito Neves B.B., Fuck R.A. 1981. Brazilian Structural Provinces: an introduction. *Earth-Science Reviews*, **17**: 1–29.

Almeida J.A.C., Dall'Agnol R., Leite A.A.S. 2013. Geochemistry and zircon geochronology of the Archean granite suites of the Rio Maria granite-greenstone terrane, Carajás Province. *Brazil Journal of South American Earth Sciences*, **42**: 103–126.

Almeida J.A.C., Dall'Agnol R., Oliveira M.A., Macambira M.J.B., Pimentel M.M., Rämö O.T., Guimarães F.V., Leite A.A.S. 2011. Zircon geochronology and geochemistry of the TTG suites of the Rio Maria granite-greenstone terrane: implications for the growth of the Archean crust of Carajás Province, Brazil. *Precambrian Research*, **187**: 201–221.

Althoff F.J., Barbey P., Boullier A.M. 2000. 2.8–3.0 Ga plutonism and deformation in the SE Amazonian craton: the Archean granitoids of Marajoara (Carajás Mineral Province, Brazil). *Precambrian Research*, **104**: 187–206.

Andersen T., Andersson U.B., Graham S., Aberg G., Simonsen S.L. 2009. Granitic magmatism by melting of juvenile continental crust: new constraints on the source of Paleoproterozoic granitoids in Fennoscandia from Hf isotopes in zircon. *Journal of the Geological Society*, **166**: 233–247.

Araújo O.J.B. & Maia R.G.N. 1991. *Serra dos Carajás, Folha SB-22-Z-A*. Rio de Janeiro, CPRM. Relatório Final. 136 p.

Avelar V.G. 1996. *Geocronologia Pb-Pb por evaporação em monocristal de zircão do magmatismo da região de Tucumã, SE do estado do Pará, Amazônia Oriental*. MS Dissertation, Programa de Pós-Graduação em Geologia e Geoquímica, Instituto de Geociências, Universidade Federal do Pará, Belém, 149 p.

Avelar V.G. 2002. *Geocronologia Pb-Pb em zircão e Sm-Nd em rocha total da porção centro-norte do estado do Amapá – Brasil: implicações para a evolução geodinâmica do setor oriental dos Escudo das Guianas*. PhD Thesis, Programa de Pós-Graduação em Geologia e Geoquímica, Instituto de Geociências, Universidade Federal do Pará, Belém, 213 p.

Avelar V.G., Lafon J.M., Correia Jr. F.C., Macambira E.M.B. 1999. O magmatismo arqueano da região de Tucumã – Província Mineral de Carajás: novos resultados geocronológicos. *Revista Brasileira de Geociências*, **29**(4): 453–460.

Barbosa J.P.O. 2004. *Geologia estrutural, geoquímica, petrografia e geocronologia de granitoides da região do Igarapé Gelado, norte da Província Mineral de Carajás*. MS Dissertation, Programa de Pós-Graduação em Geologia e Geoquímica, Instituto de Geociências, Universidade Federal do Pará, Belém, 96 p.

Barros C.E.M., Barbey P., Boullier A.M. 2001. Role of magma pressure, tectonic stress and crystallization progress in the emplacement of the syntectonic A-type Estrela Granite Complex (Carajás Mineral Province, Brazil). *Tectonophysics*, **343**: 93–109.

Barros C.E.M., Sardinha A.S., Barbosa J.P.O., Macambira M.J.B. 2009. Structure, petrology, geochemistry and zircon U-Pb and Pb-Pb geochronology of the synkinematic Archean (2.7 Ga) A-type granites from the Carajás Metallogenic Province, northern Brazil. *Canadian Mineralogist*, **47**: 1423–1440.

Black L.P., Kamo S.L., Williams I.S., Mundil R., Davis D.W., Korsch R.J., Foudoulis C. 2003. The application of SHRIMP to Phanerozoic geochronology: a critical application of four zircon standards. *Chemical Geology*, **200**: 171–188.

Bouvier A., Vervoort J.D., Patchett P.J. 2008. The Lu-Hf and Sm-Nd isotopic composition of CHUR: constraints from unequilibrated chondrites and implications for the bulk composition of terrestrial planets. *Earth and Planetary Science Letters*, **273**: 48–57.

Chayes F. (Ed.). 1956. *Petrographic modal analysis: an elementary statistical appraisal*. New York, John Wiley and Sons, 113 p.

Chu N.C., Taylor R.N., Chavagnac V., Nesbitt R.W., Boella R.M., Milton J.A., German C.R., Bayon G., Burton K. 2002. Hf isotope ratio analysis using multi-collector inductively coupled plasma mass spectrometry: an evaluation of isobaric interference corrections. *Journal of Analytical Atomic Spectrometry*, **17**: 1567–1574.

Cordeiro A. C. & Saueressig R. 1980. Serra das Andorinhas: geologia e principais ocorrências de ouro. *In:* SBG, 31° Congresso brasileiro de geologia, Camboriú. *Resumos*. v. 2, p. 344.

Costa J.B.S, Araújo O.J.B., Jorge João X.S., Maia R., Macambira E.M.B., Vale A.G., Santos A., Pena Filho J.I.C., Neves A.P. 1994. Panorama tectono-estrutural da região sudeste do estado do Pará. *In:* SBG, 4° Simpósio geologia da Amazônia, Belém. *Resumos*. p. 314–317.

Costa J.B.S., Araújo O.J.B., João X.S.J., Macambira M.J.B., Lafon J.M. 1995. A Província Mineral de Carajás: aspectos tectono-estruturais, estratigráficos e geocronológicos. *Boletim do Museu Paraense Emílio* Goeldi. Série Ciências da Terra, **7**: 199–235.

Costi H.T., Dall'Agnol R., Moura C.A.V. 2000. Geology and Pb-Pb geochronology of Paleoproterozoic volcanic and granitic rocks of Pitinga Province, Amazonian craton, northern Brazil. *International Geology Review*, **42**: 832–849.

Cunha I.R.V., Dall'Agnol R., Feio G.R.L. 2016. Mineral chemistry and magnetic petrology of the Archean Planalto Suite, Carajás Province – Amazonian Craton: implications for the evolution of ferroan Archean granites. *Journal of South American Earth Sciences*, **67**: 100–121.

Dall'Agnol R. & Oliveira D.C. 2007. Oxidized, magnetite-series, rapakivi-type granites of Carajás, Brazil: implications for classification and petrogenesis of A-type granites. *Lithos*, **93**: 215–233.

Dall'Agnol R. 1982. Maciço Jamon: Evolução petrológica de um granito da Amazônia Oriental. *In:* SBG, 1° Simpósio de geologia da Amazônia, Belém. *Anais*. v. 2, p. 139–161.

Dall'Agnol R., Cunha I.R.V, Guimarães F.V, Oliveira D.C., Teixeira M.F.B., Feio G.R.L., Lamarão C.N. 2017. Mineralogy, geochemistry, and petrology of Neoarchean ferroan to magnesian granites of Carajás Province, Amazonian Craton: the origin of hydrated granites associated with charnockites. *Lithos*, **277**: 3–32.

Dall'Agnol R., Lafon J.M., Macambira M.J.B. 1994. Proterozoic anorogenic magmatism in the Central Amazonian Province, Amazonian Craton: geochronological, petrological and geochemical aspects. *Mineralogy and Petrology*, **50**: 113–138.

Dall'Agnol R., Oliveira D.C., Guimarães F.V., Gabriel E.O., Feio G.R.L., Lamarão C.N., Althoff F.J., Santos P.A., Teixeira M.F.B., Silva A.C., Rodrigues D.S., Santos M.J.P., Silva C.R.P., Santos R.D., Santos P.J.L. 2013. Geologia do Subdomínio de Transição do Domínio Carajás – implicações para a evolução arqueana da Província Carajás – Pará. *In:* SBG, 13º Simpósio de geologia da Amazônia, Belém. *Anais*. 1 CD-ROM.

Dall'Agnol R., Oliveira M.A., Almeida J.A.C., Althoff F.J., Leite A.A.S., Oliveira D.C., Barros C.E.M. 2006. Archean and Paleoproterozoic granitoids of the Carajás metallogenetic province, eastern Amazonian craton. *In:* Dall'Agnol R., Rosa-Costa L.T., Klein E.L. (Ed.), Symposium on magmatism: crustal evolution, and metallogenesis of the Amazonian Craton. Volume and field trips guide, Belém. PRONEX-UFPA/SBG-NO. *Abstracts*. p. 99–150.

Dall'Agnol R., Teixeira N.P., Rämö O.T., Moura C.A.V., Macambira M.J. B., Oliveira D.C. 2005. Petrogenesis of the Paleoproterozoic, rapakivi, A-type grantites of the Archean Carajás Metallogenic Province, Brazil. *Lithos*, **80**: 101–129.

Deer W.A., Howie R.A., Zussman J. (Ed.). 1992. *Rock-forming minerals.* 2nd ed. London, Longmans, 696 p.

Delinardo M.A.S., Monteiro L.V.S., Moreto C.P.N., Sousa S.D., Melo G.H.C. 2014. Complexo Xingu: Uma secção da crosta inferior exumada durante a evolução do Domínio Carajás, PA. *In:* SBG, 47º Congresso brasileiro de geologia, Salvador. *Anais*. 1 CD-ROM.

Delinardo M.A.S., Monteiro L.V.S., Santos T.J.S., Moreto C.P.N., Sousa S.D. 2015. Partial melting and magma generation in the Mesoarchean (ca. 3.0 Ga) TTG gneisses of the Xingu Complex, Carajás Province, Amazon Craton. *In:* 8th Hutton symposium on granites and related rocks, Florianópolis. *Abstracts*. 1 CD-ROM.

DePaolo D.J. & Wasserburg G.J. 1976. Nd isotope variations and petrogenetic models. *Geophysical Research Letters*, **3**: 249–252.

DePaolo D.J. 1981. Neodymium isotope in the Colorado Front Range and crust–mantle evolution in the Proterozoic. *Nature*, **291**: 193–196.

Dias S.B. 2009. *Caracterização geológica, petrográfica e geoquímica de granitos arqueanos da Folha Marajoara, terreno granito–greenstone de Rio Maria, sudeste do Pará*. MS Dissertation, Programa de Pós-Graduação em Geologia e Geoquímica, Instituto de Geociências, Universidade Federal do Pará, Belém, 129 p.

Domingos F.H.G. 2009. *The structural setting of the Canaã dos Carajás region and Sossego-Sequeirinho deposits, Carajás – Brazil*. PhD Thesis. University of Durham, Durham, 504 p.

Feio G.R.L. & Dall'Agnol R. 2012. Geochemistry and petrogenesis of the Mesoarchean granites from the Canaã dos Carajás area, Carajás Province, Brazil: implications for the origin of Archean granites. *Lithos*, **154**: 33–52.

Feio G.R.L., Dall'Agnol R., Dantas E.L., Macambira M.J.B., Gomes A.C.B., Sardinha A.S., Oliveira D.C, Santos R.D., Santos P.A. 2012. Geochemistry, geochronology and origin of the Neoarchean Planalto Granite Suite, Carajás, Amazonian craton: A-type or hydrated charnockitic granites? *Lithos*, **151**: 57–73.

Feio G.R.L., Dall'Agnol R., Dantas E.L., Macambira M.J.B., Santos J.O.S., Althoff F.J., Soares J.E.B. 2013. Archean granitoid magmatism in the Canaã dos Carajás area: implications for crustal evolution of the Carajás province, Amazonian craton, Brazil. *Precambrian Research*, **227**: 157–185.

Frei D. & Gerdes A. 2009. Accurate and precise in-situ zircon U-Pb age dating with high spatial resolution and high sample throughput by automated LA-SF-ICP-MS. *Chemical Geology*, **261**(3–4): 261–270.

Gabriel E.O. & Oliveira D.C. 2014. Geologia, petrografia e geoquímica dos granitoides arqueanos de alto magnésio da região de Água Azul do Norte, porção sul do Domínio Carajás, Pará. *Boletim do Museu Paraense Emílio Goeldi*. Ciências Naturais, **9**(3): 533–564.

Gabriel E.O., Oliveira D.C., Galarza M.A. 2010. Geologia, petrografia e geocronologia de granitoides do Complexo Xingu da região nordeste de Água Azul do Norte – PA, Província Mineral de Carajás. *In:* SBG, 45º Congresso brasileiro de geologia, Belém. *Anais*. 1 CD-ROM.

Galarza M.A., Oliveira D.C., Rodrigues E.A., Santos A.N., Martins A.C., Marangoanha B. 2017. Neoarchean granitoids (2.73–2.74 Ga) intrusive and associated with the Pium Diopside-Norite, Canaã dos Carajás, Carajás Province (PA). *Contribuições à geologia da Amazônia*, **10**: 225–246.

Gaudette H.E., Lafon J.M., Macambira M.J.B., Moura C.A.V., Scheller T. 1998. Comparison of single filament Pb evaporation/ionization zircon ages with conventional U-Pb results: examples from the Precambrian of Brazil. *Journal South American Earth Science*, **11**: 351–363.

Gerdes A. & Zeh A. 2006. Combined U-Pb and Hf isotope LA-MC-ICP-MS analyses of detrital zircons: comparison with SHRIMP and new constraints for the provenance and age of an Armorican metasediment in Central Germany. *Earth and Planetary Science Letters*, **249**: 47–62.

Gerdes A. & Zeh A. 2009. Zircon formation versus zircon alteration – new insights from combined U-Pb and Lu-Hf in-situ LA-ICP-MS analyses, and consequences for the interpretation of Archean zircon from the Central Zone of the Limpopo Belt. *Chemical Geology*, **261**: 230–243.

Gomes A.C.B. 2003. *Geologia, petrografia e geoquímica dos granitoides de Canaã dos Carajás, SE do estado do Pará*. MS Dissertation, Programa de Pós-Graduação em Geologia e Geoquímica, Instituto de Geociências, Universidade Federal do Pará, Belém, 160 p.

Griffin W.L., Wang X., Jackson S.E., Pearson N.J., O'Reilly S.Y. 2002. Zircon geochemistry and magma mixing, SE China: in-situ analysis of Hf isotopes, Tonglu and Pingtan igneous complexes. *Lithos*, **61**: 237–269.

Guimarães F.V. 2009. *Geologia, petrografia e geoquímica do Trondhjemito Mogno e rochas arqueanas associadas, terreno granito-greenstone de Rio Maria – SE do Pará*. MS Dissertation, Programa de Pós-Graduação em Geologia e Geoquímica, Instituto de Geociências, Universidade Federal do Pará, Belém, 102 p.

Hamilton P.J., O'Nions R.K., Evensen N.M. 1977. Sm-Nd dating of Archean basic and ultrabasic volcanics. *Earth and Planetary Science Letters*, **36**: 263–268.

Hibbard M.J. (Ed.). 1995. *Petrography to Petrogenesis*. New Jersey, Prentice-Hall Incorporation, 587 p.

Hühn S.B., Macambira M.J.B., Dall'Agnol R. 1999. Geologia e Geocronologia Pb-Pb do granito alcalino arqueano Planalto, Região da Serra do Rabo, Carajás – PA. *In:* SBG, 6º Simpósio de geologia da Amazônia, Manaus. *Anais*. v. 1, p. 463–466.

Hutchison C.S. (Ed.). 1974. *Laboratory handbook of petrography techniques*. London, John Wiley and Sons, 527 p.

Ianhez A.C., Souza A.M.S., Montalvão R.M.G. 1980. Geologia da sequência vulcano-sedimentar da Serra do Inajá – Santana do Araguaia. *In:* SBG, 31º Congresso brasileiro de geologia, Camboriú. *Anais*. v. 5, p. 2918–2928.

Jackson S.E., Pearson N.J., Griffin W.L., Belousova E.A. 2004. The application of laser ablation-inductively coupled plasma-mass spectrometry to in situ U-Pb zircon geochronology. *Chemical Geology*, **211**: 47–69.

Janoušek V., Farrow C.M., Erban V. 2003. GCDkit: new PC software for interpretation of whole-rock geochemical data from igneous rocks. *Geochimica et Cosmochimica Acta*, **67**: 186.

Jorge João X.S. & Araújo J.B. 1992. Magmatismo granítico sin-cisalhamento Itacaiúnas no SW do estado do Pará. *In:* SBG, 37º Congresso brasileiro de geologia, São Paulo. *Resumos Expandidos*. v. 2, p. 36–38.

Jorge João X.S., Neves A.P., Leal J.W.L. 1982. Ouro da Serra Pelada: aspectos da geologia e garimpagem. *In:* SBG, 1º Simpósio de geologia da Amazônia, Belém. *Anais*. v. 2, p. 52–62.

Kerr P. (Ed.). 1959. *Optical mineralogy*. 3rd ed. New York, McGraw-Hill Book Co., 492 p.

Köber B. 1986. Whole-grain evaporation for $^{207}Pb/^{206}Pb$-age-investigations on single zircons using a double-filament thermal ion source. *Contributions to Mineralogy and Petrology*, **93**: 482–490.

Köber B. 1987. Single-zircon evaporation combined with Pb^{+}-emitter bedding for $^{207}Pb/^{206}Pb$-age investigations using thermal ion mass spectroscopy, and implications to zirconology. *Contributions to Mineralogy and Petrology*, **96**: 63–71.

Lafon J.M., Macambira M.J.B., Pidgeon R.T. 2000. Zircon U-Pb SHRIMP dating of Neoarchean magmatism in the southwestern part of the Carajás Province (eastern Amazonian Craton, Brazil). *In:* 31st International geological congress, Rio de Janeiro, *Abstracts*. 1 CD-ROM.

Lafon J.M., Rodrigues E., Duarte K.D. 1994. Le granite Mata Surrão: um magmatisme monzogranitique contemporain des associations tonalitiquestrondhjemitiques-granodioritiques archéennes de la région de Rio Maria (Amazonie Orientale, Brésil). *Comptes Rendues de la Academie de Sciences de Paris*, **318**(2): 642–649.

Le Maître R.W., Streckeisen A., Zanettin B., Le Bas M.J., Bonin B., Bateman P., Bellieni G., Dudek A., Efremova J., Keller J., Lameyre J., Sabine P.A., Schmidt R., Sørensen H., Woolley A.R. (Ed.). 2002. *Igneous rocks. A classification and glossary of terms. Recommendations of the International Union of Geological Sciences Subcommission on the Systematics of Igneous Rocks*. Cambridge, Cambridge University Press, 252 p.

Leite A.A.S. 2001. *Geoquímica, petrogênese e evolução estrutural dos granitoides arqueanos da região de Xinguara, SE do Cráton Amazônico*. PhD Thesis, Programa de Pós-Graduação em Geologia e Geoquímica, Instituto de Geociências, Universidade Federal do Pará, Belém, 330 p.

Leite, A.A.S., Dall'Agnol R., Macambira M.J.B., Althoff F.J. 2004. Geologia e geocronologia dos granitoides arqueanos da região de Xinguara (PA) e suas implicações na evolução do Terreno Granito-Greenstone de Rio Maria. *Revista Brasileira de Geociências*, **34**: 447–458.

Leite-Santos P.J. & Oliveira D.C. 2014. Trondhjemitos da área de Nova Canadá: novas ocorrências de associações magmáticas tipo TTG no Domínio Carajás. *Boletim do Museu Paraense Emílio Goeldi*. Ciências Naturais, **9**(3): 635–659.

Leite-Santos P.J.S. & Oliveira D.C. 2016. Geologia, petrografia e geoquímica das associações leucogranítica arqueanas da área de Nova Canadá: Província Carajás. *Geologia USP*. Série Científica, **16**(2): 37–66.

Ludwig K.R. 2008. *User's manual for Isoplot 3.6: a geochronological toolkit for Microsoft Excel*. Berkeley, Berkeley Geochronology Center (Special Publication).

Lugmair G.W. 1974. Sm-Nd ages: a new dating method. *Meteoritics*, **9**: 369.

Lugmair G.W., Scheinin N.B., Marti K. 1975. Sm-Nd age and history of Apollo 17 basalt 75075: evidence of early differentiation of the lunar exterior. Proc. Lunar Sci. Conf. 6th vol. 2. *Geochimica et Cosmochimica Acta Suppl*. **6**: 1419–1429.

Macambira E.M.B. & Vale A.G. 1997. *Programa Levantamentos Geológicos Básicos do Brasil. São Félix do Xingu. Folha SB.22-Y-B, Estado do Pará*. Brasília, DNPM/CPRM, 384 p.

Macambira M.J.B. & Lafon J.M. 1995. Geocronologia da síntese dos dados e novos desafios. *Boletim do Museu Paraense Emílio Goeldi*. Série Ciências da Terra, **7**: 263-288.

Macambira M.J.B. & Lancelot J. 1991. Em busca do embasamento arqueano da região de Rio Maria, sudeste do estado do Pará. *In:* SBG, 3º Simpósio de geologia da Amazônia, Belém. *Resumos Expandidos*. p. 49–58.

Macambira M.J.B., Barros C.E.M., Silva D.C.C., Santos M.C.C. 2001. Novos dados geológicos e geocronológicos para a região ao norte da Província de Carajás, evidências para o estabelecimento do limite Arqueano-Paleoproterozóico no sudeste do Cráton Amazônico. *In:* SBG, 7º Simpósio de geologia da Amazônia, Belém. *Resumos Expandidos*. 1 CD-ROM.

Machado N., Lindenmayer Z.G., Krogh T.E., Lindenmayer D. 1991. U-Pb geochronology of Archean magmatism and basement reactivation in the Carajás area, Amazon shield, Brazil. *Precambrian Research*, **49**: 329–354.

Marangoanha B. & Oliveira D.C. 2014. Diabásios e anfibolitos da área de Nova Canadá: natureza e implicações tectônicas para a Província Carajás. *Boletim do Museu Paraense Emílio Goeldi*. Ciências Naturais, **9**(3): 565–596.

Medeiros Filho C.A. & Meireles E.M. 1985. Dados preliminares sobre a ocorrência de cromita na área de Luanga. *In:* SBG, 2º Simpósio de geologia da Amazônia, Belém. *Atas*. v. 3, p. 1488–1499.

Medeiros H. & Dall'Agnol R. 1988. Petrologia da porção leste do batólito granodiorítico Rio Maria, sudeste do Pará. *In:* SBG, 35º Congresso brasileiro de geologia, Belém. *Anais*. v. 3, 1488–1499.

Meireles E.M., Hirata W.K., Amaral A.F., Medeiros Filho C.A., Gato W.C. 1984. Geologia das folhas Carajás e Rio Verde, Província Mineral dos Carajás, estado do Pará. *In:* SBG, 33º Congresso brasileiro de geologia, Rio de Janeiro. *Anais*. v. 5, p. 2164–2174.

Melo G.H.C., Monteiro L.V.S., Xavier R.P., Santiago E.B.S. 2014. Geocronologia U-Pb e uma nova perspectiva sobre a evolução do depósito IOCG de classe mundial Salobo, Província Carajás, Brasil. *In:* SBG, 47º Congresso brasileiro de geologia, Salvador. *Anais*. 1 CD-ROM.

Moreto C.P.N, Monteiro L.V.S., Xavier R.P., Creaser R.A., DuFrane S.A., Tassinari C.C.G., Sato K., Kemp A.I.S., Amaral W.S. 2015. Neoarchean and Paleoproterozoic Iron Oxide-Copper-Gold events at the Sossego Deposit, Carajás Province, Brazil: Re-Os and U-Pb geochronological evidence. *Economic Geology*, **110**: 809–835.

Moreto C.P.N., Monteiro L.V.S., Xavier R.P., Amaral W.S., Santos T.J.S., Juliani C., Souza Filho C.R. 2011. Mesoarchean (3.0 and 2.86 Ga) host rocks of the iron oxide–Cu–Au Bacaba deposit, Carajás Mineral Province: U-Pb geochronology and metallogenetic implications. *Mineralium Deposita*, **46**: 789–811.

Moura C.A.V. 1992. *Geochronology and geochemistry of the basement orthogneisses of the Araguaia Belt, Brazil*. PhD Thesis, University of New Hampshire, New Hampshire, 236 p.

Noce C.M., Macambira M.J.B., Soares A.C.P. 2000. Chronology of Neoproterozoic-Cambrian granite magmatism in the Araçuai Belt, eastern Brazil, based on single zircon evaporation dating. *Revista Brasileira de Geociências*, **30**: 25–29.

Nogueira A.C.R., Truckenbrodt W., Pinheiro R.V.L. 1995. Formação Águas Claras, Pré-Cambriano da Serra dos Carajás: redescrição e redefinição. *Boletim do Museu Paraense Emílio Goeldi*. Ciências da Terra, **7**: 177–197.

Oliveira D.C., Santos P.J.L., Gabriel E.O., Rodrigues D.S., Faresin A.C., Silva M.L.T., Sousa S.D., Santos R.V., Silva A.C., Souza M.C., Santos R.D., Macambira M.J.B. 2010. Aspectos geológicos e geocronológicos das rochas magmáticas e metamórficas da região entre os municípios de Água Azul do Norte e Canaã dos Carajás – Província Mineral de Carajás. *In:* SBG, 45º Congresso brasileiro de geologia, Belém. *Resumos*. 1 CD-ROM.

Oliveira E.C., Lafon J.M., Gioia S.M.C.L., Pimentel M.M. 2008. Datação Sm-Nd em rocha total e granada do metamorfismo granulítico da região de Tartarugal Grande, Amapá Central. *Revista Brasileira de Geociências*, **38**: 114–127.

Oliveira M.A., Dall'Agnol R., Almeida J.A.C. 2011. Petrology of the Mesoarchean Rio Maria suite and the discrimination of sanukitoid series. *Lithos*, **127**: 192–209.

Oliveira M.A., Dall'Agnol R., Althoff F.J., Leite A.A.S. 2009. Mesoarchean sanukitoid rocks of the Rio Maria Granite-Greenstone Terrane, Amazonian craton, Brazil. *Journal of South American Earth Sciences*, **27**: 146–160.

Oliveira M.A., Dall'Agnol R., Scaillet B. 2010. Petrological constraints on crystallization conditions of Mesoarchean sanukitoid rocks, southeastern Amazonian Craton, Brazil. *Journal of Petrology*, **51**: 2121–2148.

Oliveira V.E.S., Oliveira D.C., Marangoanha B., Lamarão C.N. 2018. Geology, mineralogy and petrological affinities of the Neoarchean granitoids from the central portion of the Canaã dos Carajás domain, Amazonian craton, Brazil. *Journal of South American Earth Sciences*, **85**: 135–159.

Passchier C.W. & Trouw R.A.J. (Ed.). 2005. *Microtectonics*. Second ed. Berlin–Heidelberg–New York, Springer-Verlag, 371 p.

Patchett P.J. & Tatsumoto M. 1980. A routine high-precision method for Lu-Hf isotope geochemistry and chronology. *Contributions to Mineralogy and Petrology*, **75**: 263–267.

Pimentel M.M. & Machado N. 1994. Geocronologia U-Pb do Terrenos Granito-*Greenstone* de Rio Maria, Pará. *In:* SBG, 38º Congresso brasileiro de geologia, Camboriú. *Resumos Expandidos*. p. 390–391.

Pinheiro R.V.L & Holdsworth R.E. 2000. Evolução tectonoestratigráfica dos Sistemas Transcorrentes Carajás e Cinzento, Cinturão Itacaiúnas, na borda leste do Cráton Amazônico, Pará. *Revista Brasileira de Geociências*, **30**(4): 597–606.

Pinheiro R.V.L. 1997. *Reactivation history of the Carajás and Cinzento Strike-Slip System, Amazon, Brazil*. PhD Thesis, University of Durham, Durham, 408 p.

Ricci P.S.F. & Carvalho M.A. 2006. Rocks of the Pium-Area, Carajás Block, Brazil – A deep seated high-T gabbroic pluton (charnockitoid-like) with xenoliths of enderbitic gneisses dated at 3002 Ma – the basement problem revisited, *In:* SBG, 8º Simpósio de geologia da Amazônia, Manaus. *Anais*. 1 CD-ROM.

Rio Doce Geologia e Mineração – Distrito Amazônia (DOCEGEO). 1988. Revisão litoestratigráfica da Província Mineral de Carajás, Pará. *In:* SBG, 35º Congresso brasileiro de geologia, Belém. *Resumos Expandidos*. p. 11–54.

Rodrigues D.S., Oliveira D.C., Macambira M.J.B. 2014. Geologia, geoquímica e geocronologia do Granito Mesoarqueano Boa Sorte, município de Água Azul do Norte, Pará – Província Carajás. *Boletim do Museu Paraense Emílio Goeldi*. Série Ciências Naturais, **9**(3): 597–633.

Rolando A.P. & Macambira M.J.B. 2003. Archean crust formation in Inajá range area, SSE of Amazonian Craton, Brazil, based on zircon ages and Nd isotopes. *In:* 4th South American Symposium on Isotope Geology, Salvador. *Expanded Abstracts*. 1 CD-ROM.

Santos J.O.S. 2003. Geotectônica do Escudo das Guianas e Brasil-Central. *In:* Bizzi, L.A. et al. (Ed.). *Geologia, tectônica e recursos minerais do Brasil: texto, mapas e SIG*. Brasília, CPRM – Serviço Geológico do Brasil, p. 169–226.

Santos M.M., Lana C., Scholz R., Buick I., Schmitz M.D., Kamo S.L., Gerdes A., Corfu F., Tapster S., Lancaster P., Storey C.D., Basei M.A.S., Tohver E., Alkmim A., Nalini H., Krambrock K., Fantini C., Wiedenbeck M. 2017. A new appraisal of Sri Lankan BB zircon as a reference material for LA-ICP-MS U-Pb geochronology and Lu-Hf isotope tracing. *Geostandards & Geoanalytical Research*, doi: 10.1111/ggr.12167.

Santos M.N.S. & Oliveira D.C. 2016. Rio Maria granodiorite and associated rocks of Ourilândia do Norte – Carajás province: petrography, geochemistry and implications for sanukitoid petrogenesis. *Journal of South American Earth Sciences*, **72**: 279–301.

Santos P.J.L., Oliveira D.C., Galarza M.A., Macambira M.J.B. 2010. Geologia, petrografia e geocronologia das rochas granitoides do Complexo Xingu da região de Nova Canadá, município de Água Azul do Norte – Província mineral de Carajás. *In:* SBG, 45º Congresso brasileiro de geologia, Belém. *Anais*. 1 CD-ROM.

Santos R.D., Galarza M.A., Oliveira D.C. 2013. Geologia, geoquímica e geocronologia do Diopsídio-Norito Pium, Província Carajás. *Boletim do Museu Paraense Emílio Goeldi*. Série Ciências da Terra, **8**: 355–382.

Sardinha A.S. 2002. *Geologia, geoquímica e geocronologia do Granito Serra do Rabo, Província Mineral de Carajás*. MS Dissertation, Programa de Pós-Graduação em Geologia e Geoquímica, Instituto de Geociências, Universidade Federal do Pará, Belém, 118 p.

Sardinha A.S., Dall'Agnol R., Gomes A.C.B., Macambira M.J.B., Galarza M.A. 2004. Geocronologia Pb-Pb e U-Pb em zircão de granitoides arqueanos da região de Canaã dos Carajás, Província Mineral de Carajás. *In:* SBG, 42º Congresso brasileiro de geologia, Araxá. *Anais*. 1 CD-ROM.

Sato K., Basei M.A.S., Siga Jr. O., Sproesser W.M., Passarelli C.R. 2008. Novas técnicas aplicadas ao método U-Pb no CPGeo – IGc/USP: avanços na digestão química, espectrometria de massa (TIMS) e exemplos de aplicação integrada com SHRIMP. *Geologia USP*. Série Científica, **7**: 77–99.

Sato K., Tassinari C.C.G.T., Basei M.A.S., Siga Júnior O., Onoe A.T., Souza M.D. 2014. Sensitive high resolution, ion microprobe (SHRIMP IIe/MC) of the Institute of Geoscience of University of São Paulo, Brazil: analytical method and frst results. *Geologia USP*. Série Científica, **14**(3): 3–18.

Scherer E.E., Münker C., Mezger K. 2001. Calibration of the lutetium-hafnium clock. *Science*, **293**: 683–687.

Silva A.C., Dall'Agnol R., Guimarães F.V., Oliveira D.C. 2014. Geologia, petrografia e geoquímica de Associações Tonalíticas e Trondhjemíticas Arqueanas de Vila Jussara, Província Carajás, Pará. *Boletim do Museu Paraense Emílio Goeldi*. Ciências Naturais, **9**(1): 13–46.

Silva G.C., Lima, M.I.C., Andrade A.R.F., Issler R.S., Guimarães G. 1974. *Geologia das folhas SB-22 Araguaia e parte da SC-22 Tocantins*. Belém, DNPM, v. 4, p. 1–143.

Silva L.R., Oliveira D.C., Santos M.N.S. 2017. Diversity, origin and tectonic significance of the Mesoarchean granitoids of Ourilândia do Norte, Carajás province (Brazil). *Journal of South American Earth Sciences*, **82**: 33–61.

Sláma J., Košler J., Condon D.J., Crowley J.L., Gerdes A., Hanchar J.M.,Horstwood M.S.A., Morris G.A., Nasdala L., Norberg N., Schaltegger U.,Schoene B., Tubrett M.N., Whitehouse M.J. 2008. Plešovice zircon – a new natural reference material for U-Pb and Hf isotopic microanalysis. *Chemical Geology*, **249**: 1–35.

Sousa S.D., Oliveira D.C., Gabriel E.O., Macambira M.J.B. 2010. Geologia, petrografia e geocronologia das rochas granitoides do Complexo Xingu da porção a leste da cidade de Água Azul do Norte (PA) – Província Mineral de Carajás. *In:* SBG, 45º Congresso brasileiro de geologia, Belém. *Anais*. 1 CD-ROM.

Souza Z.S., Dall'Agnol R., Althoff F.J., Leite A.A.S., Barros C.E.M. 1996. Carajás Mineral Province: geological, geochronological and tectonic contrasts on the Archean evolution of the Rio Maria granite – greenstone terranes and the Carajás Block. *In:* SBG, Symposium Archaean terranes of the South American Platform, Brasília. *Extended Abstracts*. p. 31–32.

Souza Z.S., Potrel H., Lafon J.M., Althoff F.J., Pimentel M.M., Dall'Agnol R., Oliveira C.G. 2001. Nd, Pb and Sr isotopes of the Identidade Belt, an Archaean greenstone belt of the Rio Maria region (Carajás Province, Brazil): implications for the Archaean geodynamic evolution of the Amazonian Craton. *Precambrian Research*, **109**: 293–315.

Stacey J.S. & Kramers J.D. 1975. Approximation of terrestrial lead isotope evolution by a two-stage model. *Earth and Planetary Science Letters*, **26**: 207–221.

Stern R.A. 1998. High resolution SIMS determination of radiogenic trace isotope ratios in minerals. *In:* Cabri L.J., Vaughan D.J. (Ed.). *Modern approaches to ore and environmental mineralogy*. Ottawa, p. 241–268. (Mineralogical Association of Canada, v. 27).

Tassinari C.C.G. & Macambira M.J.B. 2004. Evolução tectônica do Cráton Amazônico. *In:* Mantesso-Neto V., Bartorelli A., Carneiro C.D.R., Brito Neves B.B. (Ed.). *Geologia do continente Sul Americano*: evolução da obra de F. F. M. de Almeida. São Paulo, BECA, p. 471–486.

Teixeira M.F.B., Dall'Agnol R., Santos J.O.S., Sousa L.A.M., Lafon J.M. 2017. Geochemistry, geochronology and Nd isotopes of the Gogó da Onça Granite: a new Paleoproterozoic A-type granite of Carajás Province, Brazil. *Journal of South American Earth Sciences*, **80**: 47–65.

Teixeira M.F.B., Dall'Agnol R., Silva A.C., Santos P.A. 2013. Geologia, petrografia e geoquímica do Leucogranodiorito Pantanal e dos leucogranitos arqueanos da área a norte de Sapucaia, Província Carajás, Pará: implicações petrogenéticas. *Boletim do Museu Paraense Emílio Goeldi*. Série Ciências Naturais, **8**(3): 291–323.

Vasquez L.V., Rosa-Costa L.R., Silva C.G., Ricci P.F., Barbosa J.O., Klein E.L., Lopes E.S., Macambira E.B., Chaves C.L., Carvalho J.M., Oliveira J.G., Anjos G.C., Silva H.R. 2008. Escala 1:1.000.000. *In:* Vasquez M.L. & Rosa-Costa L.T. (Ed.). *Geologia e recursos minerais do Estado do Pará*: Sistema de Informações Geográficas e SIG: texto explicativo dos mapas geológico e tectônico e de recursos minerais do Estado do Pará. Belém, CPRM, 328 p.

Williams I.S. 1998. U-Th-Pb Geochronology by ion microprobe. *In:* McKibben M.A., Shanks III W.C., Ridley W.I. (Ed.). *Applications of microanalytical techniques to understanding mineralizing processes*. [S.l.], Society of Economic Geologists, p. 1–35. (Reviews in Economic Geology, V.7).

Yardley B.W.D., Mackenzie W.S., Guilford C. 1990. *Atlas of metamorphic rocks and their textures*. New York, John Wiley and Sons, 120 p.

UNIVERSIDADE FEDERAL DO PARÁ
INSTITUTO DE GEOCIÊNCIAS
PROGRAMA DE PÓS-GRADUAÇÃO EM GEOLOGIA E GEOQUÍMICA

PARECER

Sobre a Defesa Pública da Tese de Doutorado de BHRENNO MARAGOANHA

A banca examinadora da Tese de Doutorado de **BHRENNO MARAGOANHA** orientando do Prof. Dr. Davis Carvalho de Oliveira (UFPA), composta pelos professores doutores Lena Virginia Soares Monteiro (USP), Carlos Eduardo de Mesquita Barros (UFPR), Roberto Dall'Agnol (UFPA) e Moacir José Buenano Macambira (UFPA), após apresentação da sua tese intitulada **"PETROLOGIA E EVOLUÇÃO CRUSTAL DA PORÇÃO CENTRAL DO DOMÍNIO CANAÃ DOS CARAJÁS, PROVÍNCIA CARAJÁS"**, emite o seguinte parecer:

O candidato realizou sua apresentação de forma clara, bem organizada e segura. Na arguição mostrou domínio da temática abordada e respondeu às perguntas formuladas pela banca. O trabalho escrito foi apresentado na forma de artigos, inclui um volume expressivo de dados e representa uma contribuição relevante para o conhecimento geológico da Província Carajás.

Finalmente, a banca examinadora decidiu por unanimidade aprovar a tese de doutorado.

Belém, 14 de setembro de 2018.

Prof. Dr. Davis Carvalho de Oliveira (Orientador – UFPA)

Prof.ª Dr.ª Lena Virginia Soares Monteiro (USP)

Prof. Dr. Carlos Eduardo de Mesquita Barros (UFPR)

Prof. Dr. Roberto Dall'Agnol (UFPA)

Prof. Dr. Moacir José Buenano Macambira (UFPA)